

PUBLISHER :



Address of Publisher & Editor's Office :

GDAŃSK UNIVERSITY
OF TECHNOLOGY
Faculty
of Ocean Engineering
& Ship Technology

ul. Narutowicza 11/12
80-952 Gdańsk, POLAND
tel.: +48 58 347 13 66
fax : +48 58 341 13 66
e-mail : office.pmr@pg.gda.pl

Account number :
BANK ZACHODNI WBK S.A.
I Oddział w Gdańsku
41 1090 1098 0000 0000 0901 5569

Editorial Staff :

Tadeusz Borzęcki Editor in Chief
e-mail : tadbtor@pg.gda.pl

Przemysław Wierzychowski Scientific Editor
e-mail : e.wierzychowski@chello.pl

Jan Michalski Editor for review matters
e-mail : janmi@pg.gda.pl

Aleksander Kniat Editor for international relations
e-mail : olek@pg.gda.pl

Kazimierz Kempa Technical Editor
e-mail : kkempa@pg.gda.pl

Piotr Bzura Managing Editor
e-mail : pbzura@pg.gda.pl

Cezary Spigarski Computer Design
e-mail : biuro@oficynamorska.pl

Domestic price :
single issue : 20 zł

Prices for abroad :
single issue :
- in Europe EURO 15
- overseas US\$ 20

ISSN 1233-2585



**POLISH
MARITIME
RESEARCH**

in internet

www.bg.pg.gda.pl/pmr/pmr.php



POLISH MARITIME RESEARCH

No 1(59) 2009 Vol 16

CONTENTS

- 3 TOMASZ CEPOWSKI**
*Modelling of green water ingress into holds of an open-top
containership in its preliminary design phase*
- 8 BARTŁOMIEJ ŻYLIŃSKI**
*Finite element local analysis
of wave slamming on offshore structure*
- 13 JANUSZ KOLENDA**
*Failure criteria of viscoelastic
materials under multiaxial loads*
- 22 HASSAN GHASSEMI**
*Hydrodynamic performance
of coaxial contra-rotating propeller (CCRP) for large ships*
- 29 TADEUSZ KORONOWICZ,
ZBIGNIEW KRZEMIANOWSKI,
TERESA TUSZKOWSKA, JAN A. SZANTYR**
*A complete design of ship propellers
using the new computer system*
- 35 LECH MURAWSKI**
*Identification of shaft line alignment
with insufficient data availability*
- 43 LESZEK MATUSZEWSKI**
Ring thruster – a preliminary optimisation study
- 47 MAREK DZIDA**
*On the possible increasing of efficiency of ship power plant
with the system combined of marine diesel engine, gas turbine
and steam turbine, at the main engine - steam turbine
mode of cooperation*
- 53 ANDRZEJ GĘBURA**
*Diagnosing turbine engine bearing structures
with the aid of FAM-C and FDM-A methods*
- 61 RYSZARD JASIŃSKI**
*Problems of the starting and operating of hydraulic
components and systems in low ambient temperature (Part II)*
- 73 ALFRED BRANDOWSKI**
*Estimation of the probability of propulsion loss
by a seagoing ship based on expert opinions*
- 78 HOANG NGUYEN**
*The application of the ahp method
in ship system risk estimation*
- 83 RAFAŁ SZŁAPCZYŃSKI, ROMAN ŚMIERZCHAŁSKI**
*Supporting navigator's decisions
by visualizing ship collision risk*

The papers published in this issue have been reviewed by:

*Prof. A. Balawender ; Prof. J. Girtler ; Prof. M. Hann
Prof. Y. I. Nyashin ; Prof. M. Sperski
Prof. T. Szelangiewicz ; W. Syrocki, M.Sc.*

Editorial

POLISH MARITIME RESEARCH is a scientific journal of worldwide circulation. The journal appears as a quarterly four times a year. The first issue of it was published in September 1994. Its main aim is to present original, innovative scientific ideas and Research & Development achievements in the field of :

Engineering, Computing & Technology, Mechanical Engineering,

which could find applications in the broad domain of maritime economy. Hence there are published papers which concern methods of the designing, manufacturing and operating processes of such technical objects and devices as : ships, port equipment, ocean engineering units, underwater vehicles and equipment as well as harbour facilities, with accounting for marine environment protection.

The Editors of POLISH MARITIME RESEARCH make also efforts to present problems dealing with education of engineers and scientific and teaching personnel. As a rule, the basic papers are supplemented by information on conferences , important scientific events as well as cooperation in carrying out international scientific research projects.

Scientific Board

Chairman : Prof. **JERZY GIRTLEK** - Gdańsk University of Technology, Poland

Vice-chairman : Prof. **ANTONI JANKOWSKI** - Institute of Aeronautics, Poland

Vice-chairman : Prof. **MIROSLAW L. WYSZYŃSKI** - University of Birmingham, United Kingdom

Dr **POUL ANDERSEN**
Technical University
of Denmark
Denmark

Prof. **STANISŁAW GUCMA**
Maritime University of Szczecin
Poland

Dr **YOSHIO SATO**
National Traffic Safety
and Environment Laboratory
Japan

Dr **MEHMET ATLAR**
University of Newcastle
United Kingdom

Prof. **ANTONI ISKRA**
Poznań University
of Technology
Poland

Prof. **KLAUS SCHIER**
University of Applied Sciences
Germany

Prof. **GÖRAN BARK**
Chalmers University
of Technology
Sweden

Prof. **JAN KICIŃSKI**
Institute of Fluid-Flow Machinery
of PASci
Poland

Prof. **FREDERICK STERN**
University of Iowa,
IA, USA

Prof. **SERGEY BARSUKOV**
Army Institute of Odessa
Ukraine

Prof. **ZYGMUNT KITOWSKI**
Naval University
Poland

Prof. **JÓZEF SZALA**
Bydgoszcz University
of Technology and Agriculture
Poland

Prof. **MUSTAFA BAYHAN**
Süleyman Demirel University
Turkey

Prof. **JAN KULCZYK**
Wrocław University of Technology
Poland

Prof. **TADEUSZ SZELANGIEWICZ**
Technical University
of Szczecin
Poland

Prof. **MAREK DZIDA**
Gdańsk University
of Technology
Poland

Prof. **NICOS LADOMMATOS**
University College London
United Kingdom

Prof. **WITALIJ SZCZAGIN**
State Technical University
of Kaliningrad
Russia

Prof. **ODD M. FALTINSEN**
Norwegian University
of Science and Technology
Norway

Prof. **JÓZEF LISOWSKI**
Gdynia Maritime University
Poland

Prof. **BORIS TIKHOMIROV**
State Marine University
of St. Petersburg
Russia

Prof. **PATRICK V. FARRELL**
University of Wisconsin
Madison, WI
USA

Prof. **JERZY MATUSIAK**
Helsinki University
of Technology
Finland

Prof. **DRACOS VASSALOS**
University of Glasgow
and Strathclyde
United Kingdom

Prof. **WOLFGANG FRICKE**
Technical University
Hamburg-Harburg
Germany

Prof. **EUGEN NEGRUS**
University of Bucharest
Romania

Prof. **YASUHIKO OHTA**
Nagoya Institute of Technology
Japan

Modelling of green water ingress into holds of an open-top containership in its preliminary design phase

Tomasz Cepowski, Assoc. Prof.
Szczecin Maritime University

ABSTRACT



In this paper a method is presented of modelling the green water ingress into holds of open-top containership, which can be useful in the preliminary ship design phase. As a result of the research a mathematical formula which makes it possible to determine a minimum freeboard height with a view of as-low-as-possible occurrence rate of green water ingress into holds at given ship design parameters, was obtained. The research was carried out under assumption of constant ship hull dimensions. The design formula was elaborated by using a method based on a goal-oriented conceptual approach to formulation of design criteria, proposed by IMO. On the basis of the concept a deterministic scenario describing operational conditions of the ship in question, was assumed, and for the conditions the research was performed.

Keywords: green water ingress into ship holds, goal-oriented stability standards, modelling, open-top containership, preliminary designing, ship hull

INTRODUCTION

The traditional design process of ships develops in an iterative way in accordance with the so-called Evans or Andrews-Evans spiral where design characteristics are evolutionarily improved by making successive trial – error steps. Knowledge about a designed ship in preliminary design phase is slight as several technical ship parameters depend on data which are not available in this phase of designing. In order to increase degree of accuracy of the preliminary design phase the designers must be fitted with appropriate tools for precise prediction of selected design characteristics in this design phase, based on ship's main design parameters.

One of the main design problems of open-top containerships is green water entering the deck resulting in water ingress into the holds. As this type of ships does not comply with the requirements of the Load Line Convention, Maritime Administration may admit the ship to service at sea provided that additional model tests described in [6] would be performed (the test conditions are described in a further part of the paper).

Amount of water ingress into the holds of open-top containership depends a.o. on: wave parameters, ship motion parameters, ship hydromechanical and geometrical parameters such as: form and dimensions of underwater part of ship's hull (especially ship length), draught, form of ship's hull stern and bow part, freeboard height, deck shape as well as bulwark structure [2, 3, 13].

Number of geometrical parameters which influence the phenomenon of water ingress into the holds is large, hence in order to eliminate unimportant ones the investigations can be carried out in two ways (according to [11]):

- ★ to change hull dimensions - keeping hull form unchanged (Fig. 1a)
- ★ to change hull form - keeping hull dimensions unchanged (Fig. 1b).

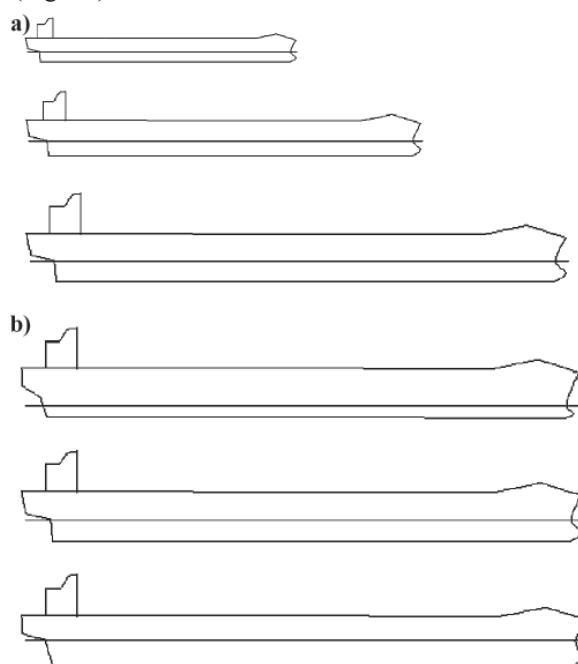


Fig. 1. Two ways of investigation of influence of hull form and hull dimensions on seakeeping qualities [11].
a) unchanged hull form, changeable hull dimensions;
b) unchanged hull dimensions, changeable hull form

Therefore the investigations in question were split in two stages:

- ☆ the investigations of influence of ship hull form parameters on green water ingress into the holds at ship hull dimensions kept unchanged
- ☆ the investigations of influence of ship hull dimensions on green water ingress into the holds at hull form kept unchanged

In this paper are presented results concerning the first stage of the investigations, i.e. the hull form influence on water ingress into holds at hull dimensions kept unchanged.

The investigations were focused only on:

- ⇒ influence of form parameters of ship's hull underwater part
- ⇒ influence of freeboard height (FB)
- ⇒ influence of initial transverse metacentric height (GM)

out of all parameters influencing the phenomenon of water ingress into the holds.

In compliance with [2, 13] these are the factors most influencing the phenomenon of green water entering the deck, which - in consequence - are capable of influencing water ingress into the holds, to a large extent. And, the initial transverse metacentric height constitutes a parameter which significantly influences ship rolling, that can in turn influence relative ship motion in the deck-side zone, hence also green water entering the deck and holds.

The investigations were performed by applying numerical calculations based on the methods not adjusted to determination of amount of water ingress into the holds (but only of statistical frequency of water entering the deck). From results of the research [1, 5] implies the relations between probability of water entering the deck and amount of water ingress into the holds (Tab. 1). And, the results concerning FPSO ships show the linear relation between the water height on the deck and freeboard height exceedance (Fig. 2) [2, 3]:

$$H_0 = a_H \cdot h \quad (1)$$

where:

H_0 – water height on the deck

a_H – a parameter dependent on location of a given point on the deck, and on bow form

h – maximum exceedance of freeboard [3]:

$$h = r - FB \quad (2)$$

where:

r – relative wave motion (Fig. 3)

FB – freeboard.

Tab. 1. Water ingress into the holds, where: V_{gw} – hourly volumetric rate of water ingress, p_{dws} – occurrence probability of water entering the deck [1, 5]

Test no.	V_{gw} [m ³ /h]	p_{dws} [%]
8057	60	4.3
8058	60	1.6
8063	0	0

Therefore in the presented investigations the linear relationship between occurrence rate of green water entering the deck and amount of water on the deck, was assumed, and the phenomenon of water ingress into the holds was modeled by applying the statistical occurrence rate of green water ingress onto the deck.

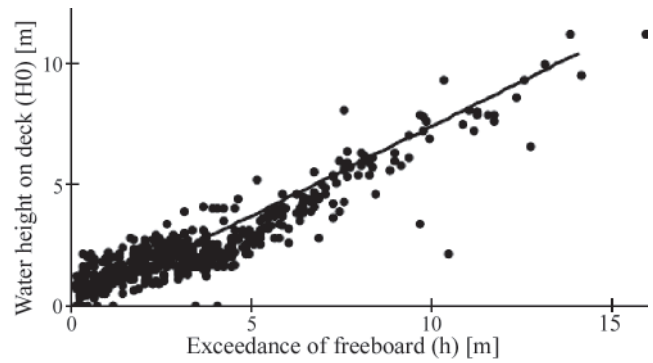


Fig. 2. Relation between the water height on the deck, H_0 , and the exceedance of freeboard, h , for a FPSO ship [3]

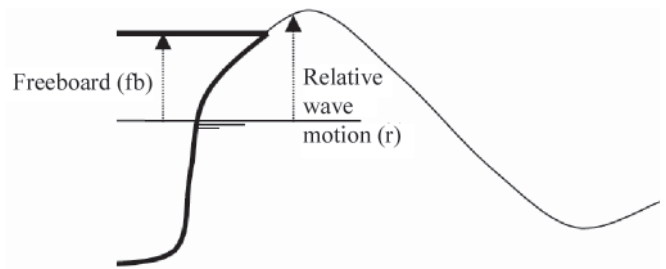


Fig. 3. Definition of the relative wave motion (r) and freeboard (fb) [3]

Hence the investigations presented in this paper were aimed at the following:

- determination of how far initial transverse metacentric height influences water ingress into the holds
- determination of which hull form parameters influence significantly water ingress into the holds at the most unfavourable values of initial transverse metacentric height kept constant
- determination of a relation between important hull form parameters, freeboard height and water ingress into the holds
- elaboration of an analytical function which would make it possible to calculate a minimum freeboard height depending on hull form parameters and an assumed occurrence rate of water ingress into the holds.

For the investigations the method shown in Fig. 4 was chosen. In the proposed method it was assumed that the criterion of water ingress into the holds was formulated for the operational conditions complying with [9, 11], assuming an appropriate deterministic scenario. Such approach is in accordance with the conceptual „goal-oriented” approach to formulation design criteria, proposed by the IMO Maritime Safety Committee [9]. As the deterministic scenario (operational conditions) was assumed the following conditions which comply with the IMO recommendations concerning execution of model tests on open-top containerhips [6] were selected:

- the recommended significant wave height $H_s = 8.5$ m
- wave periods taken every 30 s within the range from 3.5 s to 17 s
- the ship motion parameters most unfavourable with a view of green water entering the deck: (the ship speed v and wave encounter angle β)
- full load conditions (i.e. maximum ship draught)
- the investigations were performed for the point on the deck, in which the greatest green water ingress onto the deck occurs (bow part in vicinity of 1st hold).

Preliminary numerical calculations were performed to determine the ship motion parameters most unfavourable

with a view of water entering the deck. From the calculations resulted that for the assumed ship hull forms (described in a further part of this paper) the most unfavourable ship motion parameters were the following: the ship speed $v = 10$ m/s and the wave encounter angle $\beta = 60^\circ$ (in the reference frame: 0° – following wave, 180° – head wave). As a matter of fact the value of the wave encounter angle β is not in compliance with the research [1], but may be that for such β values the relative motions of underwater part of ship hull are the greatest and cause the largest amount of water to enter the deck.

Ship hull forms obtained by modelling the hull form with the use of the curve of frame section areas, were assumed the model variants.

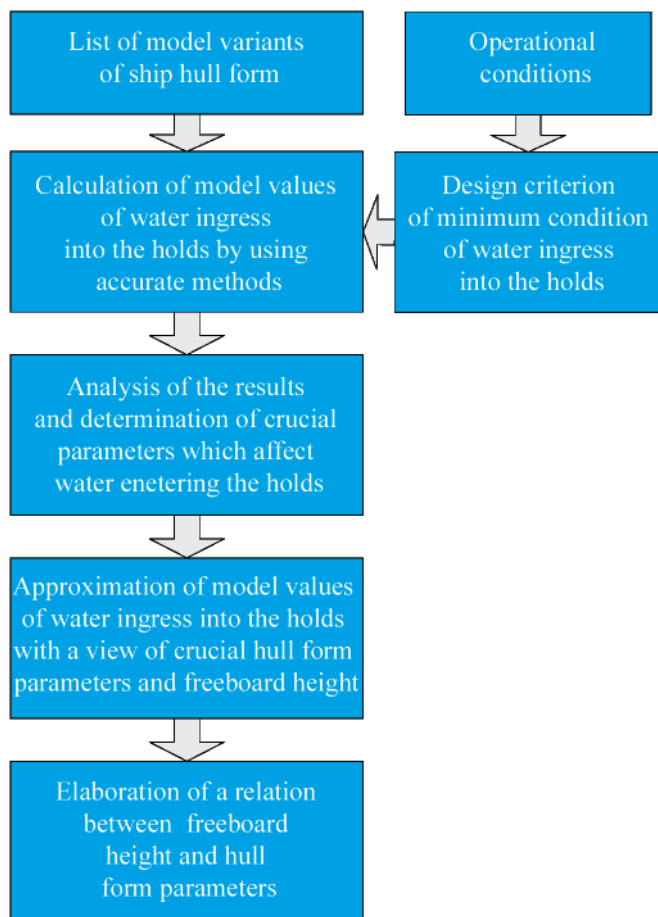


Fig. 4. Schematic diagram of the investigation method

MODELLING SHIP'S HULL FORM BY MEANS OF THE CURVE OF FRAME SECTION AREAS

In the presented investigations ship's hull form was represented by using the curve of frame section areas $F(x)$. The curve was modeled in the same way as presented in [7], i.e. by means of the following analytical functions:

$$F_A = A + Bx + Cx^2 + Dx^3 \quad (3)$$

$$F_F = E + Fx + Gx^2 + Hx^3 \quad (4)$$

where:

- F_A – values of the curve of frame section areas of stern part of hull (Fig. 5)
- F_F – values of the curve of frame section areas of bow part of hull
- x – distance
- A, B, C, D, E, F, G, H – constants determined under the following assumptions (acc. [7]):

$$F_A = 0 \text{ for } x = 0 \quad (5)$$

$$dF_A/dx = AS \text{ for } x = 0 \quad (6)$$

$$dF_A/dx = 0 \text{ for } x = L_A \quad (7)$$

$$F_A = F_{\max} \text{ for } x = L_A \quad (8)$$

$$dF_F/dx = 0 \text{ for } x = L_{AM} \quad (9)$$

$$F_F = F_{\max} \text{ for } x = L_{AM} \quad (10)$$

$$F_F = 0 \text{ for } x = L \quad (11)$$

$$dF_F/dx = FS \text{ for } x = L \quad (12)$$

where:

- L – ship length
- F_{\max} – area of frame section in the midship body zone
- L_A – length of stern part of hull
- L_{AM} – length of stern part and midship body of hull
- AS – slope of the curve $F(x)$ at aft perpendicular
- FS – slope of the curve $F(x)$ at fore perpendicular.

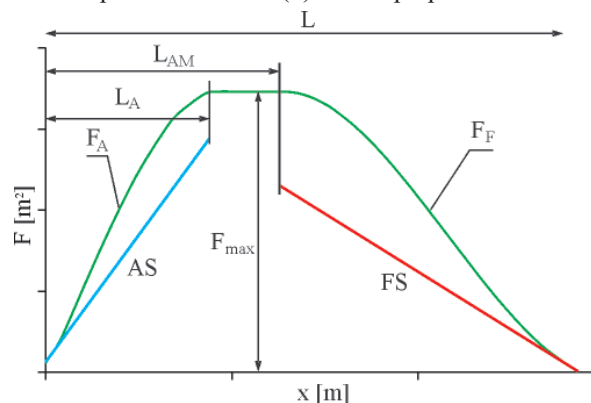


Fig. 5. The curve of frame section areas $F(x)$ in a parametric form

The solution of the Eqs. (3) and (4) together with the conditions: (5), (6), (7), (8), (9), (10), (11) and (12) made it possible to determine the constants as follows:

$$A = 0 \quad (13)$$

$$B = AS \quad (14)$$

$$D = (-2F_{\max} + AS L_A)/L_A^3 \quad (15)$$

$$C = -AS/(2L_A) - 1,5 D L_A \quad (16)$$

$$H = [2 F_{\max} - SF (L - L_{AM})]/(L - L_{AM})^3 \quad (17)$$

$$G = [-F_{\max} - H(L^3 + 2 L_{AM}^3 - 3 L_{AM}^2 L)]/(L - L_{AM})^2 \quad (18)$$

$$F = -2 G L_{AM} - 3 H L_{AM}^2 \quad (19)$$

$$E = -F L - G L^2 - H L^3 \quad (20)$$

On the basis of the parametrized curve of frame section areas the following ship hull form parameters were formulated:

- ❖ length of stern part of hull: L_A
- ❖ length of stern part and midship body of hull: L_{AM}
- ❖ slope of the curve $F(x)$ at aft perpendicular: AS
- ❖ slope of the curve $F(x)$ at fore perpendicular: FS
- ❖ block coefficient of underwater stern part of hull: CBA

$$CBA = \frac{\int_0^{L_A} F(x) dx}{\nabla} \quad (21)$$

where:

- L – ship length
- ∇ – volumetric displacement of underwater part of hull
- $F(x)$ – parametrized curve of frame section areas

❖ block coefficient of underwater bow part of hull - CBF:

$$CBF = \frac{\int_0^L F(x) dx}{L_{AM} \nabla} \quad (22)$$

LIST OF MODEL VARIANTS OF SHIP'S HULL

The list of model variants of ship's hull was elaborated under the following limitations:

- ✦ ship length: $L = 144$ m
- ✦ frame section area in the midship body zone: $F_{max} = 173$ m²
- ✦ design draught: $d = 8.255$ m
- ✦ length of stern part of hull: $L_A = 46 \div 60$ m
- ✦ length of stern part and midship body of hull: $L_{AM} = 64 \div 95$ m
- ✦ slope of the curve $F(x)$ at aft perpendicular: $AS = 1 \div 5$ m
- ✦ slope of the curve $F(x)$ at fore perpendicular: $FS = 1 \div 5$ m
- ✦ freeboard heights: $FB = 0.75 \div 7.75$ m.

Hull block coefficient values were calculated on the basis of the above given parameters (in compliance with Eqs. (21) and (22)) and amounted to:

- ✦ block coefficient of underwater stern part of hull: $CBA = 0.53 \div 0.61$
- ✦ block coefficient of underwater bow part of hull: $CBF = 0.54 \div 0.62$.

On the basis of the above given limitations and Eqs. (3) and (4) 16 model variants of underwater part of hull form were elaborated. For each of the variants, 5 variants of above-water part of hull form were designed by applying various values of freeboard height. As a result, 80 model variants of ship's hull were obtained.

In the first phase of the research influence of initial transverse metacentric height on frequency of water ingress into the holds was analyzed.

INFLUENCE OF INITIAL TRANSVERSE METACENTRIC HEIGHT ON OCCURRENCE RATE OF WATER INGRESS INTO THE HOLDS

In order to determine influence of initial transverse metacentric height on frequency of water ingress into the holds calculations were performed by assuming ship motion parameters and wave parameters in compliance with the assumed deterministic scenario.

The calculations were carried out by means of SEAWAY software. This is a computer program based on the theory of two-dimensional flow around a body, by which ship motions on regular wave and irregular one can be calculated. Its validation tests, presented in [8], demonstrate a high accuracy of calculations.

The influence of the initial transverse metacentric height GM on occurrence rate of water ingress into the holds was more or less similar for all the variants of underwater part of hull form and depended first of all on the height of freeboard FB. In Fig. 6 the influence of GM on frequency of water ingress into the holds is presented for one selected variant of underwater part of hull form.

As results from Fig. 6 the metacentric height GM influences significantly the water ingress into the hold in the range of the freeboard (FB) value equal to or greater than 3.75 m (for smaller FB values the influence of GM is negligible). In such

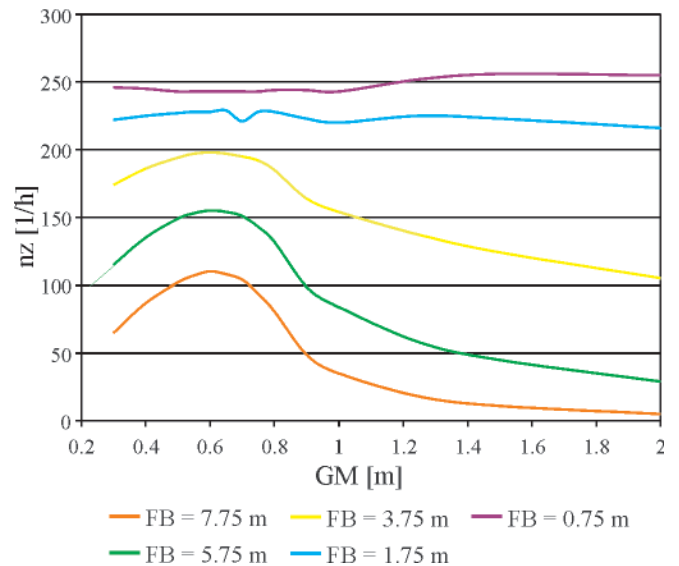


Fig. 6. The influence of the initial transverse metacentric height GM on occurrence rate of water ingress into the hold no. 1, $FB = \text{var}$; the hull form parameters: $L_{AM} = 95$ m, $L_A = 60$ m, $AS = 1$, $FS = 2.2$, $CBA = 0.53$, $CBF = 0.62$, ship speed $v = 10$ m/s, wave encounter angle $\beta = 60^\circ$, significant wave height $H_s = 8.5$ m

cases for GM value greater than about 1 m significant drop of intensity of water ingress into the hold is observed, and the greatest intensity occurs when $GM = 0.6$ m.

As initial transverse metacentric height is an operational parameter dependent a.o. on ship weight and location of its centre of gravity, it is hard to consider it to be a design parameter. Hence in the further part of the research it was decided not to take the parameter into account and to conduct calculations of water ingress into the hold of model ship variants for a GM value at which the water ingress into the hold is the greatest. Such approach allows to decrease number of independent variables in regression model and leads to errors on the so called „safe side“.

APPLICATION OF STATISTICAL METHODS FOR APPROXIMATION OF WATER INGRESS INTO THE HOLDS

In this part of the research calculations of water ingress into the holds were performed for all design ship variants and the assumed value of the initial transverse metacentric height $GM = 0.6$ m. The calculations were performed with the use of accurate methods (namely the SEAWAY software) and input data selected from operational ones resulting from the assumed deterministic scenario.

By making use of statistical methods (namely analysis of variance) and those based on artificial neural networks (namely sensitivity analysis) it was determined which design parameters affect occurrence rate of water ingress into the holds. Next, by making use of linear regression method the following analytical relation between the crucial design parameters and the occurrence rate of water ingress into the holds, nz , was determined:

$$nz = \alpha_0 - \alpha_1 \cdot FB - \alpha_2 \cdot L_A + \alpha_3 \cdot CBF - \alpha_4 \cdot CBA \quad (23)$$

where:

nz – statistical hourly occurrence rate of water ingress into the holds

FB – freeboard height [m]

L_A – length of ship hull stern part (acc. Fig. 6) [m]

CBF – block coefficient of underwater ship hull bow part [-]

CBA – block coefficient of underwater ship hull stern part [-]

$$\begin{aligned}\alpha_0 &= 1111.63 \\ \alpha_1 &= 25.93 \\ \alpha_2 &= 5.23 \\ \alpha_3 &= 229.68 \\ \alpha_4 &= 729.82.\end{aligned}$$

The relation (23) is characterized of:

- ♦ high value of the determination coefficient $R^2 = 0.96$ (explained variance)
- ♦ high significance of free terms and all independent variables, being on the significance level $\alpha = 0.05$,

which proves that the proposed relations are properly adjusted to the model data.

The regression of the dependent variable nz indicate that all components of Eq. (23) including its free term are significant.

After transforming Eq. (23) a design guideline was achieved for determining the minimum freeboard height, FB, in assumed operational conditions and for an arbitrary value of the hourly occurrence rate of water ingress into the holds, nz :

$$FB = \frac{\alpha_0 - \alpha_2 \cdot L_A - \alpha_3 \cdot CBF - \alpha_4 \cdot CBA - nz}{\alpha_1} \quad (24)$$

SUMMARY

In this paper the influence was presented of ship hull form parameters on water ingress into the holds, that made it possible the formula for elaborating the minimum value of freeboard height for open-top containership. The presented method may be used in the preliminary designing of ships of this type. The investigations were performed by applying a method complying with the concept of „goal-oriented” approach to formulation of design criteria, proposed by IMO. Such approach made it possible to elaborate relatively accurate approximations and practical guidelines for designing the open-top containerships and provides comprehensive information on merits of a considered ship already in the preliminary designing phase.

The discussed investigations constitute only a part of research on influence of ship design parameters on the phenomenon of water ingress into the holds. Such investigations should be extended to research on influence of ship dimensions on water ingress into the holds. It may be expected that after determination of crucial ship dimension parameters affecting the water ingress into the holds it would be possible to make the coefficients in Eqs. (23) and (24) dependent on the parameters. Results of such research may be very useful in solving the design problems of open-top containerships.

As results from [1, 2, 3, 4] the linear relation between the occurrence rate of water ingress into the holds, nz , and the volumetric rate of water ingress into the holds, V_{gw} , may be applicable:

$$nz = \alpha \cdot V_{gw} \quad (25)$$

where:

nz – hourly occurrence rate of water ingress into the holds

α – a constant

V_{gw} – hourly volumetric rate of water ingress into the holds.

For determination of α – value to carry out additional investigations is necessary. Knowing the α – value, one is able, on the basis of Eqs. (23) and (24), to elaborate a design criterion for determining the minimum freeboard height, which takes into account the phenomenon of water ingress into the holds. It is possible that such research may be based on determination of influence of exceedance of the freeboard height H_0 [acc. Eq. (1)] on the volumetric rate of water ingress into the holds, V_{gw} .

As resulted from the performed investigations, the phenomenon of green water ingress into the holds is affected by the initial transverse metacentric height. And, the parameter, being operational one, depends on ship load conditions and hence it can be hardly considered a design parameter. Fig. 7 presents the relations which take into account influence of the metacentric height and freeboard height on water ingress into the holds for a ship of constant dimensions. Such relations may be used to plan, in the ship operation phase, a ship loading state in advance of ship departure.

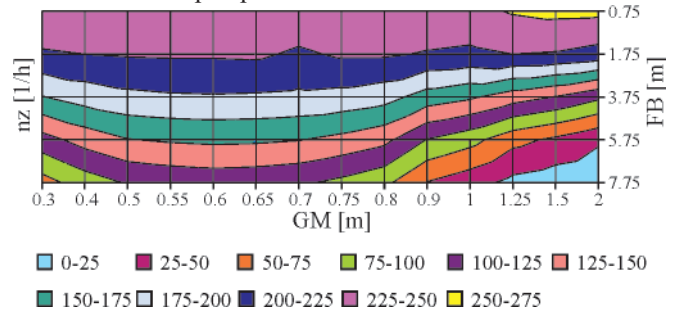


Fig. 7. Statistical hourly occurrence rate of water ingress into the holds, nz , in function of the initial transverse metacentric height GM and the freeboard height FB ; for open-top containership of the length $L = 144$ m, at speed $v = 10$ m/s, wave encounter angle $\beta = 60^\circ$, and significant wave height $H_s = 8.5$ m

BIBLIOGRAPHY

1. Baranowski A., Bech T., Lech R.: *Seakeeping qualities of open-top containerships*. Polish Maritime Research vol. 4 no. 4(14), 1997
2. Buchner B., Joaquín Lopez-Cortijo Garcia.: *Design aspects of green water loading on FPSOs*, The 22nd International Conference on Offshore Mechanics & Arctic Engineering, Cancun, Mexico, 8-13 June, 2003
3. Buchner B.: *Green Water on Ship-type Offshore Structures*, PhD-thesis, Delft University of Technology, 2002
4. Chądzyński W.: *Elements of contemporary design methods of floating units* (in Polish), Szczecin 2001
5. Chądzyński W.: *Open Top Container Vessel Design Problems*, Marine Technology Transactions., Technika Morska, Vol. 9, 1998
6. International Maritime Organization: *Interim guidelines for open top container ships*. MSC/Circ.608/Rev.1, 05.07 1994
7. Jorde J.H.: *The Synthetic Lines Plan – An Aid in the Preliminary Design Phase*, 1st International Euro-Conference on Computer Applications and Information Technology in the Marine Industries COMPIT 2000, Potsdam, 2000
8. Journée J.M.J.: *Verification and Validation of Ship Motions Program SEAWAY*, Report1213a, Delft University of Technology, The Netherlands, 2001.
9. Kobyliński L.: *Goal-based stability standards*, Proceedings of the 9th International Ship Stability Workshop, Germanischer Lloyd Operating 24/7, Hamburg 2007
10. Kobyliński L.: *Appraisal of goal-oriented and risk approach to stability requirements*. 5th International Scientific Technical Conference ExploShip 2008, Kołobrzeg-Bornholm 2008
11. Lloyd A.R.J.M.: *Seakeeping: ship behaviour in rough weather*. Ellis Horwood Limited, England, 1989
12. Szozda Z.: *A Concept of Ship Stability Criteria Based on Cargo Shift Caused by Rolling due to Gust*, Scientific Bulletins No 2(74), Szczecin Maritime University, Szczecin, 2004
13. Watanabe, I., Ueno, M. and Sawada, H.: *Effect of Bow Flare Shape to the Wave Loads of a Container Ship*. JSNA Japan, Vol. 166, 1989.

CONTACT WITH THE AUTHOR

Tomasz Cepowski, Ph. D.
Institute of Marine Navigation,
Maritime University of Szczecin
Wały Chrobrego 1/2
70-500 Szczecin, POLAND
e-mail : cepowski@am.szczecin.pl

Finite element local analysis of wave slamming on offshore structure

Bartłomiej Żyliński, M.Sc.

West Pomeranian University of Technology in Szczecin

ABSTRACT



Offshore platforms are exposed to waves slamming event. Waves hitting the columns with a high velocity are in many cases the design criteria for column structure. This paper focuses on the analysis of wave slamming on floating platform column. Significant for wave slamming pressure is load history, which is usually based on model test. Wave slamming loads were defined on all four walls of column to assess the worst place. For south wall of column three positions exposed to slamming loads between elevation 21.000 (SWL) and elevation 35.500 were checked. Dynamic analysis has been performed with nonlinear FEM program ABAQUS /explicit. The steel was modeled as an elastic-plastic material with isotropic hardening.

Key words: explicit analysis, FEM, offshore structures, wave slamming

INTRODUCTION

Wave forces on offshore structures have very often been analyzed especially for slender cylinder and walls. For non – breaking waves on vertical cylinders those forces are described by well known Morrison equation [1]. Morrison equations are widely used in engineering practice although can not be used for all wave conditions.

Forces responsible for breaking waves, (especially plunging waves) can be more than two times higher than those of non-breaking waves of comparable size [2]. Duration of these impact forces (also called slamming) is extremely short. Many laboratory and experimental studies [3] for regular and non regular waves describe intensity, peak pressure, time history and distribution on cylindrical surface of piles. Theoretical description of impact (forces) was first developed by von Karman [4].

According to these theories the maximum line forces on vertical piles can be given by following equation:

$$f_i = C_s \cdot \rho \cdot R \cdot v^2 \quad (1)$$

where:

C_s – slamming coefficient, is equal π (due to von Karman theory) or 2π (according to Wagner),

ρ – mass density of fluid,

R – radius of the cylinder,

v – velocity of the mass of water.

Time history of impact loads was usually calculated according to Goda [5]. The new approach to description of load

time of impact forces was developed by Wienke [6]. Numerical simulation of slamming based on CFD and comparison with results obtained from [6] can be found in [7].

Complexity of real wave breaking and different types of plunging breakers (i.e. early, perfect breaking) maximum forces calculated according to theories and measured in experiments are well described in [8].

Due to this complexity maximum impact pressure on walls (as on cylindrical structures) forces calculated according to Karman theory (water - hammer analysis) are 8-10 times greater than the measurements. Also, other theoretical attempts for prediction of maximum impact pressure give unreasonable results [8].

The safe and economic design of offshore structures such as (floating platforms) depends significantly on the designed wave loads. In DNV recommended practice [9] prediction of wave impact on plates is based on water-hammer analysis models but experiments are also recommended, in order to give correct estimates of impact loads.

Space averaged slamming pressure over broader area should be calculated from formula:

$$p_s = \frac{1}{2} \rho C_{pa} v^2 \quad (2)$$

Slamming coefficient for flat panels should not be taken as less than C_{pa} equal 2π . There is not given any other information about loading time history, area, etc. According to formula (2) calculated value of averaged pressure can be very high. For ultimate load state (ULS) local plastic deformation of structure should be considered.

WAVE SLAMMING ON COLUMN

Analysed platform has almost identical columns. Wave slamming analysis is based on one of columns. The column is located at the south / west side of the platform hull. Platform north coincides with geographical north for all analysis purposes (i.e wave slamming directions). The column structure itself shows lack of symmetry. Wave slamming can occur on one of four walls. Loads on the inner column walls were reduced by 20% due to shielding effect from the other columns.

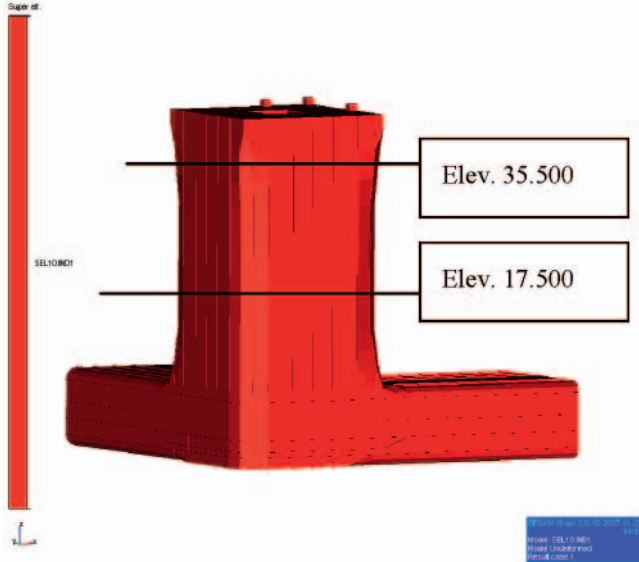


Fig. 1. Model of the analyzed sector of the column

Analysis methodology / design criteria

This section describes the methodology used to verify the structural strength of column exposed to breaking waves based on waves taken from Metocean [10]. Load time history (Fig. 2) is derived from model tests and applied in dynamic analysis with non-linear FEM program ABAQUS. The slamming event has a duration of 160 ms with a peak value at 30 ms. After the peak value the pressure decreases to 10% of the maximum value. This load history is very similar to the one shown in [8]. In the analysis, it is assumed that the main load is the wave breaking pressure and platform has no initial speed.

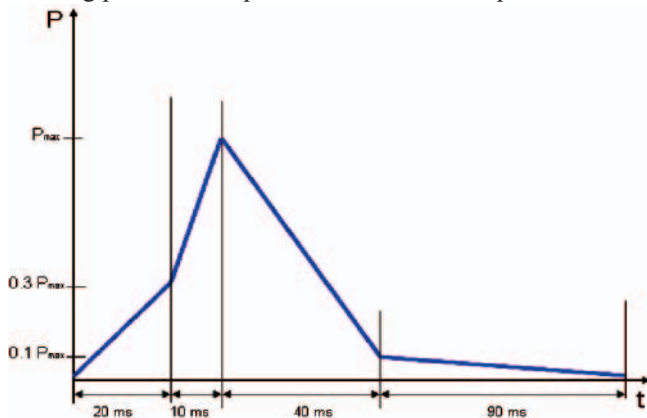


Fig. 2. A design load history for slamming loads on the column face.

The formula for calculating the pressure is shown below:

$$p = LF \cdot \frac{1}{2} \cdot \rho \cdot C_s \cdot v^2 \quad (3)$$

Slamming coefficient C_s is equal to 2π and load factor LF is assumed as 1.30.

Used slamming coefficient, load factor, wave velocity and pressure are calculated according to DNV recommended practice [9]. Due to the mix of air and to the water density ρ is equal to 0.9 t/m^3 .

Tab. 1. Wave slamming pressure parameters

Slamming load on panel (according to DNV CN 30.5)								
Wave from direction	100 year RP Hs	Wave height $H_b = 1.4 \times H_s$	Elevation for top of wave crest	Crest above SWL	Height of window	Velocity [m/s]	Pressure [MPa]	Line load [N/mm]
North 0°	13.1	18.3	31.2	10.2	4.6	14.2	0.736	460
East 90°	3.1	4.3	24.4	3.4	1.1	6.9	0.174	109
South 180°	14.9	20.9	32.8	11.8	5.2	15.1	0.837	523
West 270°	12.2	17.1	30.5	9.5	4.3	13.7	0.686	428

Slamming can only affect areas above still water level (SWL), SWL is at elevation of 21 metres.

Exposed area could be anywhere between still water line (el. 21 m) and the top of wave crest. Different positions are analysed for south wall of column c1 where calculated wave slamming pressure was the highest. Areas used to apply wave slamming pressure are shown on Fig.3. Width, height, and wave slamming pressure value for each area can be seen in Tab. 2. Horizontal width: the flat surface between bilges, but limited to a width of about 8 meters corresponding to a sector of 45° (with origin in the centre of the column). Vertical height: one fourth of the wave height (given in Tab. 2).

Tab. 2. Areas exposed to wave slamming pressure on south wall of column

Flat plate pressure distribution area south wall of c1:	A1	A2	A3
Top of exposed area	el. 32250	el. 29250	el. 26250
Width [m]	8.125	8.125	8.125
Height [m]	5.5	5.5	5.5
Peak Pressure [MPa]	0.837	0.837	0.837

Design criteria were defined as follows: stiffeners / web frames should have ultimate strength to sustain slamming pressure from breaking wave with a return period of 100 year including a load factor of 1.3, It must be ensured that

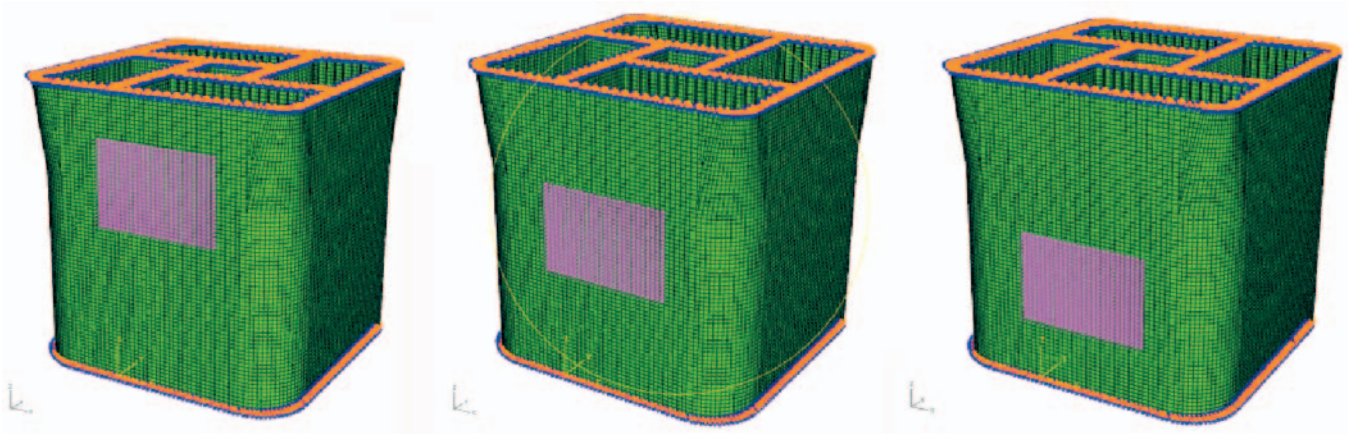


Fig. 3. Column c1 south wall. Wave slamming pressure exposed area A1 -A3

the structure hit by the breaking wave will stabilize in a load history, non-linear analysis using plastic strain formulation (acc. to NORSOK N-004 [11]).

DYNAMIC FEM ANALYSIS

Explicit solution method

Abaqus V6.7 explicit was used for the calculations. The explicit method is very well suited for the analysis of high speed dynamic events and complex and highly non-linear problems [12].

Explicit calculations are conditionally stable and the maximum time increment is limited by the element size and the element mass. Automatic time incrementation was used and time increment was about $7.75E-06$ s. Total time of explicit dynamic analysis in ABAQUS was set to 0 - 1.1 [s] and it is much longer than the duration of slamming loads (0 - 0.16 [s]). The averaged slamming pressure was applied to the structure, load history was defined by using amplitude options. Amplitude is varying between 0.0 and 1.0, (see Fig. 2). Mass proportional damping value was defined as 0.02. For improving numerical solution artificial damping is also included in explicit calculation procedures by default. Upon wave impact, kinetic energy of wave slamming is absorbed by elastic-plastic deformation of column structure.

Material model

All plates and stringers in the column are made of 420 MPa steel. In the calculations, the yield stress of the material was taken as 420 MPa. An isotropic hardening model was defined in ABAQUS.

The hardening behavior (engineering as well as true stress-strain) of the material is explained in Fig. 3. In a tensile test, the force and the elongation are measured. True stress is the force per unit of deformed cross section, engineering (nominal) stress is the force per unit of the initial cross section. True strain is based on the deformed length, whereas engineering strain is the elongation divided by the original length. An engineering strain of 20% is the same as a true (logarithmic) strain level of 18%.

Geometry and FEM mesh

The relevant part of the column for the slamming analysis is between the elevation of 17.5 m and 35.5 m. Below deck at elevation of 26.5 m, each side of the external shell is supported by 2 bulkheads. Over this deck, the shell is supported by one bulkhead and one cross-over I-beam from the central void. Only the upper part is considered, since the horizontal framing is much weaker than below the deck. The outer skin and the bulkhead walls are reinforced by stringers HP 320x12 that are equally spaced at 0.625 m. In horizontal planes, the outer skin

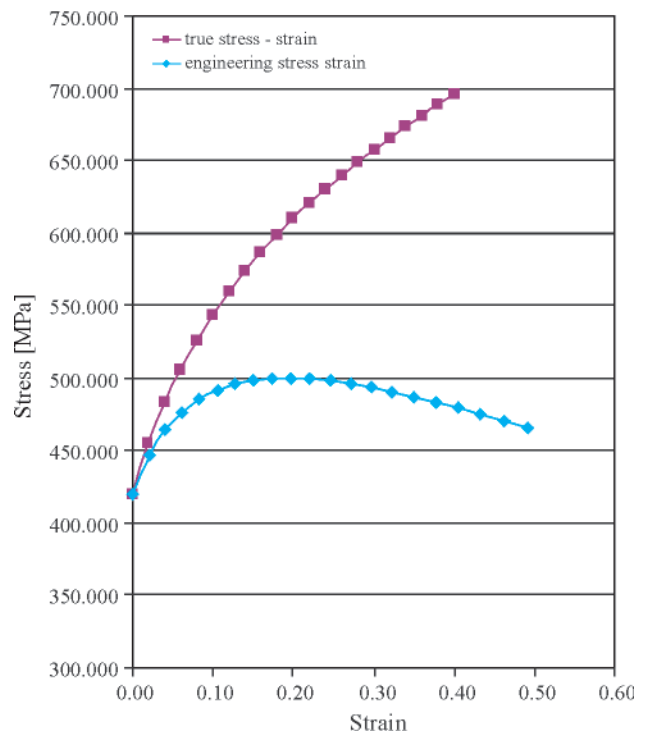


Fig. 4. Hardening behavior of 420 MPa steel

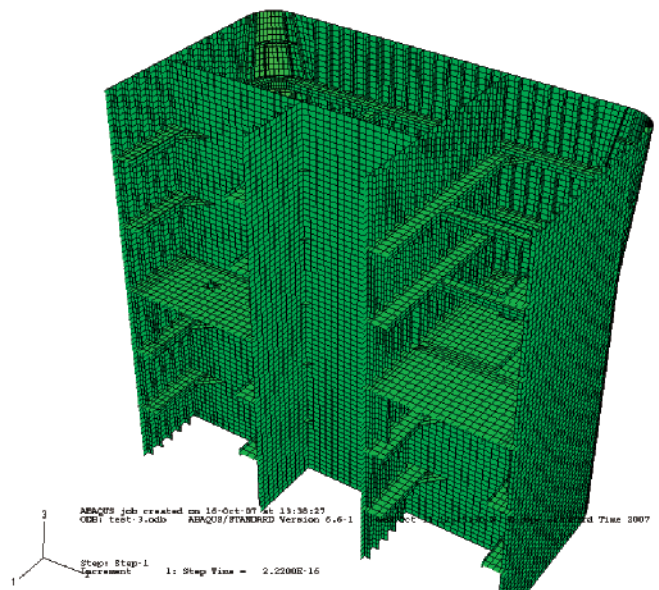


Fig. 5. Cross sectional view of the column

and the bulkhead walls are supported by frames, which are equally spaced at 3.0 m. An I-beam connects the corner of the central void with the outer skin.

The FEM model was made with a grid of nodes that were spaced in horizontal direction of 312.5 mm and 250 mm in vertical direction and the mesh is almost square. In the FEM model, the frame flanges were therefore modeled as 300 mm high and 20 mm thick. Stiffener web was assumed as 300 mm long and 12 mm thick. For the stiffeners on south wall the bulb was modeled with T3D2 elements .

With the given mesh size, there are 5 elements over the web of the frames and their behavior will be described quite accurately. The stringers have two elements in their web, and their behavior is less accurate, but still sufficient. Square shell elements of type S4 were used everywhere, except for the brackets where some triangular shell elements of type S3R were used as well. The brackets between bulkhead and frames were modeled as triangles whose short sides are about 1600 mm long. The I-beams were modeled with shell elements of type S4.

Eight millimeters corrosion allowance was used for column skin plates (up to 5 meters above SWL) and used shell thickness = 16 mm. Thickness of bulkhead and deck was 12 mm.

Load cases

A wave slamming load is a local load. Waves hit only selected (relative small) area of column outer surface. Although wave breaking pressures act only local, deformation and stress level can be very serious. We can compare this results to results obtained from global analysis. Displacements from global model (SESAM) have been applied as prescribed displacements in the corresponding nodes of the column local model (ABAQUS). ABAQUS model used in wave slamming analysis was more detailed than the model used in the global analysis. Load cases for wave slamming on all four walls correspond to loads described in Tab. 1. Load cases on south wall correspond to Tab. 2. Gravity was included and gravity constant equal to 9.81 m/s^2 .

FEM RESULTS

Global and slamming loads

Analysis show that stress level from global model loads is very small especially if we compare it to the results from wave slamming analysis. Von Mises stress distribution on east and north wall of column can be seen on Fig. 6.

Values of wave breaking pressure acting on south, west, and north walls are considerable. Von Mises's stresses level exceeded yield limit of 420 steel. On east wall von Mises's stresses level didn't exceed yield limit and structure of east wall deforms only elastic. For south, west and north walls the highest plastic equivalent strains (PEEQ) occurred in the web of frame (Fig. 7). The highest strain level was 2.8 % on south wall in the web of the frame. Plastic equivalent strains for other walls and other parts of column are shown in Tab. 3.

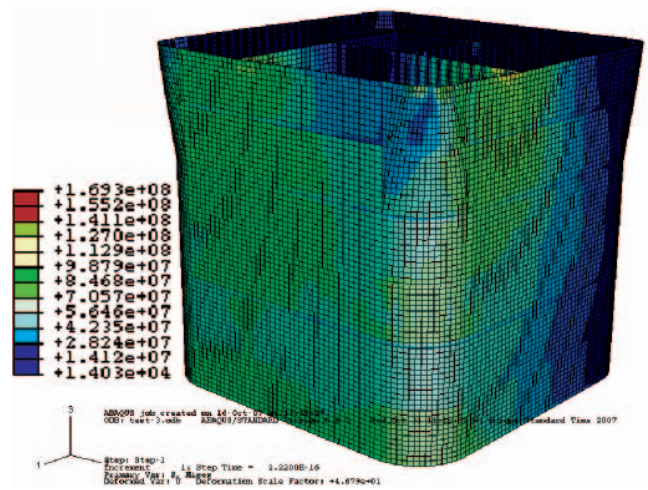


Fig. 6. Von Mises stress distribution from global model load [Pa]

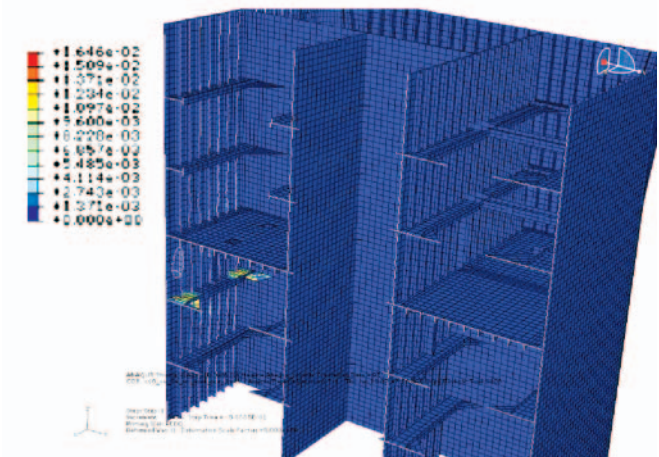
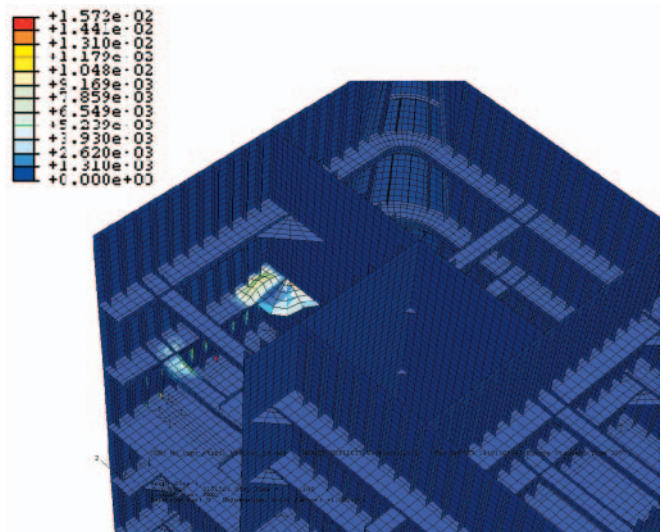


Fig.7. PEEQ strains on south wall of column

Tab. 3. Maximum plastic equivalent strains PEEQ in columns parts

Maximum equivalent plastic strain (%)							
	slamming pressure			frame		stiffener	
Load case	(MPa)	skin	bracket /frame bulkhead/	web	flanges	midspan	end
south wall	0.837	-	1.4	2.8	0.6	1.9	0.4
west wall	0.686	-	0.5	-	-	1.4	1.1
north wall	0.736	-	1.3	1.1	0.3	0.9	1.5
east wall	0.174	N/A	N/A	N/A	N/A	N/A	N/A

Plastic strains as a function of time

It is important to check whether plastic strains level reminds constant after first occurrence. It is possible when dynamic/explicit analysis time is much longer then duration of slamming pressure load. Analysis time was set from 0.0 to 1.1 s. Local plastic strains were checked for different exposed areas (acc to Tab. 2) on the south wall.

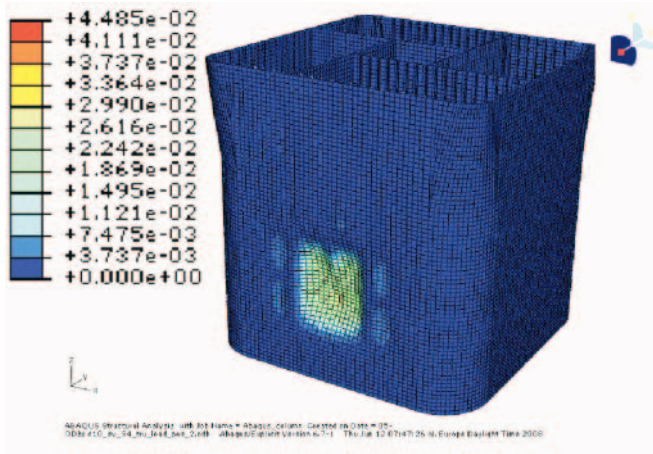


Fig. 8. South wall – exposed area A3, Displacement [m] at Time =50 ms.

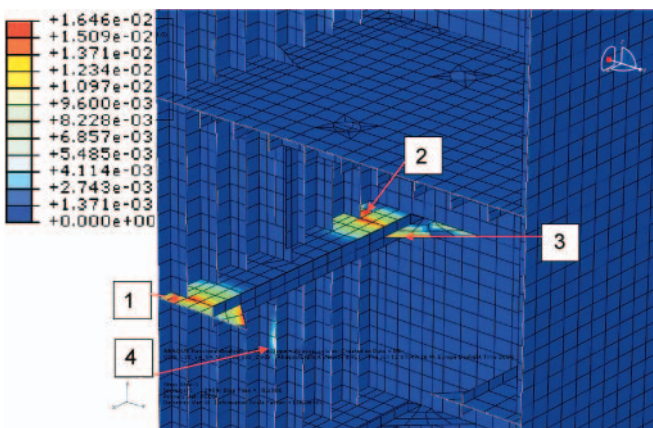


Fig. 9. South wall – exposed area A3, Time =50 ms, PEEQ strains level

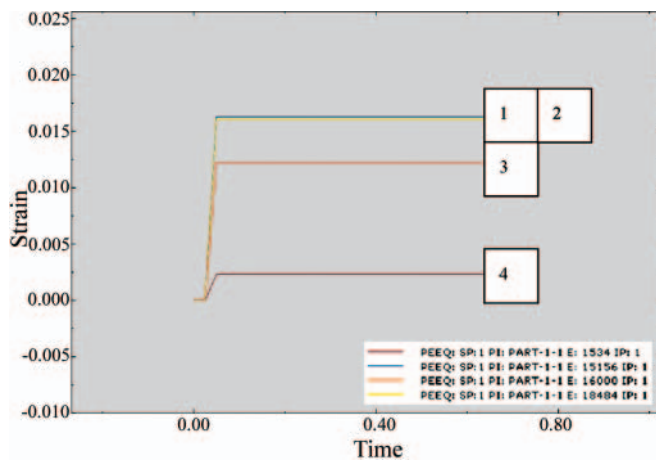


Fig. 10. South wall – exposed area A3. Local plastic equivalent strains (PEEQ) at selected elements as function of time.

CONCLUSION

The results shown herein presents the dynamic nonlinear elasto-plastic analysis of structure of floating platform. Slamming pressures calculated according to DNV recommended practice for ultimate load state (ULS) may compound the difficulties in adequately design. Stresses from global analysis are very small especially if compare to wave slamming results. In the column structure loaded with the 100 year wave slamming loading (used load factor 1.3) local yielding occurred. Maximum plastic equivalent strains (PEEQ) level was about 2.8%, found at time equal to 30 [ms] (maximum of load amplitude). During rest of analysis time (30 to 110 [ms]) PEEQ strains level remained constant. Local plastic deformation of structure should be acceptable. The numerical results satisfy equilibrium and symmetry (Fig. 7). Further investigation of other aspects of analysis i.e: local mesh refinement, possible imperfection and local buckling of stiffeners can be also quickly performed with ABAQUS system.

BIBLIOGRAPHY

1. Morison J. R., O'Brien M. P., Johnson J. W., Schaaf S. A.: *The forces exerted by surface waves on piles*. Journal of Petroleum Technology, Petroleum Transactions, AIME 189, 1950
2. Chakrabarti S. K., Kriebel D., Berek E. P.: *Forces on single pile caisson in breaking waves and current*. Applied Ocean Research 19, 1997
3. Chan E. S., Cheong H. F., Tan B. C.: *Laboratory study of plunging wave impacts on vertical cylinders*. Coastal Engineering 25, 1995
4. von Karman T.: *The impact on seaplane floats during landing*. National Advisory Committee for Aeronautics. Technical Note, vol. 321, 1929
5. Goda Y.: *Wave forces on a vertical circular cylinder: Experiments and a proposed method of wave force computation*. Report No. 8, Port and Harbour Technical Research Institute, 1964
6. Wienke J., Oumeraci H.: *Breaking Wave Impact Force on a Vertical and Inclined Slender Pile – Theoretical and Large-scale Model Investigations*. Journ. Coastal Engineering, Vol. 52, 2005
7. Cortel C., Grilli S. T.: *Numerical Modeling of Extreme Wave Slamming on Cylindrical Offshore Support Structures*. Proceedings of the Sixteenth (2006) International Offshore and Polar Engineering Conference San Francisco, California, USA, May 28-June 2, 2006.
8. Kirkgoz M. S.: *Breaking Wave impact on vertical and sloping coastal structures*. Ocean Eng., Vol. 22, No. 1, 1995
9. Recommended Practice DNV-RP-C205, April 2007 *Environmental conditions and environmental loads*
10. Metocean Design Basis - C097-GJO-Z-IP-0018, rev.5
11. Design of Steel Structures – NORSOK N-004, Rev.2
12. Abaqus inc., *Abaqus Analysis user Manuals*, Providence. USA.

CONTACT WITH THE AUTHOR

Bartłomiej Żyliński, M.Sc.
 Division of Applied Mechanics
 West Pomeranian University
 of Technology in Szczecin
 Al. Piastów 41
 71-065 Szczecin, POLAND
 e-mail: bartek.zylinski@StrataMarineOffshore.no

Failure criteria of viscoelastic materials under multiaxial loads

Janusz Kolenda, Prof.
Polish Naval Academy

ABSTRACT



The load capacity of homogeneous, isotropic viscoelastic materials subjected to multiaxial stresses is considered. For this purpose uniaxial equivalent stresses in selected load cases are determined and relevant criteria applied. It is shown that in the case of constant load the yield criterion does not differ from that for perfectly elastic materials. Similar conclusion has been drawn for the fatigue and yield criteria at in-phase and out-of-phase stresses. On the contrary, the criteria derived for viscoelastic materials subjected to periodic loads do not coincide with those for perfectly elastic materials.

Keywords: viscoelastic material, multiaxial stress, fatigue criteria, yield criterion, static load, vibratory load

INTRODUCTION

Even in the region below the limit of proportionality, metals are not perfectly elastic, and their deformation is accompanied by internal friction. As a result, their strain response to static loads is time-dependent, and when the load varies in time, the strain lags behind the stress. In particular, after the rapid shortening of a bar that occurs when its axial tensile load is removed, the bar continues to shorten gradually until the initial length has been reached. This gradual return to the initial length following unloading is called anelastic behaviour or viscoelasticity [1, 2]. Anelastic strain differs from plastic strain because it is recoverable rather than permanent, and it differs from elastic strain because it is recoverable at a rate which is slow in comparison to the rate of recovery of elastic strain. The elastic behaviour of metals and structural steels is much more significant than their anelastic properties, which enables the strength criteria to be formulated with the aid of the Hooke's law for perfectly elastic materials. However, as shown in the present paper, dissipative properties of engineering materials may be also taken into account in design considerations, especially in the case of periodic load when an equivalent reduced stress is to be determined in calculations of a structural limit state.

During the last two decades, the emphasis in structural design has been moving from the allowable stress design to the limit state design [2]. Generally, four types of limit states may be specified:

- ✗ serviceability limit state,
- ✗ ultimate or yield limit state,
- ✗ fatigue limit state,
- ✗ accidental limit state.

This paper concerns the yield and fatigue limit states of viscoelastic materials under combined static and vibratory loads.

YIELD CRITERION OF VISCOELASTIC MATERIALS UNDER MULTIAXIAL STATIC LOADS

The stress and strain at which a material either begins to yield or fractures due to a uniaxial load can be measured relatively easily. But for an arbitrarily shaped body under arbitrary loads, the prediction of yield or fracture is very difficult. Some criterion is needed to make predictions without testing every material under every possible loading. An ideal criterion would be one that is based on a simple uniaxial test. Then the normal stress, normal strain, shear stress, the strain energy, or the distortion energy, among other possibilities, could be taken into account. Each of these reaches its failure value at the same load in a uniaxial test, but this is no longer true if the state of stress is either two- or three-dimensional. Therefore various theories regarding the initiation of yielding have been developed. The earliest, and the simplest, relation describing the conditions for initiating plastic flow under static or quasi-static load is the shear stress law. This law states that the metal will yield when the largest shear stress reaches a critical value, irrespective of the stress state. A somewhat more accurate law is the "energy-of-distortion" criterion, also called the Huber-Mises-Hencky (HMH) strength theory [2-4]. It embodies the physical hypothesis that yielding occurs when a certain critical value of distortion energy is reached, which corresponds to that where the equivalent reduced stress, σ_{eo} ,

reaches the yield strength, R_e , determined from the uniaxial tension test. Experiments show that this is an excellent criterion for the yielding of ductile materials [2]. This criterion is also useful for ductile materials under multiaxial proportional loading and high-cycle fatigue [5]. Therefore it will be also used in the present paper.

To begin with, let us consider a perfectly elastic solid under general state of static load resulting in normal and shear stress and strain components σ_{j_0} , ε_{j_0} , τ_{k_0} , γ_{k_0} , ($j = x, y, z$; $k = xy, yz, zx$).

The elastic strain energy per unit volume is [4]:

$$\Psi_o = \frac{1}{2} \left(\sum_j \sigma_{j_0} \varepsilon_{j_0} + \sum_k \tau_{k_0} \gamma_{k_0} \right) \quad (1)$$

where:

$$\begin{aligned} \varepsilon_{x_0} &= \frac{1}{E} [\sigma_{x_0} - \nu(\sigma_{y_0} + \sigma_{z_0})] \\ \varepsilon_{y_0} &= \frac{1}{E} [\sigma_{y_0} - \nu(\sigma_{x_0} + \sigma_{z_0})] \\ \varepsilon_{z_0} &= \frac{1}{E} [\sigma_{z_0} - \nu(\sigma_{x_0} + \sigma_{y_0})] \\ \gamma_{k_0} &= \frac{1}{G} \tau_{k_0} \end{aligned} \quad (2)$$

In Eqs (2), expressing the Hooke's law for multiaxial stress in elastic solids, E is the Young modulus, ν is the Poisson's ratio, and:

$$G = \frac{E}{2(1+\nu)} \quad (3)$$

is the shear modulus. Substitution of Eqs (2) and (3) into Eq. (1) results in:

$$\Psi_o = \frac{1}{E} \left[\frac{1}{2} (\sigma_{x_0} + \sigma_{y_0} + \sigma_{z_0})^2 + (1+\nu) \left(\tau_{xy_0}^2 + \tau_{yz_0}^2 + \tau_{zx_0}^2 - \sigma_{x_0} \sigma_{y_0} + \sigma_{y_0} \sigma_{z_0} + \sigma_{z_0} \sigma_{x_0} \right) \right] \quad (4)$$

which can be rewritten as [4]:

$$\Psi_o = \Psi_{do} + \Psi_{vo} \quad (5)$$

where:

$$\Psi_{do} = \frac{1+\nu}{6E} \left[(\sigma_{x_0} - \sigma_{y_0})^2 + (\sigma_{y_0} - \sigma_{z_0})^2 + (\sigma_{z_0} - \sigma_{x_0})^2 + 6(\tau_{xy_0}^2 + \tau_{yz_0}^2 + \tau_{zx_0}^2) \right] \quad (6)$$

is the strain energy of distortion, and:

$$\Psi_{vo} = \frac{1-2\nu}{6E} (\sigma_{x_0} + \sigma_{y_0} + \sigma_{z_0})^2 \quad (7)$$

is the strain energy of volume change. According to the HMM theory, at yield, the distortion energy at a point in a three-dimensional state of stress is equal to the distortion energy at yield in the uniaxial case. Thus:

$$\Psi_{deo} = \Psi_{do} \quad (8)$$

where:

$$\Psi_{deo} = \frac{1+\nu}{3E} \sigma_{eo}^2 \quad (9)$$

is the strain energy of distortion per unit volume under reduced stress σ_{eo} in tension. Hence [2, 4, 5]:

$$\sigma_{eo} = \left[\sigma_{x_0}^2 + \sigma_{y_0}^2 + \sigma_{z_0}^2 - \sigma_{x_0} \sigma_{y_0} - \sigma_{y_0} \sigma_{z_0} + \sigma_{z_0} \sigma_{x_0} + 3(\tau_{xy_0}^2 + \tau_{yz_0}^2 + \tau_{zx_0}^2) \right]^{1/2} \quad (10)$$

and the criterion in question reads:

$$\sigma_{eo} < R_e \quad (11)$$

Now suppose that the considered load is applied to a viscoelastic solid at the time $t = 0$ and the stress components σ_{j_0} and τ_{k_0} are maintained constant. Then the constitutive equations for strains are [6]:

$$\begin{aligned} \varepsilon_j(t) &= \varepsilon_{j_0} \left(1 - e^{-\frac{E}{\eta} t} \right) \\ \gamma_k(t) &= \gamma_{k_0} \left(1 - e^{-\frac{E}{\eta} t} \right) \end{aligned} \quad (12)$$

and the elastic strain energy becomes time-dependent:

$$\Psi(t) = \frac{1}{2} \left[\sum_j \sigma_{j_0} \varepsilon_j(t) + \sum_k \tau_{k_0} \gamma_k(t) \right] \quad (13)$$

In Eqs (12), η is the coefficient of viscous damping of normal strain in the Kelvin-Voigt's model of the material [2, 6]. Substitution of Eqs (2) and (12) into Eq. (13) gives:

$$\Psi(t) = \Psi_o \left(1 - e^{-\frac{E}{\eta} t} \right) \quad (14)$$

with:

$$\lim_{t \rightarrow \infty} \Psi(t) = \Psi_o \quad (15)$$

Hence it is clear that Eq. (10) and the criterion (11) are applicable also to viscoelastic materials under constant loads.

FAILURE CRITERIA OF VISCOELASTIC MATERIALS UNDER MULTIAXIAL HARMONIC LOADS

Under dynamic loading conditions, the strength of a structural element is degraded due to the cyclic application of load or strain which may lead to fatigue damage. It is why in this paper not only the yield criterion but also fatigue criteria are considered.

The fatigue load that a structure can withstand is often significantly less than the load which it would be capable of if the load were applied only once. For the case of combined dynamic loading, where torsion, bending and/or tension loads vary in time, no one strength theory is universally accepted, and all existing multiaxial fatigue criteria can demonstrate large scatter [7]. Only multiaxial in-phase stresses with constant principal directions can be treated fairly well using the conventional strength theories [8]. In [9] an attempt was made to extend the application range of the HMM theory to other stress states, in particular to those with variable principal directions. In what follows, the results obtained in [6, 9] are taken into account.

If a multiaxial harmonic load is producing in a perfectly elastic solid the zero mean stress with in-phase components:

$$\begin{aligned} \sigma_j &= \sigma_{ja} \sin \omega t ; \quad j = x, y, z \\ \tau_k &= \tau_{ka} \sin \omega t ; \quad k = xy, yz, zx \end{aligned} \quad (16)$$

the equivalent reduced stress in tension-compression takes the form:

$$\sigma_e = \sigma_{ea} \sin \omega t \quad (17)$$

where:

σ_{ja}, τ_{ka} – amplitudes of the stress components ; ω – circular frequency ; σ_{ea} – amplitude of the reduced stress given by [8]:

$$\sigma_{ea} = \left[\begin{array}{l} \sigma_{xa}^2 + \sigma_{ya}^2 + \sigma_{za}^2 - \sigma_{xa} \sigma_{ya} - \sigma_{ya} \sigma_{za} + \\ - \sigma_{za} \sigma_{xa} + 3(\tau_{xya}^2 + \tau_{yza}^2 + \tau_{zxa}^2) \end{array} \right]^{1/2} \quad (18)$$

Consequently, the criterion of an infinite fatigue life and the yield criterion read:

$$\sigma_{ea} < Z_{rc} \quad (19)$$

$$\sigma_{ea} < R_e \quad (20)$$

where:

Z_{rc} – the fatigue limit of the material under fully reversed tension-compression.

In the high-cycle fatigue regime, the criterion of a finite fatigue life based on the S-N curve (Wöhler's curve) is commonly accepted [10]. According to this approach, in the case of fully reversed tension-compression under the stress (17) one gets:

$$\frac{N_d}{K} \sigma_{ea}^m < 1 \quad (21)$$

where:

N_d – required number of stress cycles to achieve a given design life

K – fatigue strength coefficient

m – fatigue strength exponent.

If, however, the in-phase stress (16) is applied to a viscoelastic material, its strain response is [6]:

$$\begin{aligned} \varepsilon_x &= \frac{1}{\sqrt{E^2 + \eta^2 \omega^2}} [\sigma_{xa} - \nu(\sigma_{ya} + \sigma_{za})] \sin(\omega t - \alpha) \\ \varepsilon_y &= \frac{1}{\sqrt{E^2 + \eta^2 \omega^2}} [\sigma_{ya} - \nu(\sigma_{xa} + \sigma_{za})] \sin(\omega t - \alpha) \\ \varepsilon_z &= \frac{1}{\sqrt{E^2 + \eta^2 \omega^2}} [\sigma_{za} - \nu(\sigma_{xa} + \sigma_{ya})] \sin(\omega t - \alpha) \\ \gamma_k &= \frac{2(1+\nu)}{\sqrt{E^2 + \eta^2 \omega^2}} \tau_{ka} \sin(\omega t - \alpha), \quad \alpha = \arctg \frac{\eta \omega}{E} \end{aligned} \quad (22)$$

So, the elastic strain energy per unit volume:

$$\Psi = \frac{1}{2} \left(\sum_j \sigma_j \varepsilon_j + \sum_k \tau_k \gamma_k \right) \quad (23)$$

becomes:

$$\begin{aligned} \Psi &= \frac{1}{2\sqrt{E^2 + \eta^2 \omega^2}} \left\{ \sigma_{xa} [\sigma_{xa} - \nu(\sigma_{ya} + \sigma_{za})] + \sigma_{ya} [\sigma_{ya} - \nu(\sigma_{xa} + \sigma_{za})] + \sigma_{za} [\sigma_{za} - \nu(\sigma_{xa} + \sigma_{ya})] + \right. \\ &\quad \left. + 2(1+\nu) \sum_k \tau_{ka}^2 \right\} \sin \omega t \sin(\omega t - \alpha) = \frac{1}{\sqrt{E^2 + \eta^2 \omega^2}} \left[\frac{1}{2} (\sigma_{xa} + \sigma_{ya} + \sigma_{za})^2 + \right. \\ &\quad \left. + (1+\nu) (\tau_{xya}^2 + \tau_{yza}^2 + \tau_{zxa}^2 - \sigma_{xa} \sigma_{ya} - \sigma_{ya} \sigma_{za} - \sigma_{za} \sigma_{xa}) \right] \sin \omega t \sin(\omega t - \alpha) \end{aligned} \quad (24)$$

On the other hand, for the reduced stress (17) and corresponding reduced strain:

$$\varepsilon_e = \frac{1}{\sqrt{E^2 + \eta^2 \omega^2}} \sigma_{ea} \sin(\omega t - \alpha) \quad (25)$$

the elastic strain energy per unit volume is given by:

$$\Psi_e = \frac{1}{2} \sigma_e \varepsilon_e = \frac{1}{2\sqrt{E^2 + \eta^2 \omega^2}} \sigma_{ea}^2 \sin \omega t \sin(\omega t - \alpha) \quad (26)$$

Consequently, the relationships for distortion energies per unit volume in the actual and reduced stress states read:

$$\Psi_d = \frac{1+\nu}{6\sqrt{E^2 + \eta^2\omega^2}} \left[(\sigma_{xa} - \sigma_{ya})^2 + (\sigma_{ya} - \sigma_{za})^2 + (\sigma_{za} - \sigma_{xa})^2 + 6(\tau_{xya}^2 + \tau_{yza}^2 + \tau_{zxa}^2) \right] \sin \omega t \sin(\omega t - \alpha) \quad (27)$$

$$\Psi_{de} = \frac{1+\nu}{3\sqrt{E^2 + \eta^2\omega^2}} \sigma_{ea}^2 \sin \omega t \sin(\omega t - \alpha) \quad (28)$$

Equating the right-hand sides of Eqs (27) and (28) yields again Eq. (18) so that the criteria (19) through (21) remain valid.

In the case of non-zero mean stress with in-phase components:

$$\sigma_j = \sigma_{jo} + \sigma_{ja} \sin \omega t \quad ; \quad \tau_k = \tau_{ko} + \tau_{ka} \sin \omega t \quad (29)$$

the equivalent reduced stress can be expressed as:

$$\sigma_e = \sigma_{eo} + \sigma_{ea} \sin \omega t \quad (30)$$

where: σ_{eo} is the mean value of the reduced stress. In Eq. (30), there are two unknown parameters of the reduced stress (σ_{eo} and σ_{ea}) which cannot be determined from the single equation, corresponding to the HMM theory, without additional assumptions. On the other hand, since this theory can be applied to the stress (29) when:

$$\sigma_{jm} \neq 0 \quad ; \quad \tau_{km} \neq 0 \quad ; \quad \sigma_{ja} = \tau_{ka} = 0$$

and when:

$$\sigma_{jm} = \tau_{km} = 0 \quad ; \quad \sigma_{ja} \neq 0 \quad ; \quad \tau_{ka} \neq 0$$

it should be also applicable to the stress (29) when:

$$\sigma_{jm} \neq 0 \quad ; \quad \tau_{km} \neq 0 \quad ; \quad \sigma_{ja} \neq 0 \quad ; \quad \tau_{ka} \neq 0$$

Therefore the following hypothesis (“average-distortion-energy strength hypothesis”) was formulated [11].

The reduced stress (30) is equivalent in terms of static and dynamic effort of a material to the stress (29) if:

(i) the time-independent parts of distortion energies per unit volume in these both stress states are equal

(ii) the reduced stress and the stress components (29) have the same frequency

(iii) the integral time averages of instantaneous values of distortion energies per unit volume in these both stress states are equal.

The distortion energy per unit volume in the general state of stress is given by [4]:

$$\Psi_d = \frac{1}{2} \left[\sigma_x (\epsilon_x - \epsilon_m) + \sigma_y (\epsilon_y - \epsilon_m) + \sigma_z (\epsilon_z - \epsilon_m) + \sum_k \tau_k \gamma_k \right] \quad (31)$$

where:

$$\epsilon_m = \frac{1}{3} (\epsilon_x + \epsilon_y + \epsilon_z) \quad (32)$$

When the stress (29) is applied to a viscoelastic material, according to Eqs (2), (12) and (22) one gets:

$$\begin{aligned} \epsilon_x &= \frac{1}{E} [\sigma_{xo} - \nu(\sigma_{yo} + \sigma_{zo})] \left(1 - e^{-\frac{E}{\eta}t} \right) + \frac{1}{\sqrt{E^2 + \eta^2\omega^2}} [\sigma_{xa} - \nu(\sigma_{ya} + \sigma_{za})] \sin(\omega t - \alpha) \\ \epsilon_y &= \frac{1}{E} [\sigma_{yo} - \nu(\sigma_{xo} + \sigma_{zo})] \left(1 - e^{-\frac{E}{\eta}t} \right) + \frac{1}{\sqrt{E^2 + \eta^2\omega^2}} [\sigma_{ya} - \nu(\sigma_{xa} + \sigma_{za})] \sin(\omega t - \alpha) \\ \epsilon_z &= \frac{1}{E} [\sigma_{zo} - \nu(\sigma_{xo} + \sigma_{yo})] \left(1 - e^{-\frac{E}{\eta}t} \right) + \frac{1}{\sqrt{E^2 + \eta^2\omega^2}} [\sigma_{za} - \nu(\sigma_{xa} + \sigma_{ya})] \sin(\omega t - \alpha) \\ \gamma_k &= \frac{1}{G} \tau_{ko} \left(1 - e^{-\frac{E}{\eta}t} \right) + \frac{2(1+\nu)}{\sqrt{E^2 + \eta^2\omega^2}} \tau_{ka} \sin(\omega t - \alpha), \quad \alpha = \arctg \frac{\eta\omega}{E} \end{aligned} \quad (33)$$

or, after sufficiently long time:

$$\begin{aligned}
 \varepsilon_x &= \frac{1}{E} [\sigma_{x0} - \nu(\sigma_{y0} + \sigma_{z0})] + \frac{1}{\sqrt{E^2 + \eta^2 \omega^2}} [\sigma_{xa} - \nu(\sigma_{ya} + \sigma_{za})] \sin(\omega t - \alpha) \\
 \varepsilon_y &= \frac{1}{E} [\sigma_{y0} - \nu(\sigma_{x0} + \sigma_{z0})] + \frac{1}{\sqrt{E^2 + \eta^2 \omega^2}} [\sigma_{ya} - \nu(\sigma_{xa} + \sigma_{za})] \sin(\omega t - \alpha) \\
 \varepsilon_z &= \frac{1}{E} [\sigma_{z0} - \nu(\sigma_{x0} + \sigma_{y0})] + \frac{1}{\sqrt{E^2 + \eta^2 \omega^2}} [\sigma_{za} - \nu(\sigma_{xa} + \sigma_{ya})] \sin(\omega t - \alpha) \\
 \gamma_k &= \frac{1}{G} \tau_{k0} + \frac{2(1+\nu)}{\sqrt{E^2 + \eta^2 \omega^2}} \tau_{ka} \sin(\omega t - \alpha), \quad \alpha = \arctg \frac{\eta \omega}{E}
 \end{aligned} \tag{34}$$

Substitution of Eqs (3), (32) and (34) into Eq. (31) results in:

$$\begin{aligned}
 \Psi_d &= \frac{1+\nu}{3E} \left(\sigma_{x0}^2 + \sigma_{y0}^2 + \sigma_{z0}^2 - \sigma_{x0} \sigma_{y0} - \sigma_{y0} \sigma_{z0} - \sigma_{z0} \sigma_{x0} + 3 \sum_k \tau_{k0}^2 \right) + \\
 &+ \frac{1+\nu}{3\sqrt{E^2 + \eta^2 \omega^2}} \left(\sigma_{xa}^2 + \sigma_{ya}^2 + \sigma_{za}^2 - \sigma_{xa} \sigma_{ya} - \sigma_{ya} \sigma_{za} - \sigma_{za} \sigma_{xa} + 3 \sum_k \tau_{ka}^2 \right) \sin \omega t \sin(\omega t - \alpha) + \\
 &+ \frac{1+\nu}{6E} [\sigma_{xa} (2\sigma_{x0} - \sigma_{y0} - \sigma_{z0}) + \sigma_{ya} (2\sigma_{y0} - \sigma_{x0} - \sigma_{z0}) + \sigma_{za} (2\sigma_{z0} - \sigma_{x0} - \sigma_{y0}) + \\
 &+ 6 \sum_k \tau_{ka} \tau_{k0}] \sin \omega t + \frac{1+\nu}{6\sqrt{E^2 + \eta^2 \omega^2}} [\sigma_{x0} (2\sigma_{xa} - \sigma_{ya} - \sigma_{za}) + \sigma_{y0} (2\sigma_{ya} - \sigma_{xa} - \sigma_{za}) + \\
 &+ \sigma_{z0} (2\sigma_{za} - \sigma_{xa} - \sigma_{ya}) + 6 \sum_k \tau_{k0} \tau_{ka}] \sin(\omega t - \alpha)
 \end{aligned} \tag{35}$$

Hence the distortion energy per unit volume of the viscoelastic solid under the reduced stress (30) is:

$$\begin{aligned}
 \Psi_{de} &= \frac{1+\nu}{3E} \sigma_{e0}^2 + \frac{1+\nu}{3\sqrt{E^2 + \eta^2 \omega^2}} \sigma_{ea}^2 \sin \omega t (\omega t - \alpha) + \\
 &+ \frac{1+\nu}{3E} \sigma_{ea} \sigma_{e0} \sin \omega t + \frac{1+\nu}{3\sqrt{E^2 + \eta^2 \omega^2}} \sigma_{e0} \sigma_{ea} \sin(\omega t - \alpha)
 \end{aligned} \tag{36}$$

The condition (i) gives Eq. (10), and the condition (iii), i.e.,

$$\frac{1}{T} \int_0^T \Psi_{de} dt = \frac{1}{T} \int_0^T \Psi_d dt ; \quad T = \frac{2\pi}{\omega} \tag{37}$$

leads to Eq. (18). Then the criterion of an infinite fatigue life reads [2, 10]:

$$\frac{\sigma_{e0}}{R_e} + \frac{\sigma_{ea}}{Z_{rc}} < 1 \tag{38}$$

and the yield criterion is:

$$\frac{\sigma_{e0}}{R_e} + \frac{\sigma_{ea}}{R_e} < 1 \tag{39}$$

At the stress (30), the criterion of a finite fatigue life of ductile materials becomes [10]:

$$\frac{N_d}{K} \left(\frac{\sigma_{ea}}{1 - \frac{\sigma_{e0}}{R_e}} \right)^m < 1 \tag{40}$$

Eq. (40) is valid if:

$$Z_{rc} < \frac{\sigma_{ea}}{1 - \frac{\sigma_{eo}}{R_e}} \leq L \quad (41)$$

where:

L – the maximum stress amplitude under fully reversed tension-compression in the high-cycle fatigue regime (above which the low-cycle fatigue may occur).

Another stress state which can be dealt with the aid of the aforementioned hypothesis is that with non-zero mean out-of-phase components:

$$\sigma_j = \sigma_{jo} + \sigma_{ja} \sin(\omega t + \varphi_j) \quad ; \quad \tau_k = \tau_{ko} + \tau_{ka} \sin(\omega t + \varphi_k) \quad (42)$$

where: φ_j and φ_k are the phase angles. With the known strain response of viscoelastic materials to the stress (42) [6] and with the reduced stress in the form (30), it is easy to prove that the mean value of the reduced stress is given again by Eq. (10), but now the formula for its amplitude reads:

$$\sigma_{ea} = \left[\begin{aligned} &\sigma_{xa}^2 + \sigma_{ya}^2 + \sigma_{za}^2 - \sigma_{xa} \sigma_{ya} \cos(\varphi_x - \varphi_y) - \sigma_{ya} \sigma_{za} \cos(\varphi_y - \varphi_z) + \\ &- \sigma_{za} \sigma_{xa} \cos(\varphi_z - \varphi_x) + 3(\tau_{xya}^2 + \tau_{yza}^2 + \tau_{zxa}^2) \end{aligned} \right]^{1/2} \quad (43)$$

It means that in the considered above load cases the fatigue and yield criteria for elastic and viscoelastic solids coincide. Of course, to be on the safe side, in Eqs (38) through (40) arbitrary safety margins may be introduced.

FAILURE CRITERIA OF VISCOELASTIC MATERIALS UNDER MULTIAXIAL PERIODIC LOADS

In general, structural elements and machinery details are simultaneously subjected to static and dynamic loads. In addition to the time-varying stress, the steady stress resulting from static load, and the mean stress (the average of the maximum and minimum of the cyclic stress) influence the strength of an element. It is important to recognize that the total strength of the element is altered if residual stresses (caused by cold forming, heat treatment, welding, etc.) exist. Since residual stresses have a similar influence on the fatigue behaviour of materials as do mechanically imposed constant stresses of the same magnitude [12], in what follows no distinction will be made between any kind of static stresses.

Among the types of dynamic loads encountered in practice, one of the most important is periodic load. In the general state of periodic stress, its components can be expanded in Fourier series:

$$\begin{aligned} \sigma_j &= \sigma_{jo} + \sum_n \sigma_{jn} \sin(n\omega t + \varphi_{jn}) \quad ; \quad j = x, y, z \\ \tau_k &= \tau_{ko} + \sum_n \tau_{kn} \sin(n\omega t + \varphi_{kn}) \quad ; \quad k = xy, yz, zx \end{aligned} \quad (44)$$

where:

σ_{jo}, τ_{ko} – mean values ; $\varphi_{jn}, \varphi_{kn}$ – phase angles of n-th terms ; $\omega = 2\pi/T$ – fundamental circular frequency ; T – stress period.

Our aim is to determine such a reduced stress:

$$\sigma_e = \sigma_{eo} + \sigma_{ea} \sin(\omega_e t) \quad (45)$$

of mean value σ_{eo} , amplitude σ_{ea} and circular frequency ω_e , that would be equivalent to the original stress in terms of fatigue and yield strengths of viscoelastic materials. For this purpose the theory of energy transformation systems [13] can be used, which links the dissipated energy with the breakdown time of a system. According to this theory, two stress states are equivalent in terms of time to failure if the energies dissipated internally and externally in both these states are respectively equal. Apparently, the dissipated energy can be estimated by evaluation of certain symptoms, e.g., the externally dissipated energy by the vibration, and the internally dissipated energy by the temperature [13]. For viscoelastic materials the use can be made of the following relationship derived in [14] for the internally dissipated energy per unit volume under periodic stress with the components (44) during the period T :

$$\begin{aligned} \phi(T) &= \frac{1}{2} \omega T \sum_n \frac{n \sin \alpha_n}{\sqrt{E^2 + (\eta n \omega)^2}} \left\{ \sigma_{xn}^2 + \sigma_{yn}^2 + \sigma_{zn}^2 - 2\nu [\sigma_{xn} \sigma_{yn} \cos(\varphi_{xn} - \varphi_{yn}) + \right. \\ &\left. + \sigma_{yn} \sigma_{zn} \cos(\varphi_{yn} - \varphi_{zn}) + \sigma_{zn} \sigma_{xn} \cos(\varphi_{zn} - \varphi_{xn})] + 2(1 + \nu)(\tau_{xya}^2 + \tau_{yza}^2 + \tau_{zxa}^2) \right\} \end{aligned} \quad (46)$$

where:

$$\alpha_n = \arctan \frac{\eta n \omega}{E} \quad (47)$$

Consequently, the following equivalency condition can be postulated:

$$\varphi_e(T) = \varphi(T) \quad (48)$$

where:

$\varphi_e(T)$ – the energy dissipated in the viscoelastic material per unit volume under the reduced stress (45) during T seconds. Under assumption that:

$$\omega_e = r\omega \quad (49)$$

where:

r – natural number to be determined, on the basis of Eqs (46) and (47) one can write:

$$\phi_e(T) = \frac{1}{2} r\omega T \frac{\sin \alpha_e}{\sqrt{E^2 + (\eta r\omega)^2}} \sigma_{ea}^2 \quad (50)$$

$$\alpha_e = \arctan \frac{\eta r\omega}{E} \quad (51)$$

Thus:

$$\frac{r \sin \alpha_e}{\sqrt{E^2 + (\eta r\omega)^2}} \sigma_{ea}^2 = A \quad (52)$$

where:

$$A = \sum_n \frac{n \sin \alpha_n}{\sqrt{E^2 + (\eta n\omega)^2}} \left\{ \sigma_{xn}^2 + \sigma_{yn}^2 + \sigma_{zn}^2 - 2\nu [\sigma_{xn} \sigma_{yn} \cos(\varphi_{xn} - \varphi_{yn}) + \sigma_{yn} \sigma_{zn} \cos(\varphi_{yn} - \varphi_{zn}) + \sigma_{zn} \sigma_{xn} \cos(\varphi_{zn} - \varphi_{xn})] + 2(1+\nu)(\tau_{xyn}^2 + \tau_{yzn}^2 + \tau_{zxn}^2) \right\} \quad (53)$$

As for the remaining equations, necessary for determination of the reduced stress (45), in [9] it was assumed that the energy dissipated externally by materials subjected to multiaxial loads is proportional to the average strain energy of distortion per unit volume. Bearing in mind the role of distortion energy in evaluation of effort of ductile materials under multiaxial stresses, in the present paper the same assumption is retained. Derivation of similar equations based on the strain energy of volume change or total strain energy is analogous.

In conformity with the aforesaid, we have:

$$\frac{1}{T} \int_0^T \psi_{de} dt = \frac{1}{T} \int_0^T \psi_d dt, \quad T = \frac{2\pi}{\omega} \quad (54)$$

where:

$$\begin{aligned} \psi_{de} = & \frac{1+\nu}{3E} \sigma_{eo}^2 + \frac{1+\nu}{3\sqrt{E^2 + (\eta r\omega)^2}} \sigma_{ea}^2 \sin r\omega t \sin(r\omega t - \alpha_e) + \\ & + \frac{1+\nu}{3E} \sigma_{ea} \sigma_{eo} \sin r\omega t + \frac{1+\nu}{3\sqrt{E^2 + (\eta r\omega)^2}} \sigma_{eo} \sigma_{ea} \sin(r\omega t - \alpha_e) \end{aligned} \quad (55)$$

is the strain energy of distortion per unit volume under reduced stress (45) and ψ_d is that under periodic stress (44). To determine the latter from Eqs (31) and (32), the strain response of a viscoelastic material to periodic stress must be known. This problem was solved in [6] to give:

$$\boldsymbol{\varepsilon} = \boldsymbol{\varepsilon}_o + \sum_n H_n \text{Im} \left[\bar{\sigma}_n e^{i(n\omega t - \alpha_n)} \right] \quad (56)$$

where:

$$\boldsymbol{\varepsilon}_o = [\varepsilon_{xo} \ \varepsilon_{yo} \ \varepsilon_{zo} \ \gamma_{xyo} \ \gamma_{yzo} \ \gamma_{zxo}]^T$$

is the vector of mean strain components given by Eqs (2),

$$H_n = \frac{1}{\sqrt{E^2 + (\eta n\omega)^2}} \begin{bmatrix} 1 & -\nu & -\nu & 0 & 0 & 0 \\ -\nu & 1 & -\nu & 0 & 0 & 0 \\ -\nu & -\nu & 1 & 0 & 0 & 0 \\ 0 & 0 & 0 & 2(1+\nu) & 0 & 0 \\ 0 & 0 & 0 & 0 & 2(1+\nu) & 0 \\ 0 & 0 & 0 & 0 & 0 & 2(1+\nu) \end{bmatrix}$$

is the matrix of dynamical flexibility of the viscoelastic material at the load circular frequency ω ,

$$\bar{\sigma}_n = [\bar{\sigma}_{xn} \bar{\sigma}_{yn} \bar{\sigma}_{zn} \bar{\tau}_{xyn} \bar{\tau}_{yzn} \bar{\tau}_{zxn}]^T$$

is the vector of complex amplitudes of n -th terms of the stress components, defined as:

$$\bar{\sigma}_{jn} = \sigma_{jn} e^{i\varphi_{jn}} ; \quad \bar{\tau}_{kn} = \tau_{kn} e^{i\varphi_{kn}}$$

i is the imaginary unity, Im is the imaginary part, and:

$$\alpha_n = \text{arctg} \frac{\eta n \omega}{E}$$

is the phase angle of n -th terms of the strain components.

Eqs (31), (32) and (54) through (56) lead to:

$$\begin{aligned} \frac{1+\nu}{3E} \sigma_{eo}^2 + \frac{(1+\nu) \cos \alpha_e}{6\sqrt{E^2 + (\eta r \omega)^2}} \sigma_{ea}^2 = \frac{1+\nu}{3E} [\sigma_{xo}^2 + \sigma_{yo}^2 + \sigma_{zo}^2 - \sigma_{xo} \sigma_{yo} - \sigma_{yo} \sigma_{zo} + \\ - \sigma_{zo} \sigma_{xo} + 3(\tau_{xyo}^2 + \tau_{yzo}^2 + \tau_{zxo}^2)] + \frac{1+\nu}{6} \sum_n \frac{\cos \alpha_n}{\sqrt{E^2 + (\eta n \omega)^2}} [\sigma_{xn}^2 + \sigma_{yn}^2 + \sigma_{zn}^2 - \sigma_{xn} \sigma_{yn} \cos(\varphi_{xn} - \varphi_{yn}) + \\ - \sigma_{yn} \sigma_{zn} \cos(\varphi_{yn} - \varphi_{zn}) - \sigma_{zn} \sigma_{xn} \cos(\varphi_{zn} - \varphi_{xn}) + 3(\tau_{xyn}^2 + \tau_{yzn}^2 + \tau_{zxn}^2)] \end{aligned} \quad (57)$$

Hence:

$$\sigma_{eo}^2 = \sigma_{xo}^2 + \sigma_{yo}^2 + \sigma_{zo}^2 - \sigma_{xo} \sigma_{yo} - \sigma_{yo} \sigma_{zo} - \sigma_{zo} \sigma_{xo} + 3(\tau_{xyo}^2 + \tau_{yzo}^2 + \tau_{zxo}^2) \quad (58)$$

which results in Eq. (10) for the reduced mean stress, and:

$$\frac{\cos \alpha_e}{\sqrt{E^2 + (\eta r \omega)^2}} \sigma_{ea}^2 = B \quad (59)$$

where:

$$\begin{aligned} B = \sum_n \frac{\cos \alpha_n}{\sqrt{E^2 + (\eta n \omega)^2}} [\sigma_{xn}^2 + \sigma_{yn}^2 + \sigma_{zn}^2 - \sigma_{xn} \sigma_{yn} \cos(\varphi_{xn} - \varphi_{yn}) - \sigma_{yn} \sigma_{zn} \cos(\varphi_{yn} - \varphi_{zn}) + \\ - \sigma_{zn} \sigma_{xn} \cos(\varphi_{zn} - \varphi_{xn}) + 3(\tau_{xyn}^2 + \tau_{yzn}^2 + \tau_{zxn}^2)] \end{aligned} \quad (60)$$

From Eqs (52) and (59) one obtains:

$$\sigma_{ea} = \left[\frac{E^2 + (\eta r \omega)^2}{r^2} (A^2 + r^2 B^2) \right]^{1/4} \quad (61)$$

and:

$$r \text{tg} \alpha_e = \frac{A}{B} \quad (62)$$

that is:

$$r^2 \frac{\eta \omega}{E} = \frac{A}{B} \quad (63)$$

Hence the real number ρ , close to the natural number r ,

$$r = \text{Round}(\rho) \quad (64)$$

is:

$$\rho = \left(\frac{AE}{\eta \omega B} \right)^{1/2} \quad (65)$$

With these results, the criterion of an infinite fatigue life and the yield criterion can be expressed by Eqs (38) and (39), whereas the criterion of a finite fatigue life becomes:

$$\frac{r \omega T_d}{2\pi K} \left(\frac{\sigma_{ea}}{1 - \frac{\sigma_{eo}}{R_e}} \right)^m < 1 \quad (66)$$

where: T_d – the required design life.

CONCLUSIONS

- On the basis of the Huber-Mises-Hencky (HMH) theory and constitutive equations for strains in viscoelastic solids subjected to multiaxial static loads, it is shown that the yield criterion does not differ from that for perfectly elastic solids.
- On the basis of the HMH theory and constitutive equations for strains in viscoelastic solids subjected to multiaxial zero mean in-phase loads, it is shown that the criterion of an infinite fatigue life, the criterion of a finite fatigue life and the yield criterion do not differ from those for perfectly elastic solids.
- With the aid of the average-distortion-energy strength hypothesis and constitutive equations for strains in viscoelastic solids subjected to non-zero mean in-phase loads, as well as subjected to non-zero mean out-of-phase loads, it is shown that the aforementioned criteria do not differ from those for perfectly elastic solids.
- On the basis of the theory of energy transformation systems and constitutive equations for strains in viscoelastic solids subjected to periodic loads, it is shown that the aforementioned criteria do not coincide with those for perfectly elastic solids.
- The load capacity of a homogeneous, isotropic viscoelastic material at a given temperature is completely defined by the Young modulus, tensile yield strength, S-N curve for tension-compression, Poisson's ratio and coefficient of viscous damping of normal strain.

NOMENCLATURE

- A, B – quantities defined by Eqs (53) and (60)
- E – Young modulus
- G – shear modulus
- H_n – matrix of dynamical flexibility of the viscoelastic material at the load circular frequency ω
- i – imaginary unity
- Im – imaginary part
- K – fatigue strength coefficient in equation of the S-N curve for tension-compression
- L – maximum stress amplitude under fully reversed tension-compression in the high-cycle fatigue regime (above which the low-cycle fatigue may occur)
- m – fatigue strength exponent in equation of the S-N curve for tension-compression
- n – natural number
- N_d – required number of stress cycles to achieve a given design life
- r – natural number given by Eq. (64)
- R_c – tensile yield strength
- t – time
- T – stress period
- T_d – required design life
- Z_{rc} – fatigue limit under fully reversed tension-compression
- α_j – phase angle of the strain components under in-phase loads
- α_c – phase angle defined by Eq. (51)
- α_n – phase angle defined by Eq. (47)
- γ_k – k-th shear strain component ($k = xy, yz, zx$)
- γ_{ko} – k-th strain component under static load, mean value of k-th strain component
- $\boldsymbol{\varepsilon}$ – vector of the strain components
- ε_c – reduced strain
- ε_j – j-th normal strain component ($j = x, y, z$)
- ε_{jo} – j-th strain component under static load, mean value of j-th strain component
- ε_m – quantity defined by Eq. (32)
- $\boldsymbol{\varepsilon}_o$ – vector of the mean values of strain components
- η – coefficient of viscous damping of normal strain
- ν – Poisson's ratio,
- ρ – number given by Eq. (65)
- σ_c – reduced stress
- σ_{ca} – amplitude of the reduced stress

- σ_{co} – reduced stress under static load, mean value of the reduced stress
- σ_j – j-th stress component
- σ_{ja} – amplitude of j-th stress component
- σ_n^{jn} – amplitude of n-th term in Fourier expansion of σ_j
- σ_n^{jn} – complex amplitude of n-th term in Fourier expansion of σ_j
- σ_{jo} – j-th stress component under static load, mean value of j-th stress component
- $\overline{\sigma}_n$ – vector of complex amplitudes of n-th terms in Fourier expansion of the stress components
- τ_k – k-th stress component
- τ_{ka} – amplitude of k-th stress component
- τ_{ko} – k-th stress component under static load, mean value of k-th stress component
- τ_{kn} – amplitude of n-th term in Fourier expansion of τ_k
- $\overline{\tau}_{kn}$ – complex amplitude of n-th term in Fourier expansion of τ_k
- φ_j – phase angle of j-th stress component
- φ_j^{jn} – phase angle of n-th term in Fourier expansion of σ_j
- φ_k – phase angle of k-th stress component
- φ_{kn} – phase angle of n-th term in Fourier expansion of τ_k
- φ – dissipation energy per unit volume
- φ_c – dissipation energy per unit volume under the reduced stress
- Ψ – strain energy per unit volume
- Ψ_d – strain energy of distortion per unit volume
- Ψ_{de} – strain energy of distortion per unit volume under the reduced stress
- Ψ_{deo} – strain energy of distortion per unit volume under the reduced static stress
- Ψ_{do} – strain energy of distortion per unit volume of perfectly elastic solid under static load
- Ψ_c – strain energy per unit volume under the reduced stress
- Ψ_o – strain energy per unit volume of perfectly elastic solid under static load
- Ψ_{vo} – strain energy of volume change per unit volume of perfectly elastic solid under static load
- ω – circular frequency, fundamental circular frequency
- ω_c – circular frequency of the reduced stress at periodic loads

BIBLIOGRAPHY

1. Lubahn J.D., Felgar R.P.: *Plasticity and Creep of Metals*. J. Wiley & Sons, New York, 1961
2. Haslach H.W., Jr., Armstrong R.W.: *Deformable Bodies and Their Material Behaviour*. J. Wiley & Sons, 2004
3. Paik J.K., Thayamballi A.K.: *Ultimate Limit State Design of Steel-Plated Structures*. J. Wiley & Sons, Chichester, 2003
4. Jakubowicz A., Orłóś Z.: *Strength of Materials* (in Polish). WNT, Warszawa, 1996
5. Macha E., Sonsino C.M.: *Energy criteria of multiaxial fatigue failure*. Fatigue Fract. Engng Mater. Struct., Vol. 22, 1999
6. Kolenda J.: *On the behaviour of viscoelastic solids under multiaxial loads*. Polish Maritime Research, 3, 2008
7. Łagoda T., Macha E.: *Estimated and experimental fatigue lives of 30CrNiMo8 steel under in- and out-of-phase combined bending and torsion with variable amplitudes*. Fatigue Fract. Engng Mater. Struct., 11, 1994
8. Sonsino C.M.: *Multiaxial fatigue of welded joints under in-phase and out-of-phase local strains and stresses*. Int. J. Fatigue, 1, 1995
9. Kolenda J.: *On Fatigue Safety of Metallic Elements under Static and Dynamic Loads*. 2nd Edition. Polish Naval Academy, Gdynia, 2006
10. Kocańda S., Szala J.: *Fundamentals of Fatigue Calculations* (in Polish). PWN, Warszawa, 1997
11. Kolenda J.: *Average-distortion-energy strength hypothesis*. Proc. of 17th Symp. on Fatigue and Fracture Mechanics, Bydgoszcz Pieczyńska, 1998. Technical and Agricultural Academy, Bydgoszcz, 1998
12. Osgood C.C.: *Fatigue Design*. Pergamon Press, Oxford, 1982
13. Cempel C.: *Theory of energy transformation systems and their application in diagnostic of operating systems*. Applied Math. and Computer Sciences, 2, 1993
14. Kolenda J.: *Dissipation energy in viscoelastic solids under multiaxial loads*. Polish Maritime Research, 4, 2007.

Hydrodynamic performance of coaxial contra-rotating propeller (CCRP) for large ships

Hassan Ghassemi, Assoc. Prof.
Amirkabir University of Technology

ABSTRACT



This paper describes a coaxial contra-rotating propeller (CCRP) system to calculate the hydrodynamic characteristics and then obtain the optimum operational condition to install on two different large bulk carrier and VLCC. The method is based on boundary element method (BEM) to obtain the hydrodynamic performance of any complicated configuration such as CRP system, and then the optimum propeller data is obtained by the systematical method at the design condition. We prepared a software package code, namely SPD (Ship Propeller Design), which has model mesh generation, solver and numerical output results. The comparison of the propulsive performance was made between the propeller alone and CRP arrangement. Major finding include good agreement between predictions using the numerical code and experimental data for both ships.

Keywords: boundary element method, contra-rotating propeller, CRP, optimum efficiency

INTRODUCTION

The main aims of the marine propulsor designers are to increase thrust, diminish torque, improve efficiency and to save energy. Most conventional propulsors are working behind the ship hull where the flow is non-uniform, unsteady and also limitation of the propeller diameter due to ship stern. Single propeller produces cavitation at the heavy load condition, but CCRP may provide moderate load on each blade and prevent cavitation. Another case is that the single propeller generates torque, while CCRP cancel the torque and improve the efficiency [1, 2].

The history of CRP goes back when a patent was applied by Ericsson (the inventor in 1836) to 45 feet ship. In 1909 and 1939, Italian Navy and US Navy had experimented CRP on a 46 feet and 70 feet steam ship, respectively. Rutundi [3] made a comparison test between CRP and conventional propeller for a 3500 tons naval training ship and has reported an 18% improvement in the propulsive performance.

Since then, CRP has well been used for torpedoes, small vessels, and of course for aircraft, but there is a difficulty in producing a reliable CR shafting which can support the large power for application to large merchant ships. In 1988, MHI (Japan) has succeeded in retrofitting 4200 GT with a CRP [4], and in the same year, IHI (Japan) has completed the shop test of Juno's CRP system at the outset. Having been equipped with this CRP system, Juno dealt with the official trial in which she has achieved a 15% power saving. After that, some other experimental research have been done at NMRC (in Japan) (before name was SRI) by Ukon, [5, 6, 11, 13, 14].

From the numerical approach during two decades, some work has been done to obtain a better understanding of the system in order to predict its effect on hydrodynamic performance. Yang C-J [1] and Islam et al. [8] was used lifting surface theory and vortex lattice method to calculate the blade loading.

Recently, more attention is being drawn to the development of the contra-rotating podded propulsor (CRPP) system for ship propulsion because of its attractively high energy saving rate as well as lower cavitation and better hydrodynamic performance.

In the current arrangement, a CRPP is placed at the forward end of a pod which is aligned with the local inflow. The powering and cavitation experiments show the performance prediction agree well with measurement.

Nishiyama and Sakamoto [10] designed a CRP system at IHI and on bulk carrier and VLCC.

This paper deals with the following subjects:

- ❖ numerical Method of BEM
- ❖ mesh Generation
- ❖ design concept of CRP on Behind of Ship
- ❖ design concept of CRPP
- ❖ application of the CRP system on the Ship
- ❖ systematic design

This paper is firstly calculated the hydrodynamic performance of the CCRP using BEM. The calculated results are predicted well with experimental measurements. Systematic design is finally employed to the two ships types (Bulk carrier and VLCC) to obtain the design points.

DESIGN CONCEPT OF CRP

Procedure of CCRP designing

With the principal particulars of the hull and the main engine given, a CRP can be designed as for any single propeller, namely, through reiteration of the following two steps:

(1) Propeller Design in uniform flow: try to find for an optimum design that satisfy the given engine power and revolution speed; then

(2) Modification by considering the non-uniform flow: the propeller designed thus is further modified, so as to better adapt to the non-uniform flow over what has already been considered macroscopically in step (1), in such terms as propeller cavitation, propeller-induced vibration, and strength of blade for the propeller performance in non-uniform flows.

Designing CCRP in uniform flow

There are two approaches in the design of CRP: one based on lifting surface theory [9], and other utilizing the design diagram based on open water tests on systematic CRP model series [5]. More precise results could be expected from the systematic series data than from the theoretical approach. However, a review of past reports for CRP, the method based on series test data can be found.

Fig. 1 depicts the design procedure and algorithm. Here, the relation between ship speed and resistance ($R_T - V_S$) for the hull, self propulsion test or some empirical formulae (t, w, η_R), the number of blade (Z) and axial distance between two propellers (x_A) are given. According to systematical method and flowchart, first estimate the revolution number of propeller and its diameter. Then using numerical SPD code, the hydrodynamic characteristics (open water) of propeller alone and CRP system are calculated.

How to calculate the optimum efficiency from the open water diagram? This is the systematic method to obtain the optimum design of the propeller for the ship. From the resistance and the self propulsion test or some empirical formulae, the following relation may be expressed:

★ For single conventional propeller:

$$K_T = \frac{T}{\rho n^2 D^4} = \frac{T}{\rho D^2 V_A^2} \cdot J^2 = \frac{R_T}{(1-t)\rho D^2 [V_S(1-\bar{w})]^2} \cdot J^2 = A \cdot J^2 \quad (1)$$

★ For CRP system:

$$K_T = \frac{T_F + T_A}{\rho n_F^2 D_F^4} = \frac{R_T}{(1-t)\rho D_F^2 [V_S(1-\bar{w})]^2} \cdot J^2 = B \cdot J^2 \quad (2)$$

This K_T is quadratic function of J and intersects with open water curves of $K_T - J$ and the optimum solution is obtained from the intersection point, so all the coefficients are obtained from this point (K_T, K_Q, η_o, J). Then, the thrust and torque are obtained from the following:

$$T = K_T(J_{n,D})\rho n^2 D^4 ; T_{\text{Calculated}(i+1)} \geq T_{\text{Required}(i)} \quad (3)$$

$$Q = K_Q(J_{n,D})\rho n^2 D^5 ; Q_{i+1} \leq Q_i$$

$$K_Q = \frac{n_F Q_F + n_A Q_A}{\rho n_F^3 D_F^5} \quad (4)$$

$$\eta_o = \frac{J}{2\pi} \frac{K_T}{K_Q} ; J = \frac{V_A}{n_F D_F} \quad (5)$$

The reiteration is continued unless the thrust should be bigger than the required one and torque should be less than the previous stage.

NUMERICAL APPROACH

Potential based boundary element method

Suppose the forward propeller of a CRP with Z_F blades rotates in the left hand (counter-clockwise) direction at a constant revolution number n_F , while the aft propeller Z_A blades in the right hand (counter-clockwise) direction at n_A , and the CRP as a whole advances at a constant speed V_A .

Assuming inviscid, incompressible and irrotational flow in the volume around and inside the body, a potential function exists for the perturbation velocity ϕ created by the propeller movement in the volume which satisfies the Laplace's equation. By applying Green's theorem for perturbation velocity potential ϕ at any field point on the body surface, we can get the following integral equation on the propeller and its trailing vortex wake.

$$2\pi\phi(P) = \int_{S_B} \left\{ \phi(q) \frac{\partial}{\partial n_q} \left(\frac{1}{R(p;q)} \right) - \frac{\partial \phi(q)}{\partial n_q} \left(\frac{1}{R(p;q)} \right) \right\} dS + \int_{S_W} \Delta \phi(q) \frac{\partial}{\partial n_q} \left(\frac{1}{R(p;q)} \right) dS \quad (6)$$

$R(p;q)$ is the distance from the field point p to the singularity point q . This equation may be regarded as a representation of the velocity potential in terms of a normal dipole distribution of strength $\phi(p)$ on the body surface S_B , a source distribution of strength $\partial\phi/\partial n$ on S_B , and a normal dipole distribution of strength $\Delta\phi(q)$ on the trailing wake surface S_W .

Boundary conditions

The strength of the source distribution in equation (6) is known from kinematic boundary condition (KBC) as follows:

$$\frac{\partial \phi}{\partial n} = -\vec{V}_I \cdot \vec{n} = -[V_A + \vec{\omega} \times \vec{r}] \cdot \vec{n} \quad (7)$$

where:

\vec{n} - denotes the outward normal unit vector.

The strength of dipole distribution is unknown and equal to the perturbation potential on the propeller or to the potential jump in the trailing vortex wake. On the wake surface S_W the velocity is considered to be continuous while the potential has a jump across the wake. It is expressed in the perturbation potential as:

$$\Delta \left(\frac{\partial \phi}{\partial n} \right)_{S_W} = \left(\frac{\partial \phi}{\partial n} \right)^B - \left(\frac{\partial \phi}{\partial n} \right)^F = 0 \quad (8)$$

$$(\Delta\phi)_{S_w} = \phi^B - \phi^F = \Gamma \quad (9)$$

$$\Delta p_{TE} = p_{TE}^B - p_{TE}^F = 0 \quad (10)$$

where indexes B and F mean back and face sides of the propeller, respectively.

Another important physical boundary condition is the Kutta condition and its implementation. This equal pressure Kutta condition is applied to determine the unknown $\Delta\phi_{TE}$ of the dipole strength on the wake surface. In the numerical calculation, the pressure Kutta condition at the back and face surfaces of the trailing edge (TE), can be expressed as:

A direct solution of the resulting system of equations obtained from discretized Green's formula for the perturbation velocity potential (6), along with equation (10) is difficult due to the nonlinear character of the equation (6) therefore, an iterative solutions algorithm is employed to solve the problem. We focus on the numerical implementation in the following section.

Discretization of equation (6) leads to a linear system of algebraic equations for the unknown ϕ as:

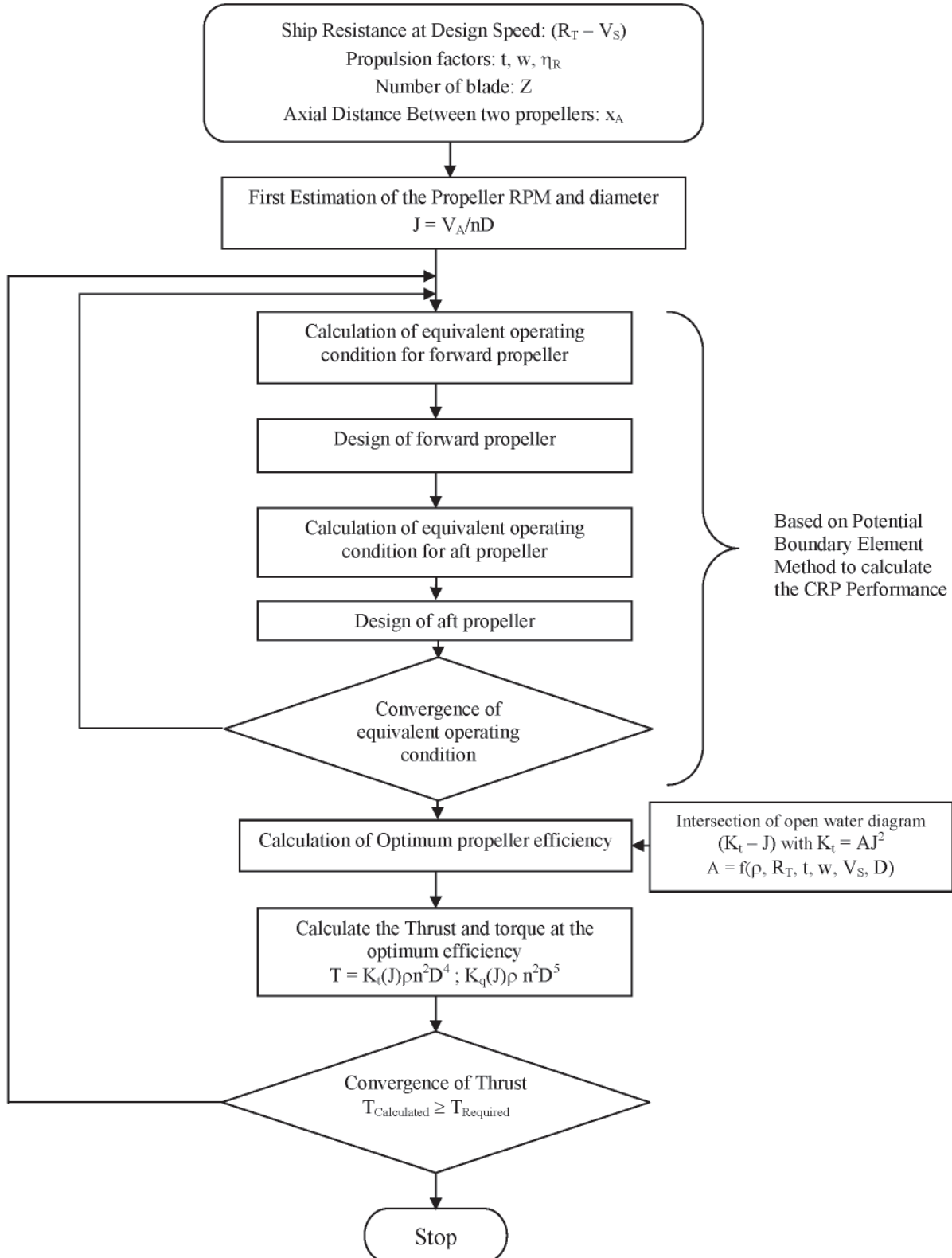


Fig. 1. Calculation flowchart of CRP

$$\begin{aligned}
2\pi\phi_i = & \sum_{N_p=1}^2 \left(\sum_{k=1}^K \sum_{j=1}^{N_{tot}} D_{ij}^k (\phi_j) \right) + \\
& + \sum_{N_p=1}^2 \left(\sum_{k=1}^K \sum_{j=1}^M \sum_{l=1}^{N_w} W_{ijl}^k (\Delta\phi_j) \right) + \\
& + \sum_{N_p=1}^2 \left(\sum_{k=1}^K \sum_{j=1}^{N_{tot}} S_{ij}^k \left(\frac{\partial\phi}{\partial n} \right)_j \right)
\end{aligned} \quad (11)$$

$i = 1, 2, \dots, N_{tot}$; where: $N_{tot} = 2 \times N \times M$
 K - number of blades

Where D_{ij}^k , W_{ijl}^k (dipole distributions on body and wake surfaces) and S_{ij}^k (source: distribution on body) are influence coefficients on panel j acting on the control point of panel i . Those influence coefficients are nearly evaluated analytically. The use of quadrilateral surface panels instead of planar panels has been found to be important for the convergence of the present potential based boundary element method. It is found to be especially so when applied to the highly skewed propeller and twisted shape.

Calculation of induced velocity

From Green's theorem in the potential field, equation (6), we can alternatively construct in the velocity field. Taking the gradient of the perturbation velocity potential at any field point, the induced velocity which can be expressed as:

$$\begin{aligned}
4\pi\vec{v}(p) = & \int_{S_B} \left\{ \phi(q) \nabla_p \frac{\partial}{\partial n_q} \left(\frac{1}{R(p;q)} \right) + \right. \\
& \left. - \frac{\partial\phi(q)}{\partial n_q} \nabla_p \left(\frac{1}{R(p;q)} \right) \right\} dS + \\
& + \int_{S_w} \Delta\phi \nabla_p \frac{\partial}{\partial n_q} \left(\frac{1}{R(p;q)} \right) dS
\end{aligned} \quad (12)$$

Here, from the discretization of the body and wake, and assuming the potential ϕ and the value of $\partial\phi/\partial n$ are constant within each panel. Then, equation (12) can be written by:

$$\begin{aligned}
4\pi\vec{v}_i = & \sum_{N_p=1}^2 \left(\sum_{k=1}^K \sum_{j=1}^{N_{tot}} (\phi_j) \nabla_p C_{ij}^k \right) + \\
& + \sum_{N_p=1}^2 \left(\sum_{k=1}^K \sum_{j=1}^M (\Delta\phi_j) \nabla_p W_{ijl}^k \right) + \\
& + \sum_{N_p=1}^2 \left(\sum_{k=1}^K \sum_{j=1}^{N_{tot}} \left(\frac{\partial\phi}{\partial n} \right)_j \nabla_p S_{ij}^k \right)
\end{aligned} \quad (13)$$

$i = 1, 2, \dots, N_{tot}$

Where $\nabla_p C_{ij}^k$, $\nabla_p W_{ijl}^k$ and $\nabla_p S_{ij}^k$ are the velocity influence coefficients. Those velocity coefficients can be evaluated

analytically by assuming that the surface elements are approximated by a number of quadrilateral hyperboloidal panels.

Calculations of the velocity influence were more sensitive than the potential coefficient, and also the required storage was three times more than the storage of the potential coefficient. There was one big advantage that the velocities can directly be obtained for any field points

The induced velocity diagram of the CRP is shown in Fig. 2, where u_a and u_t denotes the axial and circumferential induced velocities, respectively. Since the interaction between two propellers, the total induced velocities may be expressed as follows:

$$(\mathbf{u}_a)_i = (\mathbf{u}_a)_{ii} + (\mathbf{u}_a)_{ij} \quad (14)$$

$$(\mathbf{u}_t)_i = (\mathbf{u}_t)_{ii} + (\mathbf{u}_t)_{ij}$$

For two fore and aft propellers, it is given:

$$(\mathbf{u}_a)_1 = (\mathbf{u}_a)_{11} ; (\mathbf{u}_a)_2 = (\mathbf{u}_a)_{22} + (\mathbf{u}_a)_{21} \quad (15)$$

$$(\mathbf{u}_t)_1 = (\mathbf{u}_t)_{11} ; (\mathbf{u}_t)_2 = (\mathbf{u}_t)_{22} + (\mathbf{u}_t)_{21}$$

Where $(\mathbf{u}_{a(t)})_{ij}$ implies the axial or circumferential velocities at i -th propeller induced by the j -th propeller. The subscript 1 and 2 denote the forward or aft propeller, respectively. We observe that $(\mathbf{u}_a)_{21}$ is zero and $(\mathbf{u}_t)_{21}$ is very small and neglected.

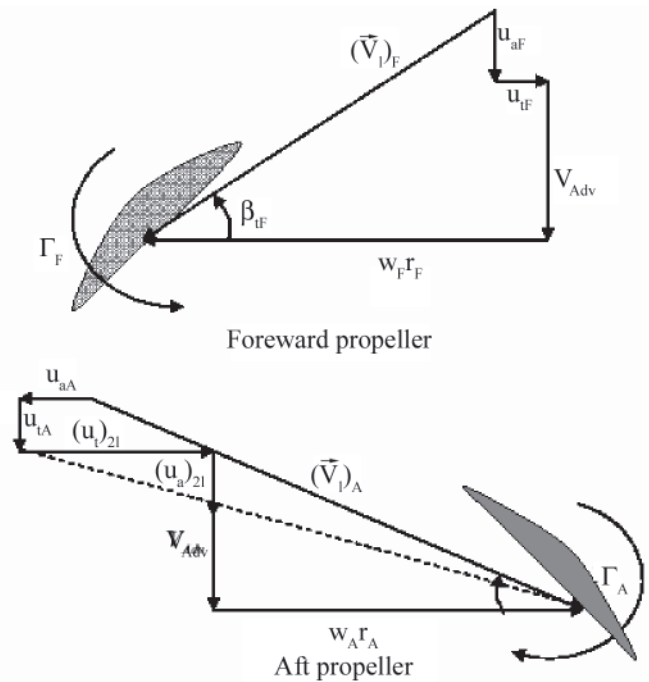


Fig. 2. Relative Velocities at Blade section of CRP

The hydrodynamic pitch angle and resultant velocities to the fore and aft propellers are expressed as follows:

$$\tan \beta_{iF} = \frac{V_{Adv} + u_{aF}}{\omega_F r_F + u_{tF}} \quad (16)$$

$$\tan \beta_{iA} = \frac{V_{Adv} + u_{aA} + (u_a)_{21}}{\omega_F r_F - u_{tA} + (u_t)_{21}}$$

Inflow velocity to the fore propeller may be obtained by:

$$\begin{aligned}
\vec{V}_{iF} = & \vec{V}_{Adv} + \vec{u}_{aF} + \vec{\omega}_F \times \vec{r}_F - \vec{u}_{tF} \\
V_{iF} = & \sqrt{(V_{Adv} + u_{aF})^2 + (2\pi r_F n_F - u_{tF})^2}
\end{aligned} \quad (17)$$

Inflow velocity to the aft propeller is expressed by:

$$\vec{V}_{1A} = \vec{V}_{Adv} + \vec{u}_{aA} + (\vec{u}_a)_{21} + \vec{\omega}_A \times \vec{r}_{AF} - \vec{u}_{tA} + (\vec{u}_t)_{21} \quad (18)$$

$$V_{1A} = \sqrt{(V_{Adv} + u_{aA} + (u_a)_{21})^2 + (2\pi r_{AF} n_A - u_{tA} + (u_t)_{21})^2}$$

NUMERICAL RESULTS AND DISCUSSION

Application of the CRP system on the bulk carrier and VLCC

We applied the method on two CRP for two different ship types where the model tests have been done in IHI and were available [9] and [10]. Main dimensions for bulk carrier and VLCC are given in Tab. 1.

Tab. 1. Main dimensions of the Bulk Carrier and VLCC

Ship Type Parameter	Bulk Carrier (Juno)	VLCC
Length (LBP)[m]	178.0	314.0
Breadth [m]	28.4	58.0
Depth [m]	10.72	19.5
Dead Weight	37000	-
Speed at full load [Knot]	15	16

For each vessel, conventional propeller and CRP have been used and the results are compared. The CRP5022 and conventional propeller (single propeller MP588) for the bulk carrier and CRP5029 and MP620 for VLCC have been selected. The principal of particulars of the both CRP propeller and single propeller are given in Tab. 2 and Tab. 3.

Tab. 2. Principal particulars of CRP and single propellers for Bulk Carrier

Propeller. Type Parameters	Single Propeller MP588	Contra-Rotating Propeller CRP5022	
		Foreward	Aft
D [mm] for model tset	277.6	250.0	213.9
D [m] for ship	5.23	4.71	4.03
Boss Ratio	0.20	0.20	0.18
Z	4	4	5
P/D	0.6	0.70	0.80
EAR	0.62	0.42	0.45
Skew angle [deg.]	7	20	20
Direction of Rotation	Left hand	Left hand	Right Hand
Section	MAU	MAU	MAU

Tab. 3. Principal particulars of CRP and single propellers for VLCC

Propeller. Type Parameters	Single Propeller MP620	Contra-Rotating Propeller CRP5029	
		Foreward	Aft
D [mm] (model)	269.3	250.0	221.0
D [m] (VLCC)	10.20	9.47	8.37
Boss Ratio	0.15	0.20	0.18
Z	5	4	5
P/D	0.79	0.92	0.93
EAR	0.55	0.35	0.35
Skew angle [Deg.]	20	20	18
Direction of Rotation	Left hand	Left hand	Right hand
Section	MAU	MAU	MAU

Grid generation

As known that the BEM is dealing with boundary of the body, so the grid generation is the necessary starting point for

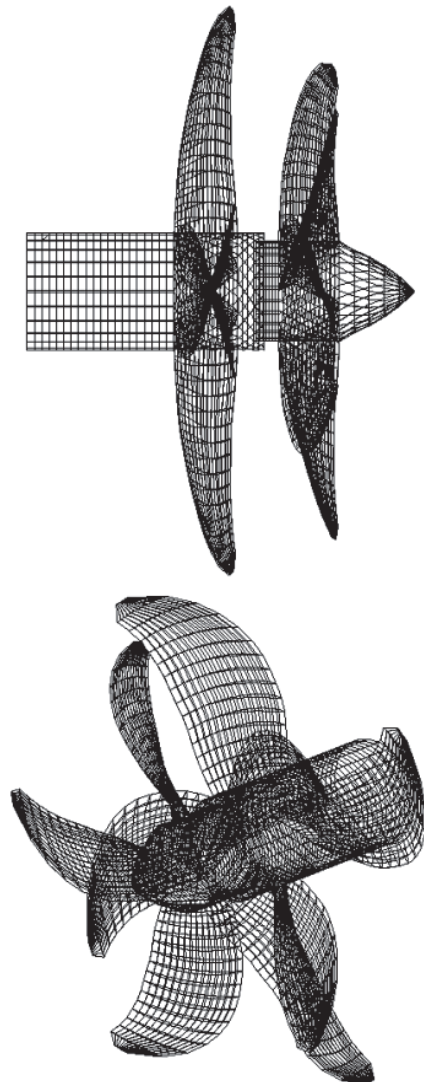


Fig. 3. Surface Mesh on CRP5022

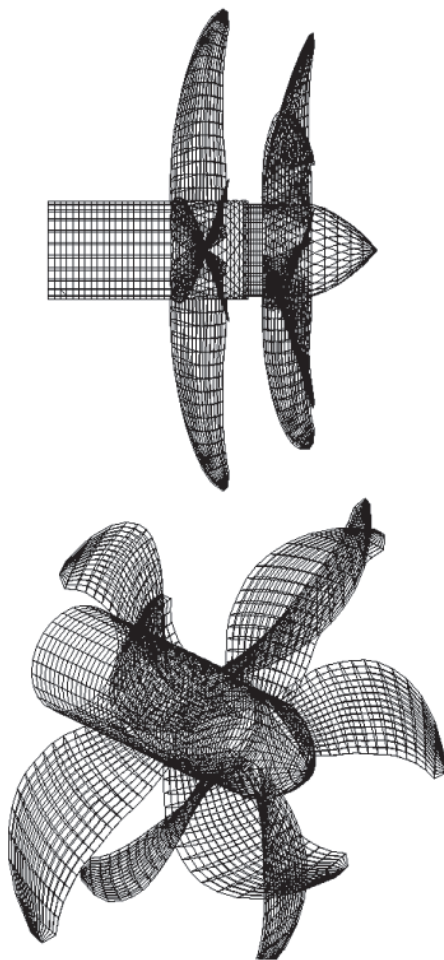


Fig. 4. Surface Mesh on CRP 5029

numerical implementation. The coordinate of the discretized surface should be sufficiently accurate since any inaccuracy can lead the hydrodynamic pressure to become noisy. According to our experience, the hyperboloidal quadrilateral element seems to be better than other elements like triangular and super element. Higher order element (quadratic or cubic order) is very complicated way to apply although it gives more precise results. This is our future plan to be done. However, for the present calculation and prepared SPD code, the hyperboloidal quadrilateral elements are used to discretize the whole body (hub and two propellers).

HYDRODYNAMICS CHARACTERISTICS AND DETERMINATION OF DESIGN POINT

Numerical results of the open water characteristics are compared with the experimental data for the CRP and conventional propellers. It is shown that the numerical results of the present method are very accurate and in good agreement with the experimental data for the open-water characteristics.

Using the equations (1) and (2), ($K_T = A \cdot J^2$; $K_T = B \cdot J^2$), in the figures of 5 and 6, intersection points are obtained between the thrust coefficients for each conventional and CRP propellers. Tab. 4 is shown the efficiency of each propeller (conventional and CRP) obtained from the figures 5 and 6 at the intersection points of K_t .

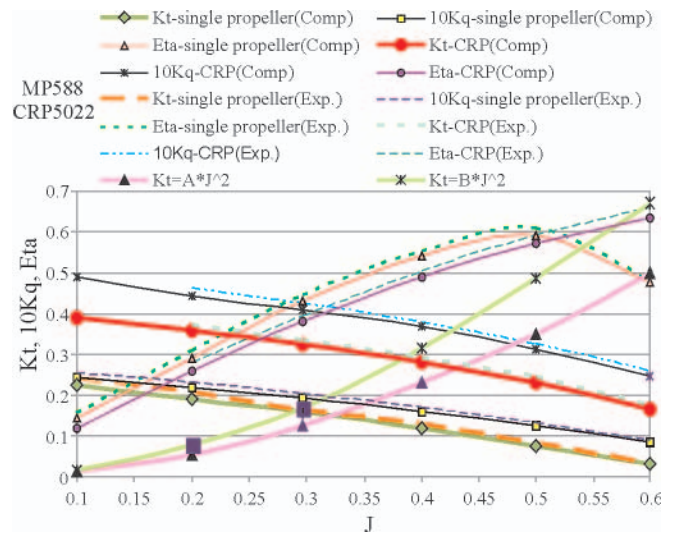


Fig. 5. Comparison of open water characteristics of conventional and CRP propellers for the Bulk-Carrier and the determination of Design point

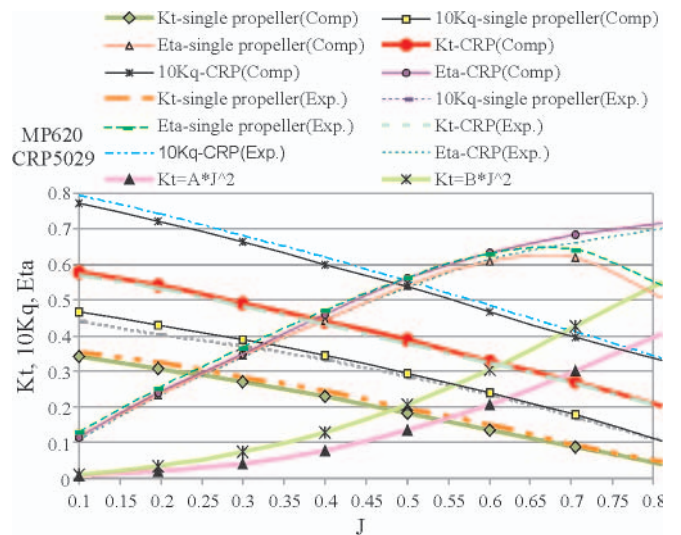


Fig. 6. Comparison of open water characteristics of conventional and CRP propellers for the VLCC and the determination of Design point

Tab. 4. Comparison of Experimental and Calculated Efficiency for Types of Ships

Ship Type	VLCC		Bulk-Carrier	
	MP620	CRP5029	MP588	CRP5022
Propeller Type	MP620	CRP5029	MP588	CRP5022
Intersection point of K_t	$J_{Exp.} = 0.54$ $J_{Cal.} = 0.55$	$J_{Exp.} = 0.62$ $J_{Cal.} = 0.61$	$J_{Exp.} = 0.32$ $J_{Cal.} = 0.325$	$J_{Exp.} = 0.375$ $J_{Cal.} = 0.38$
η_o (Exp.)	0.59	0.63	0.479	0.490
η_o (cal.)	0.57	0.64	0.467	0.469

CONCLUSIONS

In this paper, we numerically calculated the open water characteristics of the conventional and CCRP and obtained

the optimum operational condition for the large vessel using BEM. According to the results, following conclusions are drawn:

- The present method can be applied to any complicated propeller configuration and determine the open water characteristics.
- The CCRP system may raise the propeller efficiency around 2-3 percent at design condition for the present system.
- Design point is determined based on highest efficiency which is matched the generated propeller thrust and ship required thrust.

BIBLIOGRAPHY

1. Yang, C-J, Tamashima, M., Wang, G., Tamazaki R. and Kuizuka, H.: *Prediction of the steady performance of Contra-rotating Propeller by Lifting Surface Theory*, Transaction of the West-Japan Society of Naval Architects, Vol. 83, 1992
2. Nakamura, S., Ohta, T., Yonekura, K., Sasajima, T. and Saki, K.: *World's First Contra-rotating Propeller System Successful Fitted to a Merchant Ship, The Motor Ship*, Proceedings of 11th International Marine Propulsion Conf. 9-10 March 1989
3. Rutundi, C.F.: *Trials of the Training Ship Cristoforo Colombo with two Screws on a Common Axis*, Trans. Institution of Naval Architects, 1934
4. Lee, C-S, Kim, Y.G, Baik, M-C., Yoo, J-H.: *Numerical Prediction of Steady and Steady Performance of Contra-rotating Propellers*, Journal of Hydrospace Technology, Vol. 1 No. 1, 1995, pp. 29-40
5. Chen, B.Y-H, Tseng, C. L.: *A Contra-rotating Propellers Design for a High Speed Patrol Boat with Pod Propulsion*, FAST'95
6. Ukon, Y., Ohashi, K., Fujisawa, J., Hasegawa, J.: *Propulsive Performance of a Contra-rotating Podded Propulsor*, T-Pod Conference, Newcastle, April 2004
7. Chenjun, Y., Guiqiang, W.: *Hydrodynamic Performance of Contra-rotating Propellers (CRP)*, Numerical Analysis, China Society of Naval Architecture and Marine Engineering, Vol. 7, 1992
8. Islam, M.F., Veitch, B., Bose N., Liu P. : *Numerical Study of Hub Taper Angle Podded propeller Performance*, J. of Marine Technology, Vol. 43, No. 1, January 2006, pp.1-10
9. Nishiyama, S., Sakamoto, Y., Fujino, R.: *Contra-rotating Propeller System for Large Merchant Ships*, Technical Bulletin of IHI, 1991
10. Nishiyama, S., Sakamoto, Y., Ishida, S, Fujino, R. and Oshima, M.: *Development of Contra-rotating Propeller for Juno – A 37,000 DWT Class Bulk Carrier*, Trans. SNAME, Vol. 98, 1990
11. Bjarnne, E.: *Systematic Studies of contra-rotating Propellers for Merchant Ship*, Proc. IMAS'73, 1973, pp.49-59
12. Ghassemi, H., Allievi, A., : "A Computational Method for the Analysis of Fluid Flow and Hydrodynamic Performance of Conventional and Podded Propulsion Systems", Journal of Oceanic Engineering International, Vol. 3, No. 2, 1999
13. Koronowicz T., Tuskowska T., Waberska G.: *Computer software system for determining the pressure field resulting from hull flow and operation of the marine propeller*. Polish Maritime Research, December 1997
14. Ukon, Y. et. al.: "On the Design of Contra-rotating Propellers – Application to High Speed Container Ship", Trans. Of the West –Japan Society of Naval Architects, Vol. 25, 1988, pp.52-64.

CONTACT WITH THE AUTHOR

Hassan Ghassemi, Assoc. Prof.
Faculty of Marine Technology
Amirkabir University of Technology
Hafez Ave.,
Tehran, IRAN
e-mail: gasemi@cic.aut.ac.ir



CRP propulsion system,
photo: C. Spigarski

A complete design of ship propellers using the new computer system

Tadeusz Koronowicz, Prof.
Zbigniew Krzemianowski, Ph. D.
Teresa Tuskowska, Ph. D.
The Szewalski Institute of Fluid Flow Machinery
of the Polish Academy of Sciences in Gdansk
Jan A. Szantyr, Prof.
Gdansk University of Technology

ABSTRACT

The computer system presented in this article is composed of several program blocks for the complete design of ship propellers. The design calculations are based on a combination of the modified lifting line theory and on the vortex lifting surface theory. The system enables solution of the following design problems:

- *calculation of the scale effect on the ship wake velocity field, including the influence of the propeller and rudder on this field at the propeller location*
- *maximization of the propulsive efficiency*
- *optimization of the propeller blade geometry on the basis of the compromise between the cavitation and blade strength requirements*
- *optimization of the number of propeller blades and blade geometry on the basis of the acceptable level of induced pressure pulses and unsteady shaft bearing forces*
- *calculation of the blade spindle torque for the controllable pitch propellers.*

The computer system is equipped with many numerical options for graphical visualization of the input data, including an easy possibility of their correction and control of the intermediate and final results of calculations.

Key words: ship propellers, design methods, computational fluid dynamics

INTRODUCTION

In the recent years a computer system has been developed, which enables the complete design calculation of the different ship propulsor types, including their analysis in the wake velocity field behind the full scale ship hull. For this purpose the design and analysis blocks of the system are supplemented with the block for calculation of the wake scale effect and the influence of the propeller operation and presence of the rudder on the ship model wake.

The main design process is based on the modified lifting line model and on the model of vortex lifting surface theory. The analysis of the designed propeller operation in the non-uniform velocity field is based on the extensively modified program UNCA [2, 3, 4].

The propeller design system enables solution of the following design problems:

- ⇒ calculation of the effective ship wake velocity field, including the scale effect at the propeller location
- ⇒ correction of this field for the presence of the rudder (measurements of the wake in model scale are usually performed without the rudder)
- ⇒ maximization of the propeller efficiency

- ⇒ optimization of the propeller blade geometry, resulting from the compromise between the cavitation and strength requirements
- ⇒ optimization of the number and geometry of the propeller blades on the basis of the acceptable level of the pressure pulses generated on the hull and of the unsteady bearing forces
- ⇒ calculation of the blade spindle torque for the controllable pitch propellers.

The system is based on the conversational principle and it is equipped with an extensive set of graphical programs. It enables an easy control and correction of the input data and of the results of calculations of every block of the system. All data modifications are recorded and they may be used, if necessary, in any further design calculation.

The results of calculations may be presented in the form of printouts, graphical diagrams or films, showing the variation of the pressure distribution or cavitation phenomena on a rotating propeller.

The system includes three main program blocks:

- ⇒ the program for determination of the design velocity field
- ⇒ the program for propeller design,

➤ the program for analysis of propeller operation in the non-uniform inflow field.

The block diagram of the system is shown in Fig. 1. The expected final effect of the propeller design process may be achieved only through proper interaction between these programs. The calculations may be controlled from the computer screen, without preparation of the special data sets for the respective blocks of the system. The special graphical procedures enable an easy control of the input data and of the intermediate results, including also correction of the propeller blade geometry directly from the computer screen at all stages of the design process.

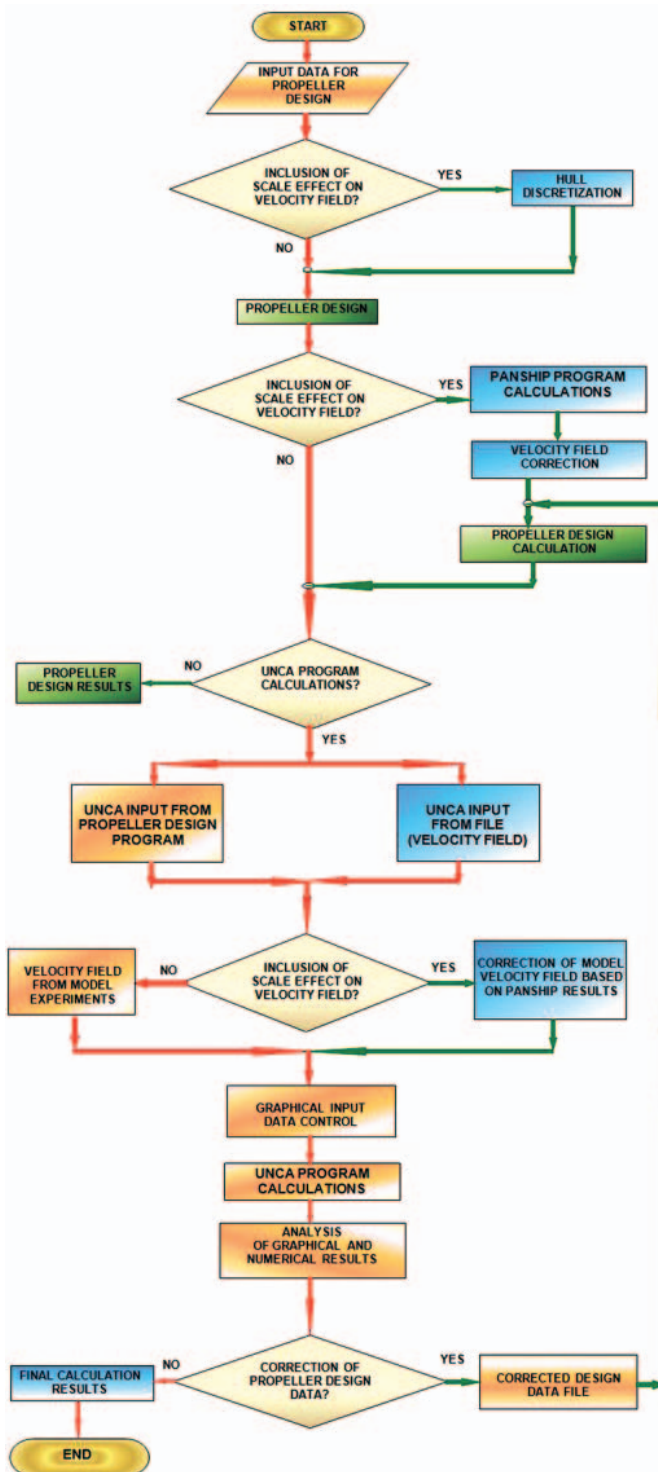


Fig. 1. The block diagram of the computer system for the complete design of ship propellers

DESCRIPTION OF THE MAIN BLOCKS OF THE SYSTEM

The input data

The input data include all quantities necessary for the initiation of the four alternative versions of the calculations:

- ★ propeller design calculation without correction of the velocity field and without the analysis of the propeller operation in the non-uniform velocity field,
- ★ propeller design calculation without correction of the velocity field, but including the analysis of the propeller operation in the non-uniform velocity field,
- ★ propeller design calculation including the correction of the velocity field for the scale effect and the analysis of the propeller operation in the non-uniform velocity field, but without the correction for the presence of the rudder,
- ★ propeller design calculation including corrections of the velocity field both for scale effect and rudder presence and including the analysis of the propeller operation in the non-uniform velocity field.

The input data may be introduced in the form of the pre-prepared input data file or they may be introduced directly from the computer screen in the conversational mode. The program is equipped with graphical procedures for control of the correctness and for modification of the input data.

The program block for calculation of the scale effect and of the rudder and propeller influence on the wake velocity field

In order to perform the calculation including the scale effect on the wake velocity field the appropriate data describing the hull geometry (typically the set of theoretical hull frames and outlines of the bow and stern) must be available. Alternatively, the earlier prepared data file containing the hull geometry defined as the set of panels may be used as input. The selection between these two options is made from the screen. In the first option the program for transformation of the hull geometry into the set of panels is used.

Calculation of the scale effect on the wake velocity field does not require a large number of panels describing the hull geometry. The practical experience shows that the sufficiently accurate results may be obtained using:

- ◆ 60 panels along the hull length
- ◆ 20 panels along the hull frame (at one side of the hull).

Such a number of panels may be accurately defined if the set of 16 theoretical frames is available, with more dense distribution in the bow and stern regions. Fig. 2 shows an example of the hull represented by the set of panels, viewed at a certain rotation angle. Such a presentation enables efficient control of the distribution of the panels, which should have the form of quadrangles possibly close to squares.

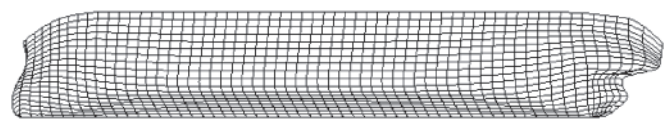


Fig. 2. The ship hull viewed at a rotation angle around the x axis

The correct representation of the hull as the set of panels allows further calculation using the PANSHIP program [9, 10, 11, 12], in order to determine the scale effect on the hull wake velocity field at propeller location and to calculate the propeller design velocity field.

The hull represented by the set of panels may be supplemented with the rudder described by a separate set of panels. The rudder is usually not taken into account in calculations for model scale (if the model experiments have been performed without the rudder), but it is always included in the full scale calculations.

The determination of the design velocity field

Taking into account the scale effect on the velocity field at propeller location is a very important aspect of the propeller design process. The design procedure itself, which determines the propeller performance and blade geometry, requires only the radial distribution of the circumferential average of the axial component of the velocity field. However, the complete design process requires information about the entire velocity field (three components distribution over the propeller disc) in full scale, including the effect of propeller operation (the effective field) and the effect of the rudder presence. This may be achieved only using the computation procedure based on the “computer model basin”. Such a procedure has been developed on the basis of the computer model basin PANSHIP [10, 12].

Example of application of such a procedure is presented in Figs. 3 and 4. Fig. 3 shows the results of measurements of the axial component of the velocity on the tanker model, while Fig. 4 shows the corresponding design velocity field calculated for the full scale ship. The influence of rudders of different thickness on the velocity field at propeller location is shown in Figs. 5 and 6 [6, 12].

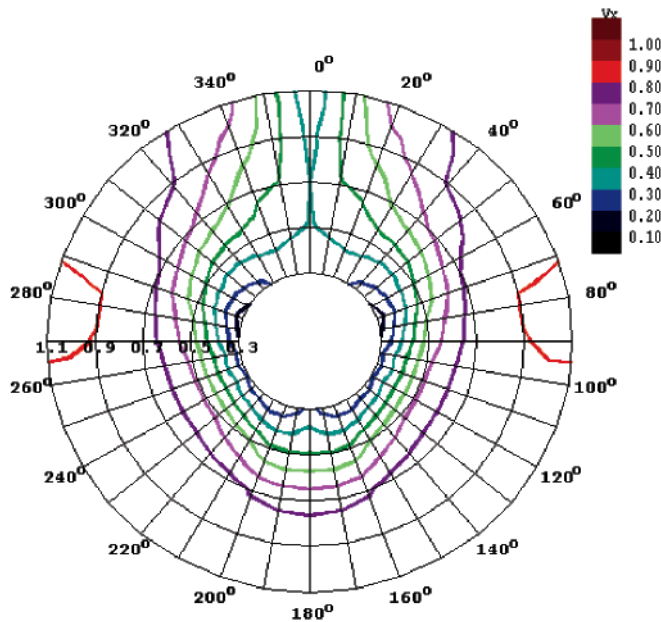


Fig. 3. Results of measurements of axial velocity component behind the tanker model $L_{pp} = 6.53$ [m]

The results presented in these figures show the meaningful scale effect and visible influence of the rudder presence on the velocity field at propeller location. The analysis of these results leads to the conclusion that either model experiments should be conducted with the rudder or the appropriate corrections may be calculated using the computer model basin (e.g. PANSHIP). As the velocity field should be corrected both for the scale effect and for the rudder effect, these corrections may be integrated in one procedure, leading to the effective full scale velocity field. Only such a velocity field enables correct analysis of the propeller operation behind the ship hull.

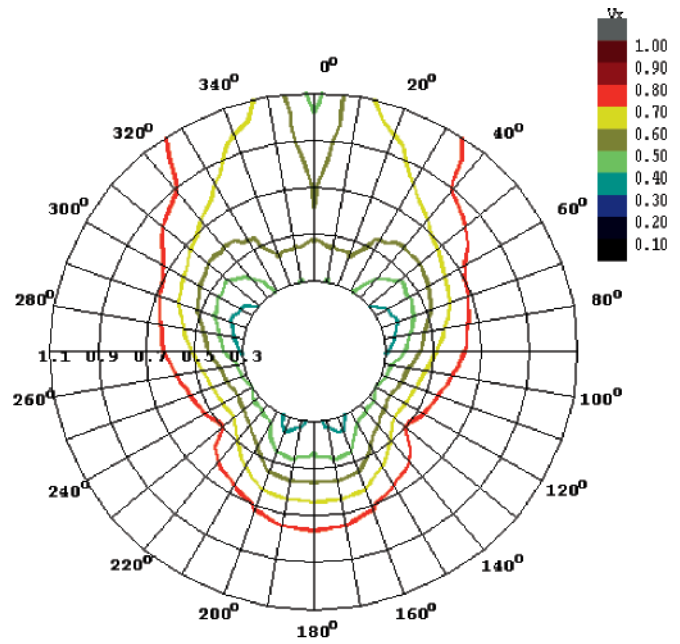


Fig. 4. Results of calculation of the design velocity field for the full scale tanker $L_{pp} = 200$ [m]

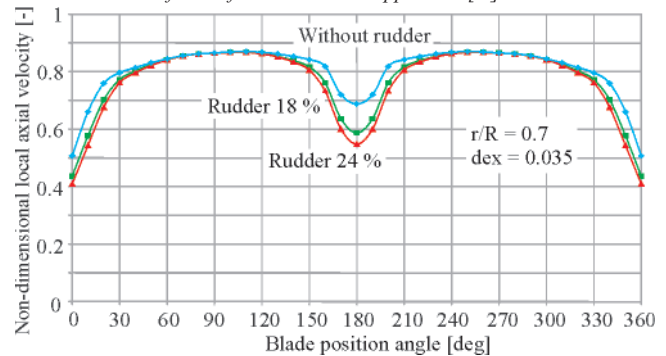


Fig. 5. Influence of the rudders of different thickness on the axial velocity component at the propeller location

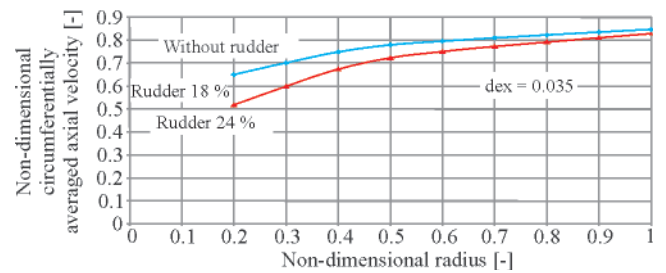


Fig. 6. Influence of the rudders of different thickness on the radial distribution of the circumferential average of the axial component of velocity at propeller location

The design program block

The algorithm of the design program has been described in great detail in [1, 8]. The program based on this algorithm has been functioning over many years and it has been extensively verified.

The design calculations are performed in all cases, irrespective of the version selected in the Section 2.1 above. In case of version **a**) these are the only and final calculations, ending with the results which are presented in the form of tables (cf. Figs. 7 and 8) and pictures shown on the computer screen (cf. Figs. 9, 10 and 11). The pictures may be easily printed. The full results are included in the file Design.OUT.

In the case of version **b**) the design calculations are conducted alternating with the analysis program UNCA, until

the appropriate criteria regarding e.g. cavitation phenomena or pressure pulses and unsteady bearing forces are fulfilled.

Summary – Propeller	
Design ship velocity [knots]	22.000
Advance coefficient [-]	0.7285
Thrust coefficient [-]	0.4855
Torque coefficient [-]	0.1027
Efficiency [-]	0.5484
Cavitation number [-]	2.4936
Cavitating tip vortex kernel diameter [mm]	138.2382
Circulation distribution coefficient [-]	0.5409
Blade area ratio [-]	0.975
Thrust [N]	2748402
Power [kW]	38741.8945
Mass of the blades [kg]	36753.66
Moment of inertia of the blades in air [kg*m ²]	494764.06
Moment of inertia of the blades in water [kg*m ²]	759142.5
Cavitation	
Laminar cavitation - suction side	Yes
Laminar cavitation - pressure side	No
Bubble cavitation – suction side	Yes
Bubble cavitation – pressure side	No
Intermittent cavitation – suction side	Yes
Intermittent cavitation – pressure side	No
Tip vortex – suction side	Yes
Tip vortex – pressure side	No

Fig. 7. The main results of the design task

*****DESIGN CALCULATION OF THE FIXED PITCH PROPELLER*****
 THE TASK WAS TO CALCULATE DELIVERED POWER FOR FIXED PROPELLER THRUST
 BLADE SECTION PROFILE NACA 35 NACA65
 STRENGTH CALCULATION ACCORDING TO ICE CLASS

NO. OF BLADES	5	WAKE FRACTION	0.3160
DIAMETER (M)	7.0000	RAKE (DEG)	0.0000
HUB DIAMETER (M)	1.4000	SKINBACK (DEG)	4.8991
DESIGN SPEED (M)	22.0000	BLADE AREA RATIO	0.9750
KEYS PER HUB	01.0000	THRUST (N)	2748402.00
SHAFT IMMERSION (M)	0.5000	POWER (KW)	38741.8945
WAT. DENS. (KGM-3)	1025.00	ADVANCE COEFF.	0.7285
CAVIT. NUMBER	2.4936	THRUST COEFF.	0.4855
TIP VORTEX KERNEL (MM)	138.2382	TORQUE COEFF.	0.1027
COEFF. OF DISTR. CIRC.	0.5409	EFFICIENCY	0.5484

X	R(M)	C(M)	LE(M)	P(M)	H(M)	T(M)	LS(M)	CL	CD
0.2000	0.7000	2.1399	1.0700	8.2679	0.1252	0.4263	0.0000	0.0000	0.0080
0.3000	1.0500	2.3594	1.2651	8.3451	0.1557	0.3290	-0.0854	0.8419	0.0080
0.4000	1.4000	2.5705	1.4014	8.4095	0.1756	0.2638	-0.1152	0.8291	0.0080
0.5000	1.7500	2.7687	1.4984	8.5046	0.1845	0.2114	-0.1141	0.8625	0.0080
0.6000	2.1000	2.9463	1.5326	8.5454	0.1830	0.1690	-0.0595	0.4804	0.0080
0.7000	2.4500	3.0672	1.5086	8.8629	0.1725	0.1288	0.0350	0.3985	0.0080
0.8000	2.8000	3.1525	1.3711	9.2855	0.1547	0.0917	0.2051	0.3121	0.0080
0.9000	3.1500	3.0096	1.0155	9.8592	0.1290	0.0560	0.4893	0.2272	0.0080
1.0000	3.5000	3.0010	-0.8995	10.4328	0.0115	0.0280	1.0500	0.0001	0.0080

X	UR	C/D	LE/D	P/D	H/C	T/D	LS/D	G	CR/CL
0.2000	0.5478	0.3057	0.1529	1.1911	0.0585	0.0609	0.0000	0.0000	*****
0.3000	0.4691	0.3371	0.1807	1.1922	0.0660	0.0470	-0.0122	0.0463	0.0125
0.4000	0.4390	0.3672	0.2002	1.2142	0.0683	0.0374	-0.0166	0.0647	0.0127
0.5000	0.4150	0.3955	0.2141	1.2149	0.0666	0.0302	-0.0163	0.0765	0.0142
0.6000	0.4090	0.4209	0.2189	1.2308	0.0621	0.0240	-0.0085	0.0833	0.0167
0.7000	0.3659	0.4410	0.2155	1.2661	0.0559	0.0184	0.0050	0.0856	0.0201
0.8000	0.2487	0.4504	0.1959	1.3265	0.0491	0.0131	0.0293	0.0802	0.0256
0.9000	0.1685	0.4299	0.1481	1.4085	0.0428	0.0080	0.0699	0.0623	0.0352
1.0000	0.1285	0.0430	-0.1285	1.4904	0.0384	0.0040	0.1500	0.0000	80.0000

Fig. 8. The table of the results of design calculations (the first page only) copied from the file Design.OUT

The program block for analysis of the propeller operation in the non-uniform velocity field

The program UNCA for the analysis of propeller operation in the non-uniform velocity field is the very important element of the propeller design process. The main part of the algorithm of this program deals with the determination of the extent and intensity of different forms of cavitation present on the blades of the propeller operating in the non-uniform velocity field. The original theoretical model integrates the unsteady vortex lifting surface theory with the dynamically varying cavitation bubbles. The detailed description of this program is included in [2, 3, 4].

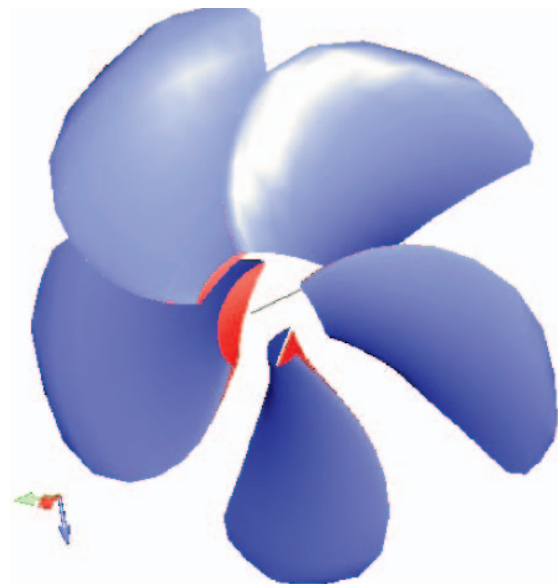


Fig. 9. The rendered picture of the designed propeller blades

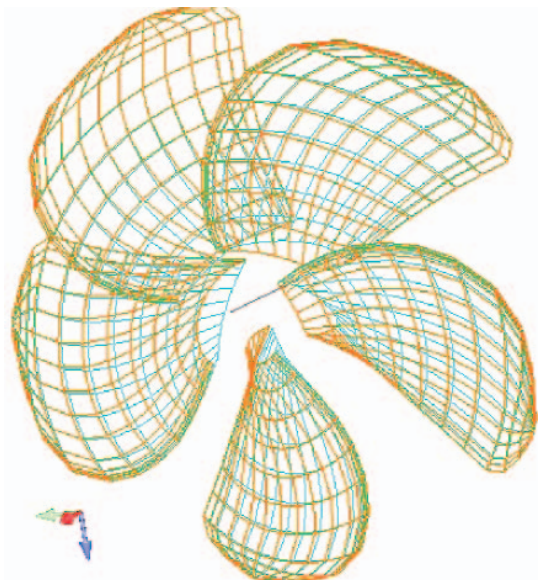


Fig. 10. The designed propeller blades shown in the grid form

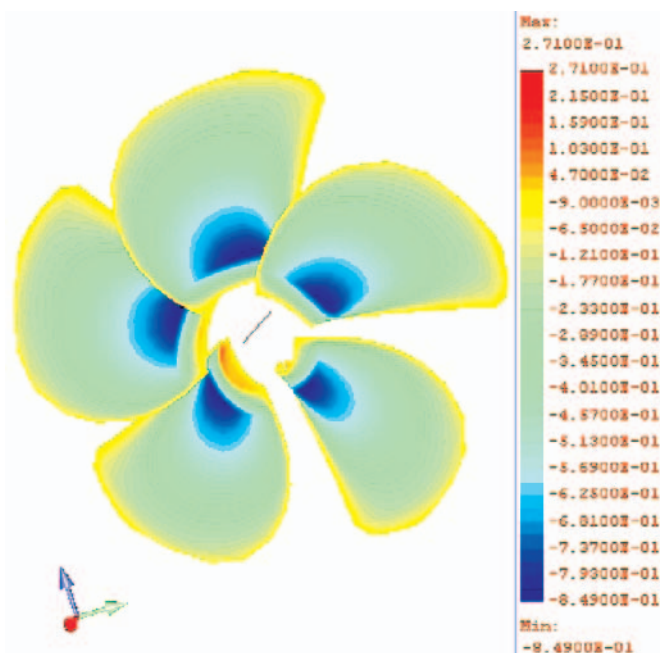


Fig. 11. The distribution of pressure coefficient on the suction side of the blades in the propeller design condition

The input data to the analysis program are introduced from the appropriate file (the velocity field – either given or computed in the system according to Section 2.3) and from the results of the design task performed in Section 2.4 (geometry of the propeller and some additional data). These input data may be controlled from the screen as the **Summary of the Analysis Task Settings**. An example of such a table is shown in Fig. 12.

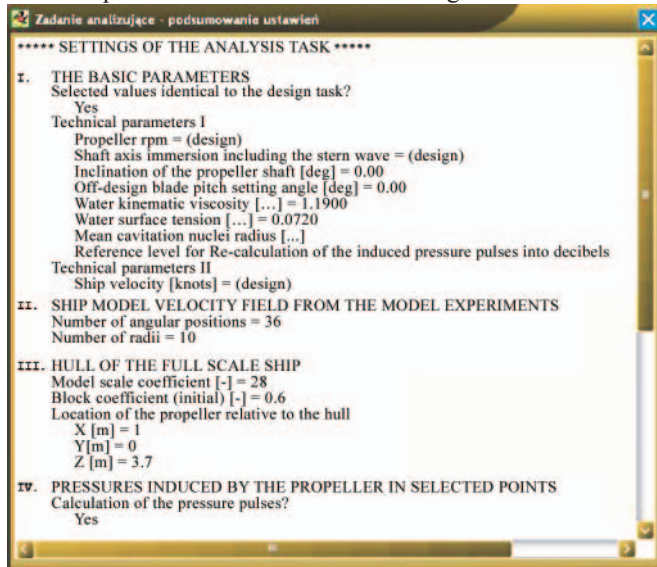


Fig. 12. Summary of the Analysis Task Settings

The newly designed propeller is analysed using the program UNCA from the following points of view:

- ★ presence of the different forms of cavitation in the selected angular propeller blade positions in the non-uniform velocity field
- ★ values of the induced pressure pulses either on the ship hull or in the surrounding space,
- ★ values of the unsteady bearing forces.

After the analysis of the results of these calculations the appropriate modifications to the designed propeller geometry may be introduced and the design calculations may be repeated. For example the following propeller geometry parameters may be changed:

- ◆ the values and the radial distribution of the blade skewback
- ◆ the values and the radial distribution of the blade profile chord lengths
- ◆ the values and the radial distribution of the blade profile maximum thickness
- ◆ the type of chord-wise profile thickness distribution
- ◆ the type of chord-wise profile mean line camber distribution
- ◆ the radial hydrodynamic loading (circulation) distribution
- ◆ the number of blades.

The analysis of propeller operation in the non-uniform field of flow may be performed for the design ship speed and propeller rate of rotation or for the off-design values of these parameters (without changing the blade geometry and the velocity field). This is very convenient when the propeller is designed for the compromise design condition, e.g. for a fishing vessel, a tug boat or a navy ship. For such ships more than one ship speed is important (e.g. towing speed, free running speed or maximum speed) and the designed propeller should ensure the optimum performance over the entire range of operating conditions.

An example of the selected results of the calculations of the unsteady bearing forces and cavitation extent is presented in the following figures.

```

UNCA93 LIFTING SURFACE PROGRAM FOR UNSTEADY PROPELLER CAVITATION ANALYSIS
*****
PROJECT NO= 1
CALCULATED FOR=Desmax
PAGE NO= 1

CONTROL PRINTOUT OF THE INPUT DATA
*****
R1= 1 M1= 9 NZ = 5 (-) CVC = 1.1900*10-6 (M2S-1)
K2= 3 M2=15 VS = 11.3178 (MS-1) WCP = 2500.00 (NM-2)
K3= 1 M3= 9 PD = 7.0000 (M) SDW = 1025.00 (KGM-3)
K5= 3 M4=36 HD = 1.4000 (M) WTS = 0.0720 (NM-1)
K7= 1 M5= 8 RPS= 1.5167 (S-1) RAVE= 0.0500*10-3 (M)
K8= 2 M6=70 WSD= 4.5000 (M) RLF =0.100000 (PA)
SFI= 0.0 (DEG) DLF = 0.0 (DEG)

RR PI CI SI RKI THI CHI RLI
0.20000 1.18110 2.13990 0.00000 0.00000 0.42630 0.12520 0.05000
0.30000 1.19220 2.35970-0.08540 0.00000 0.32900 0.15570 0.04000
0.40000 1.21420 2.57040-0.11620 0.00000 0.26180 0.17560 0.03500
0.50000 1.21490 2.76850-0.11410 0.00000 0.21140 0.18440 0.03000
0.60000 1.22080 2.94630-0.05950 0.00000 0.16800 0.18300 0.02500
0.70000 1.26610 3.08700 0.03500 0.00000 0.12880 0.17260 0.02000
0.80000 1.32650 3.15280 0.20510 0.00000 0.09170 0.15480 0.01500
0.90000 1.40850 3.00930 0.48930 0.00000 0.05500 0.12880 0.01000
1.00000 1.49040 0.30100 1.05000 0.00000 0.02800 0.01160 0.00500
*****
UNCA93 LIFTING SURFACE PROGRAM FOR UNSTEADY PROPELLER CAVITATION ANALYSIS
*****
    
```

Fig. 13. The table of results of the analysis of the propeller in the non-uniform velocity field (the first page only) copied from the file Unca.OUT

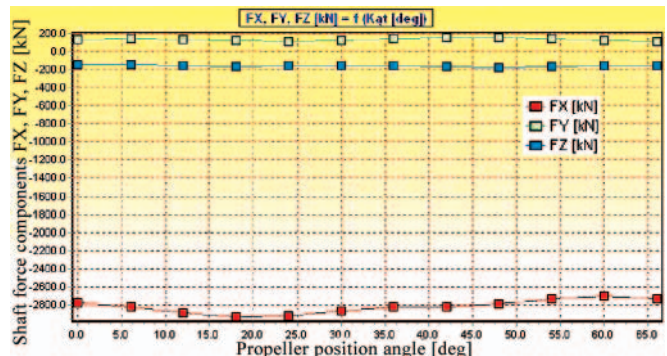


Fig. 14. The components of the unsteady bearing force as the function of propeller angular position

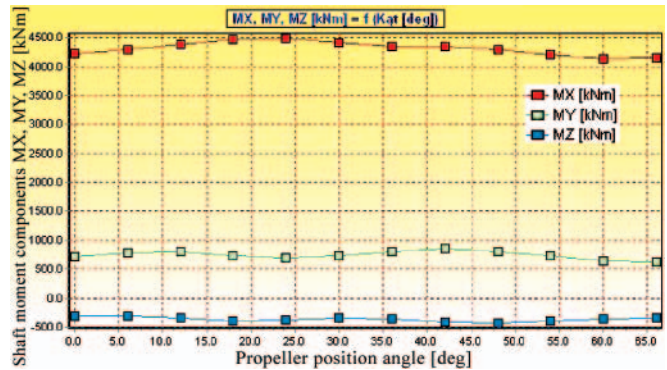


Fig. 15. The components of the unsteady bearing moment as the function of the propeller angular position

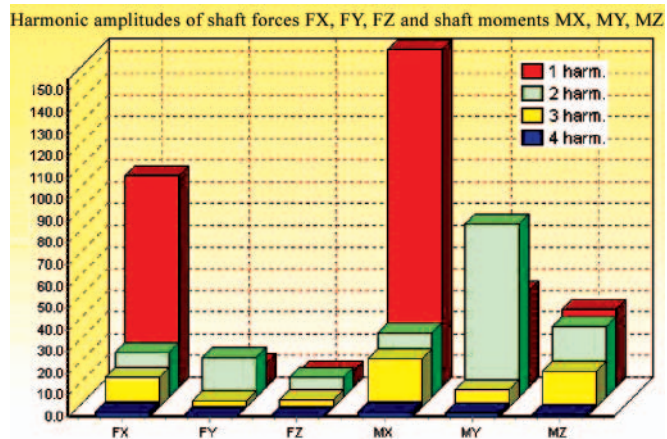


Fig. 16. The harmonic amplitudes of the three components of the bearing force and three components of the bearing moment

Apart from the static pictures of the calculated cavitation phenomena on the propeller (Figs. 17 and 18), the program can generate a moving picture of the cavitating propeller. In this film the propeller performs full revolution, showing the dependence of the cavitation phenomena on the local details of the inflow velocity field. All numerical results of the program UNCA are included in the file Unca.OUT.

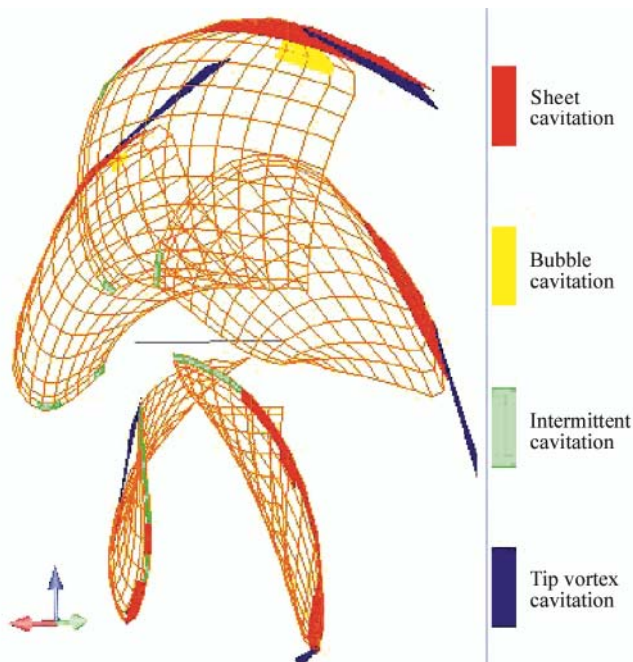


Fig. 17. The example of visualization of the calculated cavitation phenomena on the propeller

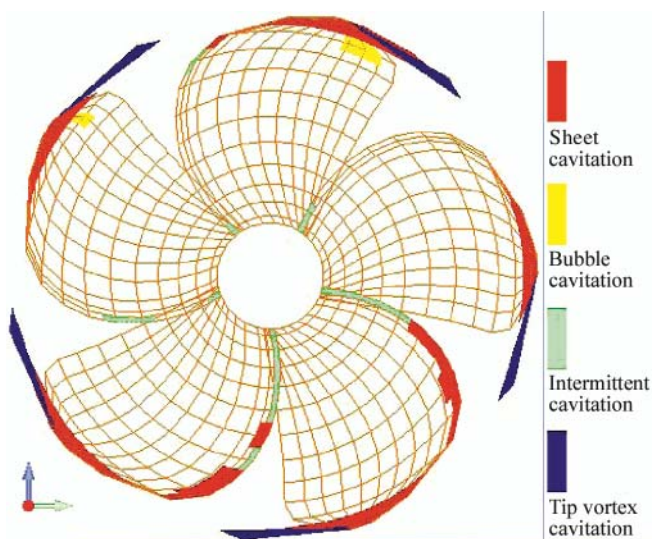


Fig. 18. The frontal view of the calculated cavitation phenomena on the propeller

FINAL REMARKS

- The above presented system for the complete design of ship propellers enables an integral treatment of the hull-propeller-rudder system in the process of propeller design. The extensive graphical procedures for input data control and modification and for presentation of the results in the form of pictures and films are an important practical advantage of the system, facilitating its practical use by the designers.
- The system has been developed with the support of the Research Grant No. 4T07C06630 of the Polish Ministry of

Science and Higher Education, together with other design systems for three special ship propulsor types, namely:

- ♦ ducted propellers
- ♦ tandem co-rotating propellers
- ♦ tandem contra-rotating propellers.

- Description of these systems will be the subject of separate publications in the future.

BIBLIOGRAPHY

1. Koronowicz T.: *Algorithm of the Design Program Based on the Single Layer Lifting Surface Model Applied to the Arbitrarily Skewed Propellers* (in Polish), IFFM Report No. 295/86
2. Szantyr J. A.: *A Computer Program for Calculation of Cavitation Extent and Excitation Forces for a Propeller Operating in the Non-uniform Velocity Field*, Int. Shipbuilding Progress, Vol. 26, No.296, 1979
3. Szantyr J. A.: *A Deformable Lifting Surface Method for Determination of Unsteady Cavitation on the Propeller Blade and Its Hydrodynamic Consequences* (in Polish), Bulletin of IFFM No. 183/1110/84, 1984
4. Szantyr J. A.: *A Method for Analysis of Cavitating Marine Propellers in Non-uniform Flow*, Intern. Shipbuilding Progress, Vol. 41, No. 427, 1994
5. Koronowicz T., Tuszowska T., Waberska G., Krzemianowski Z., Chaja P., Góralczyk A.: *Design Algorithm of Screw Propellers* (in Polish), IFFM Report No. 6103/06
6. Koronowicz T., Waberska G., Krzemianowski Z.: *The Influence of the Rudder on the Velocity Field Behind the Hull* (in Polish), IFFM Report No. 4493/03
7. Koronowicz T., Waberska G., Krzemianowski Z., Góralczyk A.: *The Scale Effect of the Velocity Field Behind the Hull* (in Polish), IFFM Report No. 7103/07
8. Koronowicz T., Szantyr J. A., Krzemianowski Z., Tuszowska T. Waberska G.: *The System of Programs for Screw Propeller Design* (in Polish), IFFM Report No. 148/08
9. Bugalski T., Koronowicz T., Szantyr J. A., Waberska G.: *A Method for Calculation of Flow Around the Hull of a Ship Moving in Calm Water with Constant Velocity*, Mar. Tech. Transactions, Vol. 5, 1994
10. Koronowicz T.: *The Computer Method for Prediction of the Velocity Field Behind a Full-scale Ship Hull*, Polish Maritime Research Vol. 10, No. 1, 2003
11. Koronowicz T., Szantyr J. A., Chaja P.: *A Computer System for the Complete Design of Ship Propellers*, paper presented at the XVII International Conference on Hydrodynamics in Ship Design, Polanica Zdrój, Poland 19-21 September 2007
12. Koronowicz T., Krzemianowski Z., Szantyr J.: *Numerical Determination of the Propeller Design Velocity Field Including Scale Effect and Rudder Influence*, paper presented at the 11th Numerical Towing Tank Symposium, Brest, France, September 7-9, 2008.

CONTACT WITH THE AUTHORS

Tadeusz Koronowicz, Prof.
 Zbigniew Krzemianowski, Ph. D.
 Teresa Tuszowska, Ph. D.
 Institute of Fluid-Flow Machinery,
 Polish Academy of Sciences
 Fiszerka 14
 80-952 Gdańsk, POLAND
 e-mail : ttk@intercho.com

Jan A. Szantyr, Prof.
 Department of Turbomachinery
 and Fluid Mechanics,
 Gdańsk University of Technology
 Narutowicza 11/12
 80-958 Gdańsk, POLAND
 e-mail : jas@pg.gda.pl

Identification of shaft line alignment with insufficient data availability

Lech Murawski, Ph. D.
The Szewalski Institute of Fluid-Flow Machinery
Polish Academy of Sciences

ABSTRACT



The paper presents a method of identification parameters of shaft line alignment in case of the lack of producers' data. Proper shaft line alignment is often a problem for repair shipyards, for aged ships without sufficient documentation. Author proposed combined experimental-analytical method for identified some existing parameters and checking (and eventually correcting) power transmission system's foundation. Specialised software has been developed for shaft line alignment calculations with influence coefficients. An example analysis has been performed for cargo ships with medium-speed main engine and second one with slow-speed propulsion system. Multivariant computations supported by measurements of the ships' shaft line have been carried out.

Key words: shaft line alignment, bearings reaction, crankshaft external forces, shaft line stresses, aged ships

INTRODUCTION

Propulsion system's foundation might be changed dangerously during ship hull repairing (especially welding works) even if there is no work with power transmission system. What is more, improvement of the shaft line - crankshaft alignment is difficult because very often aged ships haven't available documentations. Repair shipyard does not know if foundation parameters of propulsion system are acceptable or not. Some of them (like shafts' diameters, intermediate bearings' reactions) are easy to measured but the others are practically inaccessible (shaft line deformation, shaft line - crankshaft interaction, stern tube and main engine bearings' reactions, stresses). The analysis become much more difficult if our software take into account isolated power transmission system from ship hull (Fig. 1) without boundary conditions (e.g. without hull displacements and stiffness) [9]. Usually, similar parameters of shaft line alignment before and after repair is a shipyard's target.

There is no, well known, cheap methods for inspection and eventually improvement of propulsion system foundation after ship hull repairing [13]. Abnormalities of the propulsion system's working parameters are often detected after ship's repairing, during sea trial or even after certain period of ship's voyage. Then, the failure repairing is very costly. Sometimes, tube of stern bearing or engine's main bearing must be replaced and the proper shaft line alignment must be performed.

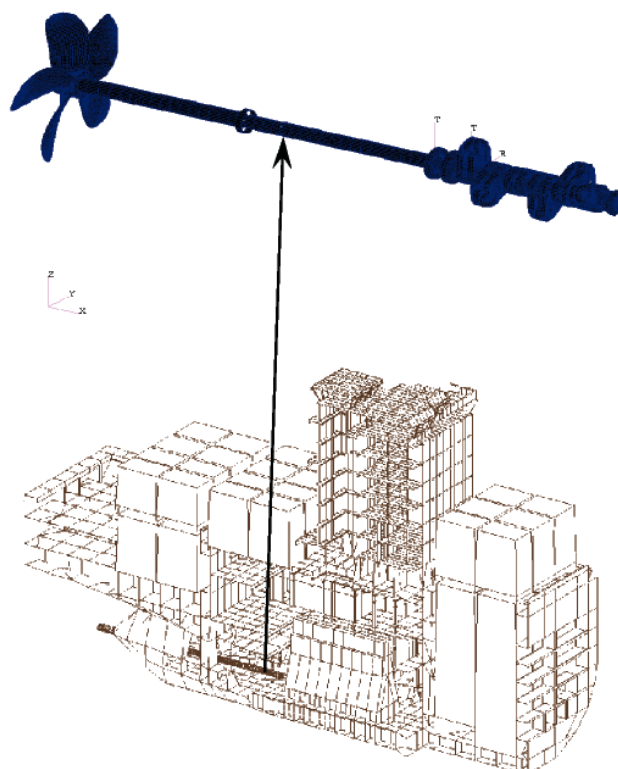


Fig. 1. Typical model of the power transmission system isolated from ship hull

Author proposed a method of shaft line alignment identification based on easy to measured parameters and numerical analysis. Elaborated specialised software can calculate influence coefficients for each bearing. Shaft line alignment identification should be performed before and after repairing process. Analysis shows if correction is necessary (if shaft line alignment parameters have been changed significantly during repairing). If yes, analysis, based on influence coefficients, give us advice how easily improve propulsion system's foundation.

IDENTIFICATIONS' METHOD

Just before starting hull repairing some typical measurements [1, 6, 7] should be performed. First of all, the jack-up test should be realized for intermediate bearings' reaction identification. Also identification of shafts' diameters is necessary. In the same time, the base of location of bearings body and shaft line position should be done.

Position changes of the shaft line can be controlled (Fig. 2) by bending stresses measurement (e.g. by strain gauge technique) [2, 3]. Bending stresses should be recorded during full rotation of the shaft (with usage of turning gear) just before and after ship repair process. Changes of the stress level in the horizontal and vertical plane may be simulated by numerical analysis and then changes of the shaft line alignment may be identified.

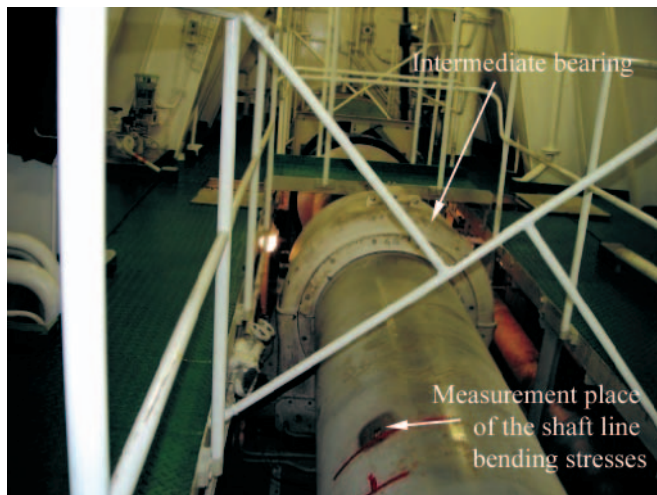


Fig. 2. Bending stress measurement of the shaft line

The relative position of bearing body might be based on measuring stress level [8] on foundation pads (Fig. 3) or on the other sensitive element of the bearing foundation (Fig. 4). Stress level should be recorded during jack-up test, before ship repair process. The simultaneous measurements can be treated as calibration process. After measurements the dependence between bearing reaction and stress level of the foundation pads (or foundation knee) is recognised. The same measurements (even without jack-up test) performed after ship repairing, give us changes of the bearing reaction which are induced during overhaul.

Whole (before and after repairing process) measurements investigation gives us necessary data for shaft line alignment's changes identification. The next step during expertises must be an assessment if identified changes are acceptable or not. The following limitations should be checked: loadings of the stern tube bearing, intermediate bearings and main bearings of the engine; stresses of the shaft line; interaction between shaft line and crankshaft. The shaft line alignment correction should be proposed if some limits are exceeded. Correction should be

practicable and cheap. Generally, it should be restricted to displacements of the intermediate bearings in horizontal and vertical plane. Author made a specialised computer program which can be useful for all this tasks (identification, assessment and correction) with limited (without design documentation) data availability.



Fig. 3. Stress measurement of bearing's foundation pads

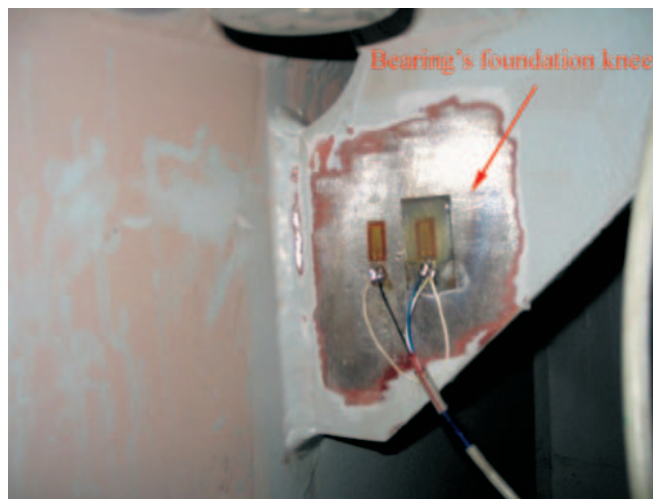


Fig. 4. Stress measurement of bearing's foundation knee

SOFTWARE DESCRIPTION

Assessment of the shaft line alignment for aged ships requires specialised software. The data for the software might be based on the measurements before and after ship's repairing in case of insufficient design data availability. During ship hull repairing (especially during welding works) power transmission system's axis might be unacceptable displaced even if there is no work with propulsion system. Assessment of the shaft line alignment before ship repairing process as well as determination of propulsion system's sensitivity on

stable hull deformation is very important from technical and economical point of view. Author performed specialised software for bearing reactions' identification and shaft line alignment's influence coefficients determination.

Identification of shaft line alignment with knowledge only of bearings' reaction and shafts' geometry is reverse mathematical problem [4]. This problem is often ambiguous with multi solutions. For that reason equation no. 1 [5, 14] is solved during iteration process.

$$([K] - [K_G]) \cdot \{x\} = \{F\} \quad (1)$$

where:

- K – global stiffness matrix,
- K_G – geometric stiffness matrix,
- x – displacement vector,
- F – generalised force vector.

Matrix equation no 1 is a system of algebraic equations with constant coefficients. Modified Gauss algorithm is used for solving the equations. The shaft line is modeled by 2-node (with 6 degree of freedom for each node) linear beam elements with nonlinear boundary conditions. The beams can be cylindrical or conical and drilled or not. Bearings might be modeled by point wise or continuous support with taking into account bearing's clearance and stiffness. Stiffness of the continuous bearing (e.g. stern tube bearing) is modeled by polynomial of 10 order. In the program there are procedures for field solution's searching. Finding out variants fulfilling measured values is a target of the algorithm. All variables are declared in the program as dynamic one so there are no limitations for number of elements and bearings. An example of multi bearings shaft line is presented on Fig. 5.

ANALYSIS EXAMPLE FOR THE CONTAINER SHIP

As a first step, the analysis has been performed for the container ship with typical propulsion system – constant pitch propeller driven directly by slow speed main engine. An example analysis has been made for container ship 4500 TEU. The hull stiffness characteristics on the base of FEM ship model analyses [10] like presented on Fig. 6. This kind of the model contains about 50 000 ÷ 150 000 degrees of freedom.

The methods of the characteristics determination of ship hull and main engine have been presented in the other author's articles [11, 12]. The examples of ship hull with propulsion system dynamic characteristics are presented on Fig. 7-8.

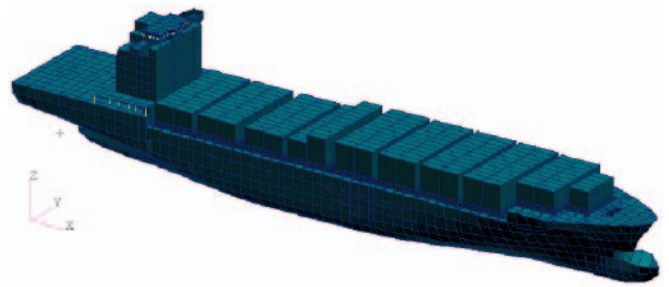


Fig. 6. FEM model of container ship

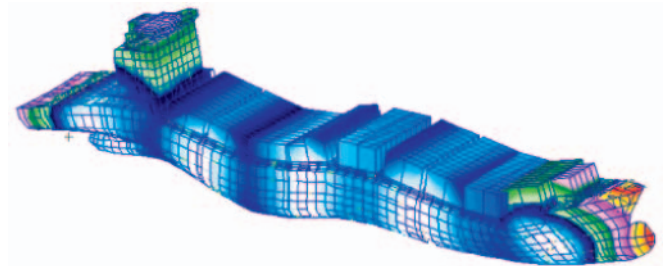


Fig. 7. 5-node mode of ship hull vibration

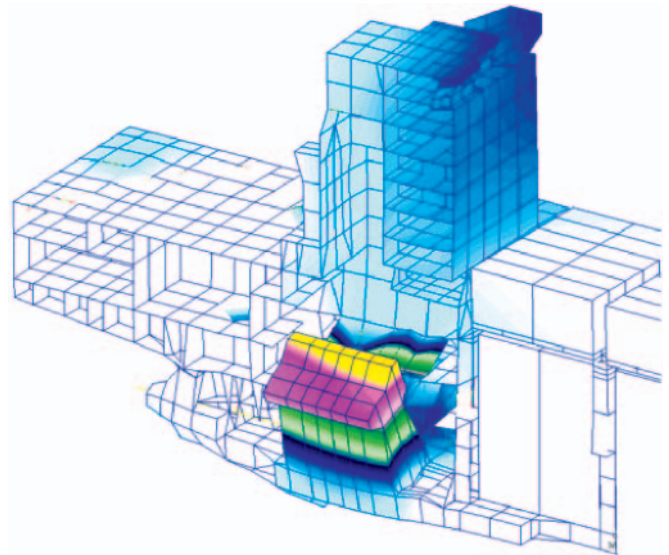


Fig. 8. Transverse mode of main engine vibration

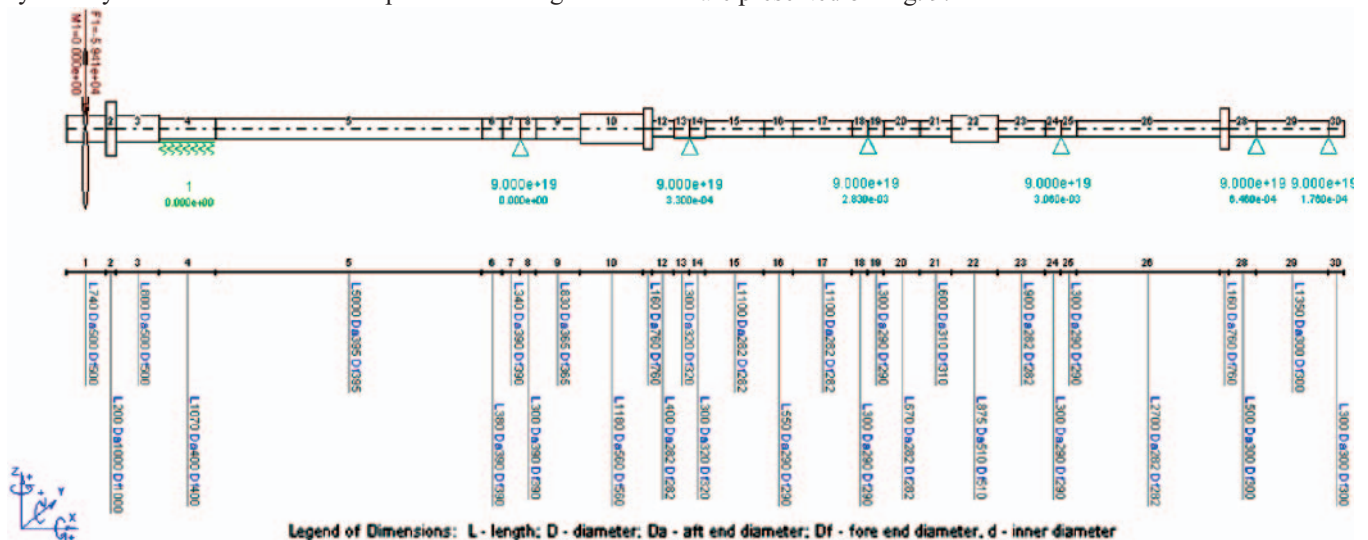


Fig. 5. Shaft line model of two shaft's universal supply ship

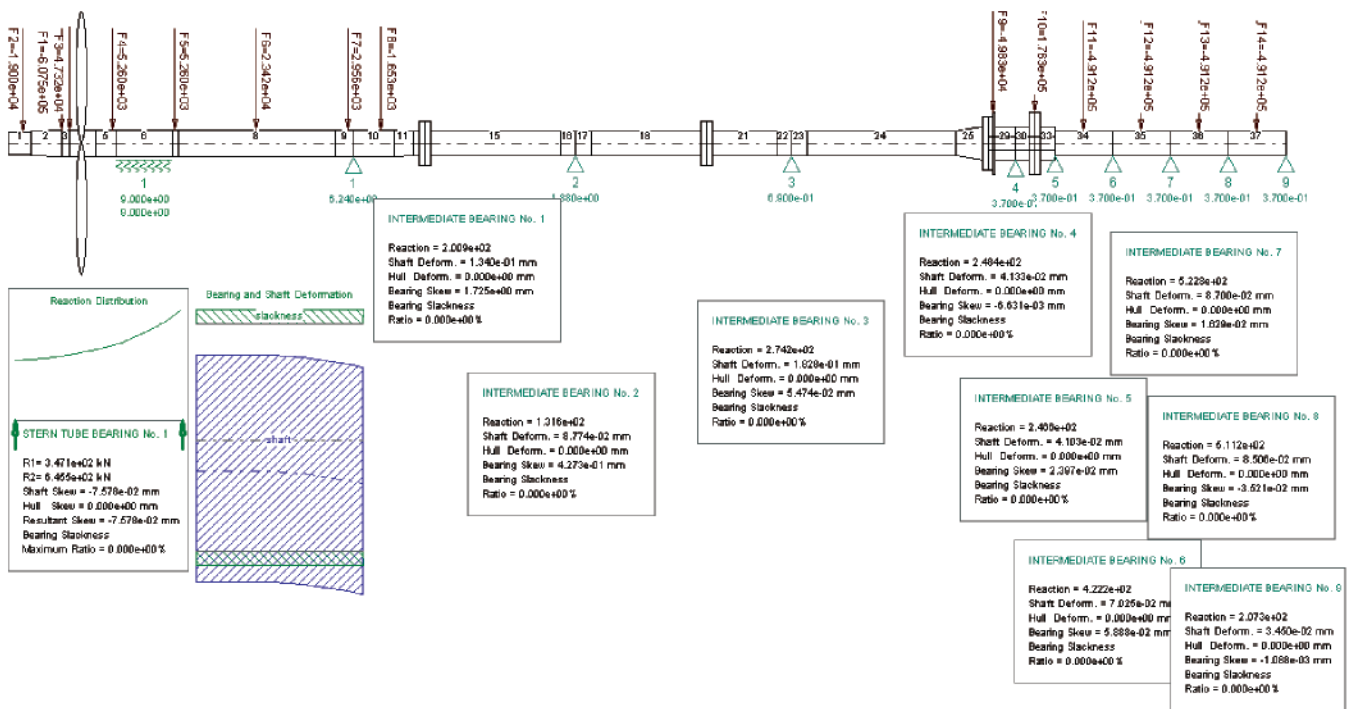


Fig. 9. Container's shaft line reactions determined by the software for standard alignment

The standard shaft line alignment might be improved by equalization of the aft stern tube bearing's reaction and by reduction of the aft engine's main bearing. Loading enlargement of the fore stern tube bearing (and aft stern tube bearing's loading equalization) is a consequence of reaction reduction of the aft intermediate bearing (to 100 kN, ~24%). Resultant skew of the propeller shaft in the bearing tube is then decreased of about 8%. Loading reduction of the main bearings (of about 9%) is an effect of reaction increasing (to 300 kN) of fore intermediate bearing. The algorithm find out automatically new (for given intermediate bearings' reactions) shaft line alignment. The modified parameters of the new shaft line alignment are presented on Fig. 10÷12.

coefficients of the bearings reaction under the influence of bearings' longitudinal and vertical movements are also determined.

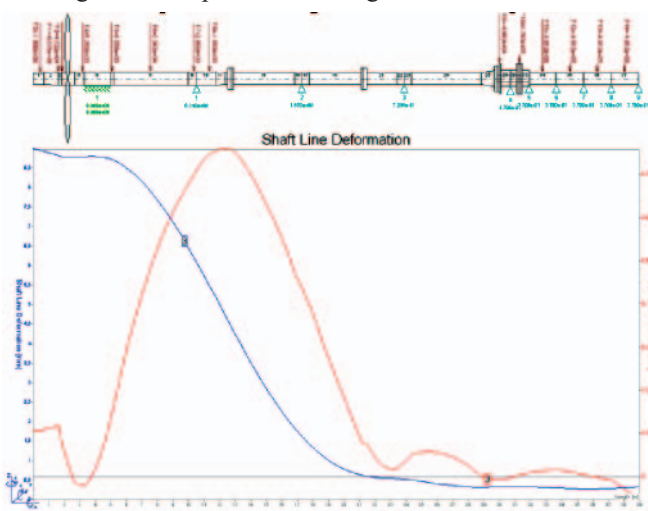


Fig. 10. Modified shaft line deformation

Influence coefficients are also determined by the program. The coefficients are useful for designers because they show the relative changing of the shaft line parameters (shaft line deformation, reactions, bending moments, shear forces, stresses) if chosen bearing is moved vertically or longitudinally. An example of influence coefficients for vertical movement of aft intermediate bearing is presented on Fig. 13 ÷ 15. Influence

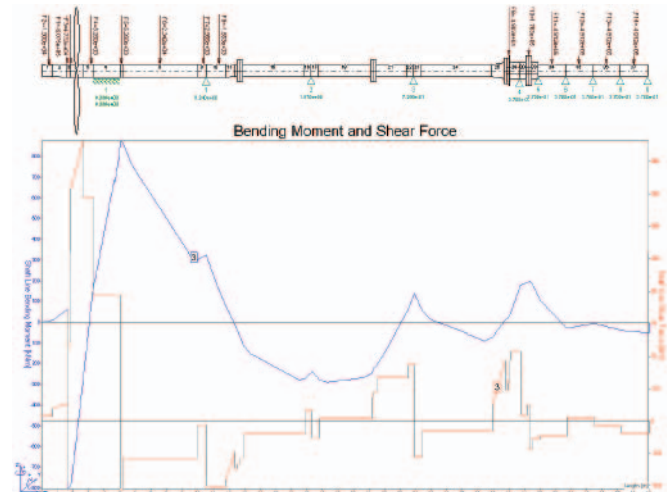


Fig. 11. Modified shaft line bending moments and shear forces

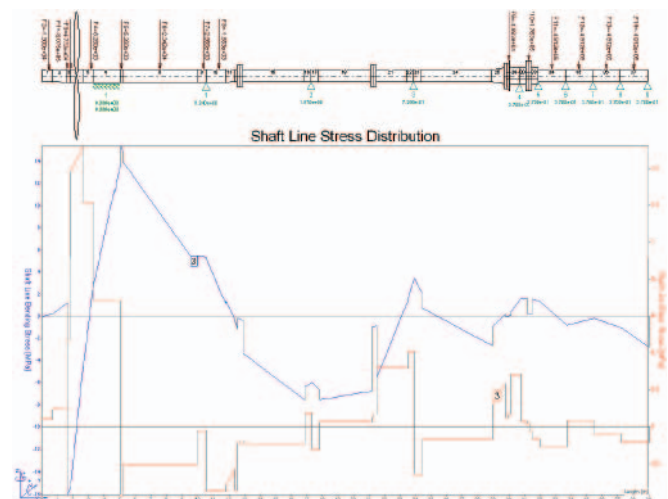


Fig. 12. Modified shaft line stresses distribution

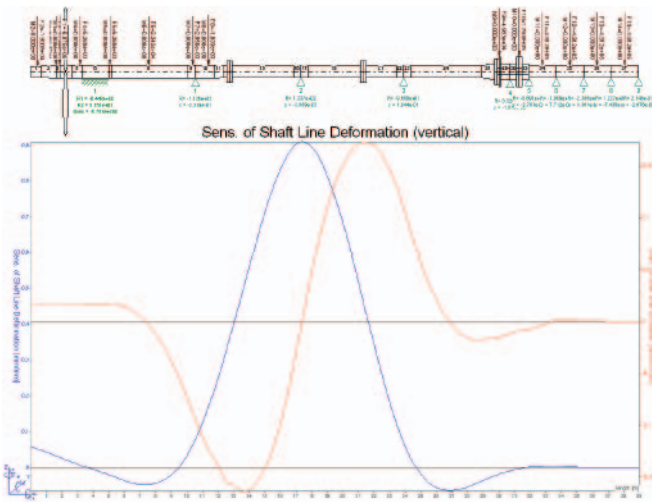


Fig. 13. Influence coefficients of shaft line deformation under the influence of vertical movement of aft intermediate bearing

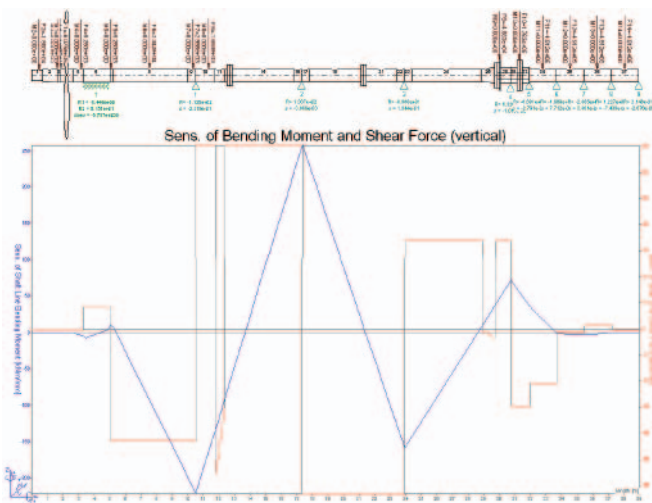


Fig. 14. Influence coefficients of bending moments and shear forces under the influence of vertical movement of aft intermediate bearing

The analysed shaft line is relatively stiff – it is short with big diameter and the propulsion system is equipped in many lateral bearings. For that reason, displacement of one bearing have an influence on only one shaft segment limited by adjacent

bearings. Longitudinal movement of the intermediate bearings has hardly perceptible influence on the analysed shaft line alignment parameters.

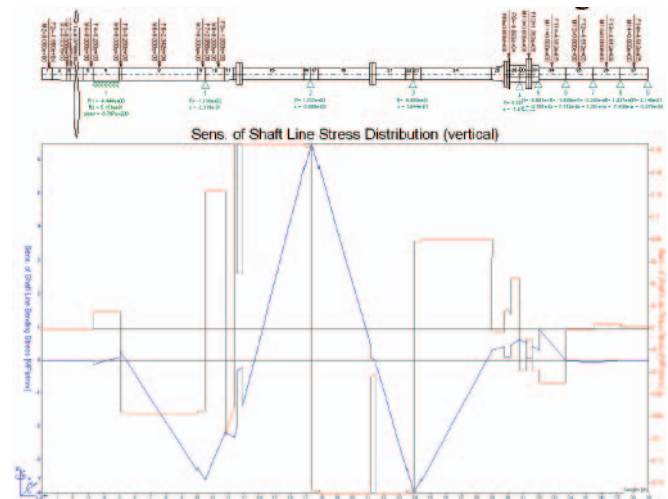


Fig. 15. Influence coefficients of shaft line stresses under the influence of vertical movement of aft intermediate bearing

IDENTIFICATION OF THE MIDDLE-SPEED PROPULSION SYSTEM

Identification has been performed for aged ship destined for heavy repair process. It is universal supply ship with double-shaft, middle-speed propulsion system (with gear box). The shaft line is more flexible than previous one: $\phi 282$ is a diameter of intermediate shaft and $\phi 400$ is a diameter of propeller shaft. In the ship's documentation, only design bearings' reactions are available. Real reactions are known after measurements. Design and real shaft line alignment have been identified by the discussed software. Identified shaft line reactions are presented on Fig. 16 and 17. Significant difference between design and real reactions are observed. The most important differences (which needed improvements) are as follows: unloaded aft edge and overloaded fore part of stern tube bearing and insufficiently loading of stern intermediate bearing. Shaft line alignment should be improved.

The author's software determine given shaft line alignment as a first step, and searching the field of optimal solutions in

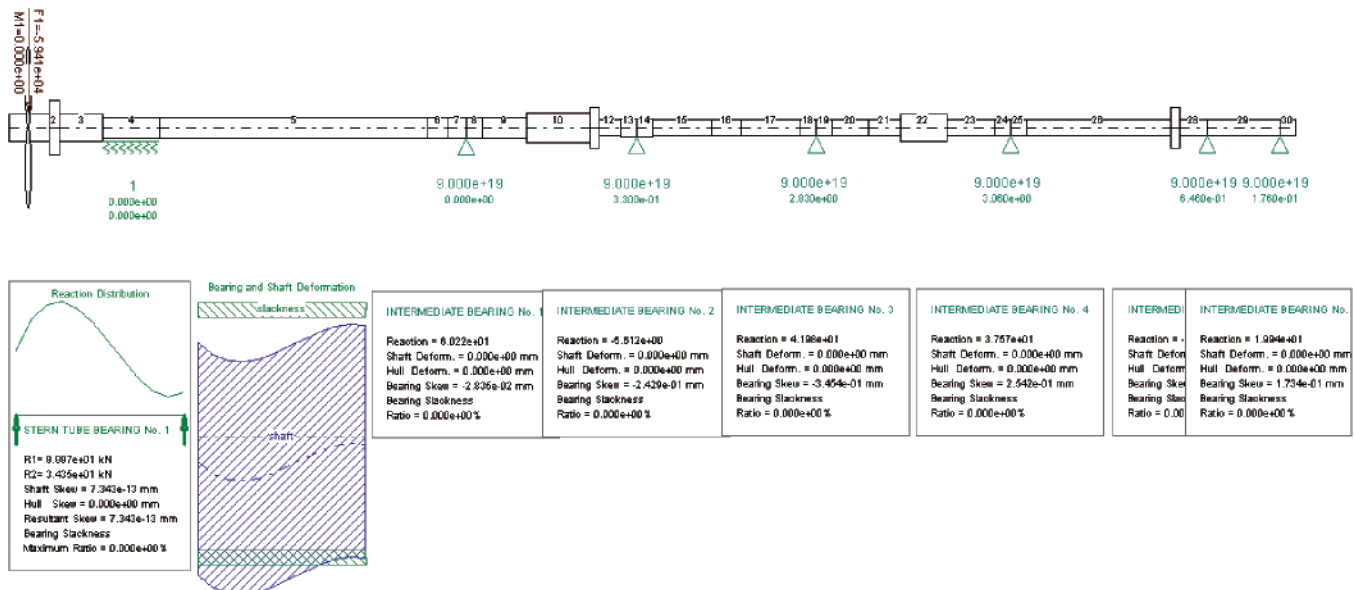


Fig. 16. Design shaft line alignment and reactions

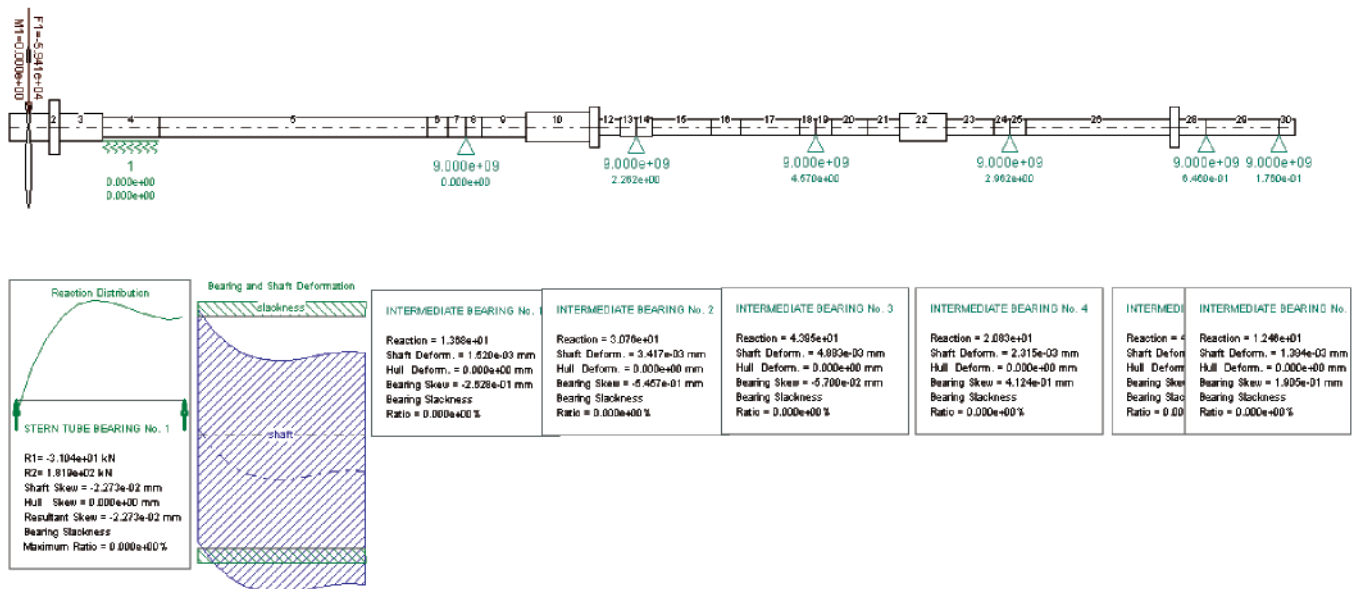


Fig. 17. Real shaft line alignment and reactions

the second step. In the third step the influence coefficients are determined by the program. The coefficients are useful for fast and precisely determination of proper bearings position in vertical and longitudinal plane. Determined influence coefficients are presented in Tab. 1. Denotations: ST – stern tube bearing, I1 – first (starting from the stern) intermediate bearing, etc.

Tab. 1. Vertical influence coefficients

Bearing:	I2 [kN/mm]	I3 [kN/mm]	I4 [kN/mm]
ST	-5.85 15.41	0.69 -1.82	-0.16 0.43
I1	-32.89	9.74	-2.29
I2	40.26	-23.48	8.06
I3	-23.48	26.28	-17.12
I4	8.06	-17.12	24.50

Target of the shaft line alignment is determining proper and uniform bearings reaction, acceptable stress level and good interaction between shaft line and crankshaft or gearbox [15]. Proper shaft line alignment has been determined (based on coefficients presented in tab. 1) by following lift of the intermediate bearings: I1 – 4.8 mm, I2 – 6.1 mm, I3 – 4.5 mm, I4 – 2.0 mm. Improved bearings reaction distribution is presented on Fig. 18. Comparison of the shaft line alignment's parameters, before and after improvements, is shown on Fig. 19 ÷ 21.

Shaft line alignment after correction is characterised by smoother axis deformation and uniform bearings reaction. Intermediate bearing no. 1 is heaviest loaded by the others because of desirable loading of stern tube bearing. After correction loading of the fore edge of stern tube bearing is reduced two times, while loading of aft edge become acceptable. Before correction the aft edge of stern tube bearing was unloaded and was threaten by hammering phenomenon.

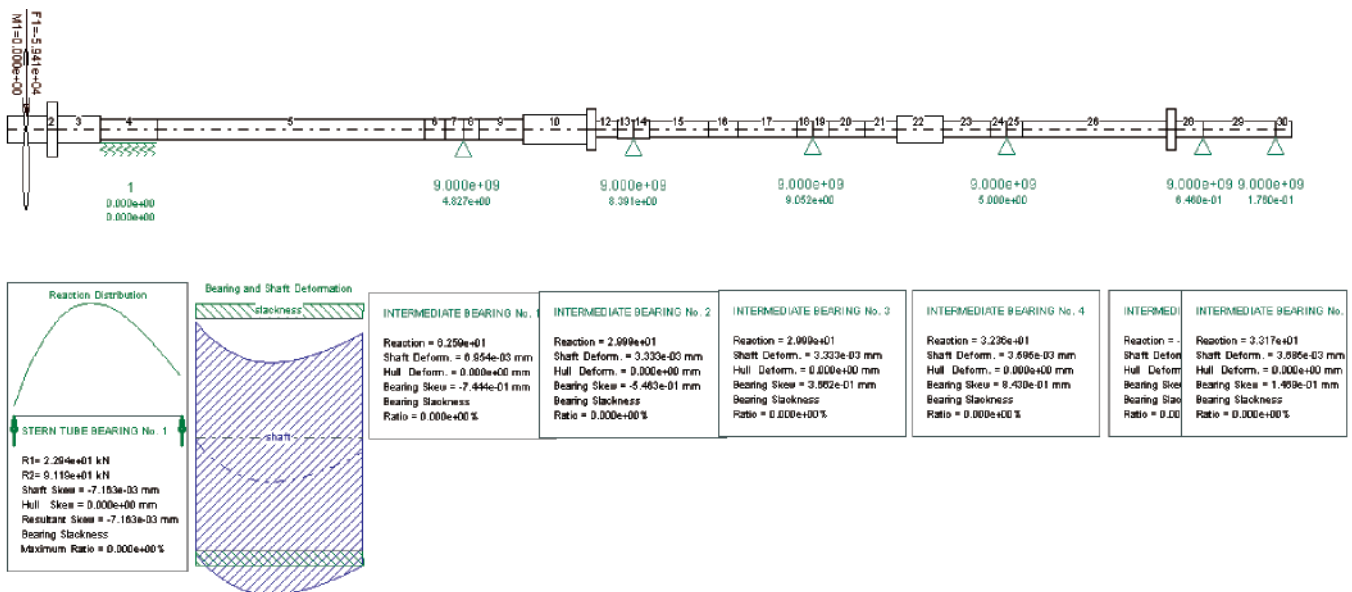


Fig. 18. Shaft line alignment and reactions after correction

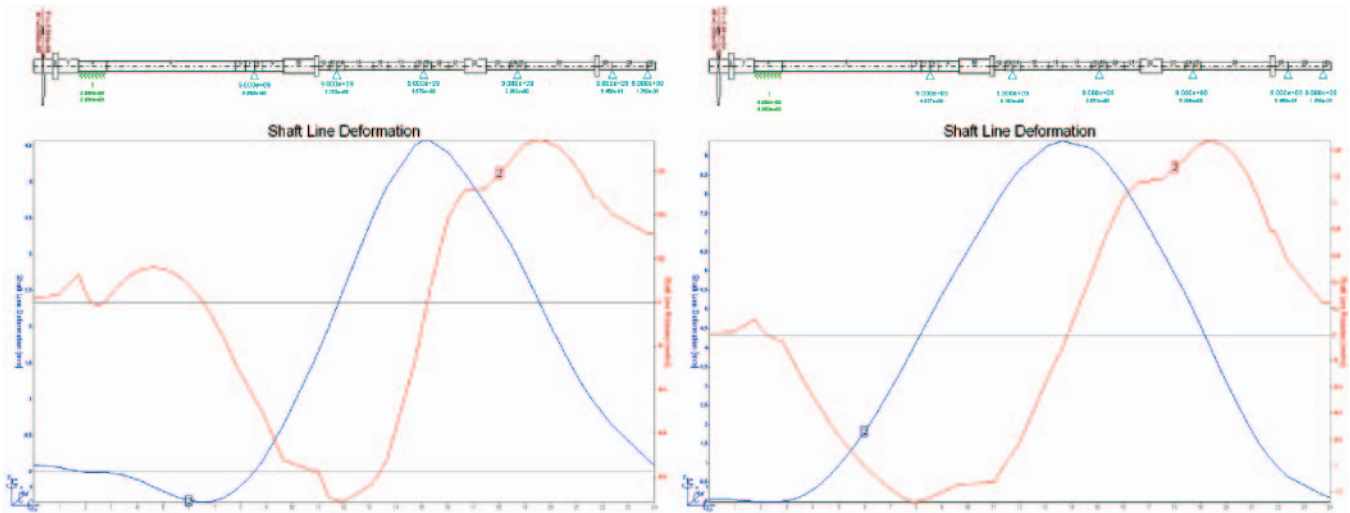


Fig. 19. Shaft line deformations before and after correction

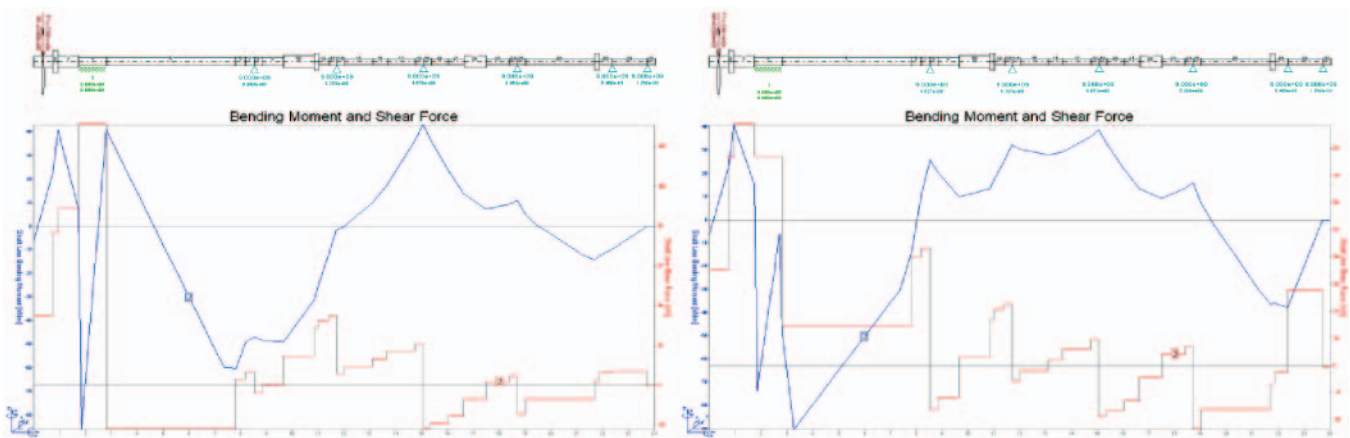


Fig. 20. Shaft line bending moments and shear forces before and after correction

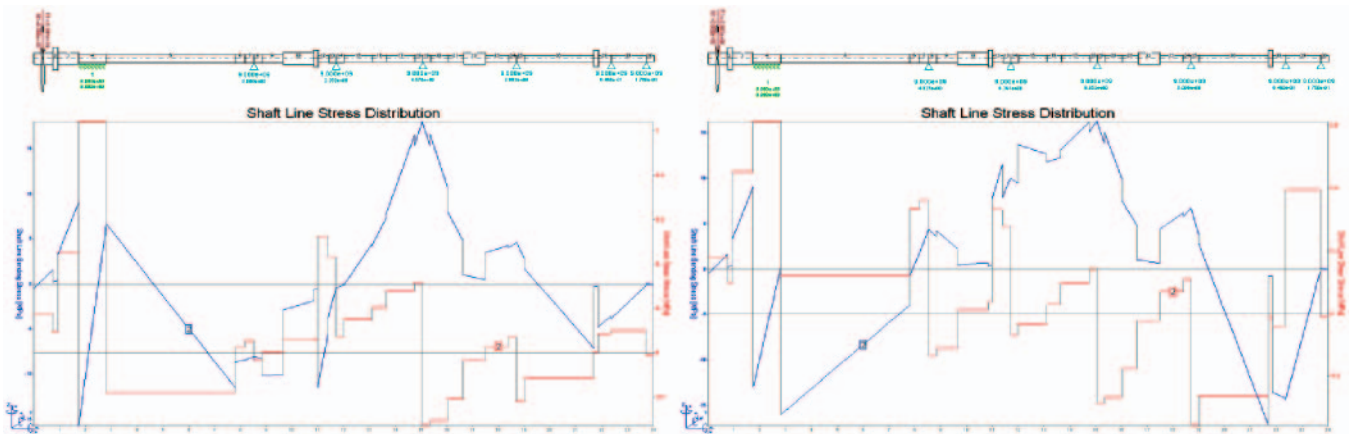


Fig. 21. Shaft line stresses distribution before and after correction

SUMMARY

Changes of shaft line alignment of aged ship with insufficient data availability have been difficult for proper realisation with standard methodology. Shipyards are looking out for well experienced workers because shaft line alignment has been performed by tests and errors method. Usually, it is very costly and the cost of the process is depended on engineer's experience. Sometimes, repair shipyards make an assumption that bearing reaction deviation $\pm 50\%$ is acceptable!

In the paper author proposed a quite simple and cheap method for identification of shaft line alignment parameters

in case of the lack of producers' data. It is proposed combined experimental-analytical method for identification and correcting some existing parameters of power transmission system's foundation. Specialised software has been developed and verified for shaft line alignment

BIBLIOGRAPHY

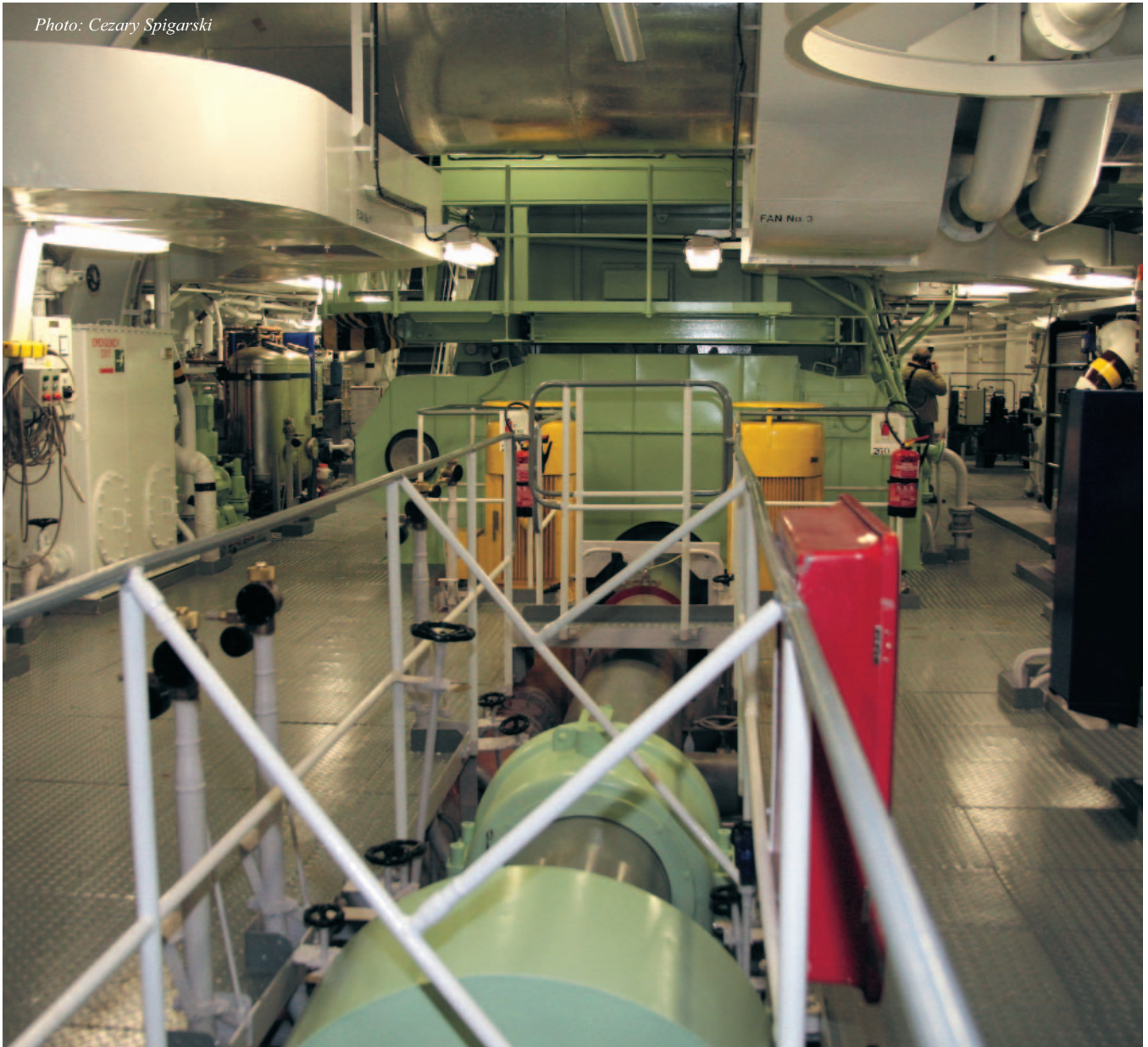
1. Charchalis A., Grządziela A.: *Diagnosing the shafting of alignment by means vibration measurement*. ICSV Congress (electronic ver.), Garmisch-Partenkirchen, 2000
2. Cowper B., DaCosta A., Bobyn S.: *Shaft alignment using strain gauges*. Marine Technology, vol. 36, no 2, pp. 77 ÷ 91, 1999.

3. Keshava Rao M. N., Dharaneopathy M. V., Gomathinayagam S., Ramaraju K., Charkravorty P. K.: *Computer-aided alignment of ship propulsion shafts by strain-gage methods*. Marine Technology, vol. 28, March 1991
4. Kielbasiński A., Schwetlick H.: *Numerical linear algebra* (in Polish). Scientific Technical Publishing House, Warszawa 1992
5. Kruszewski J., Gawroński W., Ostachowicz W., Tarnowski J., Wittbrodt E.: *Finite element method in structural dynamics* (in Polish). Arkady Publishing House, Warszawa 1984
6. Murawski L.: *Analysis of measurement methods and influence of propulsion plant working parameters on ship shafting alignment - part I*. Polish Maritime Research No 2(12), Vol. 4, June 1997
7. Murawski L.: *Analysis of measurement methods and influence of propulsion plant working parameters on ship shafting alignment - part II*. Polish Maritime Research No 3(13), Vol. 4, September 1997
8. Murawski L.: *Static and Dynamic Analyses of Marine Propulsion Systems*. Oficyna Wydawnicza Politechniki Warszawskiej, pp. 148, Warszawa 2003
9. Murawski L.: *Shaft line alignment analysis taking ship construction flexibility and deformations into consideration*. Marine Structures No 1, Vol. 18, January 2005
10. Murawski L.: *Statical and dynamical operational characteristics of ship propulsion systems and their influence on ship hull and superstructure vibrations* (in Polish). Scientific Bulletins of Institute of Fluid Flow Machinery, Gdansk Branch of Polish Academy of Sciences, No. 542/1501/2006, Gdańsk 2006
11. Murawski L.: *Ship structure dynamic analysis – effects of made assumptions on computation results*. Polish Maritime Research No 2(48), Vol. 13, April 2006.
12. Murawski L., Szmyt M.: *Stiffness characteristics and thermal deformations of the frame of high power marine engine*. Polish Maritime Research No 1(51), Vol. 14, January 2007
13. Pressicaud J. P.: *Correlation between theory and reality in alignment of line shafting*. Bureau Veritas, III, Paris 1986
14. Zienkiewicz O. C., Taylor I. R. L.: *The Finite Element Method. Fourth edition, V. 1/2*. McGraw-Hill, London 1992.
15. *Shafting Alignment for Direct Coupled Low-Speed Diesel Propulsion Plants*. MAN B&W Diesel A/S, Copenhagen 1995.

CONTACT WITH THE AUTHOR

Lech Murawski, Ph. D.
The Szewalski Institute
of Fluid-Flow Machinery
Polish Academy of Sciences
Fiszera 14
80-952 Gdańsk, POLAND
e-mail: lemur@imp.gda.pl

Photo: Cezary Spigarski



Ring thruster – a preliminary optimisation study

Leszek Matuszewski, Ph.D.
Gdansk University of Technology

ABSTRACT



The ring thruster is a new type of propeller, for which there is no experimental data to verify analytical design calculations. A significant feature of the ring thruster is the absence of a shaft. Propeller blades are mounted to the ring rotating inside the housing, which has the shape of a nozzle. For this reason the ring thruster is closest, with respect to both the construction and principle of operation, to the Kort nozzle propeller. The absence of a shaft and no gap between the blades and the nozzle make it impossible to fully rely on results obtained from Kort nozzle propeller examination. What is more, the already existing computer codes developed for designing Kort nozzle propellers cannot be directly used for designing ring thrusters either. That is why for this purpose a new code determining hydrodynamic characteristics based on the theory of the vortex lifting surface will be used. When using the above method, some differences between calculated and experimentally recorded results are expected to be observed. To a significant extent, the level of the torque taken by the thruster will be affected by drag of the rotating ring to which the blades are fixed. Examining a propeller equipped with a rotating ring has revealed that the expected torque increment may reach as much as a few per cent, at the comparable level of axial force (thrust). At the present stage of ring propeller investigations there is no data available on how to shape the ring propeller blades. Possible comparison calculations, done using the existing computer code, will allow, the most, the shape of the blades to be determined for preliminary tests in the cavitation tunnel and on a self-propelled model. And only the results obtained in these tests will provide opportunities for verification of preliminary design calculations. It should be stressed, however, that developing design procedures for this type of propellers will require additional optimisation calculations, with further experimental verification. And this should be the subject of separate investigations.

Key words: hydrodynamics, marine engine, thruster

GOAL AND SCOPE OF EXAMINATION

The goal of the reported activities was to perform preliminary hydrodynamic tests of the prototype ring thruster delivered by the employer. The main dimensions of the examined thruster were the following :

- | | |
|--------------------------------|----------------------------|
| ★ outer ring diameter | $D_{zd} = 0.208 \text{ m}$ |
| ★ inner diameter of ring motor | $D_w = 0.130 \text{ m}$ |
| ★ width of housing (nozzle) | $B = 0.1365 \text{ m}$ |
| ★ number of blades | $z = 6$ |

The scope of the examination includes measurement of the axial force induced by the ring thruster at different propeller revolutions and different velocities of the water approaching the thruster.

A tensometric dynamometer JK-21-2-500N-2003 IMP PAN allows total thrust force of the Tpx unit to be measured. This force comprises the thrust generated by the propeller and the nozzle, and the drag generated by the elements connecting the thruster with the dynamometer (connectors and a cable).

The torque is determined from the power calculated based on measurements of parameters of the electric current supplying the rotor, and therefore it can be burdened with some error.

RESEARCH RIG

The research rig, which is the cavitation tunnel K11-MH IMP PAN, was prepared for examining the new generation ring thruster (a general view of the rig is shown in Photo 1).

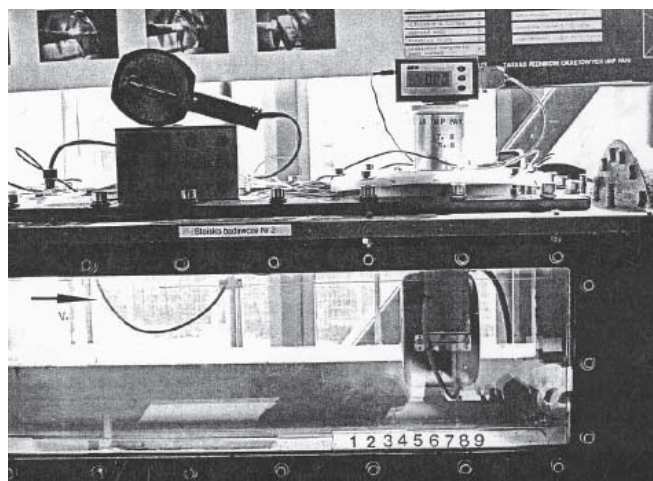


Photo 1. Research rig for ring thruster examination

A prototype strain-gauge dynamometer JK-21-500N-2003 IMP PAN, mounted with relevant accessories and fixing system, is shown in Photo 3.

The system for measuring, storing and processing of changing forces T_{px} and R_{ox} makes use of a microprocessor measuring amplifier AWO 100, linked with the computer via RS 232C interface.

The average velocity in the measuring section of the cavitation tunnel was determined from the pressure difference measured in the tunnel confusor using a liquid-column gauge.

The propulsion system of the ring thruster consists of the nozzle-shaped housing and the internal ring with six blades fixed to it, (Photo 2).

Revolutions of the propulsion motor were controlled using a programmable inverter.

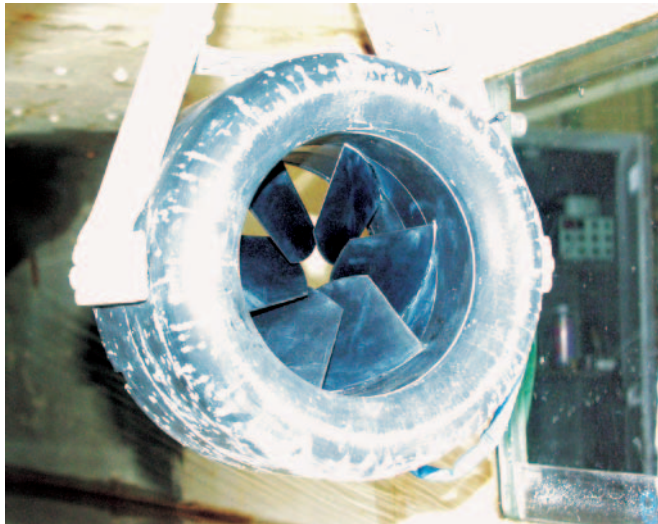


Photo 2. Ring thruster installed in the cavitation tunnel

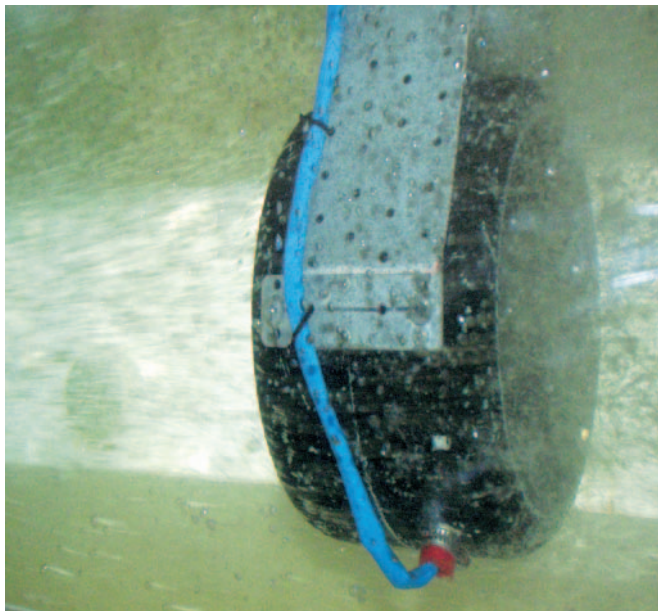


Photo 3. Ring thruster in operation

EXAMINATION PROCEDURES

The substitute ring thruster ($D_w = 0.13$ m) delivered by the employer was mounted in a strain-gauge dynamometer JK-21-2-500N-2003 IMP PAN, especially manufactured for this purpose, and then installed on the properly instrumented research rig No. 2 (Cavitation Tunnel, type K11-MH) in the Szwalski Institute of Fluid-Flow Machinery PAS, Gdansk.

- Ring thruster examination included the following tests:
- ✦ drag generated by a dummy ring thruster at different water velocities
 - ✦ mechanical drag generated by the ring thruster in the air for different propeller revolutions
 - ✦ ring thruster examination for different water velocities and different rotational speeds of the propeller.

During the examination the following quantities were recorded:

- ◆ Propeller revolutions n [rev/min]
- ◆ Speed of water in tunnel measuring section V [m/s]
- ◆ Total thrust and drag generated by ring thruster T_{px} [N]
- ◆ Drag generated by dummy ring thruster, console, and cable R_o [N]
- ◆ Total torque taken by thruster Q [Nm]
- ◆ Internal ring thruster drag torque in air Q_o [Nm]
- ◆ Other recorded quantities included electric current intensity and voltage generated by the inverter supply system in the ring thruster motor.

The examination was performed for steady water velocities and changing ring propeller revolutions.

The examination was divided into test series, and the results of measurements were stored in the computer, in files named for instance „1200-01.dat” which means the first test series at revolutions 1200 rev/ min.

Instantaneous torque values were stored in computer's memory and then averaged, while the thrust generated by the thruster were averaged in the microprocessor based measuring instrument, by introducing a filter. The averaged results were then presented on a digital display.



Photo 4. Research rig during ring thruster examination

RESULTS OF EXAMINATION

The tables below collect selected results of measurements, recorded on the research rig in the cavitation tunnel with the ring thruster. These results are grouped in properly numbered series.

Quantities mentioned in the tables :

Water velocity at the entrance to the measuring section is given in mm water column Δh . Real velocity is determined from the relation:

$$\Rightarrow V = 0.1412 \sqrt{\Delta h} \text{ [m/s]}$$

\Rightarrow total thrust (measured) T_{px} generated by the entire set is given in [kG]

\Rightarrow torque is given in [kGm]

\Rightarrow revolutions are given in [rev/min].

Tab. 1. Results of ring thruster examination

File	n [rev/min]	Tpx [kG]	Δh [mm]	Q [kGm]	No. of series
1200-01.dat.	1200	11.4	15		1
1000-01.dat.	1000	7.75	10		1
1200-01.dat.	1200	11.32	11.32		1
800-01.dat.	800	4.96	6		1
700-01.dat.	700	3.76	5		1
1250-01.dat.	1250	12.35	16		1
1100-02.dat.	1100	8.0	35		2
1000-02.dat.	1000	6.32	30		2
800-02.dat.	800	3.35	30		2
700-02.dat.	700	2.26	30		2
1200-02.dat.	1200	9.2	40		2
1000-02.dat.	1000	5.91	40		2
1200-02.dat.	1200	9.2	40		2
1300-03.dat.	1300	7.8	76		3
1200-03.dat.	1200	6.57	90		3
1000-03.dat.	1000	3.37	86		3
800-03.dat.	800	0.9	82		3
700-03.dat.	700	-0.14	80		3
1300-04.dat.	1300	3.22	200		4
1200-04.dat.	1200	-1.62	196		4
1000-04.dat.	1000	-1.3	190		4
1400-05.dat.	1400	15.2	20		5
1300-05.dat.	1300	13.1	18		5
1200-05.dat.	1200	11.1	16		5
1000-05.dat.	1000	7.76	10		5
800-05.dat.	800	4.88	6		5
800-06.dat.	600	-0.8	85	0.24	6
1000-06.dat.	1000	3.26	87	0.5	6
1200-06.dat.	1200	6.33	93	0.6	6
1300-06.dat.	1300	8.1	96	0.75	6
1400-06.dat.	1400	10.12	100	1.0	6
1400-07.dat.	1400	5.16	205	0.9	7
1300-07.dat.	1300	3.19	204	0.65	7
1200-07.dat.	1200	1.47	202	0.5	7
1000-07.dat.	1000	1.44	198	0.3	7
800-07.dat.	800	-3.71	195		7
1500-07.dat.	1500	6.91	215		7
1450-08.dat.	1450	16.74	24		8
1400-08.dat.	1400	15.32	20	1.0	8
1300-08.dat.	1300	13.13	18	0.7	8
1200-08.dat.	1200	11.2	16	0.6	8
1000-08.dat.	1000	7.74	10	0.4	8
800-08.dat.	800	4.96	6		8
1477-08.dat.	1477	16.9	24	0.9	8

Tab. 2. Torque generated by ring thruster working in air Q_0

Series	n [rev/min]	Q_0 [kGm]
MOM 1400	1400	0.15
MOM 1200	1200	0.125
MOM 800	800	0.085

The results of measurements, obtained after doing relevant recalculations to dimensionless coefficients of thrust, K_T , and torque, K_Q , are given in Figs 1 and 2.

Fig. 1 shows the results of measurements of thrust (axial force) induced by the entire ring thruster, in the arrangement: dimensionless thrust coefficient K_T vs. advance coefficient J .

Fig. 2 presents the results of measurements of the torque taken by the ring thruster, in the similar arrangement: dimensionless torque coefficient K_Q vs. advance coefficient J . The dimensionless coefficients are defined as:

$$K_T = T / (\rho n^2 D^4)$$

$$K_Q = Q / (\rho n^2 D^5)$$

$$J = V / (nD)$$

Figs 1 and 2 show two curves, of which the broken curve refers to the thruster working in water. The continuous curve was obtained by deducting torque Q_0 , representing internal drag, from the total torque Q .

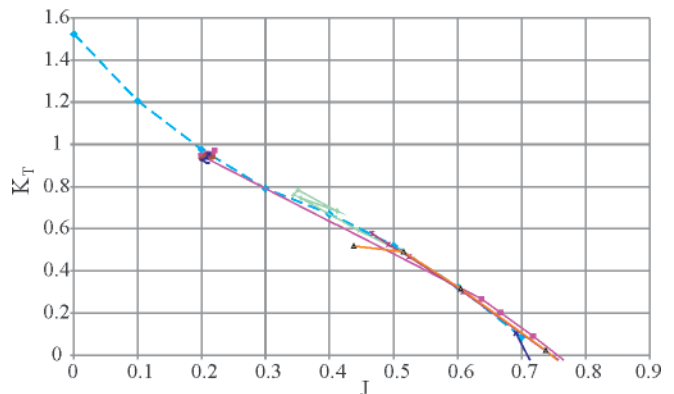


Fig. 1. Results of calculations of thrust coefficient K_T induced by the entire thruster

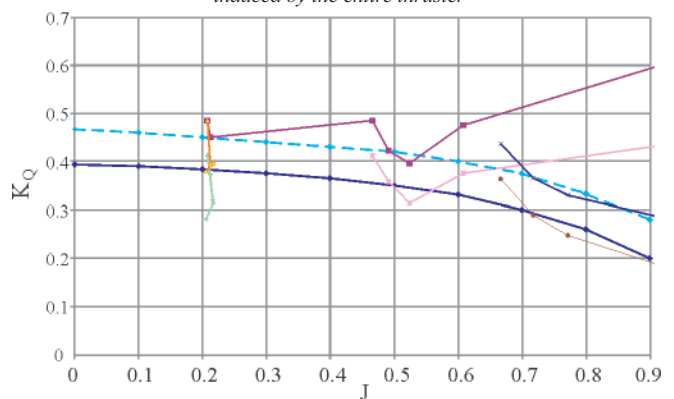


Fig. 2. Results of calculations of torque coefficient K_Q

The scope of measurements included thruster operation above $J = 0.2$ (measuring points are shown in the figures). For J lower than 0.2, including $J = 0$, the curves were extrapolated using the analogy to other Kort nozzle examinations. Using the same analogy the thrust induced by the entire thruster was hypothetically divided into part induced by propeller blades and that induced on the nozzle (ring). The proposed division is shown in Fig. 3.

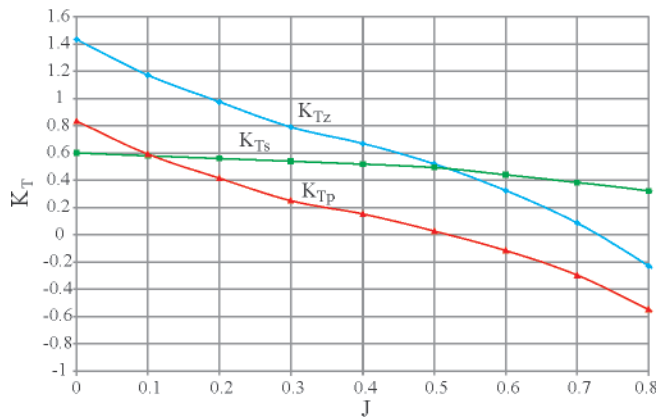


Fig. 3. Approximate division of total thrust K_{Tz} into part K_T induced by thruster blades and part K_{Tp} induced by the surrounding ring (nozzle)

The presented results should be treated as concerning preliminary investigations of this type of propellers in Poland. Very interesting results were obtained for total thrust and torque induced by the entire thruster. Diagrams in Figs 1 and 2 deliver a lot of new information on the performance of these types of propellers, but at the same time new problems can be addressed which need solving.

What needs clarifying first is why the measured torque, induced on the blades and the ring, differs so dramatically (more than twice) from the calculated value of the torque induced by the blades alone. It would mean that the torque induced on the ring is very high and considerably affects thruster's performance. If so, its reduction is a priority for improving thruster's performance.

It would also mean that the substitute seal and bearings of the examined thruster do not fulfil requirements concerning the minimisation of drag forces generated by the ring moving in the gap.

In this type of investigations, good preparation and execution of measurement of a torque attributed to viscous losses on the ring, irrelevant of the torque induced by the blades, is the high priority.

The analysis of thrust examination results (table 1) reveals that the ring surrounding the propeller has favourably affected the total thrust. Fig. 3 shows a diagram with hypothetical division of the total thrust K_{Tz} into part K_{Ts} induced by the blades and part K_{Tp} induced by the ring.

The curve K_{Ts} was created using as a basis the point calculated for the blades alone and assuming the analogy to the Kort nozzle propeller examination. The shape of the curves is realistic, but it should be confirmed (or verified) by relevant examination of a propeller driven in a way classical for the Kort nozzle propeller system.

CONCLUSIONS

- To sum up, from the point of view of hydromechanics, independently of definite design solutions (including the motor, bearings, lubrication, seals) worked out for the

presented propulsion system, more comprehensive model investigations should be carried out to determine relevant empirical corrections which would allow these propellers to be designed in a way similar to that followed when designing Kort nozzle propellers.

- High efficiency and dynamics of electric drive systems used on watercraft resulted in their increased proportion in total number of drive applications. Thanks to the development of mechatronics, electrotechnics and hydrodynamics, the time has come when earlier solutions in this area can be put in practice. Among water propulsion systems, especially attractive properties are represented by ring-type propellers, but only equipped with electromagnetic bearings. A characteristic feature of the motor, being an extension of a classical synchronous motor with permanent magnets, is that the ring with propeller blades is a part of the rotor. Dimensions of the nozzle in which the winding is mounted do not exceed dimensions resulting from the optimum geometry of the Kort nozzle propeller for the assumed power. As recently as a few years ago the development in the field of magnetic materials, ferrofluid liquids, non-linear control techniques and hydrodynamics reached a level providing opportunities for effective introduction of ring-type propulsion systems on a large scale. A drive which is expected to be especially promising in the nearest future is the ring thruster, used as a manoeuvring drive, and the main drive on smaller watercraft. The experience gained in designing ring thrusters with magnetic bearings has provides opportunities for manufacturing an efficiently working prototype and offering it on the market of water propulsion systems.
- Ring propulsion systems with classical bearings are slowly becoming more and more popular, but still their efficiency is lower than 20% due to relatively high drag. A quantitative break-through in the field of efficiency improvement can be only secured by the use of magnetic bearings.
- An additional advantage of the ring thruster is its ability to switch to turbine operation, in which it can be used as electric power generator. In numerous situations this property makes it possible to recover energy.

BIBLIOGRAPHY

1. Koronowicz T., Szantyr J., Bugalski T.: *Theoretical model for determination of the pressure field resulting from hull flow and operation of the marine propeller*. Polish Maritime Research, no 3 (13), Vol. 4, 1997

CONTACT WITH THE AUTHOR

Leszek Matuszewski, Ph. D.
Faculty of Ocean Engineering
and Ship Technology
Gdansk University of Technology
Narutowicza 11/12
80-952 Gdansk, POLAND
e-mail: leszekma@pg.gda.pl

On the possible increasing of efficiency of ship power plant with the system combined of marine diesel engine, gas turbine and steam turbine, at the main engine - steam turbine mode of cooperation

Marek Dzida, Assoc. Prof.
Gdansk University of Technology

ABSTRACT



This paper presents a concept of a ship combined high-power system consisted of main piston engine and associated with it: gas power turbine and steam turbine subsystems, which make use of energy contained in exhaust gas from main piston engine. The combined system consisted of a piston combustion engine and an associated with it steam turbine subsystem, was considered. An algorithm and results of calculations of the particular subsystems, i.e. of piston combustion engine and steam turbine, are presented. Assumptions and limitations taken for calculations, as well as comparison of values of some parameters of the system and results of experimental investigations available from the literature sources, are also given. The system's energy optimization was performed from the thermodynamic point of view only. Any technical – economical analyses were not carried out. Numerical calculations were performed for a Wärtsilä slow-speed diesel engine of 52 MW output power.

Keywords: combined systems, gas turbine, piston combustion engine, ship power plants, steam turbine

INTRODUCTION

For many years in domestic economy a trend to increase efficiency of both land and ship power systems has been developed. It is connected with economic problems (increasing fuel prices) and ecological ones (the lower fuel consumption the lower emission of noxious substances to atmosphere). New solutions are searched for to increase efficiency of power system by joining high-pressure combustion engines with other thermal engines, such as gas and steam turbines, into combined systems.

In recent years combined power systems such as gas - steam turbine systems have been applied to ship power plants. Such systems in land solutions are capable of achieving the efficiency of more than 60 %. In a ship solution such system was used on the passenger liner Millenium. However it has been so far an isolated example of the power system of the highest efficiency. The system requires to be supplied with a more expensive fuel oil, i.e. diesel oil (Marine Diesel Oil). Majority of merchant ships is driven by slow-speed diesel engines which combust a relatively inexpensive heavy fuel oil (Heavy Fuel Oil). It seems that such tendency will be still continued for many years in the world merchant fleet.

High-pressure combustion engine (self-ignition one) is still the basic one used as a ship main engine, as on one hand it combusts the most inexpensive fuel oil (heavy oil), and on the

other hand it has the highest efficiency as compared with all other heat engines. In exhaust gas from diesel engine is contained a huge amount of energy which can be utilized in another device (engine), that results in increasing the system's efficiency and lowering emission of noxious substances to the atmosphere.

One of such solutions represents a combined cycle of piston combustion engine and gas and steam turbines which utilize waste heat contained in exhaust gas from diesel engine. The piston combustion engine is the leading device in such system. It seems that now when fast containerships of 8 ÷ 12 thousand TU capacity enter to service their propulsion systems require engines of a very large output power, of over 50 ÷ 80 MW. On the other hand marine fuel oil is more and more expensive, and restrictive ecological limits for NO_x and CO₂ emission to the atmosphere shall force to apply new power system's solutions capable of increasing propulsion efficiency and lowering noxious gas emission to the atmosphere.

For ship main propulsion large slow-speed marine diesel engines working on heavy fuel oil will be still used as their efficiency reaches today 48 ÷ 51 %. At such large unit output values a huge amount of heat contained in exhaust gas and possible to be further utilized, is emitted from the engines.

This paper presents a concept of a combined ship power plant fitted with a main slow-speed, piston combustion engine, as a leading one, and a steam turbine subsystem which utilizes waste heat from exhaust gas.

A CONCEPT OF COMBINED SHIP POWER SYSTEM

The assumed combined power system for large containership, having main slow-speed diesel engine and gas and steam turbines which utilize waste heat from the engine's exhaust gas, is shown in Fig. 1.

Exhaust gas discharged from particular cylinders of the main engine is gathered in the exhaust gas collector to supply the constant-pressure turbocharger. For the reason of high efficiency of turbochargers [1, 6], the power required for compression of supercharging air is achieved only from a part of exhaust gas flux. The remaining gas flux from the exhaust gas collector can be decompressed in an additional gas turbine, i.e. power turbine. In further considerations it was assumed that the power gas turbine drives additionally – through reduction gear – ship's screw propeller.

Exhaust gas from the turbocharger and power gas turbine flows to the waste heat boiler installed before the silencer in the main engine's exhaust pipeline. The waste heat boiler produces steam used both for driving the steam turbine which delivers its power to the screw propeller, and for ship's overall purposes.

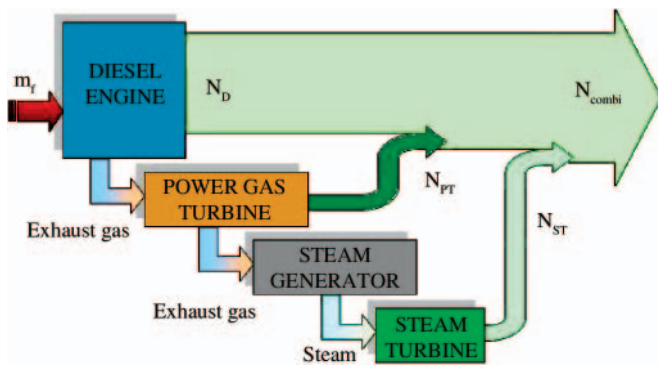


Fig. 1. A concept of combined ship power system

Energy assessment of the combined ship power system

The proposed concept of combined ship power system should be subjected to assessment of energy of its cycle. On the basis of the assumed schematic diagram shown Fig. 1, formulas for determining the power system's efficiency, were elaborated.

The power of the combined power system is determined by summing up power values of the system's particular components (main engine, power gas turbine and steam turbine):

$$N_{\text{combi}} = N_D + N_{PT} + N_{ST} \quad (1)$$

hence the combined system's efficiency is equal to:

$$\eta_{\text{combi}} = \frac{N_{\text{combi}}}{m_{fD} \cdot W_u} = \eta_D \cdot \left(1 + \frac{N_{PT}}{N_D} + \frac{N_{ST}}{N_D} \right) \quad (2)$$

Tab. 1. Parameters of 9RTA 96C engine [7]

N_D [%CMCR]	N_D [kW]	N [rpm]	b_{eD} [g/kWh]	b_{gD} [kg/kWh]	$t_{\text{ex_TC}}$ [°C]	m_{air} [kg/h]	p_D [bar]
100	51480	102.0	174.0	7.48	314.1	379819	2.67
90	46332	98.5	169.8	7.72	301.1	353420	2.39

and the specific fuel oil consumption is expressed by:

$$b_{e\text{combi}} = b_{eD} \cdot \frac{1}{\left(1 + \frac{N_{PT}}{N_D} + \frac{N_{ST}}{N_D} \right)} \text{ [g/kWh]} \quad (3)$$

where:

η_D, b_{eD} - main engine's efficiency and its specific fuel oil consumption, respectively.

From the relations (2) and (3) yields that every additional power in the power system makes the system's efficiency higher and in consequence the specific fuel oil consumption lower. The higher power values achieved from utilization of waste heat contained in exhaust gas from main engine, the lower specific fuel oil consumption, therefore as large as possible output power values should be obtained from both the gas power turbine and steam turbine. Worth mentioning that output of gas power turbine depends to a large extent on turbocharger's efficiency - hence a greater amount of exhaust gas can be decompressed in the gas power turbine (increasing its power) - as well as on efficiency of the gas power turbine itself. In steam turbine its power depends to a large extent on selection of live steam parameters as well as condenser parameters.

Variants of combined ship power systems

Depending on an assumed concept of combined system, systems consisted either of main engine and steam turbine, or main engine, gas turbine and steam turbine, can be considered. Contemporary design solutions of piston engine turbochargers require not very large amount of exhaust gas (due to their high efficiency). In such cases to apply the combined systems consisted of diesel engine, gas power turbine and steam turbine, is possible. This paper describes a combined power plant consisted of a piston combustion engine (serving as main engine) and a steam turbine subsystem.

SELECTION OF MAIN ENGINE AND PRELIMINARY DESIGN ASSUMPTIONS FOR THE COMBINED SHIP POWER SYSTEM

A 9RTA-96C Wärtsilä Sulzer slow-speed, two-stroke engine was assumed for calculations of the combined power system. The printout of its data calculated by means of the winGTD software [7] achieved from the engine's producer, is presented in Tab. 1.

For the so selected main engine the calculations of the combined system were carried out for tropical operation conditions on two main engine load levels (according to Tab. 1), i.e. 100% and 90 % CMCR (Contract Maximum Continuous Rating).

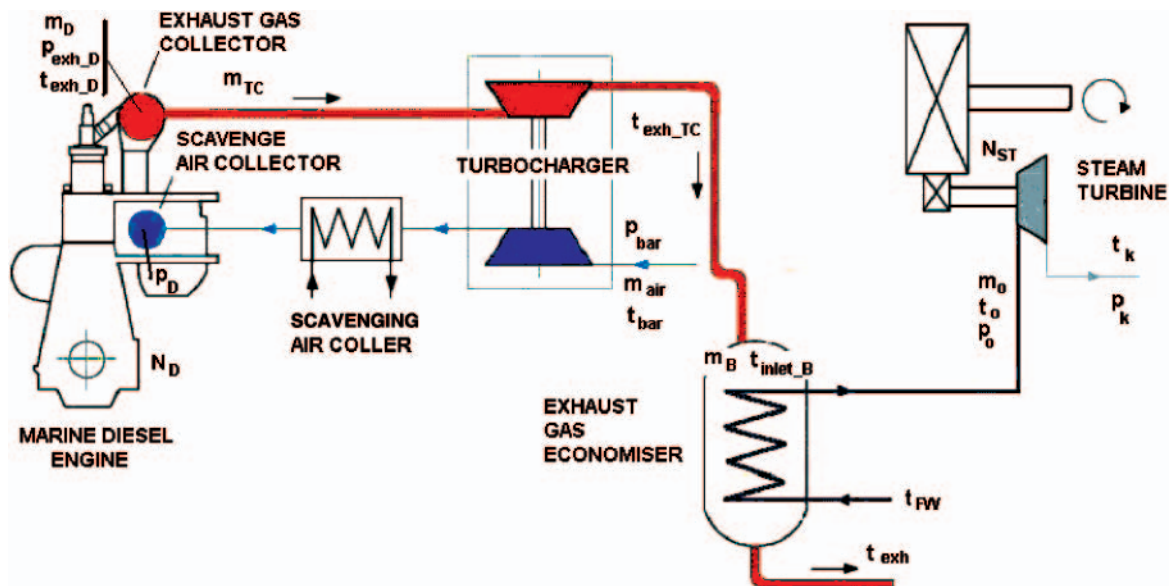


Fig. 2. The ship combined power system consisted of main slow-speed diesel engine and steam turbine (a concept)

THE COMBINED SHIP POWER SYSTEM CONSISTING OF MAIN ENGINE AND STEAM TURBINE SUBSYSTEM

The combined ship power system assumed for calculations in this section, consisted of the slow-speed piston engine and a steam turbine subsystem utilizing waste heat contained in exhaust gas from the engine, is presented in Fig. 2. Exhaust gas from the main engine turbocharger's turbine flows into the waste heat boiler. The boiler produces the steam for driving the steam turbine which transmits its power to propeller shaft, as well the steam necessary for ship overall purposes. For the so assumed combined system, steam turbine subsystem (cycle) parameters were determined in two calculation points.

CALCULATIONS OF STEAM TURBINE CYCLE

A two-pressure waste heat boiler was assumed according to [3],[7]. Fig. 3 presents the schematic diagram of steam turbine subsystem with waste heat boiler. Exhaust gas flows from the turbocharger through the waste heat boiler transferring the heat to the steam cycle. In the high-pressure cycle (p_{II}) is produced the overheated live steam of the parameters (p_o, t_o) and mass flux m_o , which supplies the steam turbine. The low-pressure cycle (p_I) produces the saturated steam whose one part of m_{ss} in amount is extracted for ship overall purposes, and the remaining part is delivered to the steam turbine increasing its power. The applied steam turbine of condensating type additionally drives – through a reduction gear – the ship screw propeller. The assumed deaerating heater of boiling type supplies the water of the temperature t_{FW} to the waste heat boiler. The condensate m_k from the condenser and the condensate m_{ss} from the cooling box of the subsystem for overall ship purposes flows into the deaerating heater. An additional heat necessary to increase water temperature up to its boiling point in the deaerating heater is taken from the steam turbine's extraction point; the heat is contained in the extracted steam flux m_u . The exhaust gas leaves the waste heat boiler at the temperature t_{exh} .

In each case it was assumed that the overheated live steam temperature at outlet from the boiler is lower than that of flowing-in exhaust gas by Δt , i.e.:

$$t_o = t_{inlet_B} - \Delta t \quad (4)$$

The calculations were carried out in function of the pressure p_o (equal to the p_{II} cycle pressure enlarged by hydraulic losses).

$$p_{II} = 1.05 p_o \quad (5)$$

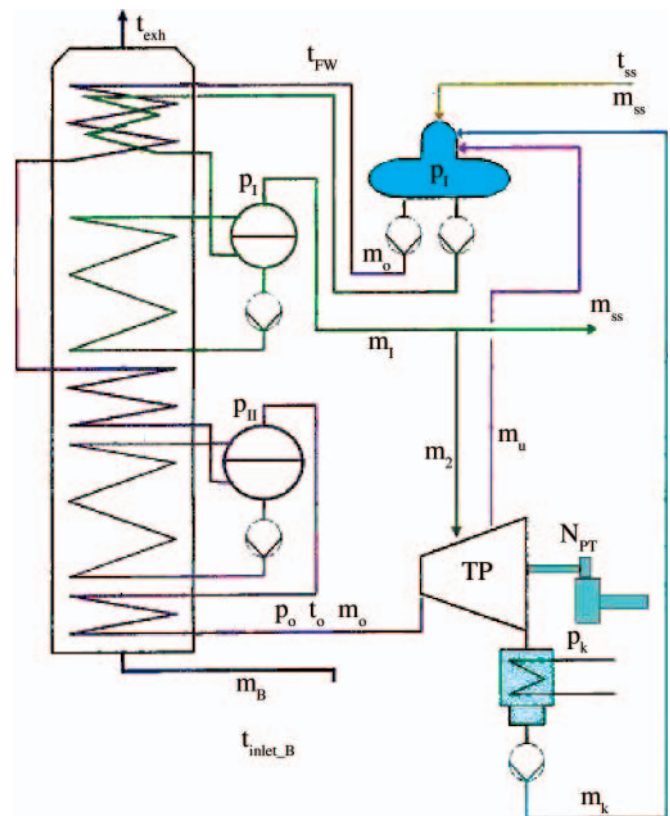


Fig. 3. The schematic diagram of the steam turbine subsystem with waste heat boiler. Note: for explanation of symbols – see Nomenclature

Limitations of parameters and input values assumed for steam turbine cycle calculations

Limitations of values of steam cycle parameters result from strength, technical and durability conditions of particular elements of the subsystem as well as from design and economical factors. The calculations of the steam subsystem of the ship combined power system were performed under the assumptions and limitations given below.

The temperature difference between exhaust gas temperature and that of live steam, Δt , for waste heat boilers of marine application, was assumed $\Delta t = 15^\circ\text{C}$ in compliance with the literature sources [5, 6]. The value of the „pitch point” recommended by the firm MAN B&W [8] for ship boilers is equal to $\delta t = \delta t_1 = \delta t_2 \approx 10^\circ\text{C}$. The limit steam dryness ratio behind the steam turbine was assumed $x_{\text{limit}} = 0.88$. For ship outboard – water – cooled condensers the firm MAN B&W [8] recommends to assume the pressure inside the condenser equal to $p_k = 0.065$ bar. Temperature of water supplying the boiler should not be lower than 120°C , at the sulphur content greater than 2% [8]. The reason is that outer surface of heater pipes from the exhaust gas side has its temperature higher by $8 \div 15^\circ\text{C}$ than that of the supply water, and that materials of a higher resistance against acid corrosion are applied; hence for the calculations it was assumed that the supply water temperature can not be lower than $t_{\text{FW}} > 120^\circ\text{C}$. It was also assumed that the exhaust gas temperature at outlet from the boiler must be higher by 15°C than that of supply water, i.e.: $t_{\text{exh.}} > t_{\text{FW}} + 15^\circ\text{C}$. Every ship combusting the heavy oil for propulsion uses a large amount of heat to prepare the fuel. For the considered containership’s power plant the mass steam flow rate for power plant use in compliance with the MAN B&W recommendations [8] was assumed. The flow rate was made greater by the steam flow rate necessary for ship living purposes, which was estimated to be $m_{\text{ss}} = 2000$ kg/h of saturated steam. According to [8] the steam pressure for living purposes should be kept within the range $p_{\text{ss}} = 7 \div 9$ bar. In the assumed scheme of steam turbine cycle, the pressure of the steam for living purposes is equal to that of the boiler’s low-pressure cycle: $p_l = p_{\text{ss}}$. The temperature in the cooling box was assumed $t_{\text{ss}} = 50^\circ\text{C}$, Fig. 3, in compliance with the recommendation [8].

Steam cycle optimization

On the basis of the presented algorithm of steam turbine cycle calculations a computer software for determining the cycle parameters with the assumed quantities and limitations, was elaborated. Numerical calculations were carried out in variants, i.e. for:

- ★ the assumed pressure range of high-pressure cycle (of live steam): $p_o \in \langle p_{o,\text{min}}, p_{o,\text{max}} \rangle$
- ★ the assumed pressure range of the boiler’s low-pressure cycle: $p_l \in \langle p_{l,\text{min}}, p_{l,\text{max}} \rangle$
- ★ the assumed pressure in the deaerating heater: $p_g \in \langle p_{g,\text{min}}, p_{g,\text{max}} \rangle$.

Optimization of the steam cycle should be so performed as to make use of the heat contained in exhaust gas. Hence it is equivalent to determination of such steam cycle parameters at which the steam turbine reaches its maximum output power. The area of searching for optimum steam cycle parameters, shown in Fig. 4, should be narrowed down to that in which the above assumed limitations imposed on the steam subsystem are satisfied.

The application of the steam subsystem with the waste heat boiler makes output power of the entire power system increasing both at 100% and 90 % CMCR load of the main engine.

In the Tab. 2 the optimum steam cycle parameters for the two load levels of the high-pressure combustion engine, are presented. The maximum output power of the steam turbine obtained from optimization calculations, equal to $N_{\text{STmax}} = 3414$ kW for the diesel engine load of 90%, is marked Δ in Fig. 4. No limitations were taken into account in this case. However in the real system limitations imposed on the steam subsystem should be taken into account. For the assumed limitations, i.e. the narrowed down area of permissible parameters of steam subsystem, the point of the maximum steam cycle output power $N_{\text{STmax}} = 3182$ kW, is marked o. The addition of the steam turbine to the high-pressure combustion engine system resulted in the increase of the power system’s output by $\Delta N_{\text{ST}}/N_D = +7.43\%$ and 6.87% for 100% and 90% load, respectively, at the simultaneous decrease of fuel oil consumption in the combined system from 174g/kWh to 162 g/kWh, and from 169.8 g/kWh to 158.9 g/kWh, respectively, see Tab. 3. The specific fuel oil flux is lowered by 6.91% for 100 % load and by 6.43 % for 90 % load of the marine diesel engine as compared to those of the marine diesel engine alone. In the combined system its efficiency

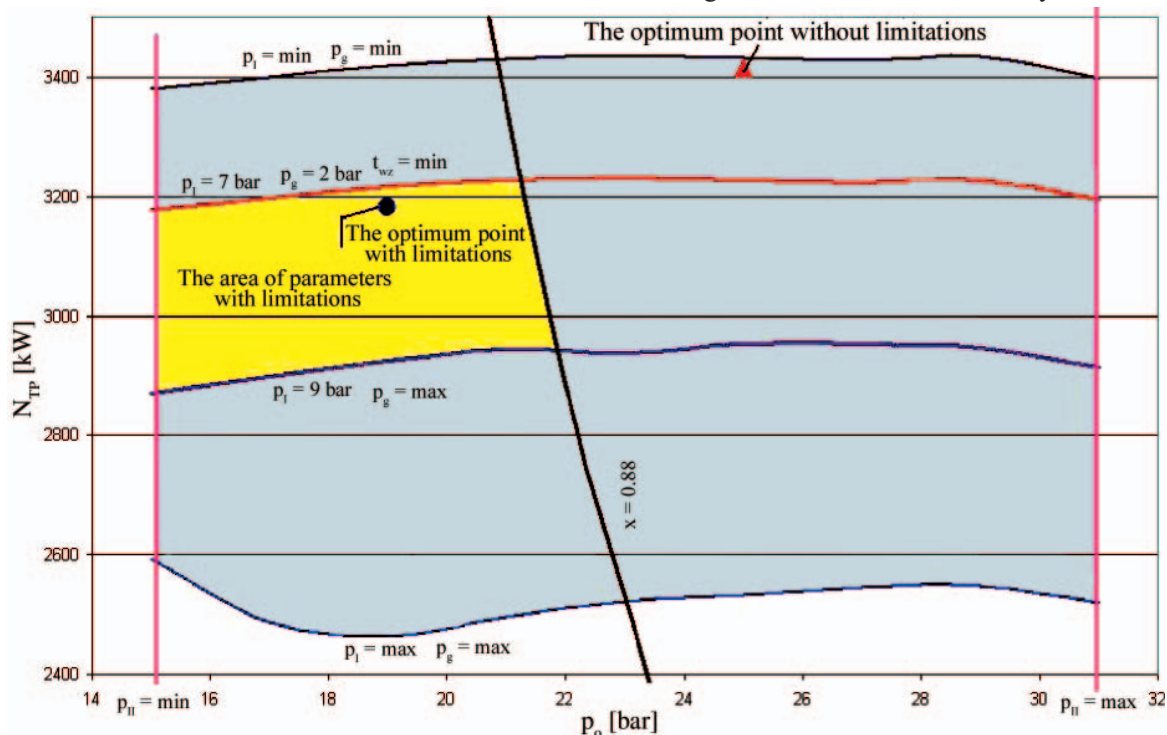


Fig. 4. The permissible area of parameters of the calculated steam cycle

Tab. 2. The optimum steam cycle parameters in the combined system of high-pressure combustion engine and steam turbine

No.	N_D [%]	t_o [°C]	p_o [bar]	p_1 [bar]	t_1 [°C]	p_g [bar]	t_{exh} [°C]	t_{FW} [°C]	x	m_o [t/h]	m_l [t/h]	m_u [t/h]	N_{ST} [kW]	N_{ST}/N_D
without limitations														
1	100	299	27.0	7.0	165	0.50	153	82	0.8715	15.02	10.78	1.93	4073	0.0791
2	90	289	25.0	7.0	165	0.50	154	82	0.8709	12.88	9.30	1.79	3414	0.0737
with limitations														
1	100	299	19.0	7.0	165	2.00	163	121	0.8874	18.10	7.32	3.47	3823	0.0743
2	90	289	19.0	7.0	165	2.00	165	121	0.8830	15.02	7.15	2.86	3182	0.0687

increased from 49.66% to 53.06% ($\Delta\eta_{combi}/\eta_D = +7.43\%$) for 90 % load and from 48.46% to 52.05% ($\Delta\eta_{combi}/\eta_D = +6.87\%$) for 100 % load.

In the steam subsystem with limitations, for e.g. 90% load, the mass flow rate $m_o = 15.02$ t/h of live overheated steam of the parameters: $t_o = 289^\circ\text{C}$ and $p_o = 19$ bar, and $m_l = 7.15$ t/h of live wet steam of the temperature $t_1 = 165^\circ\text{C}$ and the pressure $p_1 = 7$ bar, is produced from the heat contained in exhaust gas discharged from the piston engine, see Tab. 2.

THERMODYNAMIC ANALYSIS OF THE COMBINED POWER SYSTEM

The application of the combined power system to ship propulsion results in the increasing of propulsion system's efficiency and – in consequence – in the lowering of specific fuel oil consumption and – additionally – in the increasing of output power without any additional fuel oil consumption. In Tab. 3 the obtained values of output power, efficiency and fuel oil consumption for the considered ship combined power system with limitations taken into account, are presented.

Tab. 3. Output power, efficiency and specific fuel oil consumption of the combined power system consisted of 9RTA 96C two-stroke diesel engine and steam turbine

No.	ENGINE RTA96C		STEAM TURBINE		COMBINED POWER SYSTEM	
	N_D [%]	N_{ST} [kW]	$\Delta N_{ST}/N_D$ [%]	N_{combi} [kW]	N_{combi}/N_D [%]	
1	100	51480	3823	7.43	55303	107.43
2	90	46332	3182	6.87	49514	106.87
No.	N_D [%]	b_{ed} [g/kWh]	$b_{e\ combi}$ [g/kWh]	$\Delta b_{e\ combi}/b_{ed}$ [%]		
1	100	174.0	162.0	- 6.91		
2	90	169.8	158.9	- 6.43		
No.	N_D [%]	η_D [%]	η_{combi} [%]	$\Delta\eta_{combi}/\eta_D$ [%]		
1	100	48.46	52.05	+ 7.43		
2	90	49.66	53.06	+ 6.87		

CONCLUSIONS

- The proposed concept of the ship combined power plant consisted of slow-speed piston engine and additional steam turbine which uses the heat contained in exhaust gas from the piston engine, makes it possible to lower its specific fuel oil consumption by about 6.4 %.
- Additionally, without any change of main engine power output the whole power plant output can be increased by about 7% due to utilization of the heat contained in exhaust gas.
- 9RTA96C diesel engine consumes 205 t/day of fuel oil at 96% CMCR power output, and in the case of application of the combined power plant the same power output is obtained at 90% CMCR load of main engine and the specific fuel oil consumption of 189 t/day. This way the shipowner obtains measurable profits in the lowering of the fuel oil consumption by 16 t/day, i.e. 7.8% savings in the daily fuel oil consumption.
- Application of the additional steam turbine subsystem makes it possible to utilize waste heat from exhaust gas and in consequence to increase ship power plant output at a lower fuel oil consumption, and a lower emission of NO_x , CO_2 and SO_x compounds to the atmosphere without any additional efforts.

NOMENCLATURE

- b_e - specific fuel oil consumption
- c_g, c_a - specific heat of exhaust gas and air, respectively
- i - specific enthalpy
- m - mass flux of a medium
- N - power
- p - pressure
- T, t - temperature
- W_u - calorific value of fuel oil
- η - efficiency
- κ_g, κ_a - isentropic exponent of exhaust gas and air, respectively

Indices

- bar - barometric conditions
- B - boiler
- combi - combined system
- D - marine diesel engine, supercharging
- f - fuel
- inlet - inlet passage
- k - parameters in a condenser
- o - live steam, calculation point
- air - air
- ss - ship living purposes
- π - stage of: compression in a compressor, decompression in a turbine
- C - compressor
- g - exhaust gas

- T - turbine
- TC - turbocharger
- PT - power turbine
- ST - steam turbine
- exh - exhaust passage
- FW - water supplying a waste heat boiler

BIBLIOGRAPHY

1. *A new turbocharger generation*. ABB Turbo Systems Ltd. Publication No. CH-Z 2035 98E
2. *Description of Marine GenSet- Type L28/32H*. MAN B&W Diesel A/S. November 1993
3. Dzida M., Domachowski Z.: *A combined gas-steam system in ship electric power system – prospects for large passenger liners* (in Polish). In: [Materials of] 8th International Symposium on Ship Power Plants, Szczecin Maritime Academy, Szczecin 1997
4. ISO 8L17: Net specific energy of marine fuels. 1987
5. Kehlhofer R.: *Combined-Cycle Gas & Steam Turbine Power Plants*. The Fairmont Press, INC. USA 1991
6. Schrott K. H.: *The New Generation of MAN B&W Turbochargers*. MAN B&W Publication S.A. 236 5581E. 1995
7. *Sulzer RTA 96C*. Engine Selection and Project Manual. Wärtsilä, June 2001
8. *The MC Engine*. Exhaust Gas Date. Waste Heat Recovery System. Total Economy. Publication of MAN B&W. October 1985.

CONTACT WITH THE AUTHOR

Marek Dzida, Assoc. Prof.
 Faculty of Ocean Engineering
 and Ship Technology
 Gdansk University of Technology
 Narutowicza 11/12
 80-233 Gdansk, POLAND
 e-mail: dzida@pg.gda.pl



Photo: Cezary Spigarski

Diagnosing turbine engine bearing structures with the aid of FAM-C and FDM-A methods

Andrzej Gębura, Ph. D.
Air Force Institute of Technology

ABSTRACT



The diagnostic method FDM-A [2], based on the measurement of the pulsation component frequency modulation, and the FAM-C method, making use of the alternating current frequency, were developed in the Air Force Institute of Technology. The essence of their accuracy consists in "natural" synchronisation of the sampling signal with the angular velocity of the observed kinematic links. These methods make it possible to determine the level of wear of a subsystem and its location during normal operation of the power unit. They provide opportunities for determining numerous parameters of bearings, bearing structures, and the rotor unit. Moreover, the FDM-A method makes it possible to detect resonances in particular elements and their parameters - among others, they provide opportunities for assessing the level of the mechanic quality factor of the examined structure, i.e. the time margin of structure operation until the structure reaches the state of resonance. On the other hand, the FAM-C method provides opportunities for defining numerous parameters of the phenomena connected with the rotor unit. The diagnostic system is connected to an arbitrary point of the electric network (electric junction, for instance) supplied with the direct voltage¹ or the alternating voltage² taken from the generators driven by the examined rotating system. The presented experimental material was recorded in operating investigations of the aircraft turbine engine unit, in which the role of "generators – observers" was played by: an aircraft DC generator and a three-phase AC rate generator. Generators of this type are also used in rocket cutters with turbine engines, this way the conclusions presented in the article can be easily transferred to those objects. During the measurements, performed on the decks of the examined airplanes and on engine test beds, the ranges and locations of assembly and wear defects were determined. Successive stages of wear of the rolling bearings were also observed.

Key words: technical diagnostics, diagnosing propulsion transmission ducts, skew³, frequency modulation, characteristic set, turbine engine, rolling bearing

INTRODUCTION

Industrial development observed on the turn of the ninetieth century was a source of demand for rolling bearings, to be used in machines built in large numbers in those days. At the same time, the development of technology made it possible produce, in a mass scale, precisely machined bearing components. The bearing structures had relatively low rotational speeds, which rarely reached the level of 3000 rev/min.

New challenges for rolling bearings were brought by the development of aviation – increased vibrations and the action of higher and rapidly changing temperatures made it necessary to secure higher reliability of the bearings via increasing radial clearances and more careful selection of construction materials. Even bigger challenge was connected with new constructions of jet turbine engines built after the second world war. Rotor units in these engines reached rotational speeds ranging from 10000 rev/min to 60000 rev/min, much higher than ever before.

For a relatively long time, diagnosing the technical state of rotor unit bearing supports in aircraft engines has been done using vibroacoustic methods. The vibroacoustic signal, which carries the diagnostic information, is taken from the bearing structure elements and therefore is heavily noised and damped, which makes the diagnosis extremely difficult and time consuming. This is because of the presence of strong disturbances [5] generated by vibrating metal elements of the aircraft engine construction (which is, as a rule, relatively elastic). The second factor is the attenuation of the diagnostic signal on joints between the mechanical elements and in all spaces filled with air, fuel, oils and lubricants (all these are the media revealing poor propagation of acoustic waves). And the third, last factor is the concentration of numerous vibrating elements located close to each other, which makes detecting the location of the defected objects extremely difficult.

In the article, another diagnostic method is proposed in which the diagnostic signal from the bearing supports is

¹ This method is called FDM-A (FM- frequency modulation, D - direct current, A - method advancement level)

² This method is called FAM-C (FM- frequency modulation, D - alternating current C - method advancement level- means that applications are in use in the form of automatic tester).

³ Also referred to as sweep.

transmitted via mechanical joints to an aircraft generator, in which it is converted to a synchronous, digital signal. This signal can be easily processed using present-day computers. Two variants of the proposed method were named FAM-C [2] and FDM-A by the authors. In those methods the analysed diagnostic signal is coded in the frequency and phase modulation, which is (as is well known from the theory of radio wave transmission) more resistant to disturbances than the amplitude modulation. The acoustic signal is subject to two-stage sampling:

- ☆ “synchronous sampling”, which consists in the conversion into a digital signal (instantaneous frequency time-history) by the “regular” deck generator
- ☆ “classical” sampling in time intervals between the above described “synchronous” sampling, done by a clock with properly selected frequency in the counter card.

In Ref. [7-10, 13] the author has presented his achievements concerning the application of the FAM-C method making use of a single phase output voltage in the deck generator for diagnosing simple cases of wear and assembly defects of power transmission boxes. These achievements included:

- ◇ monitoring of slips in one-way clutches,
- ◇ estimating skew angles of power transmission shafts and their parallel displacements,
- ◇ detecting cavitation phenomena in the deck generator hydraulic rotational speed stabiliser system.

Ref. [11] describes the use of a similar diagnostic method for estimating skew angles of power transmission shafts and their parallel displacements in the power transmission system in the ship engine room. The use of the three-phase measurement [13] made it possible to trace, without instrumentation change, mechanical processes revealing higher frequencies, for instance monitoring the operation of ship compression-ignition engines.

Further resolution refinement was done using the signal of the DC generator output voltage. This method, named FDM-A, makes it possible to trace mechanical processes [12] revealing even higher mechanical frequencies:

- ✧ monitoring the wear of toothed wheels, and estimating dimensions of tooth-to-tooth clearances
- ✧ estimating the operation of rolling bearings.

In author’s opinion, the here presented methods: FAM-C and FDM-A can become a valuable version of the non-interfering monitoring of the technical state of turbine engines. Some applications discussed in further sections indicate important advantages of these methods, such as:

- ⇒ no need for connecting any sensors to the object – this role is played here by the “regular” generator mounted on the object
- ⇒ the measurement can be done at an arbitrary network point, even extremely distant from the examined object
- ⇒ the primary diagnostic signal is directly “transmitted” from the examined bearing situated deep inside the structure to the generator serving as a sensor-processor via elements of the transmission construction. This way large disturbances, which can come from casing resonances, volumetric damping and other disturbances of high importance for vibroacoustic methods, can be omitted [5]
- ⇒ transient loss of the “connection” between the diagnosed element and the generator-receiver is not a problem – the clearances are presented as a separate estimate (among other actions, a separate characteristic set is created), which can also be an object of parametric analysis

- ⇒ easy automation of the diagnostic process
- ⇒ high speed of diagnostic data recording.

METHOD DESCRIPTION

A comprehensive description of the diagnostic methods is given in Ref. [2, 6 ÷ 13]. It is advisable, however, to present its main elements, which are indispensable for understanding the context of the problems discussed in the article. Each assembly or wear defect, for instance skew of the splined connections in a power transmission box, is accompanied by the modulation of the output angular velocity. The modulation interval is a characteristic parameter for the type of defect and nominal angular velocity of the given kinematic pair. At the same time the level of frequency deviation (amplitude of modulations) is proportional to the scale of the defect. These modulations are transmitted, via the transmission system, to the rotor of the generator. Being a synchronous machine, the aircraft generator reflects changes of instantaneous angular velocity in the form of output voltage frequency modulation. By measuring time increments between successive zero level crosses and drawing their doubled inverses on the (t, f_p) rectangular coordinate plane we obtain a set reflecting, in a discrete form, the course of generator rotor velocity changes. Two parameters can be attributed to each deviation, which are:

- deviation time t_{odi}
- deviation amplitude ΔF .

The deviation time can be substituted by the process frequency f_p , according to the formula:

$$f_p = 1/(2t_{odi}) \quad (1)$$

Each deviation can be presented on the rectangular coordinate plane as a point $(f_p, \Delta F)$. It was found in numerous research activities that these points tend to concentrate into sets. These sets bear the name of characteristic sets, as they characterise the wear of particular subsystems. It was found that they have different shapes, heights and locations with respect to the X-axis.

It was also found that the change in the scale of the defect results in the change of the height $\{|\Delta F_{max}| + |\Delta F_{min}|\}$ of the corresponding set, while the band $0-f_p$ occupied by the set with respect to the X-axis is characteristic for the type of the subsystem.

During numerous applications of the method the author has found that the presentations created in the above way as characteristic sets are favourable for a well known object, with well recognised relations between the change in the scale of the mechanical defect and the change of the characteristic set height. The use of these presentations has numerous advantages:

- ⇒ demodulation processes take a natural course directly in the deck generator, which simultaneously is a natural band-pass filter in the process of observation of mechanical phenomena
- ⇒ the electric signal recorded from the deck generator is synchronised in a natural way with the observed mechanical phenomena, as the rotor of the generator-observer is fixed to the diagnosed mechanical kinematic pairs
- ⇒ easy automation of the diagnostic process:
 - ◆ each type of defect of each subsystem has reserved an individual, earlier defined characteristic band on the X-axis
 - ◆ for each band, a number of diagnostic levels (usually four: A, B, C, D) are defined on the Y-axis – depending on the height of the given set the subsystem is classified as belonging to one of these diagnostic classes

- ⇒ easy observation of the time-histories of arbitrarily long duration in the same plane – of special importance when the signals appear stochastically
- ⇒ easy extraction of the pulsation component from a heavily modulated signal. Indeed, these extraction can also be done using partial Fourier analysis, but that analysis, unlike the FAM-C and FDM-A methods, has two disadvantages:
 - ♦ spectral lines for real power transmission systems are usually broadened, which makes the diagnostic pattern obscure and difficult for automation
 - ♦ that analysis neglects stochastic processes.

Despite all above named advantages of the wear presentation on the $(f_p, \Delta F)$ plane, for unknown objects⁴ it is advisable to use relations⁵ $f_i = f(t)$ for diagnostic purposes. Based on these relations, an experienced diagnostician can perform the process of state identification of the diagnosed object in a more efficient, although also more time consuming way. In that way stochastic processes can be traced, including, for instance, a temporary stop of the rolling element in its motion around the raceway due to the local appearance of the abrasion product.

Once the characteristic sets are created based on the recorded time-histories, Fig. 3, the following parameters can be calculated:

- ★ height of the first harmonic characteristic set – proportional to the dimension of the total radial clearance and the rotor unit unbalance
- ★ width of the characteristic set – proportional to the rotor unit unbalance
- ★ distance between the first harmonic characteristic subsets – proportional to the shape error (ovalisation, roundness deviation) of the bearing seat
- ★ height of the main shaft first harmonic characteristic set – proportional to the rotating unit symmetry axis skew angle (between the generator shaft and the turbine shaft)
- ★ skews and axial clearances of other rotating engine elements, such as pumps, power transmission shafts, etc.

DESCRIPTION OF THE DIAGNOSED OBJECT AND THE MEASURING SYSTEM

Turbine engines have found their immovable place in aviation. An element which is most exposed to the action of dynamic forces in those engines is the bearing cage. According to the design tradition, its only role is to separate the rolling elements, as a result of which the bearing cage is not expected to carry heavy loads. The situation of general underloading of the bearing and rapid changes increasing its load, when the bearing cage is subject to the action of impact forces, is untypical for machine design traditions. Different kinematics of the rolling elements, being the result of different friction conditions, is the origin of impact forces in the rolling unit. The energy passed to the cage during its collision with the rolling element changes its momentum in both the circumferential and radial direction, and is partially lost for an additional slip of the rolling elements on their raceways. As a result of these phenomena, the cage starts to oscillate in an undamped way between the rolling elements [6]. It also rotates, in general, around another axis than the bearing axis. The stability of the cage motion highly depends on friction conditions observed in the rolling contacts and in the areas where the cage contacts the rolling elements. According to author's experience, these forces are so large that

they can provoke cracks of the separating elements in the cage, or even cracking of the bearing perimeter. Such phenomena are frequently preceded by resonance effects.

Phenomena of this type, untypical for earlier applications of the rolling bearings, were the reason why producers and institutions involved in aviation industry often carry out, on a wide scale, research activities oriented on detecting and monitoring complicated processes of rolling bearing failures in aircraft engines. Nowadays, this problem is still unsolved and is an object of concern of designers, operators, and analysts of aviation accidents.

In order to gain more detailed information on the relations between frequency modulation phenomena and bearing defects, the process of long-lasting wear of engine bearings was examined on the engine test bed, and was complemented by observations of engines directly on the decks of the airplanes. The object of investigations was a single-shaft turbine engine, Fig. 1. The main shaft is divided into the compressor shaft and the turbine shaft, which are linked together via the splined connection, Fig. 2. The shaft is supported on three rolling bearings.

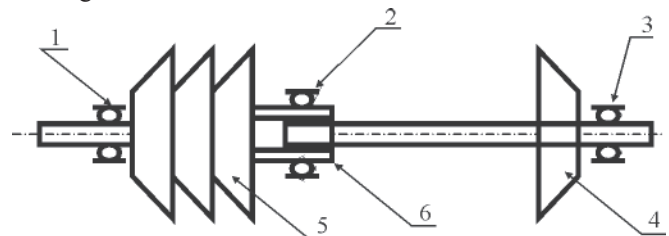


Fig. 1. Kinematic diagram of a one-watt turbine engine :
1 – front bearing; 2 – central bearing, connection between two shaft parts (turbine shaft, compressor shaft); 3 – rear bearing; 4 – turbine; 5 – compressor; 6 – central bearing journal



Fig. 2. Central bearing journal, connection between two shaft parts (turbine shaft, compressor shaft)

The front bearing has a different number of rolling elements that the central bearing – that is why their characteristic sets are easily recognisable using the FDM-A method, Figs. 1 and 2. The central bearing structure is the most heavily loaded subsystem of all three engine supports, due to most difficult cooling conditions and the highest deflection of the rotor unit. The outer ring of the central bearing is pressed into an elastic sleeve, the splines of which are fixed to the engine body.

⁴ With unknown relations between the defect of the unit and changes in the depth of the generator output voltage frequency modulation.

⁵ In fact, the presentation $f_i = f(t)$ has a discrete form as a set of points. In diagnostic practice, however, presentations are in use in which points are distributed with such a fine resolution that they give an impression of a continuous curve.

Occasionally, traces of rotation (slips) of the bearing ring in the sleeve can be observed during engine repairs. Also cases are recorded of cracks of the sleeve that fixes the central bearing outer raceway to the engine body.

The inner bearing ring is pressed onto the compressor journal. The turbine shaft is introduced inside the journal by a splined connection. This connection makes it possible to transmit the torque from the turbine shaft to the compressor shaft. Longitudinal connection between these two parts is executed, in turn, by two half-rings and a special nut screwed onto the end of the central bearing journal. Breaking this connection may result in a disaster, as it disconnects the power turbine – there is no drive for pumps and other units necessary for proper engine operation. In this structure skews are frequently recorded which are the sources of additional dynamic loads, along with the forces generated by bearing assembly errors and radial clearances.

From the point of view of journal load, very dangerous are large skew angles accompanied by small radial clearances in the central support – a source of heavy bending loads of the journal. The most dangerous cases of bearing operation include slips of the inner bearing ring on the journal, as they are the sources of not only of excessive dynamic forces, but also the increased level of temperature field, which can provoke journal plasticisation and reduce its mechanical strength.

Due to the specific construction of the engine, of high importance it securing the coaxiality of the bearing seats during their assembly. Theoretically, all three bearings are to be situated along one axis, with a small permissible tolerance. Coaxiality changes lead to disturbances in bearing operation. Of high importance for each bearing is the state of the cage separating the rolling elements in the bearing. Its smooth motion guaranties correct motion of the rolling elements. The investigations were performed in two paths, Fig. 3, using signals from a DC generator (DC channel) and a three-phase AC rate generator (AC channel). These two paths complemented each other.

The three-phase AC rate generator was a source of information on situations connected with slow-speed processes, including:

- ❖ technical state of the power transmission box
- ❖ unbalance of the main shaft (with compressor and turbine), and ranges of radial clearances in bearing supports
- ❖ skew of the main shaft – assessment could be made whether the skew of the compressor shaft with respect to the turbine shaft is increasing. As a final result, an assessment can be made whether this skew does not exceed a permissible limit defined by the bearing producer
- ❖ crack of the sleeve that fixes the central bearing
- ❖ increased ovalisation (circular shape error) of the bearing seat
- ❖ number of cracked separation sections in the cage
- ❖ error of journal perpendicularity with respect to the compressor disc rotation plane
- ❖ increased torque on the engine main shaft.

The DC generator provided the information about defects connected with high-speed processes. The processes which could be observed and diagnosed include:

- ⊛ cooperation of the main shaft with the transverse vibration damper (central support)
- ⊛ increased friction force in the front bearing as a result of longitudinal movements of the compressor shaft ($h \geq N_p$, $p_s \geq 0.4$)

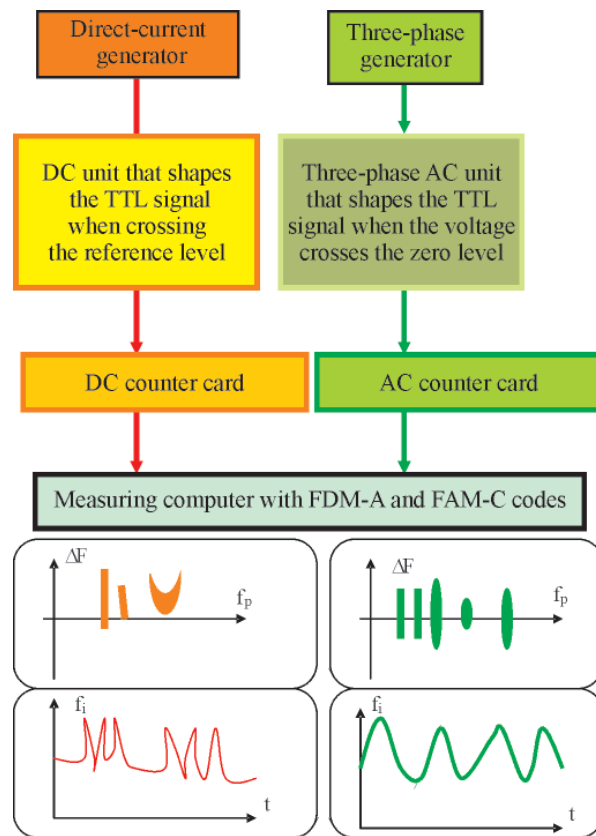


Fig. 3. Recording diagnostic signal from the examined engine using FDM-A and FAM-C methods

- ⊛ locking of the front bearing cage (separator) – the appearance of the N_p -th harmonic of the main shaft rotational speed ($h = N_p$), where N_p – number of rolling elements in the bearing
- ⊛ locking of the central bearing cage (separator) – the appearance of the N_c -th harmonic of the main shaft rotational speed ($h = N_c$)
- ⊛ general level of wear of the bearing structure.

PROBLEMS RELATING TO BEARING WEAR AND POSSIBILITIES OF THEIR OBSERVATION WITH THE AID OF FAM-C AND FDM-A METHODS

A feature characterising the designs of all types of bearings is the type of contact between the rolling elements and the ring raceways under load. This contact is of Hertzian type: linear in the roller bearings and of point nature in the ball bearings. It is decisive for determining the permissible load of the bearing⁶ defined by its load capacity. The maximum load of the rolling elements resulting from the permissible Hertzian pressure in the rolling contact is a factor decisive for potential use of the bearing in a given case of load. According to Ref. [5] the highest probability that the machine defect will be detected is secured by the observation of the bearing structure, and this probability is equal to 70%. In laboratory conditions, the main cause of bearing defects was the fatigue wear of the working surfaces of their elements. According to literature data, the observations of defects of rolling bearings in real operating conditions indicate that the fatigue raceway defects do not exceed 36%, in general, of all causes of their withdrawal from operation, while in the

⁶ According to ISO-76-1978 standard [6], permissible loads are the loads at which permanent deformation in the contact of the most heavily loaded rolling element with the raceway does not exceed 0,0001 of the rolling element diameter. In the USA, the standard ANSI/AFBMA std 9,11-1978 defines the maximum permissible limit of surface pressure as equal to 4000 Mpa.

remaining cases 55% of bearings lose their workability due to excessive friction wear, and further 9% - due to the corrosion and other destructive processes.

Durability vs. load

Fatigue durability of bearings depends on their load. As a consequence, observations of all instantaneous bearing overloads are crucial for the assessment of their lifetime. The FDM-A method makes it possible to trace, in an easy way, (high-speed) time-histories of the instantaneous velocity (DC channel), by observing the frequency, amplitude, and dynamics of retardations of the rolling elements. Indirectly, after gaining additional information from the slow-speed data recorded in the AC channel, we can also conclude about stresses taking place during rolling down the raceway.

Hence, a conclusion can be drawn that the complete aircraft engines which, diagnosed using FDM-A and FAM-C methods, reveal lower (worsened) parameters cannot be mounted on airplanes designed for tasks connected with extremely high overloads, observed in acrobatic airplanes for instance.

Friction wear

It results from the investigations carried out by the research team headed by the author that changes of clearance dimensions can be monitored in the form of a number of parameters recorded using the FDM-A and FAM-C methods. These parameters include:

- ➔ height of the characteristic set of the AC generator main shaft rotational speed first harmonic (AC measuring path) – total radial clearances
- ➔ value of the rolling coefficient p_s , defined as the ratio between the average angular velocity of the main symmetry axis of the bearing rolling element (roller) and the velocity of the main shaft. It is obtained from the quotient of the total frequency modulation band of the DC pulsation component in the bearing (DC measuring path) to the product of the rotational speed and the number of rolling elements in the bearing. The obtained p_s value facilitates assessing the smoothness of the cage motion and makes it possible to determine the slip coefficient between the rolling elements and the raceway
- ➔ relative value of the AC path total pulsation – determining circumferential clearances between the cage window and the rolling element.

Excessive bearing clearances are the sources of the raceway resonance vibration and provoke the instability of motion in the cage/rolling element system. The resonance vibrations have the high-frequency nature (of an order of a number of kHz) and can only appear when the SBK⁷ spectrum has the broad-band nature. The presence of slips in the rolling bearing differentiates the kinematics of particular rolling elements, which, as a result, leads to fluctuations of characteristic frequencies of the kinematic excitations. Due to the presence of clearances in the kinematic pair, each disturbance in the motion of the rolling elements is a source of additional impact forces in the cage/rolling element system. The volume of the energy introduced and lost during the collision depends on friction conditions between the contacting pairs composed of

the rolling elements/cage partitions and the rolling elements/bearing raceways. Intensive abrasive wear is accompanied, in turn, by higher bearing temperature, increased volume of wear products in the lubricating medium, and intensive ageing of this medium. Also the load distribution into particular rolling elements changes unfavourably, towards more heavily loading of the element which carries the highest force.

Ageing phenomena

Ageing phenomena are, perhaps, the least recognised issues. They require extremely long time intervals of engine observation, and precise records of their standstills and storage. It is well known that the fastest process of bearing ageing is observed on engines which are stored in unfavourable maintenance conditions, in high relative humidity (over $\eta = 60\%$) and at large temperature changes. Especially harmful for the bearings are electrolytic corrosion processes, due to the use of various metals, with different alloy compositions (for instance, steel with different contents of carbon) and different electrochemical potential. It results from the author's experience that the engines had smaller clearances after a few months of storage.

The literature overview suggests that possible intensification of the ageing process depends strongly on changes in the operating temperature level caused by, for instance, high ambient temperature, and/or less effective cooling of the bearing due to insufficient mass flow rate of the cooling air or oil.

A very dangerous type of ageing wear is also the abovementioned plasticisation of the bearing journal.

SUCCESSIVE TYPICAL STAGES OF BEARING WEAR OBSERVED USING FAM-C AND FDM-A METHODS DURING THE OBSERVATION OF LONG-LASTING WEAR PROCESSES

According to the practical diagnostic experience, successive stages (phases) of bearing wear [5] include noise wear, vibration wear, and thermal wear.

In the examined engine the bearing cage is covered with a galvanic silver layer. In the first stage of bearing operation, i.e. the **noise phase**⁸, first we observe the decrease of the rolling resistance and the increase of radial clearances, due to wearing-in of the bearing. Then the silver is spalled out, as a result of which more and more heavy bearing operation is observed. The height of the characteristic sets of the bearings increases systematically, Fig. 6. The turning coefficient of the central rolling bearing⁹, defined as the ratio of the total band to the frequency of the N-th harmonic (where N – number of rolling elements), also increases in this time – the bearing cage rotates with increasing resistance. A recommended action in the noise phase is to observe and possibly correct the assembly errors in the engine main shaft/bearing structure system. In the above way such defects as the lack of journal perpendicularity to the rotation plane were detected in the investigations, a defect which manifested itself by increased depth of the amplitude modulation in the instantaneous frequency time-histories recorded in the AC generator path. In author's opinion, as early as in this phase of bearing wear two different tendencies of turbine engine rotor bearing structure wear can be recorded,

⁷ SBK - total shape error.

⁸ According to the literature [5] the dominating effects in the noise phase are macro-unevennesses of bearing elements manifesting themselves as the broad-band acoustic noise.

⁹ Rolling bearing turning coefficient – the ratio of the mean angular speed of the bearing rolling element (shaft) main symmetry axis to the main shaft speed.

with two different presentation relations observed using FAM-C and FDM-A methods:

- a) type of structural-and-skew wear, in which systematic increase of the first subharmonic is observed in the AC generator path (increased skew) at relatively small increment of radial clearances in the central bearing. Most likely, at this type of wear large bending forces act on the journal, which in unfavourable situations can lead to its crack. The author did not observe such a phenomenon, and was only acquainted with the results of mechanical measurements done after the airplane crash. On the other hand, in the engines observed personally by him the bending forces did not lead to journal crack. They only provoked the increased load in the front bearing, with further multi-element resonance in the engine supports and strong destruction of the central bearing, Fig. 5. Certainly, these destruction phenomena refer to two next wear phases
- b) type of clearance wear, in which systematic increase of the first harmonic of the AC generator path is observed as a result of rapid increase of the total radial clearances in the central support. At this wear form, the failure-free operation of the bearing is observed much longer than for wear type a. In some cases, an increased level of mechanical vibrations is observed for increasing time of operation. But the verifications which were carried out in that time did not reveal the state which would threaten with bearing break-down. However, a literature overview suggests [16] that excessive clearances in rolling bearings can also be a source of excessive heat and lead to the destruction of the bearing structure. Indeed, an engine with bearings revealing excessive clearances has an unstable characteristic of changes of the load angle distribution into rolling elements at arbitrary manoeuvres of the airplane and that is why this state can be extremely dangerous, as intensive and uneven abrasive wear of the rolling elements can appear, accompanied by rapid increase of friction forces. In the areas of contacts between micro-unevennesses the temperature increases rapidly, reaching very high levels (flash temperature). As a result, the surface temperature of the contacting elements also increases, and so does their volumetric temperature. The temperature increase, especially in the micro-areas of friction contact, is a source of many changes, of both physical and chemical nature, in the materials used for bearing element and the lubricant.

In the second stage, the **vibration phase**¹⁰, systematic decrease of the height of the characteristic sets is observed due to the termination of the process of spalling out of the galvanic layer and washing out of the older spalling-out products, done by the lubricating oil system. As a result, the clearances between the bearing structure elements increase and the bearing motion resistance decreases. Also the rolling coefficient, defined in the literature [6] as the angle of the load distribution into particular rolling elements, decreases. At this stage, large clearances are observed in the bearing. The wear process is still in progress, but the mechanism of wear is controlled by the dynamic forces acting on the moving bearing elements in the environment of increased clearances.

During the investigations a value of the rolling coefficient was recorded which does not make sense from the mathematical point of view. This means that not all rolling elements of the bearing roll down the raceway. In the vibration wear stage, situations can happen when the walls of the sleeve that fixes

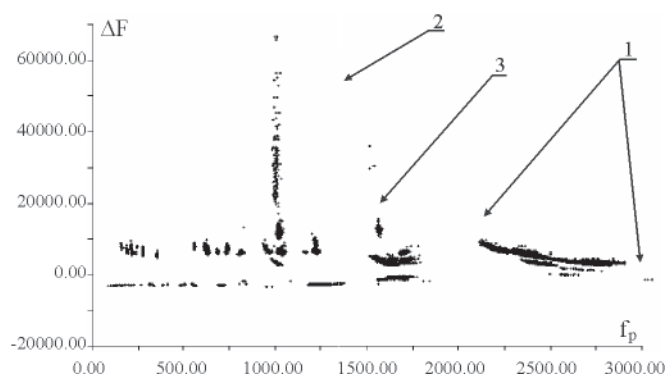


Fig. 4. Characteristic sets obtained from the DC generator path:
1 – two characteristic subsets of the central bearing and the rear bearing;
2 – characteristic set of the eighth harmonic;
3 – characteristic set of the front bearing

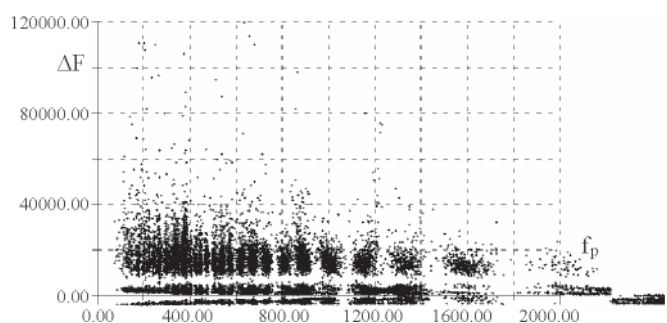


Fig. 5. Characteristic sets obtained from the DC generator path for the state of general resonance in bearing structures

the outer raceway to the engine body become thinner. This happens due to transient increase of forces locking the bearing, as a result of which the rotation-slip of the central bearing body (outer raceway) is observed in the sleeve, along with the erasing of the sleeve material due to sliding friction. The decreased thickness of the wall is observed in the FAM-C method as decreased amplitudes of the first harmonic and the first subharmonic. Most often this phenomenon is preceded by fading pulses, observed a large number of hours earlier using the FDM-A method in the DC generator path. Sometimes, due to remarkable reduction of thickness of the sleeve, or the appearance of large impact forces in the central support bearing, the sleeve cracks. Such a crack, Fig. 6, was detected using the FAM-C method in the three-phase AC rate generator path. In that time the height of the main shaft first harmonic characteristic sets decreased rapidly, by as much as nearly ten times, for all rotational speeds, except the range close to the maximum speed: $n = 15100$ rev/min (Fig. 7).

It is well known [6] that the bearing structure becomes unstable after excessive deformations of bearing elements, shafts, and casing in operating conditions, or as a result of resonance vibrations, the reason for which is the coincidence of the exciting force frequency with the free-vibration frequency of the bearing.

A very important parameter to be traced in the vibration wear stage is the quality coefficient (Q) of the turbine engine rotor/bearing system [5]. The higher value of the quality Q , the smaller the damping in the system and the longer the transient processes. This way in case of large quality coefficients, each change of the nominal speed of the rotor, change of external dynamic forces acting on the rotor during manoeuvres of the airplane, and/or change of the load introduced by the units driven from the power transmission box, are the sources of

¹⁰ Of highest importance in the vibrating phase are increased radial clearances, which result in increased amplitudes of mechanical vibrations observed in the literature on vibroacoustics [5].

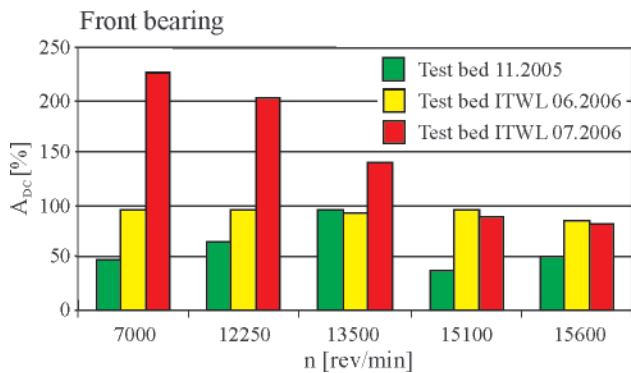


Fig. 6. Front bearing characteristic set height diagram for three successive time intervals of observation of the rolling bearing in the noise wear stage

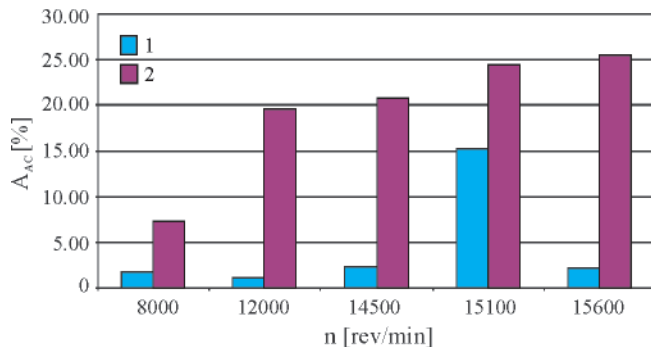


Fig. 7. AC first harmonic characteristic set height changes during the crack of the sleeve that fixes the inner bearing raceway to the engine body: 1 – after sleeve crack, 2 – before sleeve crack

strong nonlinear vibrations [15], accompanied by rubbing of the rotor elements against the casing and bearing seals, various strokes, etc. [14]. Determining the quality of the system is therefore of high importance for detecting possible causes of future failures.

According to the literature [5, 14], the permissible quality for rotating machines is equal to $Q = 5$. With the aid of the FAM-C and FDM-A methods, determining Q is relatively easy as these methods present each bearing in the form of a separate characteristic set having a well defined amplitude and band width. During the investigations, a number of cases were recorded when some symptoms of mechanical resonance were recorded – when a characteristic set, or a number of sets decrease their frequency bands, and sometimes also increase their height (so called mechanical quality of the bearing structure increases, see Fig. 4 – detail 2). Sometimes these states refer to single elements of the turbine engine rotor centre, and manifest themselves as a “jump up” of a single characteristic set obtained using the FDM-A method. In other cases almost all characteristic sets increase their heights and decrease band widths. In those circumstances a multi-element resonance takes place and, according to [18], the system is in full resonance, Fig. 5. According to author’s experience, those states indicate advanced level of destruction of the bearing structure, Fig. 8. Before disassembly, this bearing revealed $Q > 11$. During the disassembly of the bearing working in the resonance state for a relatively long time we can observe longitudinal indents on the raceways, like those reported in the literature.

When the slip of the rolling elements over the bearing raceway becomes more intensive, the motion of the majority of the rolling elements may stop completely – the phase of the **thermal wear** begins. In this time the volumes of the heat

generated in the bearing structure are so large that they cannot be fully moved away by the oil system. As a result, the strength of the material structure of particular elements of the bearing decreases, which leads to excessive increase of windows in the separator cage, or even breaking the separation, Fig. 8. This state of bearing structure is presented in the instantaneous frequency time-histories $f_i = f(t)$ recorded in the AC path as repeatable, with respect to the shape and parameters, groups of pulses with the pulse numbers in a series proportional to the number of broken cells. Simultaneously, the pulsation amplitude increases from the level of about 10% up to 160%. The increased temperature is also a source of thermal deformation of the central bearing ring, which easily loses clamp on the journal and is subject to slips.



Fig. 8. Damaged central bearing, earlier diagnosed using the FAM-C method: 1 – broken cage separator ring

Using the FDM-A method in the DC generator path we can precisely determine both the angle of these slips and the frequency of their occurrence. For this purpose the times of duration and the times of repetition of the fading pulses in the instantaneous frequency time-history $f_i = f(t)$ are observed and calculated.

In author’s opinion, the most dangerous course of thermal wear stage, with respect to possible final effects, is that taking place at relatively small radial clearances¹¹ in the central support bearing structure. In those circumstances, at large forces which tend to skew the two main shaft parts, the load is not effectively passed to the front support bearing and large part of the bending force is carried by the central bearing journal. All this can lead to the crack of the journal.

ASSEMBLY ERRORS OBSERVED USING FAM-C AND FDM-A METHODS

Bearing support assembly errors should be made distinctive and be analysed independently of the wear processes. They can act towards accelerating or delaying the time of action of particular wear stages during the bearing operation. This group of errors includes:

- radial clearances of individual bearings
- excessive circumferential clearances
- error of misalignment of three bearing supports
- error of turbine or compressor unbalance
- error of bearing seat ovalisation
- error of skew of the two shaft parts
- error of compressor journal perpendicularity.

Excessive radial clearances manifest themselves in the DC generator path as the increased amplitude of the characteristic set (presentation $\Delta F = f(f_p)$) of the central bearing. The excessive

¹¹ Small value of the radial clearance can be easily determined using the FAM-C method by detecting a relatively small amplitude of the first harmonic characteristic set on the presentation obtained from the AC generator path, and from small value (below 0.4) of the turning coefficient of this bearing, calculated using the FDM-A method.

circumferential clearance, in turn, manifests itself in the AC current generator path in the form of specific undercuts observed in the time-history $f_i = f(t)$. In general, all characteristics of the rolling coefficient are inversely proportional to the rotational speed, which can be easily explained as the effect of the increasing hydrodynamic forces which decrease the rolling friction resistance. Long-lasting observations, complemented by mechanical measurements, have led to a conclusion that if an inflexion point in the form of a minimum appears on the rolling characteristic, Fig. 9, this means remarkable misalignment between the bearing supports.

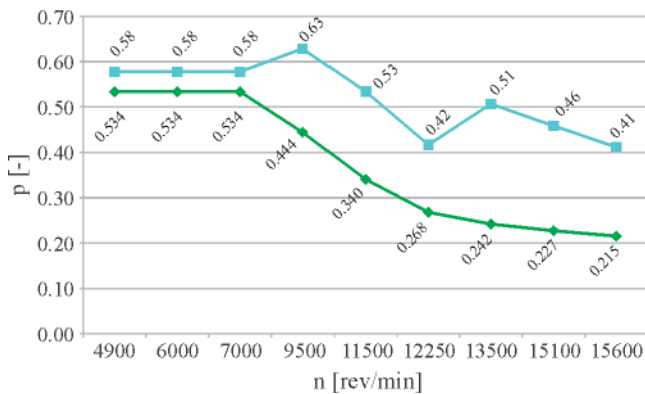


Fig. 9. Changes of central support bearing rolling coefficient: upper curve – for negative misalignment, lower curve – without misalignment error

The turbine or compressor unbalance error manifests itself in the presentations of the AC current generator paths as the increased amplitude of the characteristic set (presentation $\Delta F = f(f_p)$ of the main shaft rotational speed first harmonic), accompanied by the widening of this band. If the bearing structure ovalisation error takes place, this set breaks down into two vertical characteristic sets. Skewing of the connections linking the two shaft parts manifests itself as increased height of the first subharmonic characteristic sets. The compressor journal perpendicularity error can be assessed by measuring the amplitude modulation depth in presentations $f_i = f(t)$.

CONCLUSIONS

The article presents the applications of the diagnostic methods FAM-C and FDM-A, which base on the analysis of output voltage frequency modulation parameters, for diagnosing technical states of turbine engine bearing supports. The use of these methods makes it possible to detect relatively early a defect in the diagnosed subsystem, before it becomes dangerous for the safety of airplane motion, for instance. Various assembly errors can be detected this way, and wear effects taking place in bearing structures can be monitored. Numerous parameters of the bearing operation can be traced, including: changes of friction resistance, changes of radial clearances in the bearing, changes of circumferential clearances between the cage and the rolling element, changes of the rolling coefficient. Moreover, it is possible to observe the phenomena taking place in the rotor unit, including: the skew between the turbine shaft and the generator shaft, and/or perpendicularity errors between the journal symmetry axis and the compressor disc rotation plane. Many hours earlier than when using the “traditional” methods we can observe, without interfering into the system, numerous wear phenomena that lead to dangerous failures of turbine engine bearing structures, such as bearing journal plasticisation, and/or disintegration of the separation gaps in the cage or of the entire circuit. Systematic use of the FAM-C and FDM-A methods makes it possible to determine, in a precise way, a safe time instant when the operation of the diagnosed object is to be stopped. The presented methods are

of general use and can be successfully applied for diagnosing technical states of turbine engines used in watercraft.

BIBLIOGRAPHY

1. Abramov B. I.: *Waddle wheel with tooth primary form*, Kharkov, Ukraine, 1968
2. Biarda D., Falkowski P., Gębura A., Kowalczyk A.: *Patent description PL 175664B1: Method of technical diagnosing of coupling elements in an engine, in particular, aircraft combustion engine with AC generator* (in Polish), submitted on 08.07.1996, patent granted on 29.01.1999
3. Borgoń J., Stukonis M., Szymczak J.: *Can damages of splined connections in aircraft engines be a source of accidents in aviation* (in Polish), ITWL report no. 311/93, [in] Proc. Conf. on “Technical problems of operation and reliability of military aircraft”, Kiekrz 1993
4. Bułgakow E. B., Gałobanow W., Klimow A.W.: *Informacjonno - izmierzitel'naja sistema kontrolia sostojania aviacionnych i obszczimaszynostroitel'nyh rieduktorov, privodov i korobok pieriedacz „Informacionnyj matierial”*, Centralny Lotniczy Instytut Konstrukcji Napędów im. P. I. Baranowa, Moscow 1990
5. Cempel Cz.: *Fundamentals of vibroacoustic machine diagnostics* (in Polish). WNT, Warsaw 1982
6. Furmanek S., Kraszewski Z.: *Reliability of rolling bearings* (in Polish). Wydawnictwa Przemysłowe WEMA, Warsaw 1989
7. Gębura A., Falkowski P., Kowalczyk A.: *Airborne generators as diagnostic sensors of a power transmission system, 5-th International Conference Aircraft and Helicopters Diagnostic AIRDIAG'97*, Warsaw 1997
8. Gębura A.: *Relations between generator output voltage frequency modulation and selected defects of the power transmission system* (in Polish).. [in:] “Aircraft turbine engines in problem approach”; edited by M. Orkisz, Polskie Naukowo-Techniczne Towarzystwo Eksploatacyjne, Lublin 2000
9. Gębura A.: *Skews of splined connections vs. generator frequency modulation* (in Polish). *Zagadnienia Eksploatacji Maszyn*, vol. 4/99(120)
10. Gębura A.: *Diagnostic of aircraft power transmission track based on the analysis of generator's frequency*, *Journal of Technical Physics*, No. 1/2002
11. Gębura A., Radoń T., Tokarski T.: *Diagnosing power transmission systems based on the observation of generator output voltage frequency changes* (in Polish). II International Scientific and Technical Conference “Expo-Diesel & Gas Turbine'01”, Gdańsk-Międzyzdroje-Kopenhaga 2001
12. Gębura A.: *Pulsations of the deck DC generator output voltage as a source of diagnostic information about the state of the power transmission* (in Polish). *Zagadnienia Eksploatacji Maszyn*, vol. 1 (133) 2003
13. Gębura A.: *Possibilities of FAM-C method in diagnosing ship power plants*, *Polish Maritime Research*, No. 2 (36), Vol. 10, 2003
14. Bently-Nevada Application Notes *Machinery Protection and Diagnostic Topics*, B-N, Minden, Nevada USA
15. Harris C. M., Crede C. E.: *Shock and vibration handbook*, Self excited vibration, New York, McGraw-Hill 1976
16. Krzemiński, H.: *Rolling bearings* (in Polish). PWN, Warsaw 1985
17. Moczulski W.: *Method of vibroacoustic examination of rotating machines in start-up or shutdown conditions* (in Polish). PhD. thesis, Silesian University of Technology, Gliwice 1984
18. Andrejewicz J.: *Chaos and synchronisation in physical systems* (in Polish), Monographs, Łódź 1995.

CONTACT WITH THE AUTHOR

Andrzej Gębura, Ph. D.
Air Force Institute of Technology,
Księcia Bolesława 6,
01-494 Warsaw, POLAND
P.O. box 96
e-mail: andrzej.gebura@itwl.pl

Problems of the starting and operating of hydraulic components and systems in low ambient temperature

Part II

Determining the clearance between cooperating elements during the hydraulic components start-up in extremely low ambient temperatures on the grounds of experimental research

Ryszard Jasiński, Ph. D.
Gdansk University of Technology

ABSTRACT



Severe winters and sweltering summers which more and more often occur nowadays are the reason why machinery designers face many difficulties when designing devices which will be serviceable in extreme ambient conditions. Hence, defining the principles and conditions of safe operation of hydraulically driven machines and devices is essential for their designers and operators. For this reasons the author did a series of tests of hydraulic component and systems in thermal shock conditions (cooled-down components were supplied with hot working medium). The experimental tests were carried out in the laboratory of the Chair of Hydraulics and Pneumatics, Gdańsk University of Technology. They gave answer to the question how the effective clearance changes in such conditions and what parameters it depends on. Based on temperature graphs acquired from tests of heating up elements of hydraulic components it is possible to determine precisely change of clearance between cooperating elements.

Keywords: hydraulic machines, hydraulic drives, diagnostics, hydraulic systems

INTRODUCTION

During the hydraulic components start-up in thermal shock conditions [1-9, 12-13] dynamic change of component's elements dimensions due to thermal expansion is often encountered. Changes in the element's clearings result in changes in the effective clearing between cooperating elements. Change of clearance is influenced, inter alia, by the temperature difference between hot oil and cold hydraulic unit, flow of working fluid, construction of the component, kind of material used and shape of component's elements.

Between the hydraulic component's cooperating elements small clearances appear, measuring from few up to dozens μm . Experimental research of various hydraulic components operating in low ambient temperatures undertaken by the author, allows to answer the question how the effective clearance changes in such conditions and what parameters does it depend on. The research included three groups of hydraulic components' systems: supply system, control system and executive system. Fig. 1 presents the block diagram of typical hydraulic system exposed to sub-zero ambient temperatures. Main component of the supply system is the hydraulic pump, in the control system – valves and directional spool valve while in the executive system – hydraulic actuator (motor or cylinder).

Using own methodology [1-8], the Author has tested many components and entire hydraulic system in thermal shock conditions. Tested components were placed in the low temperatures chamber in which -35°C temperature was reached. The components were supplied with the hot Total Azolla 46 mineral oil in the temperature ranging from 20°C to 55°C . In the fixed and moving elements of components temperature sensors were placed, mainly thermocouples. The temperature, pressure and flow volume in the inlet and outlet channels of the components were also measured.

HYDRAULIC PUMPS RESEARCH

The object of the research were pumps of following various types: multi-piston axial pump of constant output with camshaft, multi-piston axial pump of variable output and two geared pumps.

Researched camshaft pump of PWK 27 type (Fig. 2) of unit capacity $27.5 \text{ cm}^3/\text{rev.}$, operates at nominal pressure of 45 MPa, nominal speed of 1500 rpm and maximum 3000 rpm [19, 23, 24]. The pump is characterized by high pressure-mechanical efficiency reaching $98 \div 99 \%$, as well as by high overall efficiency at the level of $92 \div 94 \%$ [11].

Variable output multi-piston axial pump of PVM016R1D type (Fig. 3) is the smallest in the PVplus product line [21] and

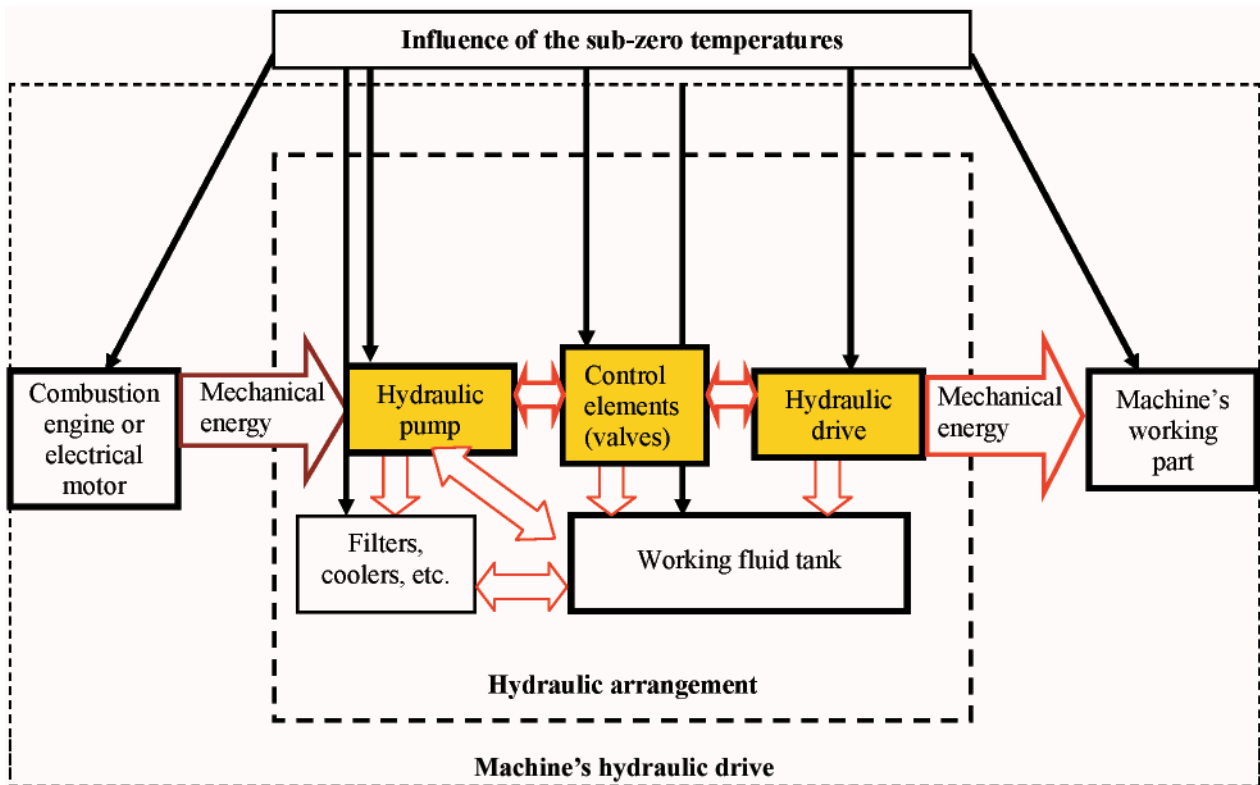


Fig. 1. Block diagram of machine's hydraulic drive with indication of the sub-zero temperatures influence on the operation of the component's systems

its characteristic parameters include: design output 16 cm³/rev., nominal pressure 28 MPa, max. pressure 35 MPa and rotation speed range between 300 and 3000 rpm.



Fig. 2. Camshaft multi-piston pumps PWK-27 and PWK-78 from Hydrotor company [10, 11, 19]

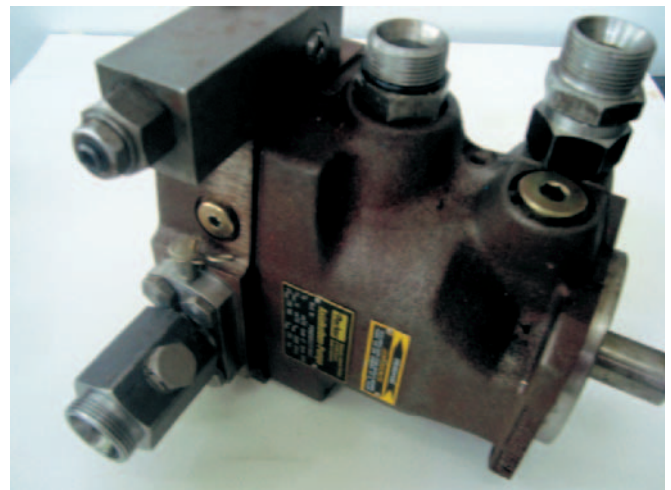


Fig. 3. Past-plate axial pump from Parker [21] company

The arrangement consisting of PZ2-K-10 gear motor (Fig. 4) driving the PZ2-K-6.3 gear pump was tested.

Determining the changes of effective clearance between cooperating elements of multi-piston pump in thermal shock conditions.

In multi-piston radial and axial pumps or motors there are several places where loss of clearance between cooperating elements may occur. One of them is the effective clearance (l_e) between pistons moving in the cylinder block holes (Fig. 5). Change of clearance may be determined during start-up (τ) according to formula:

$$l_e(\tau) = l_m + \Delta l_p(\tau) - \Delta l_t(\tau) \quad (1)$$



Fig. 4. Geared pump PZ2-K10 from Hydrotor company [19]

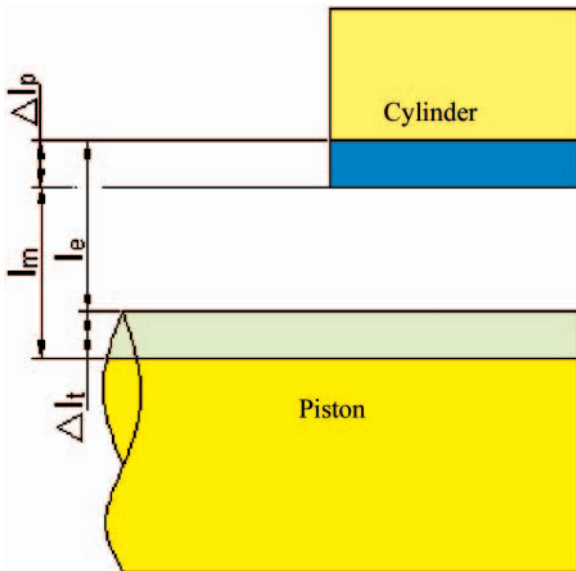


Fig. 5. Graphical interpretation of changes in the effective clearance

It describes the changes of clearance height: caused by pressure – related deformation of cylinder block and piston Δl_p and by thermal expansion of both elements Δl_t .

Change of clearance height by the Δl_t value due to difference in linear thermal expansion of cooperating pump's (motor's) elements, in the effect of non-homogenous heating during start-up in thermal shock conditions may be described by the formula:

$$\Delta l_t(\tau) = h_T \cdot \beta_T \cdot [T_T(\tau) - T_0] + h_B \cdot \beta_B \cdot [T_B(\tau) - T_0] \quad (2)$$

where:

β_T, β_B – linear thermal expansion coefficient's of piston (T) and cylinder block (B)

$T_T(\tau)$ – piston temperature

$T_B(\tau)$ – cylinder block temperature

T_0 – measuring temperature of part's linear dimensions

h_T, h_B – linear diameter dimension of: piston (T) and distribution bush openings (B).

PREPARING THE PWK27 PUMP FOR MEASURING THE CHANGE OF ELEMENTS' TEMPERATURE

In the tested pump PWK (Fig. 2), built of two groups of elements: fixed (Fig. 6) and mobile (Fig. 7) the thermocouples were placed.

Mobile elements of the pump include: piston, screw throttle, hydrostatic slipper, distribution bush, resistance shield, clamping ring, separator, shaft, cam.

Fixed components of the pump include: cover, front housing, cylinder block, cylinder block cover, rear housing, guiding bush, socket.

Constant of temperature measurements allowed determination of the clearance between cooperating elements (pistons and cylinder bushes) of the pump during start-up in thermal shock conditions.

For the sake of researching the process of piston and slipper heating, they were purposely made with bores for fixing thermocouples. (Fig. 7, 8). Thermocouple leads placed in the slipper and piston were lead through purposefully made bores in the separator and cylinder block (Fig. 9).

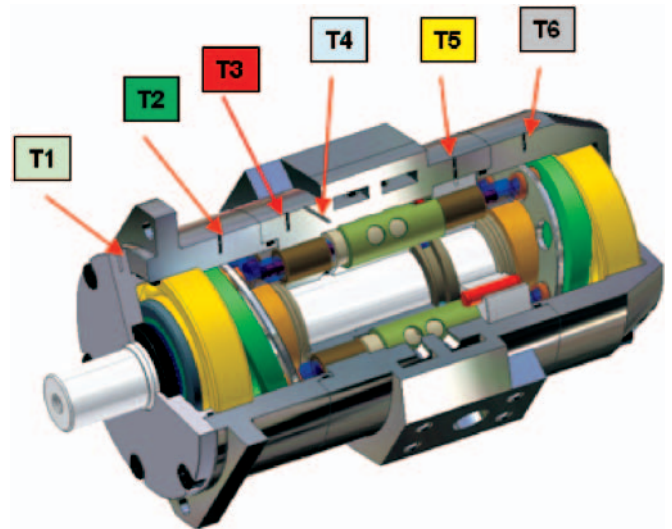


Fig. 6. Distribution of thermocouples (T1-T6) in the holes bored in PWK27 pump's fixed elements: T1 – cover, T2 – front housing, T3 – cylinder block – area no. 1, T4 – cylinder block – area no. 2, T5 – cylinder block cover, T6 – rear housing

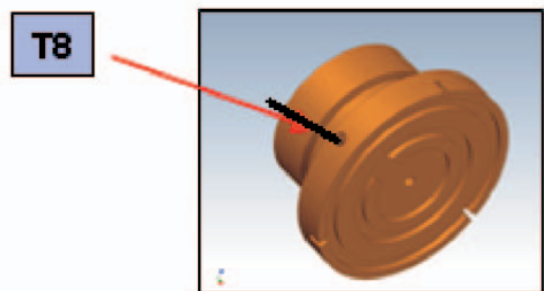
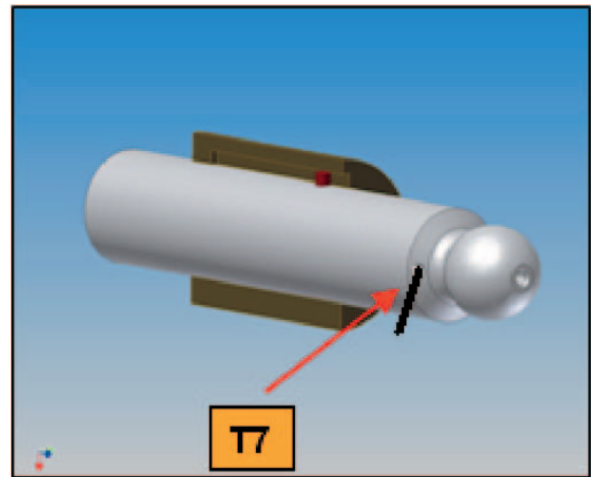


Fig. 7. Thermocouples in PWK27 pump's mobile parts: a) piston, b) hydrostatic foot



Fig. 8. Piston unit adapted to measuring the heating process

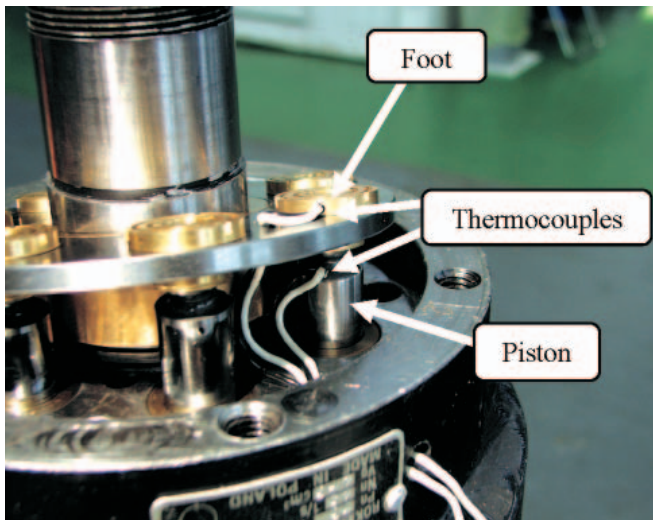


Fig. 9. Connection of thermocouples leads to the piston and hydrostatic foot in researched PWK27 pump

RESEARCH OF PWK27 PUMP IN THERMAL SHOCK CONDITIONS

Experimental research of PWK27 pump operation during start-up in thermal shock conditions were executed according to methodology [1] designated for the following start-up conditions:

- ★ oil temperature: $\sim +48^{\circ}\text{C}$
- ★ ambient temperature: $-21 \div +23^{\circ}\text{C}$
- ★ pump's shaft rotation speed: $500 \div 2500 \text{ rpm}$
- ★ pump's load: $4.5 \div 12 \text{ MPa}$.

Several measurement series of PWK27 pump start-up in thermal shock conditions were run. The results include, inter alia, characteristics of temperature change of: heating fixed elements, temperature of incoming and outgoing oil, temperature of leakages and characteristics of torque, oil pressure on the outlet, output, external leakage volume, rotation speed of the shaft, volumetric, torque and overall efficiency.

One start-up test of PWK27 pump was conducted for the following parameters: outlet pressure 9.15 MPa, output $30 \text{ dm}^3/\text{min}$, pump's shaft rotation speed 1100 rpm, oil temperature 49°C , ambient temperature -12°C .

On the grounds of recorded temperature graphs (Fig. 10) it is possible to determine that the fastest heating element in the pump is the cylinder block unit consisting of cylinder block and its cover.

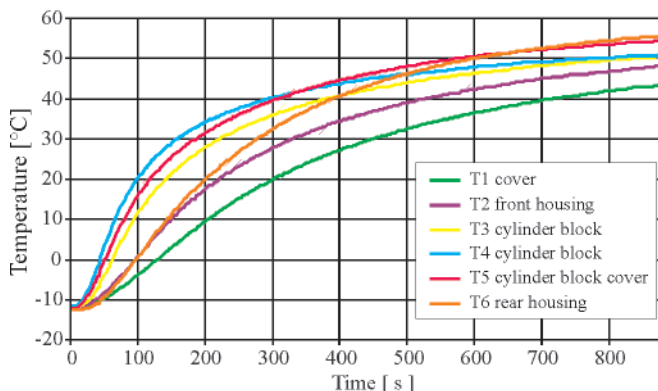


Fig. 10. Temperatures in pump's fixed parts (Fig. 6)

The fastest temperature build-up in the cylinder block occurs near the pump's internal canals that carry the main stream of hot oil and near the pump's camshaft (thermocouple measurement no. 4). Almost as quickly the temperature rises in the common areas of piston and guiding bush (thermocouple no. 5). Much slower however the temperature rises in front (thermocouple no. 2) and rear housing (thermocouple no. 6). In the first 200 seconds of pump's operation temperature graphs of the two are identical, only after that the rear housing begins to heat much quicker. It is this element that reaches the highest temperature of all the pump's fixed elements under set conditions of operation. Whereas the slowest heating up element is the pump's cover (thermocouple no. 1).

It is worth considering that some of PWK pump's fixed same elements (Fig. 10) while operating under constant pressure reach higher temperatures than this of the hot oil feeding the pump. This is exemplified by the comparison of characteristics on Fig. 11 with those on Fig. 10. It is the effect of friction heat generation in the stream of fluid flowing through pump's crankcase and mixed by the resistance shields of feet and pistons.

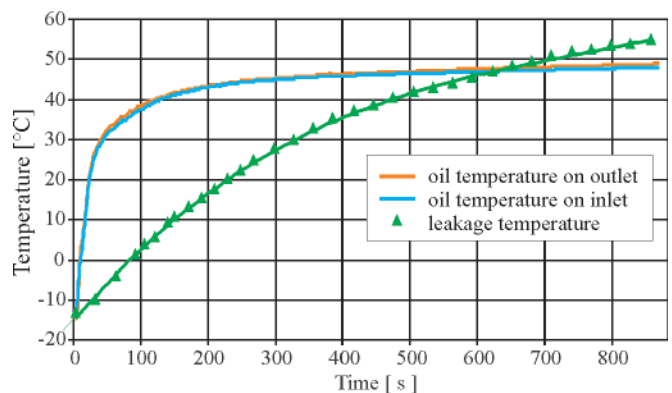


Fig. 11. Oil temperatures: on pump's inlet, on pump's outlet and external flows

In the initial period of pump's operation the temperature of leaking oil rises far slower than the temperature of main working stream on the inlet and outlet (Fig. 11). However, after some time the temperature of leakage reaches much higher temperature than the feeding stream temperature.

During tests PWK27 pump reached very high volumetric efficiency at least 0.98 (Fig. 12).

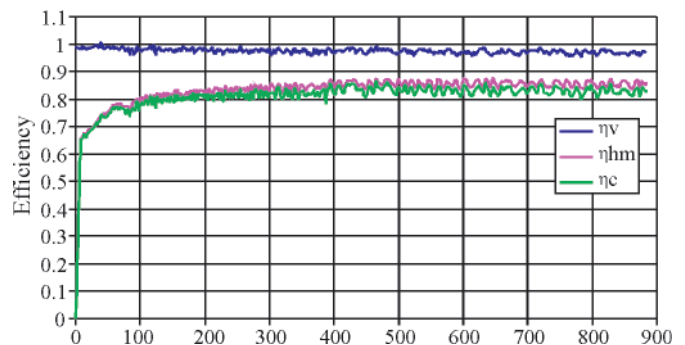


Fig. 12. Overall (η_o), volumetric (η_v) and torque (η_{tm}) efficiency for the following parameters: working pressure 9.15 MPa, output $30 \text{ dm}^3/\text{min}$, ambient temperature -12°C , oil temperature 49°C

Torque efficiency remains at the level of 0.85. It largely depends on pump's load that in the considered situation only amounted to 9 MPa. The higher is the working pressure of the pump, the higher its torque efficiency, and in the same time the lower its volumetric efficiency.

DETERMINING THE EFFECTIVE CLEARANCE BETWEEN THE PISTON AND CYLINDER OF THE PWK 27 PUMP

On the grounds of analysis of several heating cycles of the piston achieved in few series of tests it was determined that the rate of piston heating is always lower or equal to the speed of the hydrostatic slipper heating. Fig. 13 presents the heating processes of the piston and the cylinder block cover.

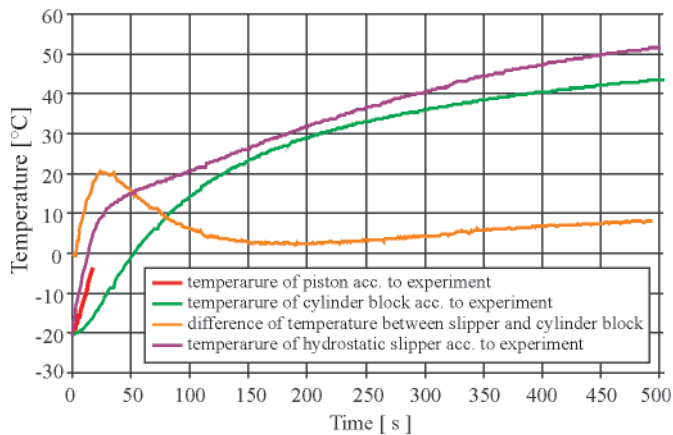


Fig. 13. Changes in temperature of piston hydrostatic slipper and cylinder block and difference of temperatures between piston and cylinder block for start-up parameters: ambient temperature -20°C , oil temperature 48°C , rotation speed 1100 rpm, pressure above piston 5.2 MPa

Changes of temperature result in changes of radial clearance shown in Fig. 14 for pump cooled to -20°C supplied with hot oil $+48^{\circ}\text{C}$ at shaft rotation speed 1100 rpm.

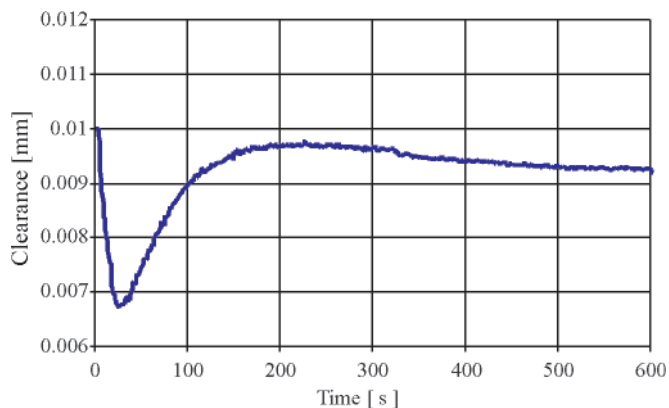


Fig. 14. Change of clearance between the piston and distribution bush for the parameters of pump's operation after start-up: ambient temperature -20°C , oil temperature 48°C , rotation speed 1100 rpm, pushing pressure 5.2 MPa

The most significant reduction of clearance occurred after ca. 30 seconds after pump's start-up (Fig. 14). It is this period when the biggest difference in temperatures occur between the temperature of the piston and distribution bush. Further on, during start-up the temperatures of cooperating elements become even resulting in increase of radial clearance to desired value.

RESEARCH OF THE GEAR PUMP PZ2-K10 OPERATING AS MOTOR

In the pump or gear motor the reduction of radial clearance between teeth points and internal surface of the housing may occur.

The lack of axial clearance however will not occur because the pump includes mobile elements providing compensation for axial clearances. Also the jamming of bearing's casing made of steel in the housing made of aluminium will not occur. Based on geometric measurements it was determined that the radial assembly clearance in the tested pump PZ2-K10 (Fig. 15) amounts to 0.087 mm in the ambient temperature of 20°C .

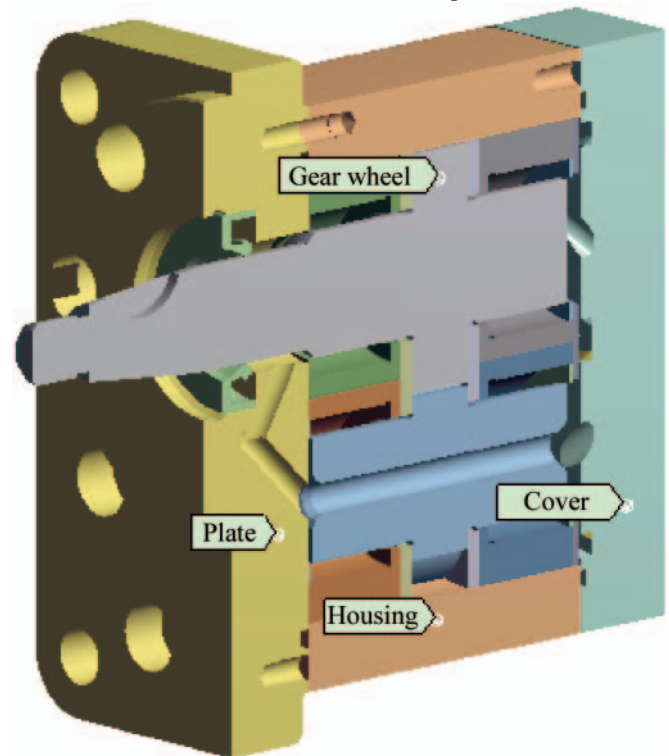


Fig. 15. Places of temperature measurement in gear pump PZ2-K10 elements: plate, cover, gear wheel, housing

According to the equation 1 the effective clearance not only depends on assembly clearance but also on deformation of elements due to influence of pressure and different thermal expansion on cooperating elements. The higher the oil pressure, the bigger is the slack of gear shaft and its displacement inside the bearing. This in turn affects the dimensions of gaps between cooperating elements. It has been assessed that at the maximum operating pressure of the tested pump the displacement of gear shaft in the bearing and its slack may reach $21\ \mu\text{m}$ [17, 19]. This would cause the decrease in dimension of gap between gear teeth tips and hole in the housing on the suction space side.

The change in element's dimensions due to difference in thermal expansion of gear pump elements with housing made of aluminium alloy in thermal shock conditions is described by the following equation:

$$\Delta l_i(\tau) = 11 \cdot 10^{-6} \cdot h_z \cdot [T_z(\tau) - 293] + 22.3 \cdot 10^{-6} \cdot h_k \cdot [T_k(\tau) - 293] \quad [m] \quad (3)$$

where:

- h_z, h_k – linear dimensions: tip diameter of gear tooth (Z) and housing opening diameter (K) [m]
- $T_z(\tau), T_k(\tau)$ – temperature of gear wheel and housing in the process of heating up [K]
- 293 – temperature of linear measurement of components [K].

Since the linear thermal expansion coefficient for aluminium alloy is almost twice that of steel when lowering the ambient temperature the initial clearance will also decrease. (Fig. 16).

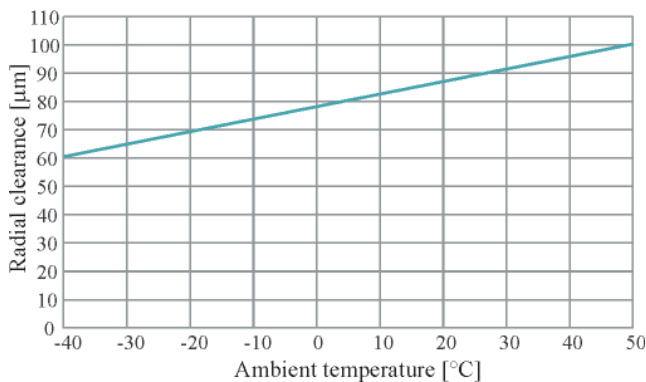


Fig. 16. Initial radial clearance in PZ2-K10 gear pump (motor) depending on ambient temperature

Based on experimental research, the courses of temperature changes in housing and gear wheel of PZ2-K10 pump (operating as motor) were determined for the flow volume in the range of: from 4.5 dm³/min to 14 dm³/min and motor's load: from 0.5 Nm to 17 Nm.

One of the tests was conducted for the following parameters: oil temperature 48°C, ambient temperature -16.8°C, working pressure 5 MPa, pumps rotation speed 1020 rpm.

It is to be noticed, that the gear wheel heated up quicker than the housing. Maximum difference in temperatures between heating elements of the unit reached 12°C in the 80th second after pump's start-up (Fig. 17).

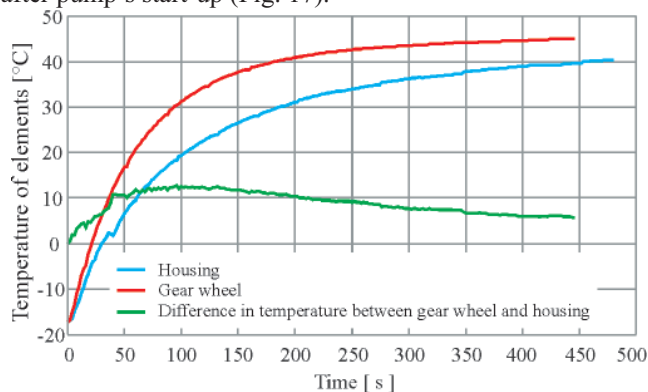


Fig. 17. Temperature of housing, gear wheel and difference in temperatures between those elements of PZ2-K10 pump operating as motor.

Based on temperature changes graph acc. to Fig. 17 it is clear that during gear pump start-up the rapid decrease of radial clearance between teeth tips and internal surface of housing does not occur (Fig. 18). In case of hydraulic components made of aluminium alloys (housing) and steel (wheel) the disappearance of radial clearance doesn't occur.

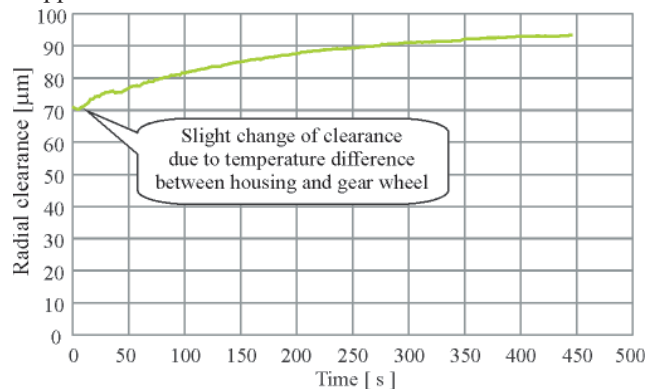


Fig. 18. Change of effective clearance between tips of teeth and internal housing of PZ2-K10 pump operating as motor, during start-up under following conditions: oil temperature 48°C, ambient temperature -16.8°C, working pressure 5 MPa

In case of pumps and gear motors with housings made of cast iron the changes of clearance will look differently than on Fig. 18. Such components will be susceptible to thermal shock conditions.

RESEARCH OF INADEQUATE OPERATION OF DIRECTIONAL SPOOL VALVES IN THERMAL SHOCK CONDITIONS

When in a hydraulic circuit a sudden case of hot oil flowing through cold valve (thermal shock conditions) occurs the uneven heating of cooperating elements of spool and casing will follow. The spool is much smaller than the casing, therefore it's thermal capacity is far smaller. In comparison to the casing it has relatively large surface flushed by passing oil. Therefore it will heat up much faster. With rising temperature of the spool its dimension increase faster against the opening in the casing leading to the decrease of the clearance. The clearances are already quite small in order to minimize leakages. Too small clearances between the spool and casing may result in substantial friction forces hindering or even preventing their movement against each other. Depending on the construction of the component and its maker the clearances between the spool and casing fit in the range of 5 - 25 μm [18].

Effective clearance (l_e) between casing and spool (Fig. 19, 20) depends on assembly clearance (l_m), elastic distortions of spool valve's elements due to pressure (Δl_p), difference in thermal expansion of various components (Δl_t).

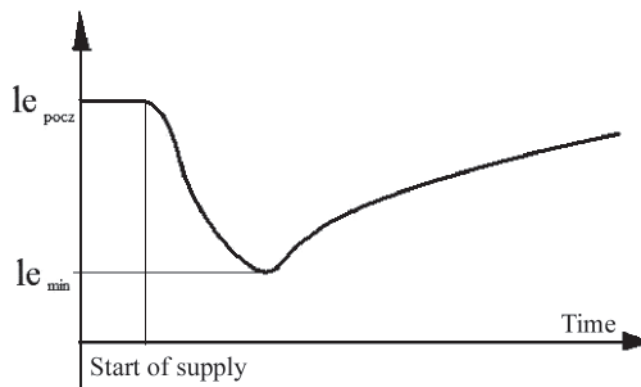


Fig. 19. Change of effective clearance between spool and casing of cooled spool valve fed with hot oil during start-up

In thermal shock conditions the operation of the spool valve is seriously affected by the thermal expansion characteristic of materials used for making specific elements of the spool valve. Spools of hydraulic spool valves are made of steel while their casings are usually of cast iron. The linear expansion coefficient for cast iron equals $10.5 \cdot 10^{-6}$ 1/K, while for steel it is $11 \cdot 10^{-6}$ 1/K [14, 15].

Taking under account the influence of thermal expansion coefficients the effective clearance may be calculated from the relation of (1) and (2).

Based on numerical calculations it was assessed that the influence of pressure on effective clearance is of lesser importance that the influence of substantial disproportion in temperature of cooperating elements (spool and casing). The confirmation of the fact is found through the calculations of the difference in thermal expansion Δl_t and distortions resulting from the influence of pressure Δl_p performed for the spool valve RE2510/101 from Hydrotor (Fig. 21), where the spool diameter measured 18 mm. With the spool and casing temperature at $\Delta T = 20^\circ\text{C}$ the assembly clearance will decrease by $\Delta l_t = 3.9 \mu\text{m}$,

for the temperature difference $\Delta T = 45^\circ\text{C}$ it will decrease by $\Delta l_t = 8.7\mu\text{m}$. The influence of oil pressure (16 MPa) on components of the spool valve will only cause the assembly clearance to change by $\Delta l_p = 1.5\mu\text{m}$.

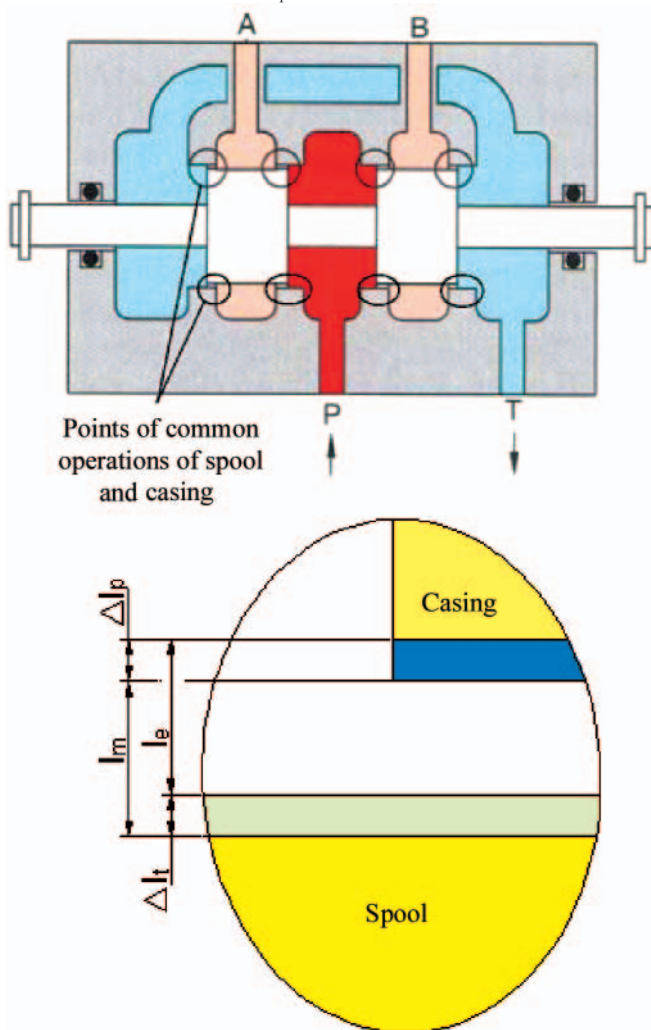


Fig. 20. Points of common operation of spool and casing and graphical interpretation of change of effective clearance

SPOOL VALVES TESTED IN LOW AMBIENT TEMPERATURES

In the lab of the Chair of Hydraulics and Pneumatics Gdańsk University of Technology following valves for control the pressure and flow direction were tested in thermal shock conditions [5, 6]:

- ✦ relief valve type UZPP16 from PONAR WADOWICE company
- ✦ relief valve type DBW 20 A2-5X/350YS6EG24N9K4R12 from REXRÖTH company
- ✦ dual stage spool valve 4WEH16C33/6AW220-50 from REXROTH company
- ✦ electro hydraulically controlled spool valve RE2510/101 from HYDROTOR company (Fig. 21)
- ✦ proportional spool valve PVG 32 from SAUER DANFOSS company (Fig. 22)
- ✦ servovalve 4WS2EM10 - 45/20B2T315Z8EM from REXROTH company (Fig. 23).

Hydraulic units are often fitted with electro-hydraulically controlled spool valve. Therefore many constructions of electrically controlled hydraulic valves were tested.

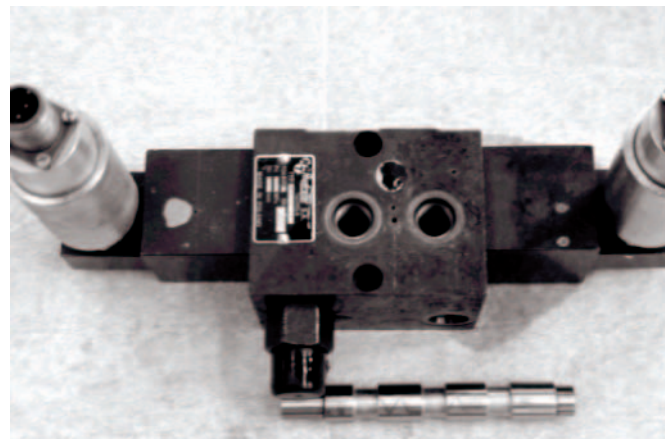


Fig. 21. Electro-hydraulic spool valve RE2510/101 [19]

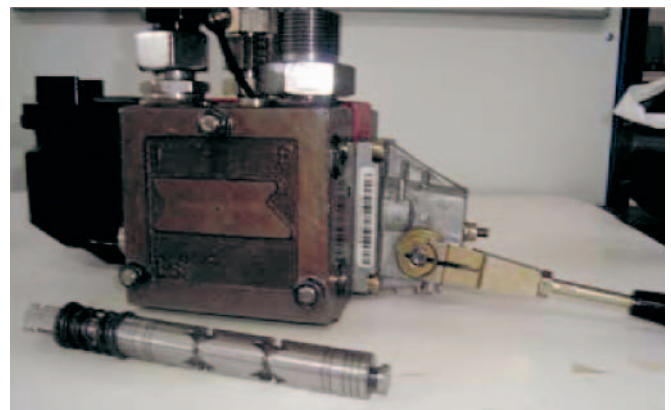


Fig. 22. Proportional spool valve PVG 32 [22]



Fig. 23. Servovalve 4WS2EM10 - 45/20B2T315Z8EM [18]

Tested sliding spool valve belong to two groups depending on their function:

- I – spool valve used for controlling the flow direction - classical (Fig. 21, 24)
- II – proportional spool valve and servovalves additionally used to control the volume of flow (Fig. 22, 23, 25, 26).

Nominal diameters of spools in case of PVG 32 and RE2510/101 spool valve amounted to 18 mm. Initial clearance between spool and casing in PVG 32 spool valve amounted $7\mu\text{m}$, while in RE2510/101 spool valve it was $6\mu\text{m}$ (measurements performed at Metrology Lab of Gdańsk University of Technology).

In the body of RE2510/101 spool valve (Fig. 24) bores were made for placing thermocouples. Bores for thermocouples T7 and T8 are placed in axis but on different depths, near the source of flowing oil while the bore for thermocouple T3 is

away from the hot oil channel. In order to test the spool two bores were made to accommodate thermocouples. The bores were made in axis however to different depths. One of the bores was located near the place where cylindrical surface of the spool was flushed with hot oil. The other was located at the spool's front.

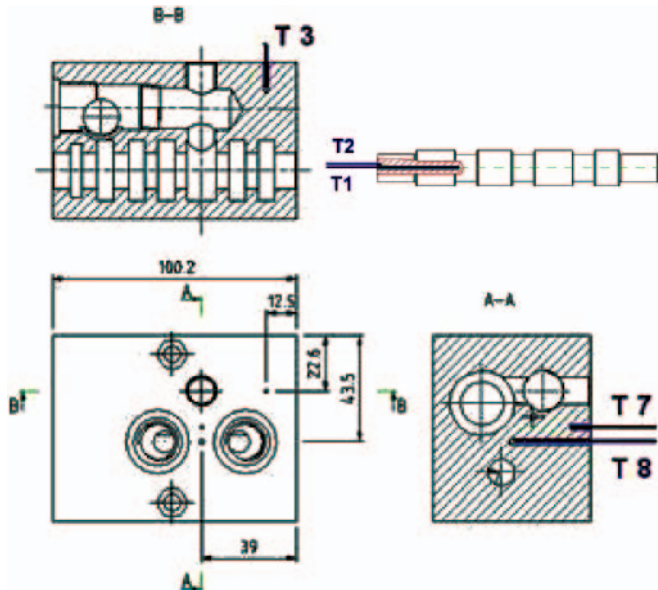


Fig. 24. Spool valve RE2510/101 from Hydrotor company T1, T2 – thermocouples placed in spool T3, T7, T8 – thermocouples placed in casing

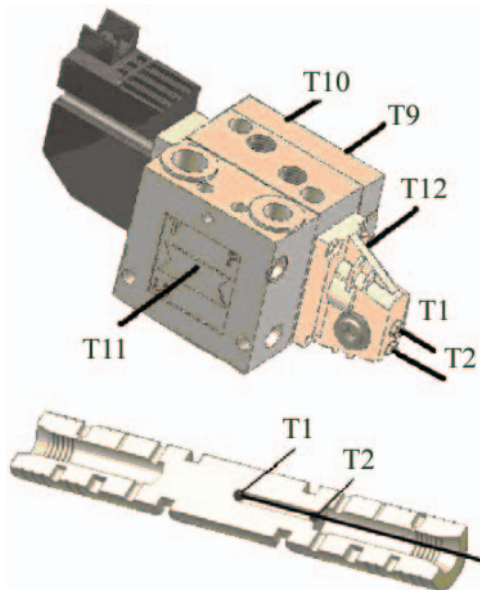


Fig. 25. Spool valve PVG 32 from Sauer Danfoss. T1, T2- thermocouples located in the spool T9, T10, T11, T12 thermocouples located in the fixed elements of the spool valve

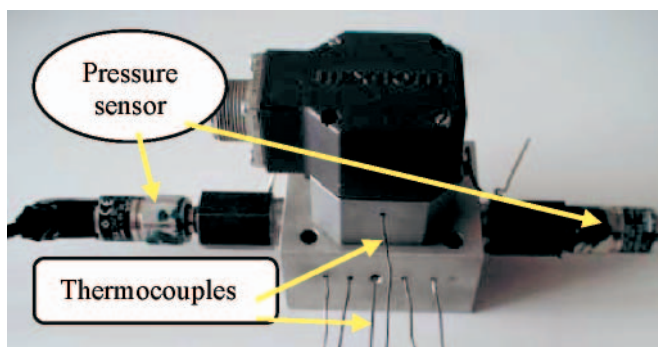


Fig. 26. Servovalve 4WS2EM10 - 45/20 from Rexroth with temperature (thermocouples) and pressure sensors

For the purpose of measuring the heating up of PVG 32 spool valve the bores were made in spool and casing in which thermocouples were inserted. Their layout is presented on Fig. 25. In the spool a bore was made reaching half of its length. T1 thermocouple was inserted into the full depth of the bore while the T2 was placed in its beginning. T9, T10, T11 and T12 thermocouples were placed in fixed elements of the spool valve.

The diameter of the researched servovalve 4WS2EM10 is 6,495 mm, while the clearance between the spool and cylindrical bush in the casing is 5 μm .

In the fixed elements of 4WS2EM10 - 45/20 servovalve 11 thermocouples were placed (Fig. 26), allowing for presentation of heating processes for various states of supply. Through pressure indication, the pressure sensors (Fig. 26) enabled the determination of reaction time to the control signal and change of this time with changing ambient temperature.

SAMPLE RESULTS OF TESTING PVG 32 SPOOL VALVE

Several tests series of PVG 32 spool valve were conducted for the temperature differences between hot oil and cooled unit kept in the range of $\Delta T = 20 \div 75 \text{ K}$.

One test of the spool valve cooled to 0°C was conducted at abrupt changes of flowing oil pressure from zero to 32 dm³/min at temperature 52°C. The difference in temperature between the spool and casing was determined (Fig. 27). Maximum difference in temperature between the body and the spool during heating reaches 27.9°C and occurs in the 30th second. In this time the temperature of casing is 13.8°C and spool's 41.7°C.

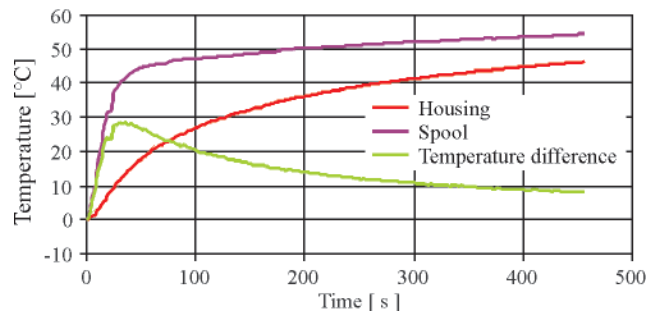


Fig. 27. Average temperatures of casing and spool and the difference in temperatures between the two during feeding: oil temperature 52°C, ambient temperature 0°C, flow volume 32 dm³/min

Using the formula (1) under assumption that the distortion of the spool and the casing due to pressure are negligible, the effective clearance between the components was determined (Fig. 28).

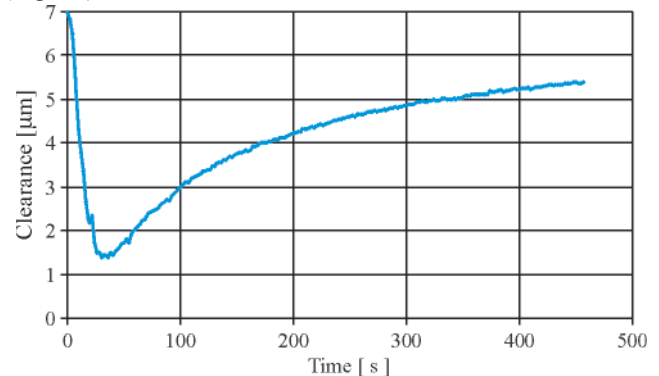


Fig. 28. Effective clearance between external surface of the spool and internal surface of the casing during feeding: oil temperature 52°C, ambient temperature 0°C, flow volume 32 dm³/min

Based on the effective clearance graph (Fig. 28) it is possible to determine that the disappearance of clearance between spool and casing due to difference in thermal expansion between the two will not occur.

RESEARCH OF THE LOW SPEED HYDRAULIC MOTORS

The first part of the article [8] deals with symptoms of correct and incorrect operation of hydraulic motors in thermal shock conditions based on pressure and turning speed. The results of tests of satellite hydraulic motor were presented.

Also low speed orbital hydraulic motors without axial clearance compensation were tested in low ambient temperatures. Such motors are commonly used in driving arrangements of machines.

Researched satellite motor SOK 100 from ZUO Hydroster [20] (Fig. 30) of geometric working capacity $0.4 \text{ dm}^3/\text{rev}$. may operate at the range of speed from 0 to 160 rpm ($n_{\text{max}} = 250 \text{ rpm}$) and nominal pressure $p_n = 16 \text{ MPa}$ ($p_{\text{max}} = 25 \text{ [MPa]}$). Assembly axial clearance was $23 \text{ }\mu\text{m}$.

Orbital motor GMR 160 from Rexroth (Fig. 33) [18] of geometric working capacity $162.9 \text{ cm}^3/\text{rev}$ according to its maker is characterized by nominal speed of 375 rpm ($n_{\text{max}} = 470 \text{ rpm}$), nominal pressure $p_n = 12 \text{ MPa}$ and max. pressure $p_{\text{max}} = 22.5 \text{ MPa}$.

TF170MW260 motor from Parker company[21] of geometric working capacity $169 \text{ cm}^3/\text{rev}$ according to its maker may be operated continuously up to the nominal speed of 355 rpm and nominal difference in pressure (between in and outtake) 13.8 MPa, and momentarily at $n_{\text{max}} = 440 \text{ rpm}$ and max. pressure difference 20.7 MPa. The maximum supply pressure may reach 30 MPa.

PREPARATION AND SAMPLE RESULTS OF TESTING THE SOK 100 MOTOR (FIG. 29) CONDUCTED IN THERMAL SHOCK CONDITIONS

The motor was made to specific order at ZUO HYDROSTER in Gdańsk. In the fixed elements specials bores for thermoelectric sensors were made for measuring temperature in front and rear covers and the housing. Following that, the motor was assembled with semiconductor temperature sensors (AD590) placed in mobile elements (two sensors in the rotor and one in the shaft).

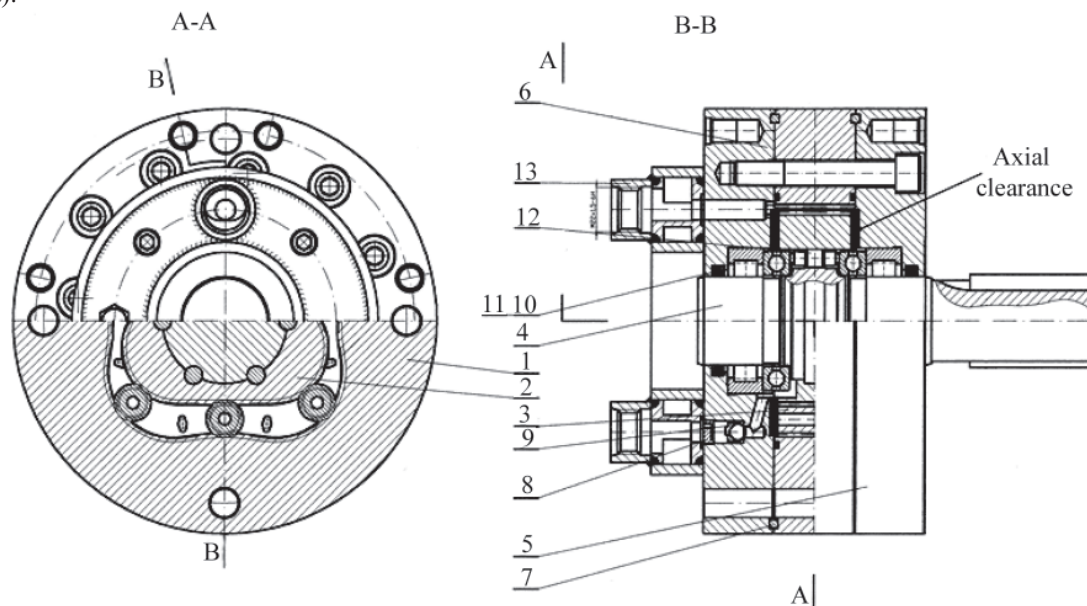


Fig. 29. Motor SOK: 1 – housing; 2 – rotor; 3 – satellite; 4 – shaft; 5, 6 – covers; 7 – setting ring; 8, 9 – non-return valve; 10, 11 – rings; 12 – pin; 13 – manifold

One test of SOK 100 when the motor operated incorrectly was conducted for the following conditions: flow volume $100 \text{ dm}^3/\text{min}$, initial temperature -20°C , oil temperature 50°C .

Start-up of motor in this conditions caused substantial rise of temperature in mobile elements of the motor. The satellites heated quicker than the rotor. Fig. 30 presents the graphs of temperature in rotor and housing. The substantial rise in rotor's temperature is clearly visible (Fig. 30). This, in turn results in great difference in temperatures of the rotor and housing leading to disappearance of clearance between the two (Fig. 31). Substantial rise in temperature caused the dry friction between the elements.

In result the friction heat appeared directly effecting elements of the motor. In turn satellites and rotor heated up quicker.

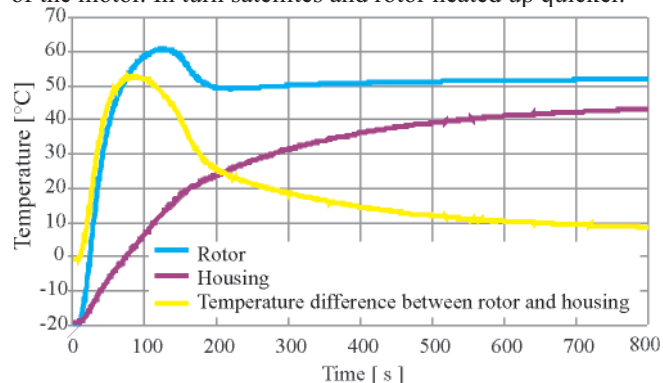


Fig. 30. Temperature of rotor and housing with difference in temperatures between the two in SOK 100 against timeline

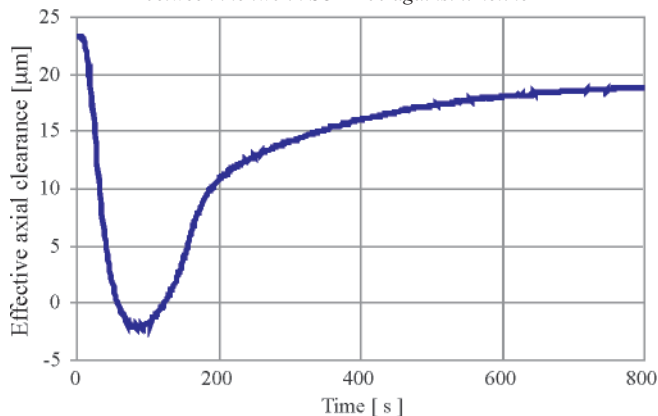


Fig. 31. Change of effective clearance between the covers and rotor of SOK 100 during start-up in thermal shock conditions

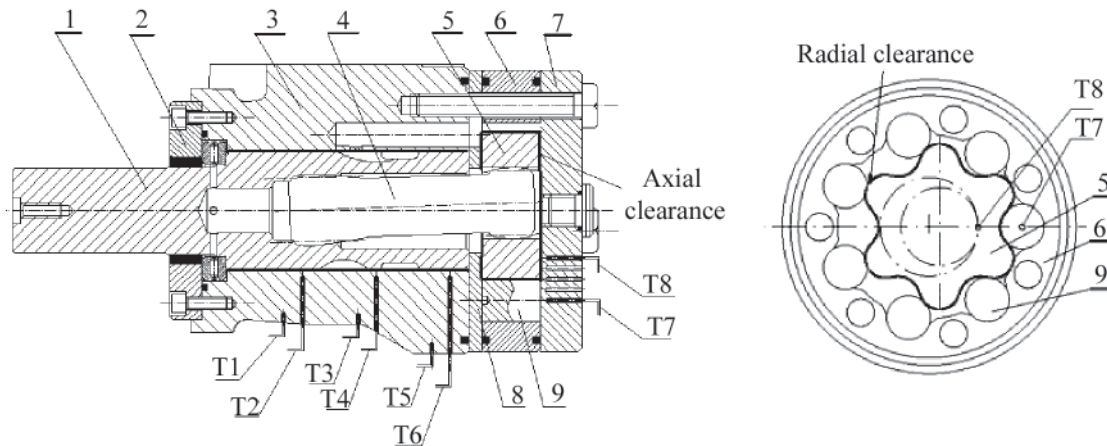


Fig. 32. Orbital motor GMR 160 with temperature sensors: 1 – shafting, 2 – front cover, 3 – housing, 4 – geared shaft, 5 – rotor, 6 – body, 7 – rear cover, 8 – distribution disc, 9 – roller (markings T1 ÷ T8 indicate place of temperature measuring using thermocouples of the same marks)

PREPARATION OF ORBITAL MOTORS FOR TESTING IN THERMAL SHOCK CONDITIONS

The orbital GMR 160 motor (Fig. 32) includes construction nodes susceptible to disappearance of clearance in thermal shock conditions.

The nodes are as follows:

- axial gaps between surfaces of rotor, cover and distribution disc
- gaps between perimeter surfaces of rotor's and housing's gear
- gaps between external surface of camshaft and internal surface of housing.

In order to assess specific elements of GMR 160 motor in various places 8 temperature sensors (thermocouples) were placed. In the rear cover thermocouples T7 and T8 were placed. Six thermocouples were inserted into the bores in the housing - thermocouples T1, T3, T5 (away from the heat source) and T2, T4, T6 (close to the heat source).

The second orbital motor tested in thermal shock conditions was TF170 (Fig. 33) with frontal distribution.

The motor was prepared for tests by making bores in fixed elements for thermocouples, i.e. in spool valve, housing near the working chamber, housing near the roller, body near the oil channel, body away from the heat source. Sensors were not placed in mobile elements due to complicated kinematics of their operation.

Orbital motors GMR 160 and TF 170 are differentiated by the distribution and the flow of oil through the channels resulting, in turn, in different way of heating up motor's elements.

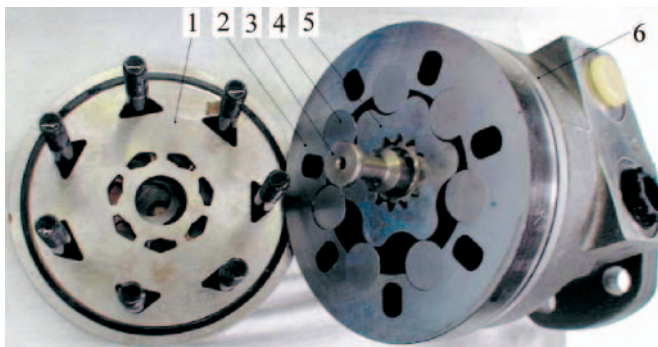


Fig. 33. Orbital motor TF 170: 1 – spool valve, 2 – housing, 3 – geared shaft, 4 – roller, 5 – rotor, 6 – body

INFLUENCE OF ORBITAL MOTORS' CONSTRUCTION ON THEIR OPERATION IN THERMAL SHOCK CONDITIONS

In order to assure proper operation of hydraulic system in thermal shock conditions suitable hydraulic motors, resistant to such conditions have to be used. Such requirements are well met by the tested orbital motor TF 170 from Parker company (Fig. 33, 34). In its housing there are additional channels for flowing oil thus enhancing the surface of heat exchange resulting in quicker heating up of the housing. It was also found out that with such construction (Fig. 35) the maximum difference in temperatures between the housing and rotor didn't exceed 20°C during start – up under thermal shock conditions for the temperature difference ΔT_{ol-ot} of oil and surrounding reaching 77°C.

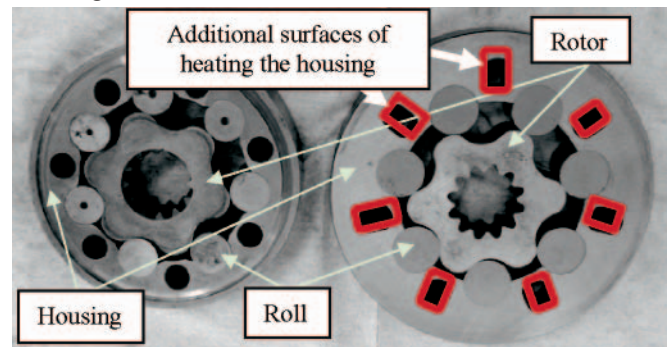


Fig. 34. Components of GMR 160 orbital motor (on the left) and TF 170 (on the right). In the TF 170 motor additional channels for flowing oil are provided

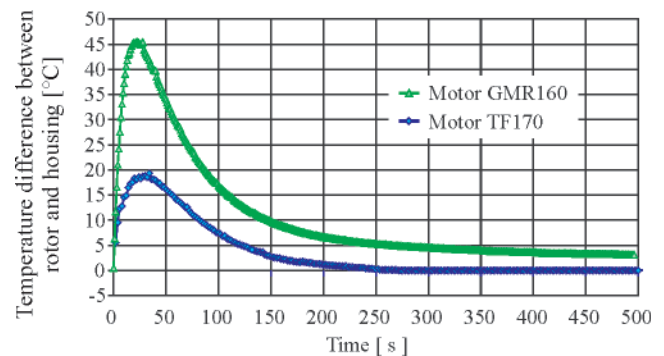


Fig. 35. Difference in temperature between rotor and housing of TF170 motor (volume of flow 64 dm³/min, initial temp. of motor -27°C, oil temp. 50°C) and GMR160 motor (volume of flow 70 dm³/min, initial temp. -26°C, oil temp. 52°C)

Orbital motor GMR 160 (Fig. 32 and 34) provides no additional heat exchange surface from oil to housing. It was also found out (Fig. 35) that the maximum difference in temperatures between the rotor and housing reached 46°C for ΔT_{ol-ot} 78°C.

Having the experimental data as per Fig. 35 and based on the relation (1) change of radial clearance was determined for motors GMR 160 and TF170 (Fig. 36).

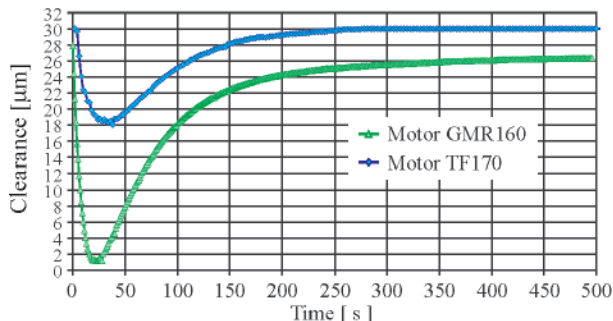


Fig. 36. Graph of radial clearance in TF170 and GMR160 motors (start-up conditions as in case of Fig. 35)

Radial clearance in TF170 motor, between the rotor and housing decreased maximum by 12μm, while in case of GMR160 motor, under similar operating conditions the clearance decreased by 27μm and was close to vanishing completely (Fig. 36).

Thanks to substantial initial clearance the GMR 160 motor proved resistant to thermal shock conditions and operated correctly at temperature difference ΔT_{ol-ot} of oil and surrounding up to 78°C.

In case of TF170 motor from Parker during start-up under thermal shock conditions only slight change of radial clearance between the rotor and housing occurs (Fig. 36). This signifies substantial resistance of such motors during operation under given conditions.

SUMMARY

- The main construction issue decisive for admissible supply parameters of cooled hydraulic components in thermal shock conditions is the effective clearance.
- Based on temperature graphs acquired from tests of heating up elements of hydraulic components it is possible to determine precisely change of clearance between cooperating elements.
- There are many factors influencing change of effective clearance, i.e.: initial clearance, initial temperature of the component, temperature of feeding oil, volume of flow, material used for making the unit and element's construction.
- Using suitable materials for cooperating elements of hydraulic components it is possible to protect them fully against thermal shock conditions. This is well exemplified by high speed pumps with housing made of aluminium alloy and gear of steel.
- During start-up in thermal shock conditions the supply and executive components present low torque efficiency and therefore low overall efficiency. This is due to substantial friction in working agent flow through the component's channels. One example is the torque efficiency of PWK 27 pump determined for start-up at temperatures -20°C

and +24°C. During start-up in thermal shock conditions the pump presents decreased torque efficiency (Fig. 37).

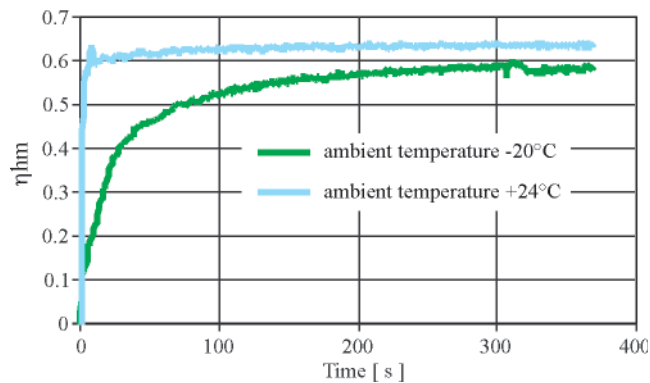


Fig. 37. Hydraulic – mechanical efficiency of start-up of PWK27 pump for the following conditions: ambient temp. $t_{o1} = +24^{\circ}\text{C}$ and $t_{o2} = -20^{\circ}\text{C}$, revolution speed $n = 1100$ [rpm], oil temp. $t_{ol} = 48^{\circ}\text{C}$, working pressure 5 MPa

- Apart from above described experimental method of determining parameters for correct start-up of hydraulic components in low ambient temperatures, Author uses and recommends two other methods: analytical and computer aided simulation. With the use of these methods one may determine, with suitable precision, parameters for correct start-up of hydraulic system in thermal shock conditions without the necessity of using costly, troublesome and often destructive experimental researches. These methods will be described in following components of this article, concerning issues addressed here.

BIBLIOGRAPHY

1. Jasiński R.: *Operation of low speed hydraulic motors in thermal shock conditions*. Doctoral dissertation, thesis supervisor: A. Balawender. Gdańsk 2002.
2. Jasiński R.: *Research methodology of low speed hydraulic motors in thermal shock conditions*, the IXth Seminar „Drives and control 2003”, Gdańsk, February 2003.
3. Jasiński R.: *Analysis of permissible start-up parameters for hydraulic motors in thermal shock conditions*, the Xth Seminar „Drives and control 2004”, Gdańsk, 2004.
4. Jasiński R.: *Operation of hydraulic system control components in low ambient temperatures when supplied with hot working agent*, the IIIrd International Technical Diagnostics Congress „Diagnostics'2004”, Poznań, 2004.
5. Jasiński R.: *Operation of hydraulic components in low ambient temperatures*. Scientific Conference, Mechanika 2005, Gdańsk 2005.
6. Jasiński R.: *Assessment of suitability of hydraulic control components operated in low ambient temperatures*, conference papers: Diagnostyka, Olsztyn, 2008
7. Jasiński R.: *Experimental research of the multi-piston axial pump PWK 27 from HYDROTOR company in low ambient temperatures*, Drives and control, professional journal 4/08
8. Jasiński R.: *Problems of the starting and operating of hydraulic components and systems in low ambient temperature (Part I)*, Polish Maritime Research 4/2008
9. Lewandowski P.: *Experimental research of the multi-piston pump PWK 27 during start-up in low ambient temperatures*. Graduation paper, thesis supervisor R. Jasinski, Gdańsk 2006.
10. Osiecki A.: *Hydrostatic drive of machines*. Science-Technical Publishing House, Warszawa 1998.
11. Osiecki L.: *Multi-piston pumps with cam distribution*. Seminar papers „Drives and control 2003”, Gdańsk 2003.
12. Rutkiewicz Ł.: *Experimental research of proportional valve in low ambient temperatures*, Graduation paper, Thesis supervisor: R. Jasiński, Gdańsk Polytechnics, 2006.

13. Szalkowski S.: *Research of hydraulic directional spool valve in thermal shock conditions*, Graduation paper, Thesis supervisor: R. Jasiński, Gdańsk Polytechnics, 2004.
14. Chełmińska H. and others: *Characteristics of steel*, volume 1, part 1, „Śląsk” Publishing House, Katowice, 1975.
15. Niezgodziński M., Niezgodziński T.: *Formulas, graphs and strength charts*, PWN Publishing House, Warszawa 1984.
16. Przychodzień T. and others: *Operation of machines in winter conditions*. Warszawa, WNT Publishing House 1990.
17. Szydelski Z., Olechowicz J.: *Parts of hydraulic and pneumatic drive and control*. PWN Publishing House, Warszawa 1986.
18. Books and catalogues from Bosch Rexroth company
19. Catalogues from Hydrotor company
20. Catalogues from ZUO Hydroster company
21. Catalogues from Parker company
22. Catalogues from Sauer-Danfoss company
23. Hydrostatic axial piston machine. European patent No. 0742870. Inventor: Osiecki A., Osiecki L. 1999
24. Hydrostatic axial piston machine. Polish patent No. 173937. Inventor: Osiecki A., Osiecki L. 1999

CONTACT WITH THE AUTHOR

Ryszard Jasiński, Ph. D.
 Faculty of Mechanical Engineering
 Gdansk University of Technology
 Narutowicza 11/12
 80-952 Gdansk, POLAND
 e-mail: rjasinsk@pg.gda.pl



Photo: C. Spigarski

Estimation of the probability of propulsion loss by a seagoing ship based on expert opinions

Alfred Brandowski, Prof.
Gdynia Maritime University

ABSTRACT



The event of the loss of propulsion function has been defined as hazardous event to a seagoing ship. It has been formalized. The procedure of acquisition of expert opinions on frequency of the event occurrence has been described. It may be considered to be of a numerical-fuzzy character. The fuzzy part was transferred to the numerical form by the pair comparison method. An example of the ship propulsion system comprising a low speed internal combustion engine and a fix pitch propeller illustrates the method presented. It may be used wherever a hazard analysis has to be performed of a system involving human and technical aspects and there is a shortage of objective data on the investigated object.

Keywords: ship, loss of propulsion, probability, estimation, expert

INTRODUCTION

Loss of the propulsion function by a ship is one of the most serious categories of *hazardous events*¹ in shipping. In specific external conditions it may lead to a loss of ship together with people aboard. The loss of propulsive power may be an effect of the propulsion system (PS) failures or of errors committed by the crew in the system operation process. In the safety engineering language we say that the *propulsion loss probability* depends on the reliability of the PS and of its operators. Determination of that probability is in practice confronted with difficulties connected with shortage of data on that reliability. This pertains particularly to the cases of estimation in connection with decisions taken in the ship operation. In such cases we have to rely on subjective estimations made by persons with practical knowledge in the field of interest, i.e. *experts*. The experts, on the other hand, prefer to formulate their opinions in the linguistic categories, in other words in the language of *fuzzy sets*. The author's experience tells also that in the expert investigations it is difficult to maintain proper correlation between the system data and the system component data. The paper presents a method of the subjective estimation of propulsion loss probability by a ship, based on the numerical-fuzzy expert judgements. The method is supposed to ensure that proper correlation. It is adjusted to the knowledge of experts from ships' machinery crews and to their capability of expressing that knowledge.

The method presented has been developed with an intention of using it in the decision taking procedures in risk prediction during the seagoing ship operation, in the shortage of objective reliability data situations.

DEFINITION OF THE SHIP PROPULSION LOSS AS A HAZARDOUS EVENT

The propulsion hazard is connected with the loss by the PS system of its capability of performing the assigned function, i.e. generating the driving force of a defined value and direction. It appears as an effect of a *catastrophic failure*² of the PS. Such failure may cause *immediate* (ICF) or *delayed* (DCF) stoppage of a ship. In the latter case the stoppage is connected with renewal, which may be carried out at any selected moment. It is obvious that only the former case of the forced stoppage creates a risk of damage or even loss of ship - it is a hazardous event.

We will relate the probability of ICF to an arbitrary time interval determined by the analyst. For instance, it may be duration of one trip, time interval between the ship class renewal surveys or one year, as it is usually assumed in risk analyses. Such an approach is useful in the ship operation risk management process.

The ICF type failure consequences may be divided into casualties and incidents (IMO 1997). In general, the ship casualties are non-repairable at sea by means of the ship own

¹ *Hazardous event* is defined as an event bringing about damage to human beings as well as to the natural and/or technical environment. It is also called "accident" or "initiating event".

² *Catastrophic failure* is defined as loss of the capability of performing by the object of its assigned function.

resources and may have very serious consequences, with the ship towing at the best and the loss of ship at the worst. The problem of consequences is not the subject of this paper.

The ICF type failure frequency depends mainly on the type of PS and the ship operation mode (liner trade, tramping etc.). On the other hand, the consequences are strongly dependent on the ship size and type and the environmental conditions, first of all the water region, season, time of day, atmospheric and sea conditions. They are also dependent on the navigational decisions and on the type and fastening of cargo in the holds and on deck. In general, these are the factors connected with the type of shipping carried out and the shipping routes the ship operates on.

FORMAL MODEL OF ICF EVENT

We assume the following:

- ☆ We are interested only in the "active" phase of ship operation, when it is in the shipping traffic. We shall exclude from the model the periods of stays in ship repair yards or in other places connected with renewals of the ship equipment.
- ☆ The investigated PS system may be only in the active usage or stand-by usage state. The ICF type PS failures may occur only in the former state.
- ☆ A formal model of the ICF type PS failures is the homogeneous Poisson process (HPP). This assumption is justified by the expert elicited data, which indicate that this type of failures occur fairly often, several times a year, but their consequences in general mean only a certain loss of operation time. More serious consequences, causing longer breaks in the normal PS system operation, occur seldom. The exponential distribution of time between failures, taken place in the HPP stream model, is characteristic of a normal operation of many system classes, including also the ship systems [1, 4]. It is appropriate in the case when the modeled object failures and the operator errors are fully random abrupt failures and not gradual failures caused by the ageing processes and/or wear of elements. This corresponds with the situation when scrupulously performed inspections and renewals prevent the latter type of failure from occurring.
- ☆ Experts are asked only about two numerical values: number of ICF type failures $N(t)$ during time period $t = 1$ year (8760 hours), and the time at sea percentage share $\kappa < 100\%$ during their seamanship period - this is within their capability of answering.
- ☆ The opinions on the failures of PS system components are elicited in the linguistic form.

The seagoing ship system active usage time $t^{(a)}$ is strongly correlated with the specific ship operational state times, mainly with the "at sea" state including "sailing", "manoeuvres" and "anchoring". The following approximation may be adopted for the system, also for the PS:

$$t^{(a)} = t^{(m)} = \kappa t \quad (1)$$

where:

- $t^{(a)}$ – active usage time
- $t^{(m)}$ – time at sea
- t – calendar time of the system observation
- $\kappa = t^{(m)}/t$ – time at sea factor ($\kappa \in \langle 0,1 \rangle$)

In view of these assumptions, the ICF type PS failures may occur only in the system active usage state, i.e. for the PS system in the $t^{(m)}$ time, although their observed yearly numbers are determined by experts in relation to the calendar time t .

The model ICF probability has the vector form:

$$\mathbf{P}\{t^{(a)}\} = \mathbf{P}\{\kappa t\} = \left[\frac{(\lambda^{(a)} \kappa t)^k}{k!} e^{-\lambda^{(a)} \kappa t}; k = 1, 2, \dots, K \right] \quad (2)$$

where:

- $\mathbf{P}\{t^{(a)}\}$ – the vector of probabilities of ICF type event occurrence within time interval $\langle 0, t \rangle$
- $\lambda^{(a)} \approx \sum_{j=1}^J N_j(t)/\kappa_j t_j$ – intensity function of HPP (ROCOF) (and at the same time the failure rate of the exponential distributions of time between failures in that process, [1/h])
- N_j – annual number of the ICF type events elicited by j -th expert, [1/y]
- κ_j – time at sea factor elicited by j -th expert
- t_j – calendar time of observation by j -th expert [h]
- J – number of experts
- K – the maximum number of possible ICF type failures in the time interval $\langle 0, t \rangle$
- t – the time of probability prediction.

The $\lambda^{(a)}$ formula is based on the theorem on the asymptotic behaviour of the renewal process [1]:

$$\lim_{t \rightarrow \infty} \frac{E[N(t)]}{t} = \frac{1}{T_0} = \lambda \quad (3)$$

where:

- T_0 – mean time between failures.

The number of ICF type events in the $\langle 0, t \rangle$ period may be $0, 1, 2, \dots$ or K with well-defined probabilities. The maximum of these probabilities is the assumed measure of the probability of ICF type event occurrence:

$$P_{\max}\{t^{(a)}\} = \max_{k \in \{1, 2, \dots, K\}} \frac{(\lambda^{(a)} \kappa t)^k}{k!} e^{-\lambda^{(a)} \kappa t} \quad (4)$$

The λ and κ parameters determined from the elicited opinions may be adjusted as new operation process data arrive on the investigated system failures.

Expressions (2) and (4) allow to estimate the probabilities of ICF type hazardous events in the determined time interval t . Another problem is estimation of the risk of consequences of these events, i.e. damage to or total loss of the ship and connected human, environmental and financial losses. This is a separate problem not discussed in this paper.

DATA ACQUISITION

The PS will be further treated as a system consisting of subsystems and those consisting of the sets of devices.

Experts are asked to treat the objects of their opinions as anthrop-technical systems, i.e. composed of technical and human (operators' functions) elements. They elicit their opinions in three layers in such a way that proper correlation is maintained between data of the system and data of the system components. In layer 0 opinions are expressed in numbers, in layers I and II - in linguistic terms. For layers I and II separate *linguistic variables* (LV) and *linguistic term-sets* (LT-S) have been defined (Piegat A. 1999).

Layer 0 – includes PS as a whole.

Estimated are the annual numbers of type ICF type failures of PS $N(t)$ and the percentage share of time at sea $\kappa < 100\%$ in the time of expert's observation.

Layer I – includes decomposition of PS to a subsystem level.

- ✦ LV = share of the number of subsystem failures in the number of type ICF failures of PS.
- ✦ LT-S = A1-very small/none, B1-small, C1-medium, D1-large, E1-very large.

Layer II – includes the decomposition of subsystems to the sets of devices (set of devices is a part of subsystem forming a certain functional entity whose catastrophic failure causes catastrophic failure of the subsystem - e.g. it may be a set of pumps of the cooling fresh water subsystem).

- ▲ LV = share of the number of failures of the sets of devices in the number of catastrophic failures of the respective PS subsystem.
- ▲ LT-S = A2-very small/none, B2-small, C2-medium, D2-large, E2-very large.

The structure of data acquisition procedure presented here implies a series form of the reliability structures of subsystems (layer I) and sets of devices (layer II). Elements of those structures should be so defined that their catastrophic failures cause equally catastrophic failures of the PS system and subsystem respectively. The division into subsystems and sets of devices should be complete and disjunctive.

The data acquisition procedure presented here takes into account the expert potential abilities. It seems that their knowledge should be more precise in the case of a large operationally important system, as the PS is, and less precise as regards individual components of the system.

ALGORITHM OF EXPERT OPINION PROCESSING

In layer 0 the experts elicit annual numbers of the ICF type failures, which, in their opinion, might have occurred during 1 year in the investigated PS type:

$$N_j(t) \quad j = 1, 2, \dots, J \quad (5)$$

and shares of the time at sea in the calendar time of ship operation:

$$\kappa_j 100\% \quad j = 1, 2, \dots, J \quad (6)$$

where:

- j – experts index
- J – number of experts.

These sets of values are subjected to selection due to possible errors made by the experts. In this case a statistical test of the distance from the mean value may be useful, as in general we do not have at our disposal any objective field data to be treated as a reference set.

If the data lot size after selection appears insufficient, it may be increased by the bootstrap method (Efron & Tibshirani 1993).

From the data (5) and (6), parameters $\lambda^{(a)}$ and κ of expression (2) and (4) are determined. Number of opinions J may be changed after the selection.

In layer I experts elicit the linguistic values of subsystem shares in the number of ICF type failures of the investigated PS type (they choose LV value from the {A1, B1, C1, D1, E1} set). The data are subjected to selection.

The elicited data with linguistic values are compared in pairs - estimation of each subsystem is compared with estimation of

each subsystem. The linguistic estimations are transformed into numerical estimations according to the following pattern:

- LT - S = B1 \Rightarrow 2
- LT - S = C1 \Rightarrow 3
- LT - S = D1 \Rightarrow 4
- LT - S = E1 \Rightarrow 5

Numerical estimates of each subsystem are subtracted from estimates of each subsystem. In this way the difference values are obtained, which may have the following values: -4, -3, -2, -1, 0, 1, 2, 3, 4. Those differences are transferred into preference estimates (as given in Tab. 1) in accordance with the following pattern:

- 4 \Rightarrow 9, *absolute preference*
- 3 \Rightarrow 7, *clear preference*
- 2 \Rightarrow 5, *significant preference*
- 1 \Rightarrow 3, *weak preference*
- 0 \Rightarrow 1, *equivalence*
- 1 \Rightarrow 1/3, *inverse of weak preference*
- 2 \Rightarrow 1/5, *inverse of significant preference*
- 3 \Rightarrow 1/7, *inverse of clear preference*
- 4 \Rightarrow 1/9, *inverse of absolute preference*.

From these differences, by the pair comparison method, a matrix of estimates is constructed. The estimates depend on the „distance” of the linguistic values LT-S of a given variable LV. For instance, preference A1 in relation to E1 has the value 9 assigned, in relation to D1 a value 7, in relation to C1 a value 5. In relation to B1 a value 3 and in relation to A1 a value 1. The inverses of those preferences have the values, respectively: 1/9, 1/7, 1/5, 1/3 and 1. The matrix of estimates is approximated by the matrix of weight quotients of the sought arrangement. The recommended processing method is the logarithmic least squares method. The result is a vector of normalized arrangements of the subsystem shares (Saaty 1980, Kwiesielewicz 2002)³:

$$\mathbf{p} = [p_1, p_2, \dots, p_i, \dots, p_I] \quad (7)$$

where:

- p_i – share of the i-th subsystem as a cause of an ICF type PS failure
- I – number of subsystems.

Now we can determine in a simple way the intensity functions of individual subsystems arising from catastrophic failures:

$$\lambda_i^{(a)} = \lambda^{(a)} p_i, \quad i = 1, 2, \dots, I \quad (8)$$

Tab. 1. Expert preference estimates acc. to Saaty (1980)

Estimate	Preference
1	Equivalence
3	Weak preference
5	Significant preference
7	Strong preference
9	Absolute preference
Inverse of the above numbers	Inverse of the above described preference

In layer II experts elicit the linguistic values of subset shares in the number of catastrophic subsystem failures (they choose LV value from the {A2, B2, C2, D2, E2} set). As in the case of subsystems, the expert opinions are processed to the form of normalized vectors of the arrangements of set shares:

³ The Saaty method, criticised in scientific circles, is widely applied in the decision-taking problems.

$$P_i = [p_{i1}, p_{i2}, \dots, p_{ik}, \dots, p_{iK}] ; i = 1, 2, \dots, I ; k = 1, 2, \dots, K \quad (9)$$

where:

- P_i – vector of the shares of i -th subsystem sets as causes of catastrophic failures of that subsystem
- p_{ik} – share of the k -th set of i -th subsystem
- K – number of sets in a given subsystem.

Then, the intensity functions of sets contained in individual subsystems arising from catastrophic failures are determined:

$$\lambda_{ik}^{(a)} = \lambda_i^{(a)} p_{ik} ; i = 1, 2, \dots, I ; k = 1, 2, \dots, K \quad (10)$$

EXAMPLE

The example discusses investigation of a PS consisting of a low speed piston combustion engine driving a fix pitch propeller, installed in a container carrier ship. Experts were marine engineers with long experience (50 ship officers with chief engineer or second engineer diploma). Special questionnaire was prepared for them containing definition of the investigated object, schematic diagrams of subsystems and sets, precisely formulated questions and tables for answers. It was clearly stated in the questionnaire that an ICF type failure may be caused by a device failures or by a crew actions. Out of 50 opinions elicited by experts, 3 were estimated as very unlikely (2 elicited numbers of the ICF events in a year were extremely underestimated and one was overestimated). They were eliminated and the remaining 47 opinions were further processed.

Figs. 1 and 2 present statistical estimates of the expert opinion data (5) and (6).

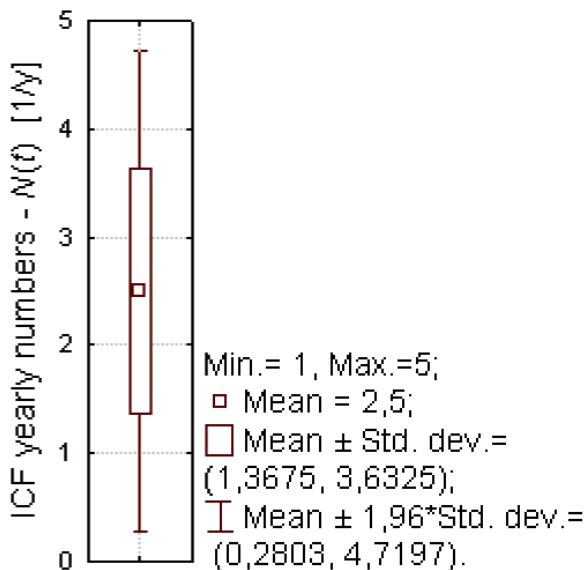


Fig. 1. Box and whiskers plot of ICF yearly numbers

Tab. 2 contains averaged basic data elicited by 47 experts in relation to the PS as a whole and the model parameters of ICF type event probability [equation (2)] determined from these data.

From the Tab. 2 data the probabilities of determined numbers of ICF type event occurrences in 1 year were calculated. Fig. 3 diagram presents results of those calculations. The numbers of probable ICF events in 1 year are equal 1, 2, ..., 5. The maximum probability is 0.2565, which stands for 2 ICF type events during 1 year, and the probability that such event will not occur amounts to 0.0821.

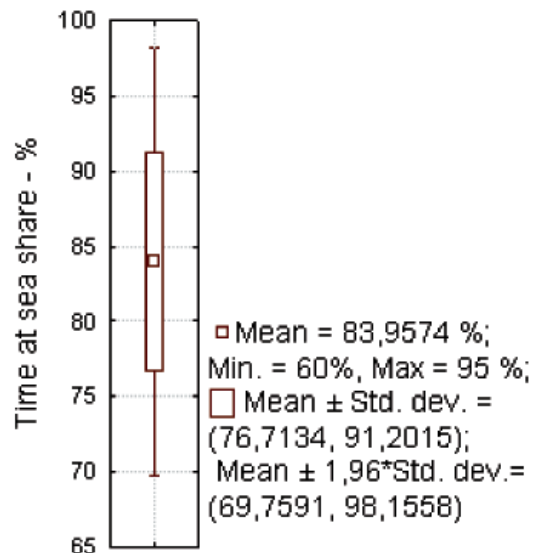


Fig. 2. Box and whiskers plot of time at sea share

Tab. 2. Basic results of propulsion system investigation

Averaged expert elicited data	$\bar{N}(1 y) = 2.5$ $\sigma[N(1 y)] = 1.1325$ $\bar{\kappa}100 = 83.95745$ $\sigma[\kappa100] = 7.24406$
Risk model parameters	$\sum_1^{47} t = 411720 \text{ h}$ $\lambda^{(a)} = 3.39922 \text{ E} - 04 \text{ 1/h}$ $\bar{\kappa} = 0.83957$

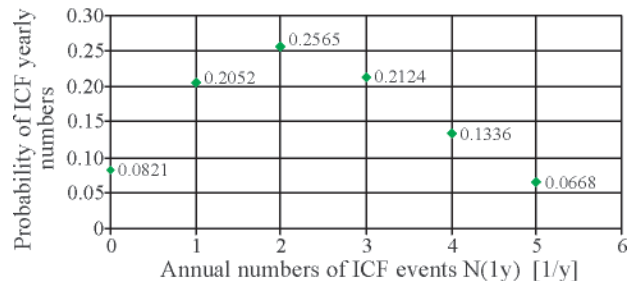


Fig. 3. Distribution of ICF event numbers' probability

Tab. 3 contains the subsystem intensity function (ROCOF) data calculated from equation (8). The main PS risk "participants" are main engine and the electrical subsystem and the least meaningful is the propeller with shaft line. This is in agreement with the experience of each shipbuilder and marine engineer.

Tab. 4 contains the fuel supply subsystem intensity function (ROCOF) data calculated from equation (10).

Tab. 3. Intensity functions of the subsystems

No	Subsystem	p_i	$\lambda^{(a)} 10^{-5}$
1	Fuel oil subsystem	0.1330	4.5203
2	Sea water cooling subsystem	0.0437	1.4852
3	Low temperature fresh water cooling subsystem	0.0395	1.3426

No	Subsystem	p_i	$\lambda^{(a)} 10^{-5}$
4	High temperature fresh water cooling subsystem	0.0620	2.1074
5	Starting air subsystem	0.0853	2.9006
6	Lubrication oil subsystem	0.0687	2.3352
7	Cylinder lubrication oil subsystem	0.0446	1.5147
8	Electrical subsystem	0.1876	6.3770
9	Main engine	0.1987	6.7536
10	Remote control subsystem	0.1122	3.8146
11	Propeller + shaft line	0.0247	0.8410

Tab. 4. Intensity functions of the fuel oil subsystem sets

No	Set	P_{ik}	$\lambda_{ik}^{(a)} 10^{-6}$
1	Fuel oil service tanks	0.0488	2.2062
2	Fuel oil supply pumps	0.1672	7.5572
3	Fuel oil circulating pumps	0.1833	8.2840
4	Fuel oil heaters.	0.0944	4.2666
5	Filters	0.1540	6.9599
6	Viscosity control arrangement	0.2352	10.6323
7	Piping + heating up steam arrangement	0.1172	5.2965

SUMMARY

- The paper presents a method of subjective estimation of the hazard connected with losing by a seagoing ship of the propulsion function capability. The estimation is based on opinions elicited by experts - experienced marine engineers. The method is illustrated by an example of such estimation in the case of a propulsion system with a low speed diesel engine and a fix pitch propeller installed in a container carrier.

- The given in section 6 do not raise any objections. The author does not have at his disposal sufficient objective data to evaluate precisely the adequacy of those data. It has to be taken into account that results of a subjective character may, by virtue of the fact, bear greater errors than the objective results achieved from investigations in real operational conditions.
- The presented method may be used in the procedures of the ship propulsion risk prediction. It allows to investigate the impact of the PS system component reliability on the probability values of ICF type event. It may also be used with other types of ship systems and not only to ship systems, particularly in the situations of hazardous event probability estimations with insufficient objective data at hand.

BIBLIOGRAPHY

1. Gniedienko B.V., Bielajev J.K., Soloviev A.D.: *Mathematical Methods in Reliability Theory* (in Polish). Warszawa: Wydawnictwa Naukowo-Techniczne, 1965
2. Saaty T.L.: *The Analytical Hierarchy Process*. New York et al: McGraw-Hill, 1980
3. Kwiesielewicz M.: *Analytical Hierarchy Decision Process. Fuzzy and Non-fuzzy Paired Comparison* (in Polish). Warszawa: Instytut Badań Systemowych PAN, 2002
4. Modarres M., Kaminskiy M., Krivtsov.: *Reliability Engineering and Risk Analysis*. New York, Basel: Marcel Dekker, Inc., 1999
5. Piegat A.: *Fuzzy Modeling and Control* (in Polish). Warszawa: Akademicka Oficyna Wydawnicza EXIT, 1999
6. IMO. Resolution A.849(20): *Code for the investigation of marine casualties and incidents*. London, 1997
7. Roland H. E., Moriarty B.: *System Safety Engineering and Management*. John Wiley & Sons, Inc. New York, Chichester, Brisbane, Toronto, Singapore, 1990.

CONTACT WITH THE AUTHORS

Alfred Brandowski, Prof.
Faculty of Marine Engineering
Department of Engineering Sciences,
Gdynia Maritime University
Morska 83
81-225 Gdynia, POLAND
e-mail: abrand@am.gdynia.pl

The application of the ahp method in ship system risk estimation

Hoang Nguyen, Ph. D.
 Gdynia Maritime University

ABSTRACT



The article presents procedures of application of the AHP method for estimating risks of ship systems. The estimation of system risk function parameters is done based on the data obtained from experts and processed using the pairwise comparative method.

Key words: AHP method, estimation, propulsion risk, expert courts, ship systems

INTRODUCTION

In sea transport, among numerous factors affecting the safety of navigation, of high importance is the reliability of the propulsion system. The situation when a ship losses its driving ability can lead, in some circumstances, to serious marine accidents, the consequences of which can be deaths of people and/or environment pollution.

The risk of appearance of such an event, which we can refer to as the propulsion risk, depends on the reliability of individual components of the propulsion system and its operators. Estimating the risk of this system is troublesome due to the complexity of the system and the lack of historical data on its reliability. In such cases subjective estimations based on opinions of experts turn out very applicable [4].

In the article, the experts were ship engineers with many years' experience who revealed numbers of propulsion system failures per year and linguistic proportions of contributions of particular subsystems to the total number of disastrous failures of this system. The estimation of risk function parameters for the subsystems included in the data presented by the experts was done by comparing in pairs. This way a proper correlation was obtained between the data referring to the entire system and its particular components (subsystems). The data obtained from comparing in pairs were processed using the Analytical Hierarchical Decision Making Process (AHP) method.

THEORETICAL BACKGROUND

The AHP method is a method commonly used in multi-attribute decision-making. The decision making process in the AHP method consists in ordering of variants, with further aggregation of the obtained ordered sets according to the defined hierarchical structure. The ordered sets are created via comparing in pairs.

The pairwise comparative method consists in comparing individual variants with each other and attributing a number from an earlier defined scale to each pair. The comparison is done by an expert who gives a precise (numerical) or fuzzy estimation to each pair. This estimation expresses individual expert's preference when comparing one variant to the other (Tab. 1).

Tab. 1. Estimations corresponding to experts' preferences, after Saaty (1980)

Estimation	Preference
1	Equivalence
3	Weak preference of ith variant over jth variant
5	Relatively strong preference of ith variant over jth variant
7	Definite preference of ith variant over jth variant
9	Absolute preference of ith variant over jth variant
2, 4, 6, 8	Intermediate numbers
Inverse numbers to those above listed	Inverse preferences to those abovenamed

Let us assume that we have n variants W_1, W_2, \dots, W_n which are to be ordered. To each pair of variants (W_i, W_j) an expert attributes a number r_{ij} from the set $S = \{1/9, 1/8, \dots, 1/2, 1, 2, \dots, 8, 9\}$ which expresses his/her individual preferences with respect to the i th variant as compared to the j th variant.

Experts' estimations are used for creating the estimation matrices \mathbf{R} (which are, as a rule, inconsistent).

$$\mathbf{R} = [r_{ij}] = \begin{pmatrix} r_{11} & r_{12} & \dots & r_{1n} \\ r_{21} & r_{22} & \dots & r_{2n} \\ \vdots & \vdots & \vdots & \vdots \\ r_{n1} & r_{n2} & \dots & r_{nn} \end{pmatrix} \quad (1)$$

Matrix \mathbf{R} is the matrix with inconsistent estimations and has the following properties:

$$r_{ij} > 0; r_{ij} = \frac{1}{r_{ji}} \quad \forall i, j = 1, 2, \dots, n$$

Matrix \mathbf{R} is considered consistent when its elements meet the condition:

$$r_{ij}r_{jk} = r_{ik}; \quad \forall i, j, k = 1, 2, \dots, n$$

Ordering of variants is obtained as a result of approximation of the estimation matrix \mathbf{R} using matrix \mathbf{P} :

$$\mathbf{P} = [p_{ij}] = \begin{pmatrix} p_{11} & p_{12} & \dots & p_{1n} \\ p_{21} & p_{22} & \dots & p_{2n} \\ \vdots & \vdots & \vdots & \vdots \\ p_{n1} & p_{n2} & \dots & p_{nn} \end{pmatrix} \quad (2)$$

the elements of which are consistent estimations presented in the form of weight ratios between particular variants:

$$p_{ij} = \frac{p_i}{p_j}; \quad i, j = 1, 2, \dots, n$$

where p_i represent weights of particular variants of the order vector \mathbf{p} :

$$\mathbf{p} = (p_1, \dots, p_n)^T \quad (3)$$

After arithmetic standardisation we obtain the standardised order vector:

$$\mathbf{p}^* = (p_1^*, \dots, p_n^*)^T \quad (4)$$

where:

$$p_i^* = \frac{p_i}{\sum_{i=1}^n p_i}$$

Three basic methods which are used for approximating the estimation matrices are the following:

- ★ maximum eigenvalue method [3]
- ★ least square method [3]
- ★ logarithmic least square method [2, 3].

a) The maximum eigenvalue method

This method consists in finding the vector \mathbf{p} which fulfils the relation:

$$\mathbf{R}\mathbf{p} = \lambda_{\max}\mathbf{p} \quad (5)$$

where:

λ_{\max} – the maximum eigenvalue of matrix \mathbf{R} .

b) The least square method

This method consists in determining a form of matrix \mathbf{P} which is closest to matrix \mathbf{R} and which fulfils the relation:

$$\min \left[\sum_{i,j=1}^n \left(r_{ij} - \frac{p_i}{p_j} \right)^2 \right] \quad (6)$$

c) The logarithmic least square method

This method consists in determining a form of matrix \mathbf{P} which is closest to matrix \mathbf{R} based on the Euclidean norm in the logarithmic scale. Matrix \mathbf{P} fulfils the relation:

$$\min \left\{ \sum_{i,j=1}^n \left[\ln(r_{ij}) - \ln\left(\frac{p_i}{p_j}\right) \right]^2 \right\} \quad (7)$$

After substituting:

$$y_{ij} = \ln(r_{ij}), \quad x_i = \ln(p_i) \quad (8)$$

we arrive at the optimisation problem:

$$\min \left\{ I = \sum_{i,j=1}^n [y_{ij} - x_i + x_j]^2 \right\}$$

the solution of which has the form:

$$\frac{\partial I}{\partial x_k} = -2 \sum_{i=1}^n [y_{kj} - x_k + x_j] = 0 \quad (9)$$

After introducing the condition of geometrical standardisation:

$$\prod_{i=1}^n p_i = 1; \quad \left(\sum_{j=1}^n x_j = 0 \right) \quad (10)$$

Equation (9) takes the form:

$$\sum_{i=1}^n y_{kj} = nx_k \quad \text{or} \quad x_k = \frac{1}{n} \sum_{j=1}^n y_{kj}; \quad k = 1, \dots, n \quad (11)$$

Finally, after taking into account (8) we get the variant order vector:

$$p_i = e^{x_i} = \left(\prod_{j=1}^n r_{ij} \right)^{\frac{1}{n}}; \quad i = 1, \dots, n \quad (12)$$

For a large number of experts estimating a given pair of variants, the estimations made by individual experts are considered equivalent to each other. Then the task is limited to the following form:

$$\min \left\{ \sum_{i,j=1}^n \sum_{k=1}^{m_{ij}} \left[\ln(r_{ijk}) - \ln\left(\frac{p_i}{p_j}\right) \right]^2 \right\} \quad (13)$$

where:

m_{ij} – the number of estimations concerning the pair (i,j) .

After introducing substitutions:

$$y_{ijk} = \ln(r_{ijk}), \quad x_i = \ln(p_i) \quad (14)$$

we arrive at the optimisation problem:

$$\min \left\{ I = \sum_{i,j=1}^n \sum_{k=1}^{m_{ij}} [y_{ijk} - x_i + x_j]^2 \right\}$$

the solution of which has the form:

$$\frac{\partial I}{\partial x_l} = -2 \sum_{j=1}^n \sum_{k=1}^{m_{lj}} [y_{ljk} - x_l + x_j] = 0; \quad l = 1, 2, \dots, n \quad (15)$$

The set of equations (15) is transformed to the set of standard equations:

$$x_i \sum_{j=1, j \neq i}^n m_{ij} - \sum_{j=1, j \neq i}^n m_{ij} x_j = \sum_{j=1, j \neq i}^n \sum_{k=1}^{m_{ij}} y_{ijk}; \quad i = 1, 2, \dots, n \quad (16)$$

In matrix notation the set (16) has the form:

$$Ax = b$$

where:

$$b = [b_i]; b_i = \sum_{j=1, j \neq i}^n \sum_{k=1}^{m_{ij}} y_{ijk}; i = 1, 2, \dots, n \quad (17)$$

$$A = \begin{pmatrix} \sum_{j=1, j \neq 1}^n m_{1j} & -m_{12} & \dots & -m_{1n} \\ -m_{21} & \sum_{j=1, j \neq 2}^n m_{2j} & \dots & -m_{2n} \\ \vdots & \vdots & \vdots & \vdots \\ -m_{n1} & -m_{n2} & \dots & \sum_{j=1, j \neq n}^n m_{nj} \end{pmatrix} \quad (18)$$

Hence, the variant order vector can be determined from the equation:

$$p = e^x = e^{A^{-1}b} \quad (19)$$

[2] has shown that, despite its popularity, the maximum eigenvalue method reveals a weakness, namely it does not have the property of relation commutation, which means that the operation of estimation matrix transposition leads to different results. At the same time the least square method does not produce a unique solution.

The logarithmic least square method is reduced to the geometric mean method for a large number of experts, as well as to the estimation matrix without missing data. The geometric mean method is a symmetrical transformation and produces the unique solution, irrelevant of scale inversion or changes in the order of particular aggregation operations. It is compatible with the estimation method of the highest credibility, which gives the reasons for its use from the point of view of the statistics. Further in the article, the logarithmic least square method is used for estimating the subjective ship propulsion risk.

Among presently available computer codes which make use of the AHP method for decision-making, the codes which are preferred are Expert Choice and Criterium Decision Plus. Due to limitations concerning the numbers of variants in those codes, a computer code was developed based on calculating algorithms which make use of the logarithmic least square method.

APPLICATION

The AHP method was used for estimating proportions of contributions of individual subsystems and units in the reliability structure of the ship propulsion system. The data were obtained from a group of 47 experts (ship engineers) using a specially prepared questionnaire [ESREL 2008].

The experts revealed their opinions on the proportions of contributions of particular subsystems in the total number of failures of the examined system in the form of linguistic values (very small, small, medium, big, very big). These values express experts' preferences concerning the contributions of particular subsystems as the causes of propulsion system failures (Tab. 2).

These data are compared in pairs and scaled using the assumed 5-stage scale to create the estimation matrices. A sample matrix which was created for the k-th expert is given below:

Tab. 2. Linguistic experts' opinions on the contributions of particular subsystems in total number of system failures.

No.	Name of subsystem	very small /zero	small	medium	big	very big
1	Fuel oil subsystem				X	
2	Seawater cooling subsystem		x			
3	Low temperature freshwater cooling subsystem		x			
4	High temperature freshwater cooling subsystem		x			
5	Starting air subsystem			x		
6	Lubrication oil subsystem			x		
7	Cylinder lubrication oil subsystem		x			
8	Electric power subsystem				x	
9	Main engine				x	
10	Main engine remote control subsystem			x		
11	Propeller and shaft line		x			

$$R_k = [r_{ijk}] = \begin{pmatrix} 1 & 5 & 5 & 5 & 3 & 3 & 5 & 1 & 1 & 3 & 5 \\ \frac{1}{5} & 1 & 1 & 1 & \frac{1}{3} & \frac{1}{3} & 1 & \frac{1}{5} & \frac{1}{5} & \frac{1}{3} & 1 \\ \frac{1}{5} & 1 & 1 & 1 & \frac{1}{3} & \frac{1}{3} & 1 & \frac{1}{5} & \frac{1}{5} & \frac{1}{3} & 1 \\ \frac{1}{5} & 1 & 1 & 1 & \frac{1}{3} & \frac{1}{3} & 1 & \frac{1}{5} & \frac{1}{5} & \frac{1}{3} & 1 \\ \frac{1}{3} & 3 & 3 & 3 & 1 & 1 & 3 & \frac{1}{3} & \frac{1}{3} & 1 & 3 \\ \frac{1}{3} & 3 & 3 & 3 & 1 & 1 & 3 & \frac{1}{3} & \frac{1}{3} & 1 & 3 \\ \frac{1}{5} & 1 & 1 & 1 & \frac{1}{3} & \frac{1}{3} & 1 & \frac{1}{5} & \frac{1}{5} & \frac{1}{3} & 1 \\ 1 & 5 & 5 & 5 & 3 & 3 & 5 & 1 & 1 & 3 & 5 \\ 1 & 5 & 5 & 5 & 3 & 3 & 5 & 1 & 1 & 3 & 5 \\ \frac{1}{3} & 3 & 3 & 3 & 1 & 1 & 3 & \frac{1}{3} & \frac{1}{3} & 1 & 3 \\ \frac{1}{5} & 1 & 1 & 1 & \frac{1}{3} & \frac{1}{3} & 1 & \frac{1}{5} & \frac{1}{5} & \frac{1}{3} & 1 \end{pmatrix}_k$$

Then the estimation matrices \mathbf{R} are approximated using the order vector component ratio matrix. The estimation matrix approximation was performed using the logarithmic least square method for the case of a large number of experts.

Matrix \mathbf{A} is obtained in the form:

$$\mathbf{A} = [a_{ij}] = \begin{pmatrix} 1 & 1 & 1 & 1 & 1 & 1 & 1 & 1 & 1 & 1 & 1 \\ -47 & 470 & -47 & -47 & -47 & -47 & -47 & -47 & -47 & -47 & -47 \\ -47 & -47 & 470 & -47 & -47 & -47 & -47 & -47 & -47 & -47 & -47 \\ -47 & -47 & -47 & 470 & -47 & -47 & -47 & -47 & -47 & -47 & -47 \\ -47 & -47 & -47 & -47 & 470 & -47 & -47 & -47 & -47 & -47 & -47 \\ -47 & -47 & -47 & -47 & -47 & 470 & -47 & -47 & -47 & -47 & -47 \\ -47 & -47 & -47 & -47 & -47 & -47 & 470 & -47 & -47 & -47 & -47 \\ -47 & -47 & -47 & -47 & -47 & -47 & -47 & 470 & -47 & -47 & -47 \\ -47 & -47 & -47 & -47 & -47 & -47 & -47 & -47 & 470 & -47 & -47 \\ -47 & -47 & -47 & -47 & -47 & -47 & -47 & -47 & -47 & 470 & -47 \\ -47 & -47 & -47 & -47 & -47 & -47 & -47 & -47 & -47 & -47 & 470 \end{pmatrix}$$

Vector \mathbf{b} , vector \mathbf{x} and the weight vector of standardised proportions of contributions of particular subsystems as causes of propulsion system failures, which were determined based on opinions obtained from a group of 47 experts, are as follows:

$$\mathbf{b} = \begin{pmatrix} 0 \\ -274.95 \\ -327.13 \\ -94.04 \\ 71.12 \\ -40.97 \\ -264.76 \\ 478.40 \\ 508.06 \\ 212.73 \\ -568.94 \end{pmatrix}, \mathbf{x} = \begin{pmatrix} 0.5812 \\ -0.5318 \\ -0.6327 \\ -0.1819 \\ 0.1375 \\ -0.0792 \\ -0.5121 \\ 0.9253 \\ 0.9827 \\ 0.4114 \\ -1.1004 \end{pmatrix}, \mathbf{p}^* = \begin{pmatrix} 0.1329 \\ 0.0436 \\ 0.0394 \\ 0.0619 \\ 0.0853 \\ 0.0686 \\ 0.0445 \\ 0.1876 \\ 0.1986 \\ 0.1122 \\ 0.0247 \end{pmatrix}$$

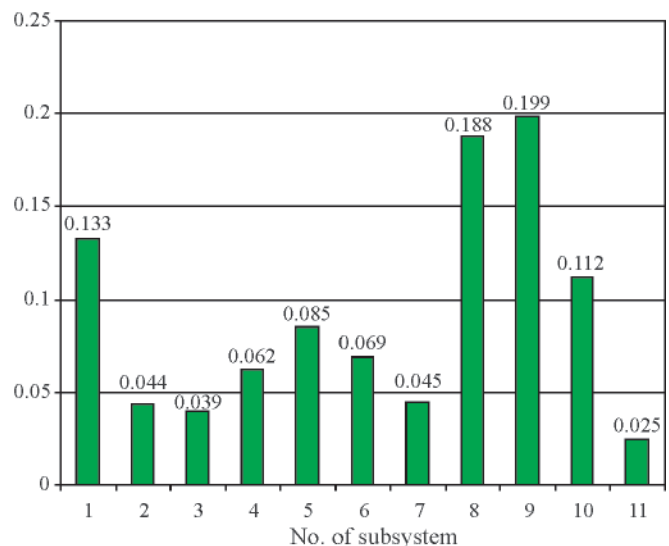


Fig. 1. Subsystem weights determined using the logarithmic least square method for the opinions obtained from 47 experts

Fig. 1 presents the estimated subsystem weights in the propulsion system function loss risk model, which were determined based on opinions given by 47 experts.

It was assumed that the system unreliability function has exponential probabilities of the time to first failure. The exponential distribution of this time is characteristic for normal operation of numerous classes of systems, including ship systems (Gniedienko B.W et al., 1965).

$$\mathcal{R}(t) = P\{\tau < t\} = 1 - e^{-\lambda t}; t \geq 0$$

where:

- λ – system failure rate
- τ – random variable representing the time to failure.

This model takes also into account standstills which are connected with renewals of the ship and its equipment and which are negligibly short compared to the ship maintenance time. Then the system failure rate λ can be evaluated from the theorem about asymptotic behaviour of the recovery process (Gniedienko B.W. & Bielajew J.K. & Sołowiew A.D. 1965):

$$\lim_{t \rightarrow \infty} \frac{E[N(t)]}{t} = \frac{1}{T_0} = \lambda$$

where:

- T_0 – mean time to failure
- $N(t)$ – number of system failures.

From the data revealed by the experts we get $\lambda = 3.34575 \text{ E} - 04 \text{ 1/h}$.

The obtained subsystem contribution order vector can be written in the form:

$$\mathbf{p} = \mathbf{p}^* = (p_1, p_2, \dots, p_i, \dots, p_n)$$

where:

- p_i – contribution of the i th subsystem as the cause of system failure
- n – number of subsystems.

The system failure rate can be determined from the relation:

$$\lambda_i = \lambda p_i, i = 1, 2, \dots, n$$

The results of the calculations are shown in Tab. 3 as the estimated weights and subsystem failure rates in the propulsion system function loss risk model.

Tab. 3. Subsystem failure rates

No.	Subsystem	p_i	$\lambda E - 05$
1	Fuel oil subsystem	0.132970	4.52026
2	Seawater cooling subsystem	0.043692	1.48517
3	Low temperature freshwater cooling subsystem	0.039497	1.34260
4	High temperature freshwater cooling subsystem	0.061996	2.10739
5	Starting air subsystem	0.085332	2.90062
6	Lubrication oil subsystem	0.068698	2.33519
7	Cylinder lubrication oil subsystem	0.044561	1.51474
8	Electric power subsystem	0.187603	6.37703
9	Main engine	0.198681	6.75360
10	Main engine remote control subsystem	0.112219	3.81457
11	Propeller and shaft line	0.024742	0.84103

CONCLUSIONS

- The article presents the procedures of application of the pairwise comparative method to the ship system risk estimation. These methods are extremely applicable when estimating expert data, which are, as a rule, inconsistent and/or burdened with error. Although in general these methods are well known and in common use, the novelty of the here presented work consists in the application of the logarithmic least square method to ordering variants, which is reduced to the geometrical standardisation. The applied procedure secures proper correlation between opinions presented by many different experts. In case some data are missing this method can also be used directly, and the missing data are assumed as consistent with the resultant order.
- Currently, activities are in progress in the Department of Engineering Sciences, Gdynia Maritime University, upon a neuron-fuzzy model of the ship propulsion risk. The estimated parameters obtained from the expert base using the AHP method are the input data for this model.

BIBLIOGRAPHY

1. Gniedienko B.W., Bielajew J.K., Sołowiew A.D.: *Mathematical methods in reliability theory* (in Polish). Warsaw: Wydawnictwa Naukowo-Techniczne, 1968
2. Kwiesielewicz M.: *Analytic hierarchical decision-making process. Fuzzy and non-fuzzy pairwise comparison* (in Polish). PAS Systems Research Institute: Warsaw, 2002
3. Saaty T.L.: *The Analytic Hierarchy Process*. New York et al: McGraw-Hill, 1980
4. Mazzuchi T., Linzey W., Brauning A.: *A paired comparison experiment for gathering expert judgement for an aircraft wiring risk estimation*. Reliability engineering & System safety 93, 2008

CONTACT WITH THE AUTHOR

Nguyen Hoang, Ph. D.
 Faculty of Marine Engineering,
 Gdynia Maritime University
 Morska 81/87
 81-225 Gdynia, POLAND
 e-mail : hoang@am.gdynia.pl

Supporting navigator's decisions by visualizing ship collision risk

Rafał Szlarczyński, Ph. D.
Gdańsk University of Technology
Roman Śmierchalski, Assoc. Prof.
Gdynia Maritime Academy

ABSTRACT

The paper introduces a visualization method that enables the navigator to estimate an encounter situation and choose collision avoidance manoeuvre, if necessary. It is based on the Collision Threat Parameters Area method and offers new features: fuzzy sectors of forbidden speed and course values, the possibility to use any given ship domain and a new formula of collision risk assessment. All these elements result in a method, which enables the navigator to differentiate between varying levels of risk and to point out the direct threats. The method is fast enough to be applied in the real-time decision support system.

Key words: ARPA display, collision avoidance manoeuvres, collision risk, navigation

INTRODUCTION

Traditional displays used in collision-avoidance systems were based on the relative Cartesian coordinate system, with the own ship in the centre of it and X and Y coordinates denoting the relative positions of all other objects including ships – here called targets. Their functionality was limited to showing all targets within a certain range and indicating the targets that were considered to be dangerous on the basis of computations performed by the system. Some of them additionally visualized Predicted Areas of Danger (PAD) and the resulting necessary course alterations [9]. What these displays failed to visualize was the nature of collision risk: the colliding combinations of courses and speeds of the own ship and the dangerous targets. Visualizing these forbidden combinations of course and speed (instead of course only) has been introduced by Lenart as a part of Collision Threat Parameters Area (CTPA) method [1].

Based on CTPA the graphical method determining necessary manoeuvre has been introduced in [6, 7, 8]. However, the display according to Lenart and the derived method naturally assume using a pre-defined safe distance D_s as a main safety parameter and consequently DCPA (Distance to the Closest Point of Approach) as a collision risk measure. Therefore they cannot be used for precise visualization of the necessary manoeuvres when domains other than circle-shaped are assumed. Also, in cases of large values of safe distance parameter D_s and multi ship encounters it might be impossible to find one combination of course and speed that avoids collisions with all targets. In such cases the targets should be ranked according to their risk factor values and a sequence of collision avoidance manoeuvres should be applied.

In [5] the following ideas have been combined: double coordinate system used in CTPA, a fuzzy ship domain [3] and approach factor f_{\min} – a new measure of collision risk derived from the concept of a ship domain [4]. Approach factor f_{\min} has been defined as the scale factor of the largest domain-shaped area that is predicted to remain free of other ships throughout the whole encounter situation. The result presented in [5] has been a new visualization method called Fuzzy Collision Threat Parameters Area (FCTPA). It has been based on Collision Threat Parameters Areas method and has extended it so as to handle any given domain, including fuzzy domains.

In this paper the FCTPA method is further modified and a generalized version of a formula for collision risk [6, 7, 8] is applied. The original formula presented in [6, 7, 8] took into account both DCPA (Distance at the Closest Point of Approach), and TCPA (Time remaining to the Closest Point of Approach), thus emphasizing the direct threat of the nearest close encounters. It also reflected the non-linearity of the collision risk (as a function of distance and time) near the critical values of minimum safe distance D_s and minimum time for manoeuvring T_s . The generalized version of the formula replaces DCPA and TCPA with f_{\min} and t_{\min} – the approach factor value and the time remaining to reaching this value. The modified version of the FCTPA visualization method applying the new formula for collision risk factor is called Two-Parameter Collision Threat Area (TPCTA).

The rest of the paper is organized as follows. Section 2 briefly describes the CTPA method. In Section 3 the formulas for collision risk assessment are provided and in Section 4 the new TPCTA method is presented. An exemplary scenario of using this method is given in Section 5. Finally Section 6 is a summary of the paper.

COLLISION THREAT PARAMETERS AREA (CTPA)

In [1] a collision threat is defined as a target ship for which the following condition holds:

$$DCPA < D_s \quad (1)$$

The method uses a double Cartesian coordinate system where the horizontal axis represents both the X coordinate of position and V_x coordinate of speed and the vertical axis represents both the Y coordinate of position and V_y coordinate of speed. The relation between the position and speed coordinates is as follows:

$$\begin{aligned} x &= V_x * \tau \\ y &= V_y * \tau \end{aligned} \quad (2)$$

where:

τ – fixed time value, for example 12 minutes.

The Collision Threat Parameters Area for a single target ship is defined as an area in the abovementioned system of coordinates that fulfils the following conditions:

- ★ placing the tip of the own speed vector V within this area would result in violating the safe distance D_s between the ships
- ★ placing the tip of the own speed vector V outside this area would result in keeping the safe distance D_s between the ships.

The Collision Threat Parameters Area for a group of target ships is defined as a superposition of the Collision Threat Parameters Areas obtained for each of the targets separately. Graphical superposition has been presented in [6, 7, 8]. The formula for the two straight lines determining the boundaries of the CTPA for a given single target is as follows:

$$\begin{aligned} y &= a_1 x - b_1 \tau \\ y &= a_2 x - b_2 \tau \end{aligned} \quad (3)$$

where the coefficients are given by the formulas:

$$a_1 = \frac{x_r y_r + D_s \sqrt{x_r^2 + y_r^2 - D_s^2}}{x_r^2 - D_s^2} \quad (4)$$

$$a_2 = \frac{x_r y_r - D_s \sqrt{x_r^2 + y_r^2 - D_s^2}}{x_r^2 - D_s^2}$$

$$b_1 = a_1 V_{tx} - V_{ty} \quad (5)$$

$$b_2 = a_2 V_{tx} - V_{ty}$$

where:

x_r, y_r – coordinates of the relative position of the target ship

V_{tx}, V_{ty} – coordinates of the true speed of the target ship.

In practice, CTPA is only this part of the determined area, where the condition $TCPA > 0$ holds, since only future collision threats are of interest. Also, in case of a multiple target encounter, the manoeuvres for which the safe distance D_s would be violated after a time longer than the critical time ($DCPA < D_s, TCPA > T_c$) may be allowed, if there is no possibility of avoiding all targets with just one manoeuvre. This means that the tip of the own speed vector may be

conditionally placed within this part of the CTPA, for which $TCPA > T_c$. When applied to the graphical display, the CTPA method enables the operator to choose manually a safe own speed vector in a very easy way – it is enough to choose a point outside the CTPA and read its speed coordinates. The method is summarized by Fig. 1 and Fig. 2.

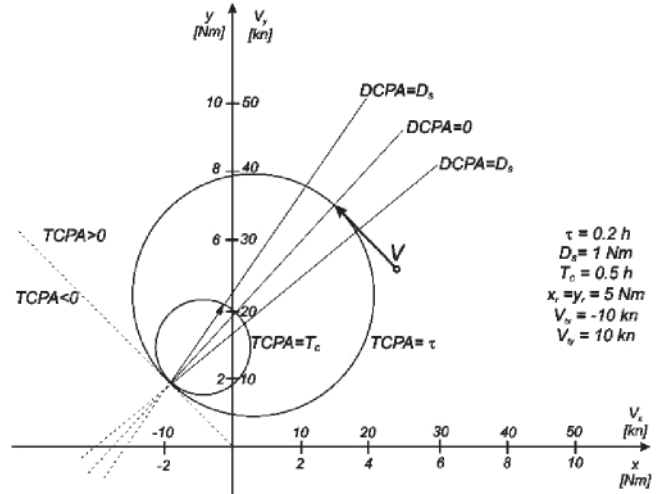


Fig. 1. Collision Threat Parameters Area by Lenart

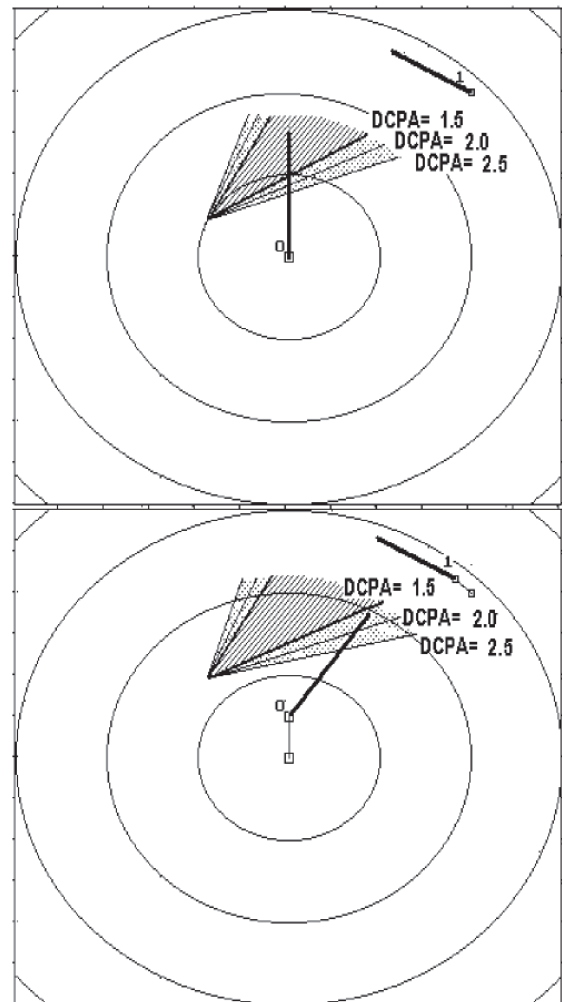


Fig. 2. Graphical interpretation of an encounter of two ships: before a collision avoidance manoeuvre (up side) and after the manoeuvre (down side)

The line of $DCPA = 0$ represents a perfect crash. If the tip of the own speed vector is placed above this line, it means that the own ship will pass ahead of a target, if below this line

– astern of a target. Fig. 2 presents a graphical interpretation of an encounter of two ships: before and after a collision avoidance manoeuvre. The own ship is moving with the speed of 15 knots and course 0 degrees and a target ship with the speed of 10 knots and course 300 degrees. The tip of the own speed vector is placed above the line for DCPA = 1.5 n. m. Therefore a collision avoidance manoeuvre is taken and the new own course is set to 35 degrees. New positions of ships are visualised after the time t representing the physical realization of this manoeuvre.

POINTING OUT THE DIRECT THREATS IN MULTI SHIP ENCOUNTER SITUATIONS

To determine which targets constitute direct threat and have to be avoided first, it is necessary to monitor their motion parameters and to assign to them values of collision risk factor according to a given formula. Such formula for collision risk factor has been proposed by Lisowski [2] and it is as follows.

$$r = \left[a_1 \left(\frac{DCPA}{D_s} \right)^2 + a_2 \left(\frac{TCPA}{T_s} \right)^2 + a_3 \left(\frac{D}{D_s} \right)^2 \right]^{-\frac{1}{2}} \quad (6)$$

where:

- r – collision risk factor
- D – current distance between the own ship and the target ship
- D_s – safe distance of approach (a radius of the circle-shaped domain),
- T_s – a safe time necessary to plan and perform a collision avoidance manoeuvre,
- a_1, a_2, a_3 – weight coefficients, dependent on the state of visibility at sea, dynamic length and dynamic beam of the ship and a kind of water region.

The advantage of this formula is that it can be applied to any target. However, the formula will indicate a considerable risk for DCPA = D_s and TCPA = 0, that is, when the ships pass each other at a safe distance and there is no risk involved any more.

It must be emphasized that the most important elements affecting collision risk are: vector of relative speed (the superposition of the own speed and the speed of a target) and the lack of change of the target's bearing. These elements have been taken into account in [6,7,8]. Additionally it has been proposed there to limit the considered range of DCPA and TCPA values to the real collision risk area. ($|DCPA| \in (0, D_s)$ and $TCPA \in (0, nT_s)$), as given by conditions of formula (7). CTPA method by Lenart has been used, with the following modification applied: the function (7) has been introduced, which is strongly non-linear around the critical values of DCPA and TCPA. Thus modified collision risk factor r as a function of DCPA and TCPA is also shown in Fig. 3.

$$r = \begin{cases} a * \left[e^{-b \left(\frac{DCPA}{D_s} \right)^2} - 0.1 \right] \left[\frac{T_s}{TCPA} - c \right] & \text{for } \begin{matrix} DCPA < D_s \\ \text{and} \\ TCPA < nT_s \end{matrix} \\ 0 & \text{for } \begin{matrix} DCPA \geq D_s \\ \text{or} \\ TCPA \geq nT_s \end{matrix} \end{cases} \quad (7)$$

where:

$$1 \geq r \geq 0 \quad n > 1$$

- a, b, c – values determined in the course of simulation:
 $a = 1.11, b = 1.52, c = 0.33.$

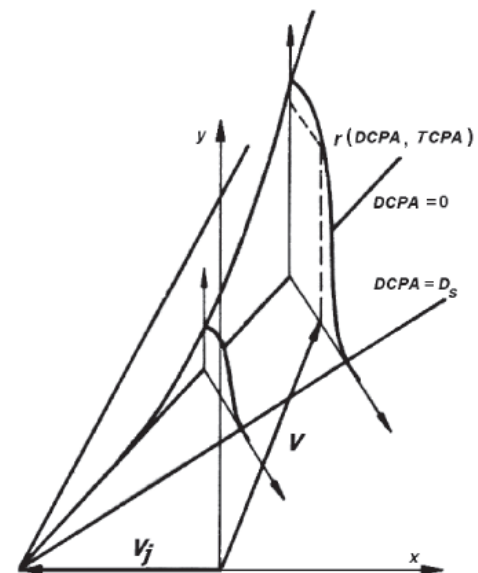


Fig. 3. Geometrical interpretation of collision risk factor

In the formula above the DCPA/ D_s quotient is used, which is exactly the approach factor value f_{min} [4] for a circle-shaped domain. In case of using a ship domain model other than that, this quotient can be replaced with the f_{min} value obtained for this model. Similarly TCPA might be replaced with the time remaining to reaching f_{min} value. The generalization of the formula (7), which would hold true for any given ship domain would thus be:

$$r = \begin{cases} a * \left[e^{-bf_{min}^2} - 0.1 \right] \left[\frac{T_s}{T_{f_{min}}} - c \right] & \text{for } \begin{matrix} f_{min} < 1 \\ \text{and} \\ T_{f_{min}} < nT_s \end{matrix} \\ 0 & \text{for } \begin{matrix} f_{min} \geq 1 \\ \text{or} \\ T_{f_{min}} \geq nT_s \end{matrix} \end{cases} \quad (8)$$

Using the formula (8), we can rank the targets according to the decreasing values of the risk factor r .

DIRECT COLLISION THREAT PARAMETERS AREA (DCTPA).

In this section a visualization tool that has been designed by the authors – Direct Collision Threat Parameters Area (DCTPA) is presented. It is based on the same concept of the forbidden area in the double Cartesian coordinate system, but instead of determining the area analytically for a fixed D_s value, it is determined numerically for a given ship domain. It works as follows. For every combination of the own course and speed the resulting f_{min} value is computed (the algorithms used to compute the f_{min} value for given courses, positions and speeds of the own ship and target ships have been presented in detail in [4]). Then for each combination of the own course and speed the risk factor for each target is computed according to formula (8) and the minimal of those risk factor values is assigned to the current combination of course and speed.

Depending on the obtained value, a point in the double Cartesian coordinate system representing a particular combination of the own speed and course is assigned a colour in the following way:

- ⊕ for $0.75 < r \leq 1$ (critical collision risk): black
- ⊕ for $0 < r \leq 0.75$ (significant collision risk): gradually changing dark grey
- ⊕ for $0 < r \leq 0.5$ (significant collision risk): gradually changing light grey
- ⊕ for $r = 0$ (safe passing): white

The proposed visualisation tool is shown in Fig. 4

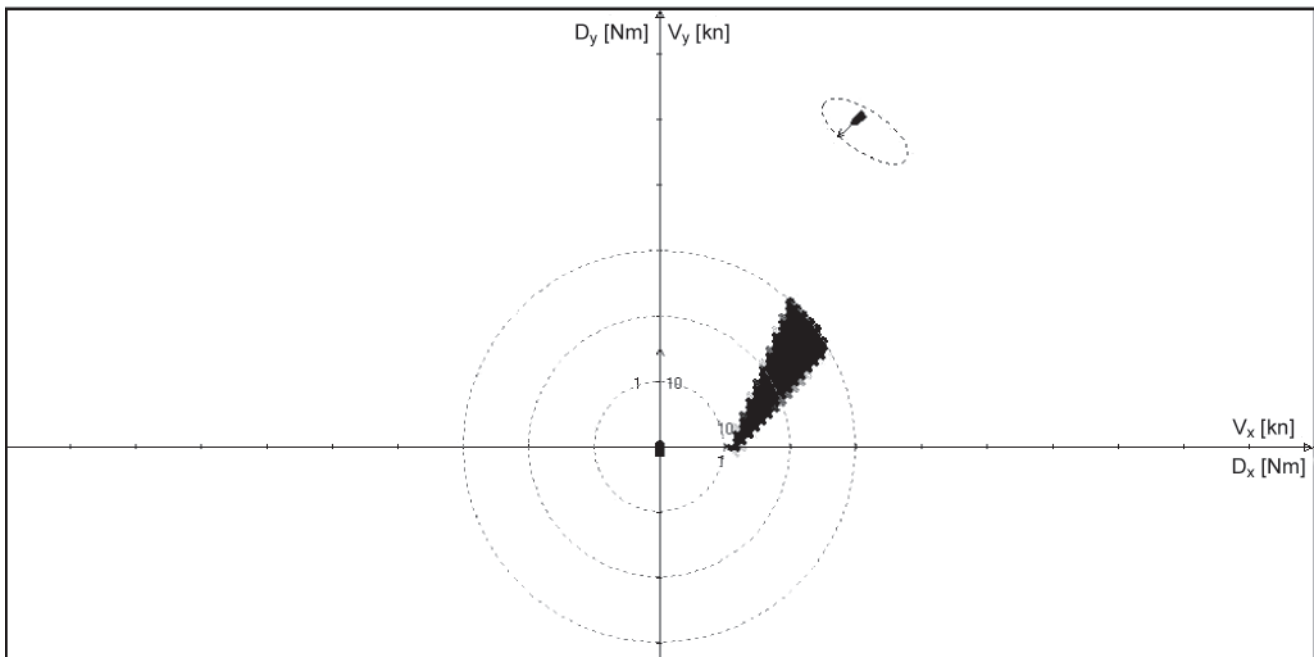


Fig. 4. Direct Collision Threat Parameters Area

Whenever the arrow indicating the end of the own speed vector appears on the dark grey or black background – a collision avoidance manoeuvre should be performed. The closest white point on the display represents a safe combination of the own speed and course. For the situation in Fig. 4 the tip of the own speed vector is on the white background (outside the forbidden sector associated with the target), hence the current combination of course and speed is safe.

AN EXEMPLARY SCENARIO

In this section it is shown, how visualizing collision risk affects navigational decision. An example, randomly generated scenario, involving 20 targets is analysed here. The initial situation is given in Tab. 1 and Fig. 5.

According to Tab. 1 and Fig. 5, the own ship is approaching a number of target ships, some of them colliding with the

Tab. 1. The positions, courses and speeds of the own ship and the target ships in the exemplary scenario

	Speed [knots]	Course [degrees]	Position coordinates at the start time		Coordinates of the destination point	
			x [n.m.]	y [n.m.]	x [n.m.]	y [n.m.]
Own ship	15	90	0	5	18	5
Target 1	19.3	270	15.6	7.3		
Target 2	16.3	223	11.1	12.0		
Target 3	9.2	334	9.8	4.4		
Target 4	14.4	233	18.9	5.9		
Target 5	6.8	174	10.9	2.5		
Target 6	12.4	167	9.4	6.9		
Target 7	13.8	5	5.7	6.9		
Target 8	14.8	265	6.6	2.8		
Target 9	9.0	306	13.3	8.6		
Target 10	9.1	349	15.0	9.4		
Target 11	13.6	223	5.4	8.3		
Target 12	6.9	49	6.4	1.7		
Target 13	10.0	322	8.4	4.4		
Target 14	15.3	2	6.9	9.8		
Target 15	15.4	3	3.0	1.0		
Target 16	18.8	21	19.9	6.6		
Target 17	19.0	146	15.6	0.5		
Target 18	15.9	352	4.0	1.6		
Target 19	15.6	66	10.8	8.2		
Target 20	7.4	280	6.6	5.8		

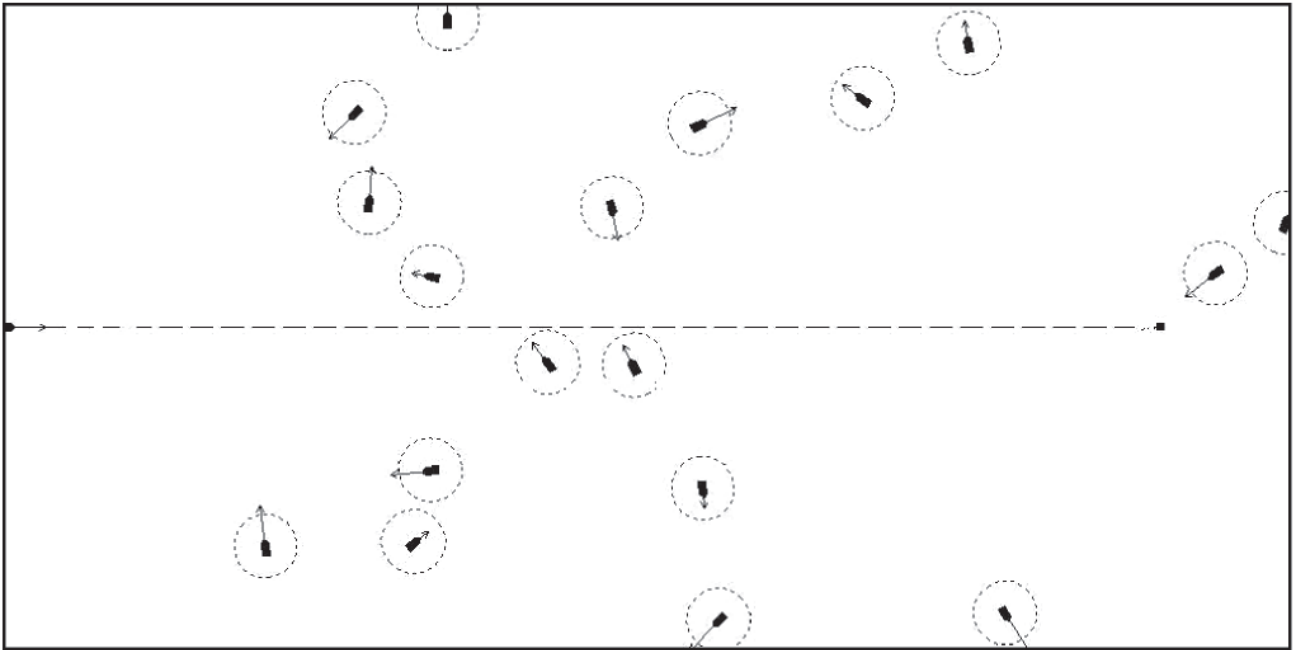


Fig. 5. Position and courses of the own ship and target ships in the exemplary scenario

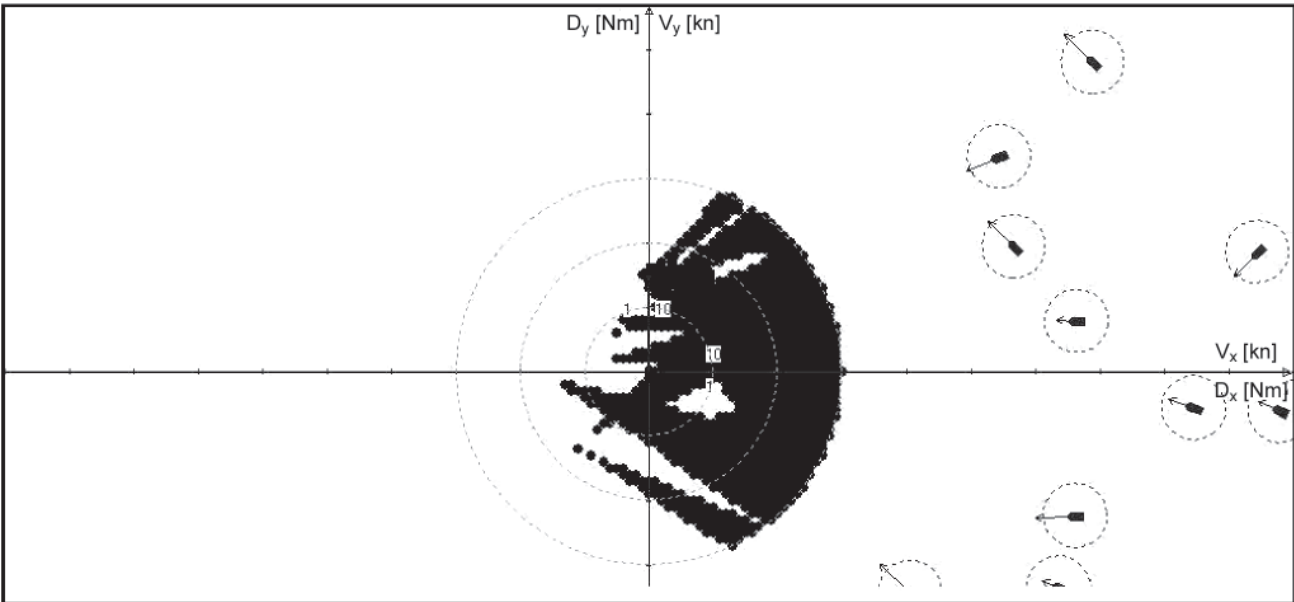


Fig. 6. Forbidden sectors of own course and speed for the exemplary scenario according to CTPA

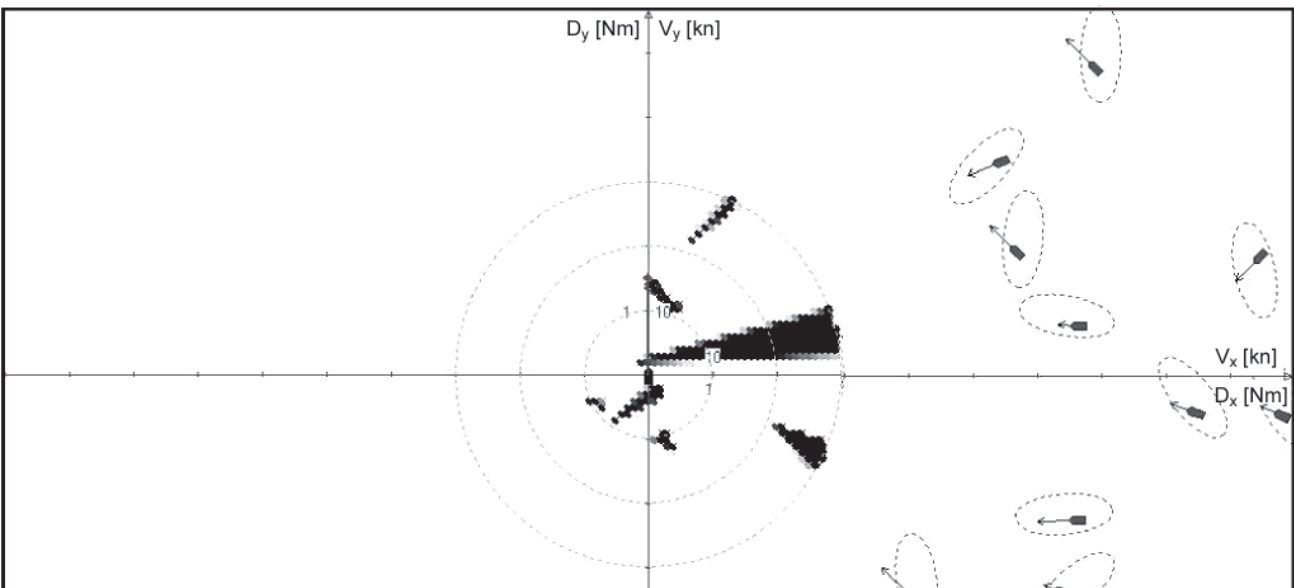


Fig. 7. Forbidden sectors of own course and speed for the exemplary scenario according to DCTPA

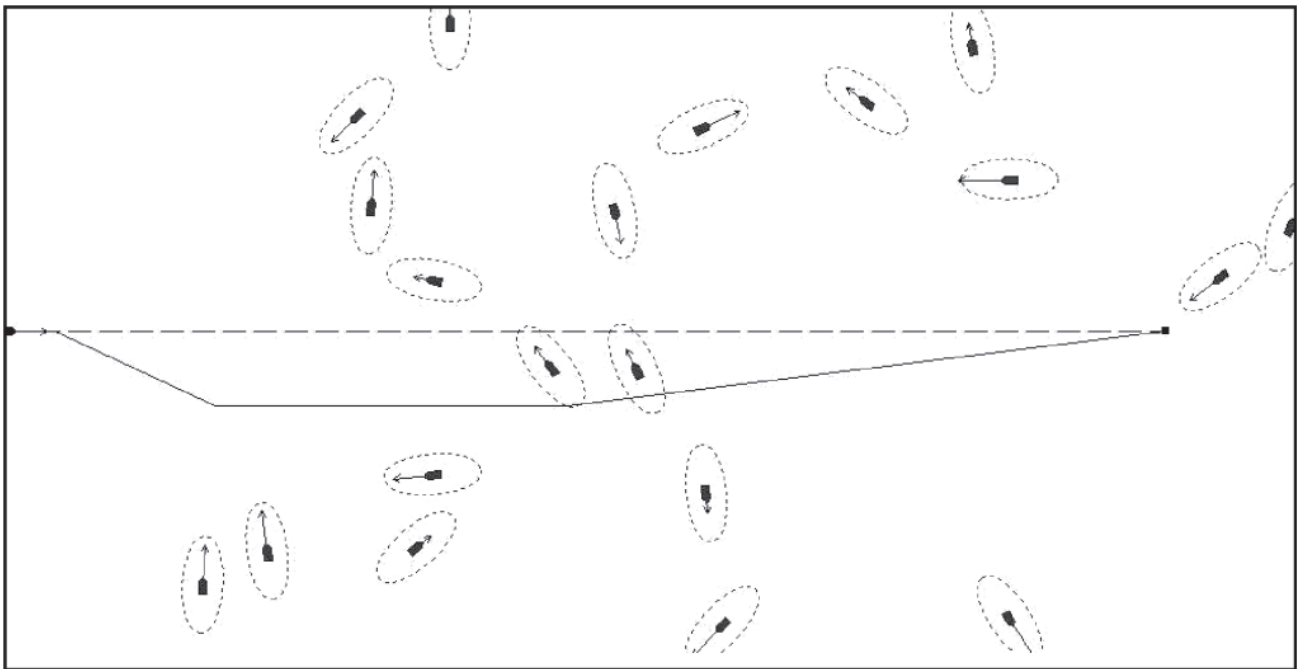


Fig. 8. A safe trajectory of the own ship resulting from a manoeuvre to starboard

own course. The forbidden sectors of own course and speed (Collision Threat Parameters Area) for the safe distance of 0.5 nautical mile look as shown in Fig. 6. Due to the large number of targets it is impossible to choose a single course alteration manoeuvre to starboard (recommended by COLREGS) that avoids collisions with all of the targets.

However, applying the proposed visualization tool enables the navigator to assess the situation better than that. According to the proposed method, the Direct Collision Threat Parameters Area for the initial situation looks as depicted in Fig. 7. The Coldwell domain is used here for target ships.

From the collision risk visualized in Fig. 7, the navigator may easily conclude, that although the current course and speed are not safe (the tip of the own speed vector is on the forbidden area), it is possible to perform a course alteration manoeuvre to starboard, which avoids collision with the directly threatening target. As a result, a trajectory containing the manoeuvre to starboard might be planned, as shown in Fig. 8.

SUMMARY AND CONCLUSIONS

Visualizing collision risk is especially important in multi-ship encounter situations, when the own course and speed collides with more than one target. Unfortunately, in such situations it is not always possible to avoid collision by performing a single, lawful collision avoidance manoeuvre. Therefore the targets have to be ranked according to the risk they constitute. This risk depends not only on the minimum distance between the ships (or the domain violation) but also on the time remaining to the point of the closest approach. Particularly threatening are situations when domain violations are accompanied by short times remaining to the encounters. In such situations the proposed solution enables the navigator to point out the most dangerous targets and avoid them in the first place. Once these targets have been safely passed, the navigator may focus on the targets constituting lesser risk. The proposed solution is fast enough to be applied in the real-time decision-support system, where fast processing of the data concerning all targets is a necessity.

BIBLIOGRAPHY

1. Lenart A.S.: *Collision threat parameters for a new radar display and plot technique*. The Journal of Navigation, 36, 1982

2. Lisowski J.: *Determining the Optimal Ship Trajectory in Collision Situation*. Proceedings of the IX International Scientific and Technical Conference on Marine Traffic Engineering, AM, Szczecin, 2001
3. Pietrzykowski Z., Gućma L.: *Theoretical Basis of the Probabilistic – Fuzzy Method for Assessment of Dangerous Situation of a Ship Manoeuvring in a Restricted Area* (in Polish). Annual of Navigation 3, Academy of Sciences, Polish Navigation Forum, Gdynia, 2001
4. Szłapczyński R.: *A unified measure of collision risk derived from the concept of a ship domain*. Journal of Navigation, 59, issue 3, 2006
5. Szłapczyński R.: *Fuzzy Collision Threat Parameters Area (FCTPA) - a new display proposal*. Proceedings of the 7th International Symposium of Navigation TransNav'2007. AM, Gdynia, 2007
6. Śmierzchałski R.: *Decision support in collision situation at sea* (in Polish). Proceedings of the 4th International Symposium Technological Progress of Military Equipment „Inter-Arms”, Gdynia, 1996
7. Śmierzchałski R.: *The Decision Support System to Design the Safe Manoeuvre Avoiding Collision at Sea*. Proceedings of the 14th International Conference Information Systems Analysis and Synthesis, Orlando, 1996
8. Śmierzchałski R.: *Practical methods to make decision of safe manoeuvre and trajectory avoiding collision at sea*. ELMAR 2000, Zadar, 2000
9. Sperry Marine ARPA – CAS II - technical documentation.

CONTACT WITH AUTHORS

Rafał Szłapczyński, Ph. D.
Faculty of Mechanical Engineering
Gdansk University of Technology
Narutowicza 11/12
80-952 Gdansk, POLAND
e-mail : rafal@pg.gda.pl

Roman Śmierzchałski, Assoc. Prof.
Faculty of Marine Engineering,
Gdynia Maritime University
Morska 83
81-225 Gdynia, POLAND
e-mail: roms@am.gdynia.pl



The Ship Handling Research and Training Centre at Ilawa is owned by the Foundation for Safety of Navigation and Environment Protection, which is a joint venture between the Gdynia Maritime University, the Gdansk University of Technology and the City of Ilawa.

Two main fields of activity of the Foundation are:

- Training on ship handling. Since 1980 more than 2500 ship masters and pilots from 35 countries were trained at Ilawa Centre. The Foundation for Safety of Navigation and Environment Protection, being non-profit organisation is reinvesting all spare funds in new facilities and each year to the existing facilities new models and new training areas were added. Existing training models each year are also modernised, that's why at present the Centre represents a modern facility perfectly capable to perform training on ship handling of shipmasters, pilots and tug masters.
- Research on ship's manoeuvrability. Many experimental and theoretical research programmes covering different problems of manoeuvrability (including human effect, harbour and waterway design) are successfully realised at the Centre.

The Foundation possesses ISO 9001 quality certificate.

Why training on ship handling?

The safe handling of ships depends on many factors - on ship's manoeuvring characteristics, human factor (operator experience and skill, his behaviour in stressed situation, etc.), actual environmental conditions, and degree of water area restriction.

Results of analysis of CRG (collisions, rammings and groundings) casualties show that in one third of all the human error is involved, and the same amount of CRG casualties is attributed to the poor controllability of ships. Training on ship handling is largely recommended by IMO as one of the most effective method for improving the safety at sea. The goal of the above training is to gain theoretical and practical knowledge on ship handling in a wide number of different situations met in practice at sea.

For further information please contact:

The Foundation for Safety of Navigation and Environment Protection

Head office:
36, Chrzanowskiego street
80-278 GDAŃSK, POLAND
tel./fax: +48 (0) 58 341 59 19

Ship Handling Centre:
14-200 ILAWA-KAMIONKA, POLAND
tel./fax: +48 (0) 89 648 74 90
e-mail: office@ilawashiphandling.com.pl
e-mail: office@portilawa.com

GDANSK UNIVERSITY OF TECHNOLOGY

is the oldest and largest scientific and technological academic institution in the Pomeranian region. The history of Gdansk University of Technology is marked by two basic dates, namely: October 6, 1904 and May 24, 1945.

The first date is connected with the beginning of the technical education at academic level in Gdansk. The second date is connected with establishing of Gdansk University of Technology, Polish state academic university. Gdansk University of Technology employ 2,500 staff, 1,200 whom are academics. The number of students approximates 20,000, most of them studying full-time. Their career choices vary from Architecture to Business and Management, from Mathematics and Computer Science to Biotechnology and Environmental Engineering, from Applied Chemistry to Geodesics and Transport, from Ocean Engineering to Mechanical Engineering and Ship Technology, from Civil Engineering to Telecommunication, Electrical and Control Engineering. Their life goals, however, are much the same - to meet the challenge of the changing world. The educational opportunities offered by our faculties are much wider than those of other Polish Technical universities, and the scientific research areas include all of 21st Century technology. We are one of the best schools in Poland and one of the best known schools in Europe – one that educates specialists excelling in the programming technology and computer methods used in solving complicated scientific, engineering, organizational and economic problems.

THE FACULTY OF OCEAN ENGINEERING AND SHIP TECHNOLOGY

The Faculty of Ocean Engineering and Ship Technology (FOEST) as the only faculty in Poland since the beginning of 1945 has continuously been educating engineers and doctors in the field of Naval Architecture and Marine Technology.

The educational and training activities of FOEST are supported by cooperation with Polish and foreign universities, membership in different international organizations and associations, as well as participation in scientific conferences and symposia. Hosting young scientists and students from different countries is also a usual practice in FOEST.

The activities of Faculty departments are related to: mechanics and strength of structures, hydromechanics, manufacturing, materials and system quality, power plants, equipment and systems of automatic control, mostly in shipbuilding, marine engineering and energetic systems.

FOEST is a member of such organizations like WEGEMT; The Association of Polish Maritime Industries and the co-operation between Nordic Maritime Universities and Det Norske Veritas. The intensive teaching is complemented and supported by extensive research activities, the core of which is performed in close collaboration between FOEST staff and industry. We take great care to ensure that the applied research meet both the long term and short term needs of Polish maritime industry. FOEST collaborates with almost all Polish shipyards. Close links are maintained with other research organizations and research institutions supporting the Polish maritime industry, such as Ship Design and Research Centre and Polish Register of Shipping, where several members of the Faculty are also members of the Technical Board.

The Faculty of Ocean Engineering and Ship Technology is a unique academic structure, which possesses numerous highly qualified and experienced staff in all above mentioned specific research areas. Moreover, the staff is used to effective co-operation and exchange of ideas between specialists of different detailed areas. This enables a more integrated and comprehensive treatment of research and practical problems encountered in such a complicated field of activity as naval architecture, shipbuilding and marine engineering.

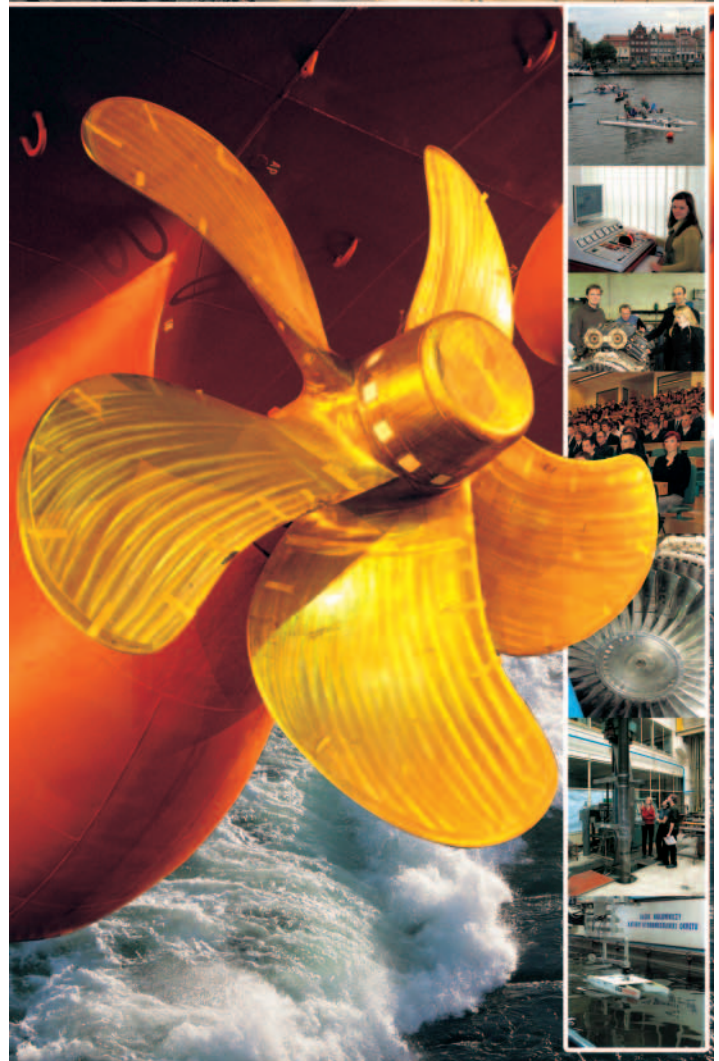
The staff of the Faculty has strong international links worldwide, being members or cooperating with international organizations like International Maritime Organization IMO, International Towing Tank Conference ITTC, International Ship and Offshore Structures Congress ISSC, International Conference on Practical Design of Ship and other floating Structures PRADS just to name a few.

GDANSK UNIVERSITY OF TECHNOLOGY
Faculty of Ocean Engineering and Ship Technology
11/12 Narutowicza Street, 80-952 Gdansk, Poland
Tel (+48) 58 347 1548 ; Fax (+48) 58 341 4712
e-mail: sekoce@pg.gda.pl



Gdansk University of Technology

Faculty of Ocean Engineering and Ship Technology



www.oce.pg.gda.pl